UNIVERSITY OF SOUTHAMPTON

Nonlinear dynamics of a nematic liquid crystal in the presence of a shear flow

Eva Vicente Alonso

Thesis submitted for the Degree of Doctor of Philosophy

Faculty of Mathematical Studies

October, 2000

UNIVERSITY OF SOUTHAMPTON

ABSTRACT

FACULTY OF MATHEMATICAL STUDIES

MATHEMATICS

Doctor of Philosophy

NONLINEAR DYNAMICS OF A NEMATIC LIQUID CRYSTAL IN THE PRESENCE OF A SHEAR FLOW

by Eva Vicente Alonso

In this thesis we describe the complex array of behaviours of a homogeneous thermotropic nematic liquid crystal in the context of a Landau-de Gennes theory. There exist two parameters that control the behaviour of the system: the temperature and the shear rate, and by employing continuation and bifurcation theory we describe the different time dependent states for the two and three dimensional cases.

For the two dimensional case we compute the steady state solution branches finding that the flow favours an in-plane nematic state at higher temperatures, while at lower temperatures it favours a nematic state with preferred direction of alignment perpendicular to the shear plane, the so-called log-rolling state. We have found excellent agreement between the numerical calculations and analytical results in the limit of very low and very large values of the shear rate. The existence of a Takens-Bogdanov bifurcation in the underlying bifurcation diagram organises the steady and the time dependent solutions in the state diagram. The periodic orbits can be either of the wagging type, at intermediate values of the shear rate or of the tumbling type at lower shear rates. We complete the analysis of the two dimensional case, by considering a general planar flow and studying the influences of strain and vorticity in the system.

We provide a very detailed account of the behaviour of the liquid crystal in the three dimensional case, when the direction of alignment of the molecules that constitute the liquid crystal is allowed out of the shear plane. We establish that the only out-of-plane steady solution of the system is an anomalous continuum of equilibria, and therefore the Landau-de Gennes model that we are employing is structurally unstable. The time dependent solutions of the liquid crystal fall into one of the following categories: in plane periodic orbits, which are the tumbling and wagging solutions and out-of-plane periodic orbits, the so-called kayaking state.

The use of bifurcation theory in the context of nematodynamics allows us to give a complete summary of the nonlinear behaviour of a nematic liquid crystal in a shear flow, for the two and three dimensional cases.

Contents

List of Figures

Acknowledgments

I would like to thank Professor Adam Wheeler for all the time and effort he has put into this thesis, he has guided me these last three years and has been a great pleasure working with him.

I have also learnt from many others but I feel I am in great debt with Professor Tim Sluckin, who introduced me to the physics of liquid crystals and with Dr. David Chillingworth, who guided me along the paths of bifurcation theory.

Many others in the Department of Mathematics at the University of Southampton have done my life easier and I would like to thank everyone here, but specially Dr. Craine and Dr. D'Alessandro, who were always very helpful. A huge thanks goes to the "Applied Girls", Gaby and Sharon. It has been wonderful sharing an office and so many unfinished cross-words with you both. Good luck girls!

I have been very happy at Southampton, where I have met wonderful people from all over the world. To all of them, wherever they are, many thanks.

But all these years would not have been the same if I would not have shared wonderful moments, and two houses with my friends Javi, Salva, Jacinto, Alberto and Gisela. I offer them all my love and my friendship.

I am grateful to the friends I still have in Galicia for keeping our friendship over the years. María, Pili, Celia and Bea made the years at University in Santiago much easier to bear.

I thank my family: my parents Emilio and Milucha, my little wonderful sister María and my grandparents. They all love me unconditionally, and I am very proud of them. *Os quiero muchísimo.*

And I couldn't forget Martiño: I love you, and now, that is my turn to support you through your PhD, I just hope I can do it as well as you have done it for me. Thank you, *corazón.*

The research presented in this thesis has been supported by EPSRC and the Faculty of Mathematical Studies at the University of Southampton and I am grateful for it.

Chapter 1

Introduction

The aim of this thesis is to give an account of the dynamical behaviour of a liquid crystal in the presence of a shear flow in the context of a Landau-de Gennes model. In order to develop the mathematical theory and present the finding of my research I first set the scene and give a brief descriptive overview of liquid crystals as well as the models that have been developed to describe them, subsequently I present an outline of the contents of the following chapters of this thesis and its motivation.

1.1 Liquid crystals

A liquid crystalline phase is a state of matter between a solid crystalline phase, when the molecules of the system form a three dimensional lattice, and an isotropic liquid phase where the molecules are not ordered in space [1, 2]. The molecules that constitute a liquid crystal have spatial orientational as well as positional disorder. Depending on the ordering of the molecules in the liquid crystalline phase we can distinguish the following phases [3]:

Nematic phase

In average, the rod-like molecules, that constitute the liquid crystal, are parallel to a given direction determined by the unit vector $\mathbf{n}$, a sketch of this phase is shown in figure 1.1. The molecules that constitute the nematic phase carry a dipole, however at a macroscopic level this is not noticeable and the system presents $\mathbf{n}$ to $-\mathbf{n}$ symmetry. When the nematic phase is uniaxial the system has cylindrical symmetry about the $\mathbf{n}$ direction. However, in some cases a secondary direction of alignment, perpendicular to **n**, appears and then the nematic phase is then said to be biaxial.

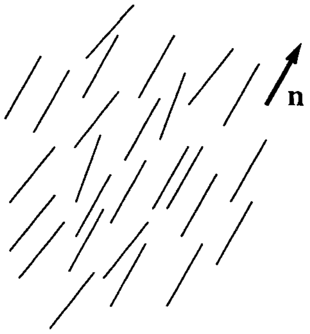

Figure 1.1: Sketch representation of the nematic phase. The rod-like molecules are represented by thin lines. The vector **n** is parallel to the average direction of alignment.

Smectic phases

In the phase the molecules, accounting for nematic order in the direction of the unit vector **n**, are also layered and the unit vector **k** indicates the direction normal to the layers. Depending on the ordering within each layer the liquid crystal can be classified into different types. We discuss each one in turn:

Smectic-A: In this state the nematic director, **n**, and the vector normal to the layers, **k**, are parallel. This phase is sketched in figure 1.2.

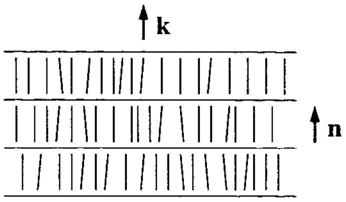

Figure 1.2: Sketch of the smectic-A phase.

Smectic-C: In this state the nematic director and the vector normal to the layers are not parallel, and the angle between them, ω, is called the tilt parameter. This phase is sketched in figure 1.3.

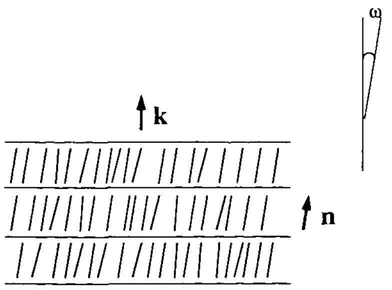

Figure 1.3: Sketch of the smectic-C phase. The angle ω that $\mathbf{n}$ forms with $\mathbf{k}$ is the tilt order parameter.

Smectic-B:In this phase, shown in figure 1.4, a smectic-A phase with rod shaped molecules forms a hexagonal pattern within each layer, with the molecules aligned perpendicular to each layer, so that $\mathbf{k}$ and $\mathbf{n}$ are parallel.

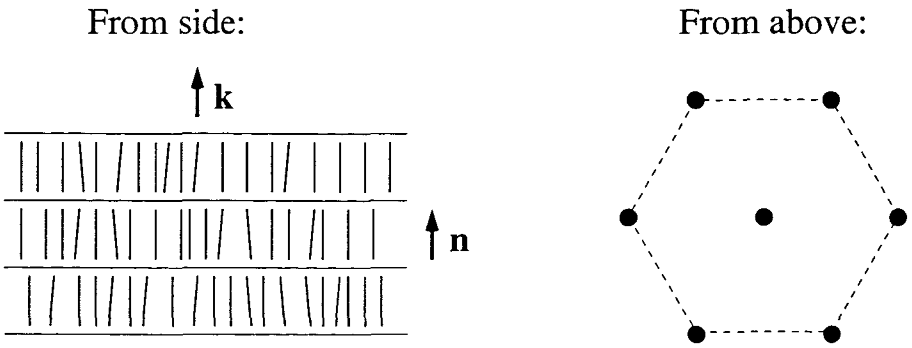
From side:

From above:

Figure 1.4: Sketch of the smectic-B phase.

Smectic-I: This phase is similar to a smectic-B phase except the molecules comprising each layer are tilted towards a vertex of their hexagonal arrangement. This phase is shown in figure 1.5.

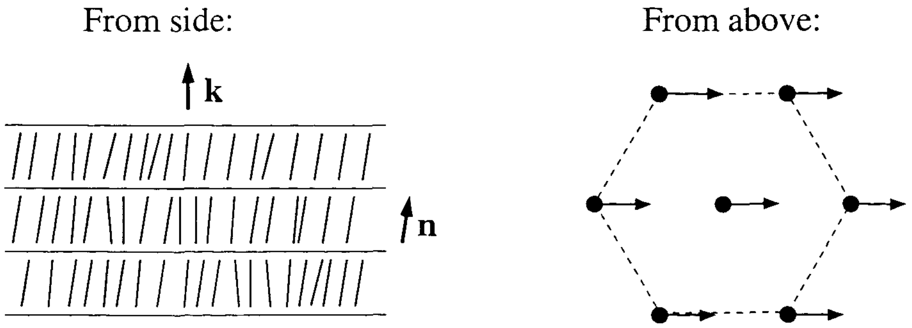
From side:

From above:

Figure 1.5: Sketch of the smectic-I phase.

Smectic-F: This phase is similar to a smectic-B phase except the molecules comprising each layer are tilted towards the middle of an edge of their hexagonal arrangement. This phase is shown in figure 1.6.

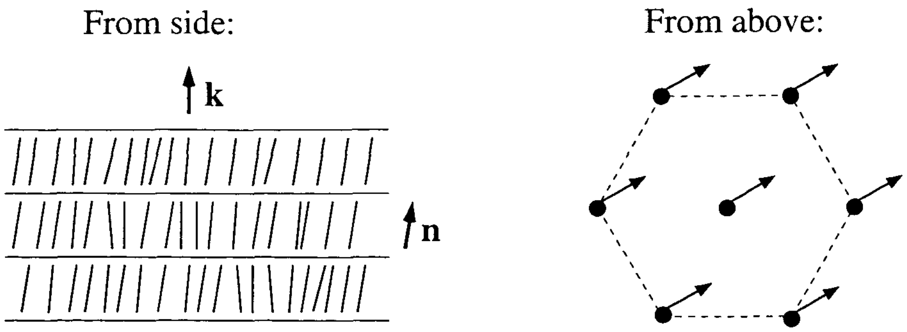

Figure 1.6: Sketch of the smectic-F phase.

These are some examples of smectic phases, but there are many other examples that we will not describe here (experimentalists have found up to smectic-Q phases). Both the nematic and smectic phases explained above are constituted by rod-like molecules (the so-called calamitic liquid crystals), but the constituents of a liquid crystal can also be disc-like molecules and then the nematic director would be the average orientation of the vector normal to the molecules.

Sometimes the molecules are chiral (different from its mirror image) and then new phases arise with helical structure. A nematic formed by chiral molecules is called a cholesteric phase.

We have, so far, classified the liquid crystal according to the symmetries of the phases, however, different criteria allow different classifications of the liquid crystals. Attending to the size of the building blocks we can consider [4]:

- Low molecular weight liquid crystals (LMWLC). The liquid crystal is constituted by small elongated molecules. The traditional examples of LMWLC are *p*-azoxyanisole (PAA) and *N*-(*p*-methoxybenzylidene)-*p*-butylaniline, also known as MBBA. The main application of these liquid crystals is in optical displays;
- Liquid crystal polymers (LCP). The constituent blocks are rigid rod-like macromolecules (polymers). Example of these materials include DNA, cellulose fibres and high-performance fibres.

When the substance is in a pure state and the liquid crystalline phases appear for certain range of temperatures, then the liquid crystal is called thermotropic, while when the substance is in solution with a solvent, and the liquid crystalline phases appear beyond a critical concentration, then the liquid crystal is called lyotropic. For the latter the role of temperature in the system is very difficult to control and slight changes in the temperature might produce catastrophic changes in the ordering of the

system.
This is a vary brief introduction on the description and classification of the liquid crystalline phases, and we now summarise the different models of nematodynamics and its suitability for our study: the dynamic behaviour of calamitic thermotropic low molecular weight liquid crystals.

1.2 The theories of nematodynamics: a literature review

The dynamics of liquid crystalline materials under a flow have been studied over the last forty years, and different theories exist applicable to different types of liquid crystals.

Leslie and Ericksen [5, 6, 7, 8, 9] were pioneers in the study of the dynamics of nematics (nematodynamics). They employ a model which regards them as an anisotropic fluid by introducing the director vector $\mathbf{n}$. Their formulation is a macroscopic formulation and takes into consideration the viscous character of the fluid as well as the long range order elasticity, i.e., the effects of inhomogeneities in the system.
The Leslie-Ericksen (LE) theory takes no account for the biaxiality of the liquid crystal and nor can it describe the nematic-isotropic phase transition, since it does not account for the effects of short range order elasticity. In section 3.2 we give a more detailed account of this theory. However, the LE theory has been widely used to model low molecular weight (LMW) nematics, and very good agreement has been achieved with experimental results.
Leslie [10] and subsequently Zúñiga and Leslie [11, 12] predicted successfully the instability at a critic shear rate of a LMW nematic liquid crystal with an initial direction of alignment perpendicular to the shear plane. This has been previously observed experimentally by Pieranski and Guyon [13].
Further instabilities were found experimentally by Cladis and Torza [14] in a Couette flow in concentric cylinders and Zúñiga [15] theoretically explained the existence of this phenomena using LE theory.
The stability and multistability of solutions was first analysed by Currie and MacSithigh [16] and by the same method, years later, by McIntosh et al. [17]. Using a more sophisticated approach to the LE theory, employing numerical adaptive methods and bifurcation theory, Han and Rey [18, 19, 20] were able to predict more complicated

textures of the liquid crystal as twisted and banded nematics.
The LE theory has also been employed to liquid crystal polymers [21], specially for predictions of director tumbling as done by Marrucci [22], Burghardt and Fuller [23, 24] and Srinivaraso and Berry [25].

However, LE theory theory is not the most widely used model to describe the dynamical behaviour of LCP. The rod-like molecular model of Doi and Edwards [26, 27] is commonly employed to describe the behaviour of this type of material.
This theory measures the degree of ordering of the system making use of the probability distribution function $f(\mathbf{u})$, where $\mathbf{u}$ is a unit vector indicating the direction of the main axis of a rod-like molecule. Thus, Doi's theory takes into account the possibility of the existence of a biaxial system. Furthermore, this theory models the nematodynamics using a Smoluchowski equation, including details on molecular behaviour and short range order elasticity, but excluding the effects of long range order elasticity. Therefore this formulation can describe the isotropic-nematic phase transition and different rheological behaviours, but it does not account for the non-homogeneity of the liquid crystal.
Considerable research has been carried out in the area of polymer nematodynamics using Doi's theory. Initially, numerical simulations of this model were able to predict shear alignment, tumbling and wagging at different values of the strain rate and nematic potential. The two dimensional case was study by Marrucci and Maffettone [28] and Larson [29] and Larson and Öttinger [30] extended the previous work to the three dimensional case.
However, a substantial advance in the understanding of the rheology of LCP using Doi's theory was made when bifurcation theory was used to solve the model. This provided a systematic explanation of the behaviour of liquid crystalline materials in terms of the nematic potential and shear rate of the system. Maffettone and Crescitelli [31] and Faraoni et al. [32] described the bifurcation set of the behaviour of a LCP in the two and three dimensional cases respectively. They approximated the distribution function by a truncated Fourier series.
Further studies in the area of applications of bifurcation theory to the dynamics of liquid crystalline materials involve the analysis and comparison of different closures approximations of the Doi model [33, 34] , since it is easier to compare state diagrams of constitutive equations than coarse numerical simulations.
Finally the comparison between Doi's theory and experimental results has only been done relatively recently, since LE theory is still the main theory of reference. However the works of Magda et al. [35], Maruyama et al [36], Friedenberg et al. [37] and Maf-

fettone et al. [38] show excellent agreement between the theoretical predictions and experiments of LCP in the presence of shear and extensional flows.

In recent years several groups have developed theories where long and short range order elasticity were included in the system, and therefore changes of phases as well as inhomogeneities could be simultaneously considered. The majority of these theories use a tensor order parameter, the second momentum of the distribution function, to measure the degree of ordering in the system. In this thesis we will use a Landau-de Gennes theory for thermotropic liquid crystals that was derived initially by Hess [39] and subsequently by Olmsted and Goldbart [40, 41] and employed by them to described the isotropic nematic phase transition [41, 42, 43], and also used by Popa-Nita et al.[44] to describe the effects of biaxiality in the phase transition. Farhoudi and Rey [45] and Tsuji and Rey [4, 46, 47] described in a series of papers their own theory that matches in different limits the LE theory and Doi's theory.

1.3 Outline of the thesis

This thesis presents the behaviour of a homogeneous nematic liquid crystal in the presence of a shear flow in the context of the Landau-de Gennes theory. The complex array of behaviours is explained in terms of the control parameters of the system: the temperature and the shear rate.

Chapter 2 introduces the basic concepts needed to develop the Landau-de Gennes theory: the distribution function and order parameter (Lubenski, [48]), which are measures for the degree of anisotropy of the system, and the Landau free energy. The equilibrium bulk states, those which minimise the free energy of the system, are also described here.

The concepts introduced in chapter 2 set the basis to discuss in chapter 3 the Landau-de Gennes theory of nematodynamics. Here we closely follow the derivation that Olmsted and Goldbart [41] made of the Landau-de Gennes model. The governing equations of our system are set in this chapter.

Once the system of governing equations has been introduced we present, in chapter 4, the concepts and tools of bifurcation theory that will be needed in the development of our research.

From chapters 1 to 4 we set the basis of our research, but it is in chapters 5, 6 and 7 where the results are presented.

In chapter 5 we study the two dimensional case, where two of the vectors of the local basis that determine the position of the distribution function are confined to the shear plane. Consequently the preferred direction of alignment of the solutions of the system can lie in the shear plane or, otherwise, in the direction perpendicular to this plane. In this chapter we describe the two different solution branches of the system: the IPN branch, where the stable steady solution is an in-plane nematic state occurring at high temperatures, and the LRN branch where the stable stationary solution is a uniaxial state with preferred direction of alignment perpendicular to the shear plane, the so-called log-rolling state. The time dependent solutions for the two dimensional case, the tumbling and wagging states, are also carefully described and a Takens-Bogdanov bifurcation is found on the system, organising the steady states and time dependent behaviours. This provide a good understanding of the difference between tumbling and wagging. The state diagram presented in section 5.5 summarises the array of behaviours of the nematic liquid crystal in the different regions of the parameter space. The dynamics of the two dimensional homogeneous liquid crystal in the presence of a more general flow are described in chapter 6 in terms of the vorticity and strain of the flow.

The study of the dynamical behaviour of a nematic concludes by allowing solutions that are not symmetric with respect to the shear plane: this is the three dimensional case. The results regarding this case are presented in chapter 7, where we find that the only stable steady state solutions are those of the two dimensional case and, moreover, the purely three dimensional stationary solutions are a degenerate continuum of equilibria, whose existence we can be explained in geometrical terms, with arguments presented in a paper by Chillingworth, Vicente Alonso and Wheeler [49]. The time dependent solutions of the three dimensional case are also studied in chapter 7. They can be either of the tumbling or wagging type, as described for the two dimensional case, or of the kayaking type, where the periodic orbits are not confined to the shear plane. The complete state diagram of the three dimensional case, as shown in chapter 7, provides full understanding of the three dimensional dynamical behaviour of the liquid crystal.

The conclusions to this thesis and directions for future research are summarise in chapter 8.

Chapter 2

Bulk states

We consider a bulk nematic liquid crystal to be constituted of rod-like molecules that have orientational order but not positional order. Therefore a nematic bulk phase is qualitatively different from an isotropic phase where neither orientational nor positional order is present in the system. In a nematic phase the molecules, averaged locally in space, are oriented parallel to a unit vector $\mathbf{n}$, the so-called director. However we can distinguish between nematics of different symmetries: so called uniaxial and biaxial nematic phases. It has been observed [1] that uniaxial nematics have rotational symmetry about the $\mathbf{n}$-axis, and the states of the director being $\mathbf{n}$ or $-\mathbf{n}$ are physically indistinguishable. In contrast biaxial nematics still have the $\mathbf{n}$ to $-\mathbf{n}$ symmetry but do not preserve the rotational symmetry about the director and hence there is a secondary preferred direction perpendicular to the director.

The classical approach of Leslie-Ericksen theory which considers a director vector $\mathbf{n}$ as a measure of the order of the system is sufficient to describe the dynamics of nematics under flow, but it does not provide a description of the microscopic behaviour of the liquid crystal, i.e., it does not account for the degree of order at molecular level. To overcome this difficulties de Gennes [1] and Lubensky [48] describe the order in a liquid crystal by using a second rank tensor that captures the microscopic properties.

We describe the distribution of the orientations of the molecules by employing a probability density function that depends on orientation through the polar coordinates $(\theta,\ \phi)$. Figure 2.1 shows sketches of the probability distribution function for three different phases of a liquid crystal; uniaxial nematic, biaxial nematic and isotropic.

Consider $\mathbf{N}$ to be the unit vector parallel to the main axis of a particular rod-like molecule. If the director $\mathbf{n}$ is considered to be in the z-direction then $\mathbf{N} = (\sin\theta\cos\phi, \sin\theta\sin\phi, \cos\theta)$, where θ and ϕ are the polar angles with respect to $\mathbf{n}$, as

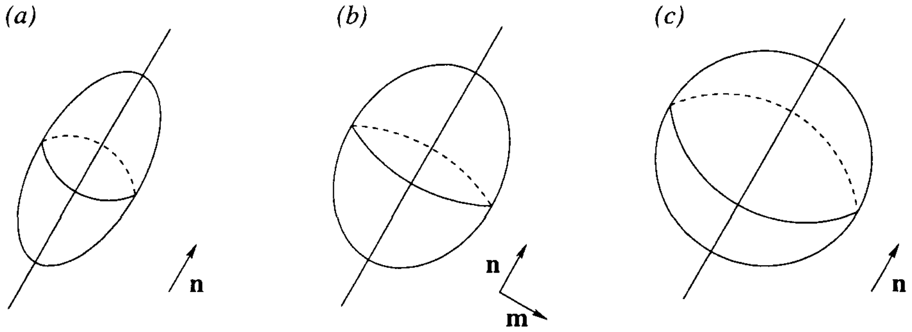

Figure 2.1: Probability distribution function for the different states. Figure (*a*) represents the distribution for the uniaxial nematic state where the molecules prefer to align in a direction parallel to the unit vector **n**, the so-called director. This state is invariant under rotations about the **n**-axis. Figure (*b*) shows the biaxial state where **n** is the principal direction of alignment but there is no rotational symmetry about **n**, but rather a secondary direction of alignment parallel to the unit vector **m** perpendicular to **n**. Figure (*c*) corresponds to the isotropic state, where all the directions have the same probability and therefore the probability distribution function is spherical.

shown in Figure 2.2. The probability of finding molecules aligned in range of angles $d\theta$, $d\phi$ around the direction (θ, ϕ) is then given by $f(\theta,\phi)\sin\theta\, d\theta\, d\phi$. By definition the integral of the distribution function over all the possible states is

$$\int_0^{2\pi}\int_0^{\pi} f(\theta,\phi)\sin\theta\, d\theta\, d\phi = 1\,, \tag{2.1}$$

and since in the isotropic phase $f(\theta,\phi)$ does not depend on the polar angles then $f(\theta,\phi) = k$, where $k = 1/4\pi$ satisfies equation (2.1).

To define the order parameter we will use averages of functions $g(\theta,\ \phi)$ over the orientations of the molecules which are defined by

$$\langle g(\theta,\phi)\rangle = \int_0^{2\pi}\int_0^{\pi} g(\theta,\phi) f(\theta,\phi)\sin\theta\, d\theta\, d\phi\,.$$

A scalar or vector order parameter is not enough to account for all the symmetries of our system, particularly a vector order parameter could not account for the **n** to $-$**n** symmetry, thus it is necessary to introduce a second rank tensor as an order parameter, and to do so we consider the second-order moment of the orientational distribution [21], given by

$$\mathrm{S} = \langle \mathrm{N}\otimes\mathrm{N}\rangle\,,$$

where $\otimes$ is the tensor product.

In the isotropic phase where $f(\theta,\phi) = 1/4\pi$ we have that

$$\mathrm{S} = \frac{1}{4\pi}\int_0^{2\pi}\int_0^{\pi} (\mathrm{N}\otimes\mathrm{N})\sin\theta\, d\theta\, d\phi = \frac{1}{3}\mathbf{I}\,,$$

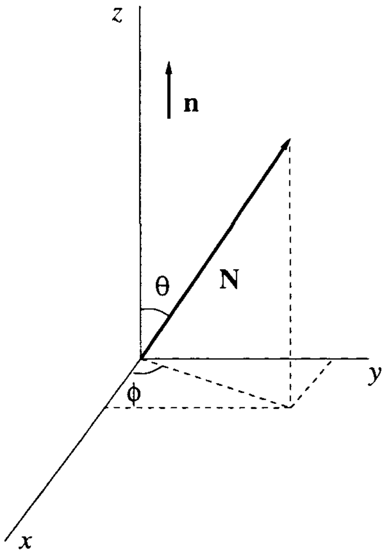

Figure 2.2: The unit vector parallel to the main axis of a road-like molecule **N** is plotted together with the director vector **n** and the polar angles θ and ϕ .

where **I** is the identity second rank tensor. It is conventional to require the tensor order parameter to be zero in the isotropic phase and non-zero otherwise. Therefore we define the tensor order parameter [1, 48] as

$$\mathbf{Q} = \mathbf{S} - \frac{1}{3}\mathbf{I} = \langle \mathrm{N} \otimes \mathrm{N} \rangle - \frac{1}{3}\mathbf{I}. \tag{2.2}$$

The second rank tensor defined by (2.2) is symmetric ($Q_{ij} = Q_{ji}$) and traceless, the latter due to the fact that N is a unit vector, so that $\mathrm{tr}\left(\langle \mathrm{N} \otimes \mathrm{N} \rangle\right) = 1$ and hence $\mathrm{tr}(\mathbf{Q}) = 0$.

We now evaluate the order tensor parameter in different phases:

In the isotropic phase we have chosen the order tensor parameter such that $\mathbf{Q} = 0$.

In the uniaxial nematic phase the tensor can be written in terms of the director vector, **n**, as follows

$$\mathbf{Q} = \frac{3}{2} S_1 \left(\mathbf{n} \otimes \mathbf{n} - \frac{1}{3}\mathbf{I} \right) , \tag{2.3}$$

where S_1 is the uniaxial scalar order parameter and it is given by

$$S_1 = \mathbf{Q} : (\mathbf{n} \otimes \mathbf{n}) = \left\langle \mathrm{N} \otimes \mathrm{N} - \frac{1}{3}\mathbf{I} \right\rangle : (\mathbf{n} \otimes \mathbf{n}) , \tag{2.4}$$

where the operator : is the inner product of the tensor space defined by $\mathbf{A} : \mathbf{B} = \mathrm{tr}(\mathbf{A}^T\mathbf{B})$. The polar angle θ is measured from **n**, hence we can re-write equation 2.4 as

$$\begin{aligned} S_1 &= \int_0^{2\pi}\int_0^{\pi} \left[\left(\mathrm{N} \otimes \mathrm{N} - \frac{1}{3}\mathbf{I} \right) : (\mathbf{n} \otimes \mathbf{n}) \right] f(\theta,\, \phi) \sin\theta \, d\theta \, d\phi \\ &= \int_0^{2\pi}\int_0^{\pi} \left[(\mathrm{N} \cdot \mathbf{n})^2 - \frac{1}{3}|\mathbf{n}|^2 \right] f(\theta,\, \phi) \sin\theta \, d\theta \, d\phi \end{aligned}$$

$$\begin{aligned} &= \int_0^{2\pi}\int_0^{\pi}\left(\cos^2\theta - \frac{1}{3}\right) f(\theta,\, \phi)\sin\theta\, d\theta\, d\phi \\ &= \left\langle \cos^2\theta - \frac{1}{3}\right\rangle . \end{aligned} \tag{2.5}$$

In the uniaxial case the cylindrical symmetry about the **n**-axis implies $f(\theta, \phi) = f(\theta)$ and the equation $f(\pi - \theta) = f(\theta)$ is a consequence of the $\mathbf{n}$ to $-\mathbf{n}$ symmetry of the system. Hence

$$\int_0^{2\pi}\int_0^{\pi} f(\theta,\phi)\sin\theta\, d\theta\, d\phi = 4\pi\int_0^{\pi/2} f(\theta)\sin\theta\, d\theta = 1\,.$$

Re-scaling the probability distribution function by $\tilde{f}(\theta) = 4\pi f(\theta)$ we get

$$\int_0^{\pi/2} \tilde{f}(\theta)\sin\theta\, d\theta = 1\,.$$

In the isotropic phase $\tilde{f}(\theta) = 1$, while in a completely aligned state the distribution function is a Dirac function peaked at $\theta = 0$ for an elongated distribution and at $\theta = \pi/2$ for a disk-like distribution where $\mathbf{n}$ is the least preferred direction. Then, from equation (2.5) we obtain that

$$S_1 = \left\langle \cos^2\theta - \frac{1}{3}\right\rangle = \int_0^{\pi/2} \tilde{f}(\theta)\sin\theta\left(\cos^2\theta - \frac{1}{3}\right) d\theta\,.$$

Integrating the different distributions we find that S_1 is zero for the isotropic phase, S_1 is positive in the uniaxial phase with an elongated distribution function, and $S_1 = 2/3$ when the system is completely ordered. If S_1 is negative we have a disk-like distribution and $S_1 = -1/3$ when the system is completely aligned perpendicular to the director. Thus we find that in general $-1/3 \leq S_1 \leq 2/3$. Figure 2.3 shows sketches of the probability distribution function for the elongated and disk-like uniaxial nematic phases.

In the biaxial phase the order parameter (2.2) can be written [48, 41] as

$$\mathbf{Q} = \frac{3}{2}S_1(\mathbf{n}\otimes\mathbf{n} - \frac{1}{3}\mathbf{I}) + \frac{1}{2}S_2(\mathbf{m}\otimes\mathbf{m} - \mathbf{l}\otimes\mathbf{l}) \tag{2.6}$$

where $\{\mathbf{n},\, \mathbf{m},\, \mathbf{l}\}$ is a local orthonormal basis, S_1 is the uniaxial order parameter as given in equation (2.5) and S_2 is similarly defined by

$$S_2 = \mathbf{Q}\colon(\mathbf{m}\otimes\mathbf{m} - \mathbf{l}\otimes\mathbf{l}) = \left\langle \mathrm{N}\otimes\mathrm{N} - \frac{1}{3}\mathbf{I}\right\rangle\colon(\mathbf{m}\otimes\mathbf{m} - \mathbf{l}\otimes\mathbf{l})\,.$$

The polar angle θ is measured from $\mathbf{n}$ and ϕ is measured from $\mathbf{m}$ and we obtain

$$S_2 = \int_0^{2\pi}\int_0^{\pi}\left[\left(\mathrm{N}\otimes\mathrm{N} - \frac{1}{3}\mathbf{I}\right)\colon(\mathbf{m}\otimes\mathbf{m} - \mathbf{l}\otimes\mathbf{l})\right] f(\theta,\, \phi)\sin\theta\, d\theta\, d\phi$$

$$
\begin{aligned}
&= \int_0^{2\pi}\int_0^{\pi} \left[(\mathbf{N}\cdot\mathbf{m})^2 - (\mathbf{N}\cdot\mathbf{l})^2 - \frac{1}{3}|\mathbf{m}|^2 + \frac{1}{3}|\mathbf{l}|^2\right] f(\theta,\,\phi)\sin\theta\, d\theta\, d\phi \\
&= \int_0^{2\pi}\int_0^{\pi} \left(\cos^2\phi\sin^2\theta - \sin^2\phi\sin^2\theta\right) f(\theta,\,\phi)\sin\theta\, d\theta\, d\phi \\
&= \left\langle \cos(2\phi)\sin^2\theta \right\rangle .
\end{aligned}
$$

Since $\mathbf{Q}$ is a symmetric traceless tensor, it is defined by five independent components, or, alternatively by S_1, S_2, and the three angles which determine the orientation of the $\{\mathbf{n},\mathbf{m},\mathbf{l}\}$ triad with respect to a fixed frame of reference.When both S_1 and S_2 are zero $\mathbf{Q}$ is zero and the probability distribution function is uniform and the state of matter is isotropic.

If $S_1 \neq 0$ and $S_2 = 0$ then $\mathbf{Q} = S_1(3\mathbf{n}\otimes\mathbf{n} - \mathbf{I})/2$ (equation (2.4)), and $\mathbf{n}$ is the average preferred direction. In this case the ordering is uniaxial; $\mathbf{n}$ is called the director and S_1 denotes the degree of order in a direction parallel to $\mathbf{n}$ in this case. We have already seen that if $S_1 > 0$ the distribution function adopts an elongated form and if $S_1 < 0$ we have a disk-like distribution.

When $S_1 \neq 0$ and $S_2 \neq 0$ the ordering is biaxial, with additional orientational nonuniformity in a direction which does not coincide with $\mathbf{n}$; S_2 denotes the biaxial amplitude.

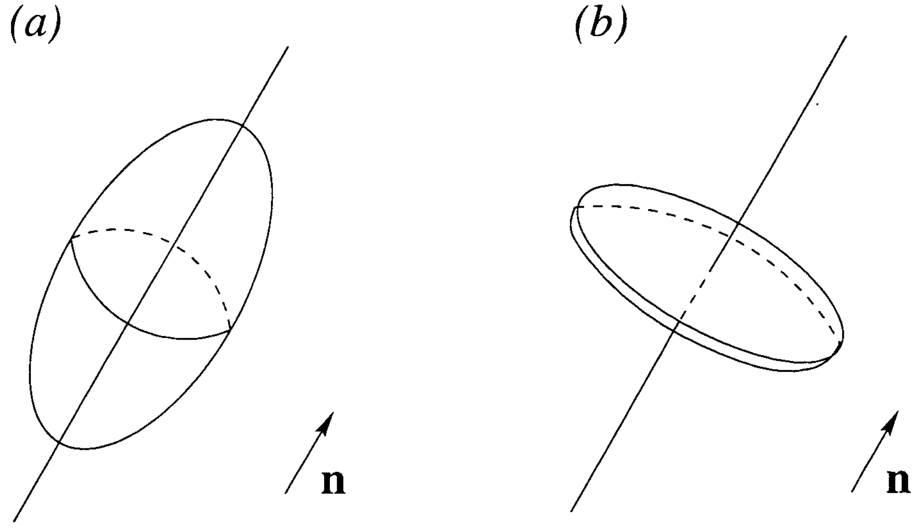

Figure 2.3: Probability distribution function for different uniaxial nematic phases. Figure (a) represents the distribution for the uniaxial nematic state where the molecules prefer to align in a direction parallel to the unit vector $\mathbf{n}$, the so-called director. Figure (b) shows the uniaxial state where $\mathbf{n}$ is the least preferred direction of alignment. Here the distribution function lies in a plane perpendicular to the director vector $\mathbf{n}$. Both states are uniaxial and therefore invariant under rotations about the $\mathbf{n}$-axis.

We observe that the uniaxial case also occurs when either $S_2 = 3S_1$ and $S_2 = -3S_1$. If

$S_2 = 3S_1$ then $\mathbf{Q} = -S_1(3\mathbf{l}\otimes\mathbf{l} - \mathbf{I})$ which corresponds to a uniaxial situation with $\mathbf{l}$ as distinguished direction; when $S_1 < 0$ then $\mathbf{l}$ is the preferred direction and the probability distribution function has an elongated form in the $\mathbf{l}$ direction, while if $S_1 > 0$ then $\mathbf{l}$ is the least preferred direction and the distribution function is disk-like in the plane containing $\mathbf{n}$ and $\mathbf{m}$. Similarly, when $S_2 = -3S_1$ then $\mathbf{Q} = -S_1(3\mathbf{m}\otimes\mathbf{m} - \mathbf{I})$ and $\mathbf{m}$ is the distinguished direction. The distribution function is elongated in a direction parallel to $\mathbf{m}$ when $S_1 < 0$ and disk-like in the plane determined by $\mathbf{n}$ and $\mathbf{l}$ when $S_1 > 0$.

The Landau-de Gennes theory [1, 50] describes the equilibrium bulk states of the system as those that minimise the free energy functional

$$\mathcal{F} = \int_V f_b \, dV ,$$

where V is the volume of the system and $f_b = f_b(\mathbf{Q}, T)$ is the bulk (Landau) free energy density.

The isotropic-nematic transition in liquid crystals is a first order phase transition so the Landau theory holds for temperatures slightly below T_{IN}, the isotropic-nematic transition temperature, and we can perform a Landau-de Gennes expansion for uniaxial nematics of the bulk free energy density [50] in terms of the invariants of $\mathbf{Q}$

$$\begin{aligned} f_b &= \frac{1}{2}A\mathrm{tr}(\mathbf{Q}^2) + \frac{1}{3}B\mathrm{tr}(\mathbf{Q}^3) + \frac{1}{4}C\left(\mathrm{tr}(\mathbf{Q}^2)\right)^2 + \mathrm{O}(\mathbf{Q}^5) \\ &= \frac{1}{2}AQ_{ij}Q_{ji} + \frac{1}{3}BQ_{ij}Q_{jk}Q_{ki} + \frac{1}{4}C(Q_{ij}Q_{ji})^2 + \mathrm{O}(Q_{ij}^5) , \end{aligned} \tag{2.7}$$

where we are using summation over repeated indices. The absence of a linear term is a consequence of $\mathbf{Q}$ being a traceless tensor. Consequently $\mathbf{Q} = 0$, the isotropic phase, is always a stationary point of the free energy, independently of the values of A, B and C. The cubic term in the expansion exists because $\mathbf{Q}$ to $-\mathbf{Q}$ is not a symmetry of our system. We can truncate the expansion of f_b to the fourth order when we are considering temperatures close to T_{IN}, and under this assumption A can be considered to depend linearly on the temperature [1, 50], $A = a(T - T_{SC})$, where T_{SC} is the supercooling limit, the temperature slightly below T_{IN} where the isotropic phase stops being metastable to become unstable. We can also assume that the dependence of B and C on the temperature can be neglected and therefore they are constants.

We introduce a non-dimensional temperature, $\overline{\tau}$, and non-dimensional order parameters, $\overline{S}_1$, $\overline{S}_2$, of the form

$$\overline{\tau} = \frac{27AC}{B^2} , \tag{2.8}$$

$$\overline{S}_1 = -\frac{9C}{2B}S_1 , \tag{2.9}$$

$$\overline{S}_2 = -\frac{3C}{2B}S_2 , \tag{2.10}$$

as well as a non-dimensional bulk free energy density given by

$$\bar{f}_b = \frac{3^6 C^3}{B^4} f_b \, .$$

Omitting the overbars we get

$$f_b = \tau(S_1^2 + 3S_2^2) - 2S_1(S_1^2 - 9S_2^2) + (S_1^2 + 3S_2^2)^2 \, .$$

The equilibrium bulk states, which are the minima of the free energy, are obtained by differentiating f_b with respect to S_1 and S_2 and equating the result to zero, which gives

$$\tau S_1 - 3(S_1^2 - 3S_2^2) + 2S_1(S_1^2 + 3S_2^2) = 0 \, , \qquad (2.11)$$

$$\tau S_2 + 6S_1S_2 + 2S_2(S_1^2 + 3S_2^2) = 0 \, . \qquad (2.12)$$

This system has solutions for S_1 and S_2 in terms of the dimensionless temperature τ.

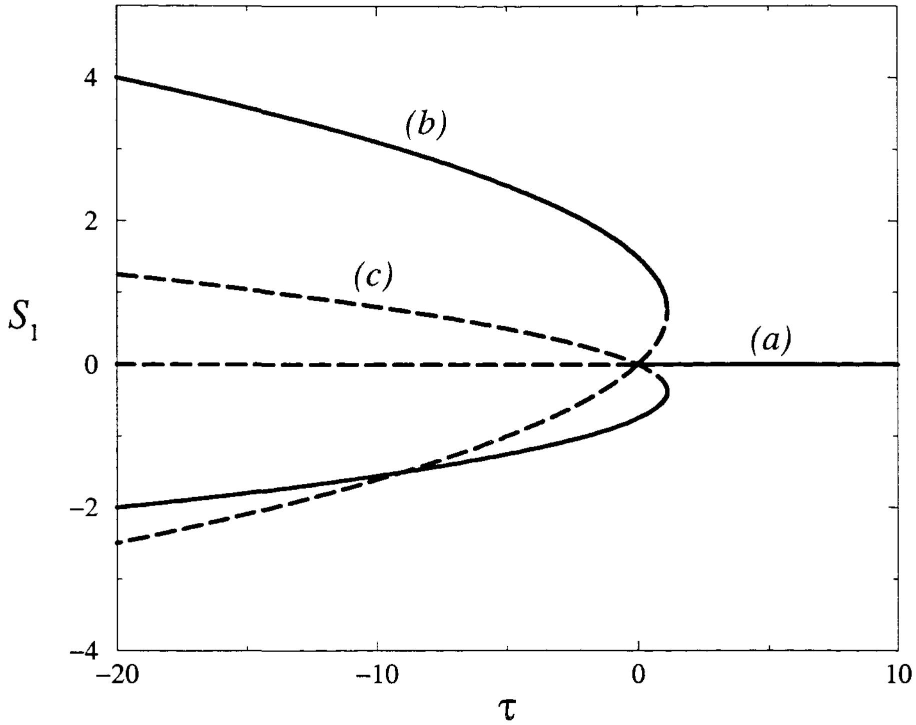

Figure 2.4: Stationary homogeneous states in the absence of flow. The uniaxial order parameter, S_1 is plotted against dimensionless temperature, τ. The isotropic state, branch (a), has $S_1 = S_2 = 0$. Solution branches (b) and (c) correspond to the uniaxial nematic states. Branch (b) is the nematic state with $S_2 = 0$ and $\tau = 3S_1 - 2S_1^2$, while parabola (c) with $\tau = -6S_1 - 8S_1^2$, corresponds to both branches $S_2 = \pm S_1$, which overlie one another in this diagram. The solid lines indicate thermodynamically stable phases, while the dashed lines indicate unstable phases.

It has four different solutions that are shown in figure 2.4. They are (*a*) the isotropic solution branch with $S_1 = S_2 = 0$ for all values of the dimensionless temperature τ;

(*b*) the uniaxial nematic branch with $S_2 = 0$ and $S_1 = \frac{3}{4} \pm \frac{1}{4}\sqrt{9 - 8\tau}$;

(*c*) and the two uniaxial nematic branches $S_2 = \pm S_1$ where $S_1 = -\frac{3}{8} \pm \frac{1}{8}\sqrt{9 - 8\tau}$.

The global minima of f_b are the thermodynamically stable states, while the local minima are the metastable phases. Figure 2.5 shows the free energy plotted against the order parameter S_1 for different values of the dimensionless temperature so that we can observe the stability of the phases:

(*a*) For values of the dimensionless temperature $\tau > 9/8$, the superheating limit, f_b has only one minimum $S_1 = S_2 = 0$, which corresponds to the isotropic phase.

(*b*) For $1 < \tau < 9/8$, f_b has three metastable minima corresponding to the nematic phase which are given by

$$(S_1, S_2) = (S_1^c, 0), \tag{2.13}$$

$$(S_1, S_2) = (-S_1^c/2, S_1^c/2), \tag{2.14}$$

$$(S_1,\ S_2) = (-S_1^c/2, -S_1^c/2), \tag{2.15}$$

where $S_1^c = \left(3 + \sqrt{9 - 8\tau}\right)/4$. These three minima are the representation of the nematic phase where the preferred direction is $\mathbf{n}$, $\mathbf{m}$ or $\mathbf{l}$ respectively. For this temperature range the global minimum of the system occurs at the isotropic phase where $S_1 = S_2 = 0$.

(*c*) At $\tau = 1$ the system undergoes the isotropic-nematic phase transition, where both minima has the same free energy.

(*d*) For $0 < \tau < 1$ the system has three global minima given by (2.13)-(2.15) which correspond to the nematic phase with different directors. The isotropic phase is metastable.

(*e*) For values of $\tau < 0$, the supercooling limit, the isotropic phase is unstable and the liquid crystal is in a stable uniaxial nematic state.

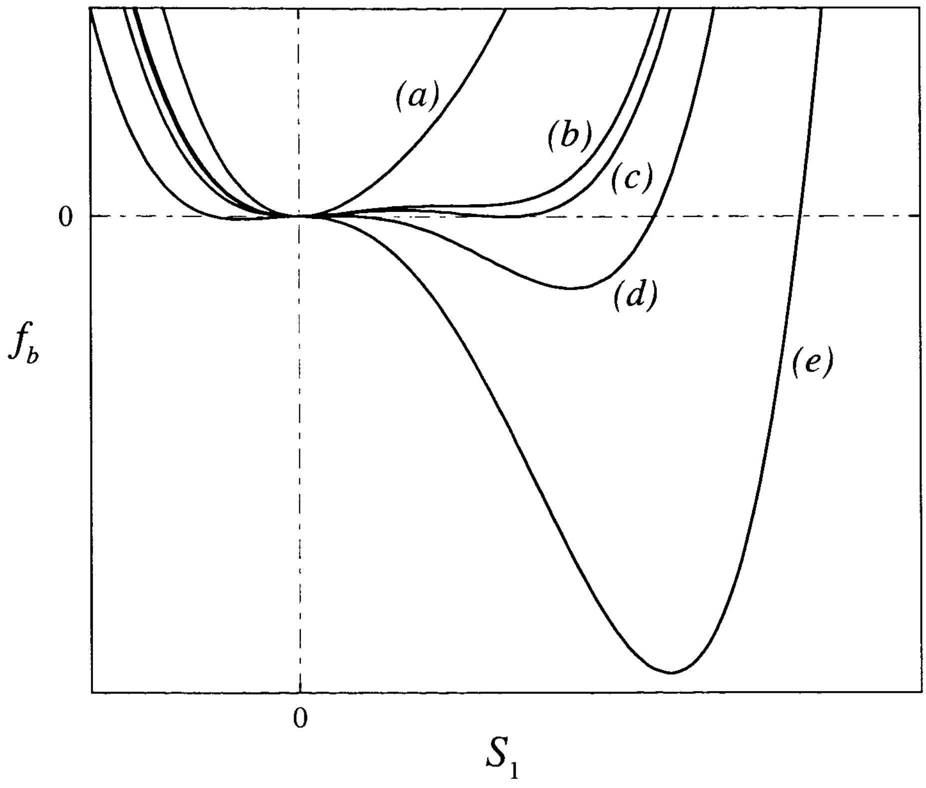

Figure 2.5: The free energy density plotted against the uniaxial order parameter, S_1 for various temperatures. For temperatures higher than the superheating limit $\tau_{SH} = 9/8$, curve (a), the isotropic phase at $S_1 = 0$ is the only minimum of the system. For temperatures between the isotropic-nematic transition, $\tau_{IN} = 1$, and the superheating limit, curve (b), the isotropic phase is the global minimum of the system, therefore this is the stable phase, while the nematic phase is metastable. For the isotropic-nematic transition temperature, curve (c), the two minima corresponding to the isotropic and nematic phases respectively have the same free energy density. For temperatures between τ_{IN} and the supercooling limit $\tau_{SC} = 0$, curve (d), the nematic phase is stable (global minimum), while the isotropic phase is metastable. For temperatures smaller than τ_{SC}, curve (e), only the nematic phases occur.

Chapter 3

Nematodynamics

The dynamics of nematic liquid crystals were first modelled by Leslie and Ericksen [5, 6, 7, 8, 9] who developed a continuum theory of uniaxial nematic liquid crystal under flow. However neither biaxiality nor changes of phase are allowed in the Leslie-Ericksen model, which makes necessary a different model in order to study the nematic-isotropic phase transition. Hess [39] and subsequently Olmsted and Goldbart [41] developed a Landau-de Gennes dynamical theory that describes the nematic-isotropic phase transition in the presence of flow employing the methods of classical linear irreversible thermodynamics [51] and the procedures of de Gennes [1] to derive the Leslie-Ericksen theory.

In this chapter we follow the derivation of the Landau-de Gennes theory and briefly present the Leslie-Ericksen model, subsequently we establish a correspondence between both of them which enable us to interpret the results obtained using the Landau model in terms of the Leslie-Ericksen theory.

3.1 Landau-de Gennes Theory

In this section we will explain the Olmsted and Goldbart derivation of the Landau-de Gennes theory of nematodynamics [41, 40]. Similar models have been also derived by Hess [39] and Qian and Sheng [52].

The Landau-de Gennes theory follows the principles of irreversible thermodynamics [51] and the method of de Gennes of derivation of the Leslie-Ericksen theory [1].

To derive the governing equations we assume local equilibrium thermodynamics and consider the conservation laws, from where we calculate the entropy production. In the resulting expression for the entropy production we identify the the forces and their conjugate fluxes. Assuming that our system is close to equilibrium we can expand the fluxes linearly in the forces. These relationships, together with the conservation laws, will provide us the governing equations of a nematic liquid crystal under flow.

We assume that the liquid crystal is under a flow with associated velocity field $\mathbf{v}$ which obeys the linear momentum equation

$$\rho\dot{\mathbf{v}} = \nabla \cdot \boldsymbol{\sigma}^T \,, \tag{3.1}$$

where ρ is the uniform density of the fluid, the dot denotes the material derivative that is defined by $\partial/\partial t + \mathbf{v} \cdot \nabla$ and $\boldsymbol{\sigma}$ is the stress tensor. We assume our fluid to be incompressible and therefore

$$\nabla \cdot \mathbf{v} = 0 \,. \tag{3.2}$$

For an isothermal process the rate of change of the energy of the system is equal to the rate of change of the free energy of the system together with the entropy production

$$\dot{\mathcal{E}} = \dot{\mathcal{F}} + T\dot{\mathcal{S}} \,, \tag{3.3}$$

where $\mathcal{E}$ is the internal energy, $\mathcal{F}$ is the Helmholtz free energy and $\mathcal{S}$ is the entropy. The total energy of the system is a conserved quantity and its transport occurs on the surface of the arbitrary volume V that we are considering

$$\dot{\mathcal{E}} = \int_\Sigma J_k^{\mathcal{E}} \, d\Sigma_k \,, \tag{3.4}$$

where $\mathbf{J}^{\mathcal{E}}$ is the total energy flux per unit surface and unit time, Σ is the boundary of the volume V and $d\Sigma_k$ is the component of surface normal to the k-th component. The expression for the free energy of the system is

$$\mathcal{F} = \int_V \left(f + \frac{1}{2}\rho|\mathbf{v}|^2 \right) \, dV \,. \tag{3.5}$$

Here f is the free energy density of the system and the second term in the integral represents the kinetic energy.

The entropy is not a conserved quantity and its dissipation, $T\dot{\mathcal{S}}$, is the result of the transport of the entropy through the surface and the entropy production in the interior of the volume

$$T\dot{\mathcal{S}} = T \int_\Sigma J_k^{\mathcal{S}} \, d\Sigma_k + \int_V T\vartheta \, dV \,, \tag{3.6}$$

where $\mathbf{J}^{\mathcal{S}}$ is the entropy production flux per unit time per unit surface and ϑ is the entropy production. Therefore substituting equations (3.4), (3.5) and (3.6) into (3.3) we obtain

$$\int_V T\vartheta \, dV = \int_\Sigma J_k^{\mathcal{E}} \, d\Sigma_k - \int_\Sigma J_k^{\mathcal{S}} \, d\Sigma_k - \dot{\mathcal{F}} \,. \tag{3.7}$$

The second law of thermodynamics states that the entropy production of our system must be non-negative, therefore

$$T\vartheta \geq 0 \,.$$

We need to calculate the rate of change of the free energy with respect to time so we consider the change in the kinetic energy and the change in the free energy density. The latter has to take into account variations in the order parameter and also material deformations keeping the order parameter unchanged, because every change in the system can be decompose independently into changes of either of these types.

We consider first variations in the order parameter given by $\mathbf{Q} \to \mathbf{Q}+\delta\mathbf{Q}$ that conserve the symmetric ($\epsilon_{kij}Q_{ij} = 0$) and traceless ($\delta_{ij}Q_{ij} = 0$) character of $\mathbf{Q}$. In order to simplify the notation we will now write the equation in components, using the Einstein summation convention, instead of the previously used tensor notation. The variation of $\mathcal{F}$ is then

$$\delta\mathcal{F} = \delta\int_V \left(f - \lambda Q_{ij}\delta_{ij} - \lambda_k\epsilon_{kij}Q_{ij}\right) dV \tag{3.8}$$

where δ_{ij} is the Kronecker delta and ϵ_{ijk} is the Levi-Civita tensor and λ and λ_k are four Lagrange multipliers introduced to account for the symmetric and traceless character of $\mathbf{Q}$.

We have $Q^{*}_{ij} = Q_{ij} + \delta Q_{ij}$ and $f = f(Q_{ij}, Q_{ij,k})$, where an index after a comma indicates partial derivative with respect to the k-th component, then we write [53]

$$\delta f = f(Q^{*}_{ij}, Q^{*}_{ij,k}) - f(Q_{ij}, Q_{ij,k}) \,,$$

and expanding for $\delta Q_{ij} \ll 1$, to the first order we have

$$\delta f = f(Q_{ij}, Q_{ij,k}) + \frac{\partial f}{\partial Q_{ij}}\delta Q_{ij} + \frac{\partial f}{\partial Q_{ij,k}}\delta Q_{ij,k} - f(Q_{ij}, Q_{ij,k}) \,, \tag{3.9}$$

then

$$\int_V \delta f\, dV = \int_V \left[\frac{\partial f}{\partial Q_{ij}}\delta Q_{ij} + \frac{\partial f}{\partial Q_{ij,k}}\delta Q_{ij,k}\right] dV \tag{3.10}$$

and integrating by parts we obtain

$$\int_V \delta f\, dV = \int_V \frac{\partial f}{\partial Q_{ij}}\delta Q_{ij}\, dV + \int_\Sigma \frac{\partial f}{\partial Q_{ij,k}}\delta Q_{ij}\, d\Sigma_k - \int_V \left(\frac{\partial f}{\partial Q_{ij,k}}\right)_{,k} \delta Q_{ij}\, dV \,,$$

Assuming that $\mathbf{Q}$ is fixed at the boundary, strong anchoring conditions, then δQ_{ij} vanishes at the surface of the volume and the correspondent integral is zero. Therefore we obtain

$$\int_V \delta f\, dV = \int_V \left[\frac{\partial f}{\partial Q_{ij}} - \left(\frac{\partial f}{\partial Q_{ij,k}}\right)_{,k}\right] \delta Q_{ij}\, dV \,.$$

and the variation of $\mathcal{F}$ with respect to δQ_{ij} (3.8) is

$$\delta\mathcal{F} = \int_V \left[\frac{\partial f}{\partial Q_{ij}} - \left(\frac{\partial f}{\partial Q_{ij,k}}\right)_{,k} - \lambda\delta_{ij} - \lambda_k\epsilon_{kij}\right]\delta Q_{ij}\,dV\,. \tag{3.11}$$

We will calculate the Lagrange multipliers from the equilibrium conditions

$$\frac{\partial f}{\partial Qij} - \left(\frac{\partial f}{\partial Q_{ij,k}}\right)_{,k} - \lambda\delta_{ij} - \lambda_k\epsilon_{kij} = 0\,, \tag{3.12}$$

and contracting this equation with δ_{ij} and with ϵ_{lij} we get

$$\begin{aligned} \lambda &= \frac{1}{3}\left[\frac{\partial f}{\partial Q_{ii}} - \left(\frac{\partial f}{\partial Q_{ii,k}}\right)_{,k}\right], \\ \lambda_l &= \frac{1}{2}\epsilon_{lij}\left[\frac{\partial f}{\partial Q_{ij}} - \left(\frac{\partial f}{\partial Q_{ij,k}}\right)_{,k}\right], \end{aligned}$$

respectively

If we define the molecular field as

$$H_{ij} = -\frac{\delta f}{\delta Q_{ij}} = -\frac{\partial f}{\partial Q_{ij}} + \left(\frac{\partial f}{\partial Q_{ij,k}}\right)_{,k}\,, \tag{3.13}$$

then the equilibrium condition (3.12) is

$$H_{ij}^{[st]} = 0\,,$$

where the script $[st]$ indicates the symmetric and traceless part of the tensor field $\mathbf{H}$ and the variation of $\mathcal{F}$ with respect to δQ_{ij}, equation (3.11), can then be re-written as

$$\delta\mathcal{F} = -\int_V H_{ij}^{[st]}\delta Q_{ij}\,dV\,. \tag{3.14}$$

Now we account for the variation of $\mathcal{F}$ with respect to $\delta\mathbf{r}$, where $\mathbf{r}$ is the position vector and its variation is given by $\mathbf{r} \rightarrow \mathbf{r}^* = \mathbf{r} + \delta\mathbf{r} = \mathbf{r} + \mathbf{u}$, such that it keeps the order tensor unchanged, i.e., $\mathbf{Q}(\mathbf{r}) = \mathbf{Q}(\mathbf{r}+\mathbf{u})$. Under this circumstances

$$\begin{aligned} \delta r_i &= u_i\,, \\ \frac{\partial r_i}{\partial r_j^*} &= \delta_{ij} - \frac{\partial u_i}{\partial r_j^*} \approx \delta_{ij} - \frac{\partial u_i}{\partial r_j} = \delta_{ij} - u_{i,j} \end{aligned}$$

and therefore

$$\delta Q_{ij} = Q_{ij}(\mathbf{r}^*) - Q_{ij}(\mathbf{r}) = 0\,, \tag{3.15}$$

$$\delta Q_{ij,k} = \frac{\partial Q_{ij}}{\partial r_k^*} - \frac{\partial Q_{ij}}{\partial r_k} \approx \frac{\partial Q_{ij}}{\partial r_m}(\delta_{mk} - u_{m,k}) - \frac{\partial Q_{ij}}{\partial r_k} = -Q_{ij,m}u_{m,k}\,. \tag{3.16}$$

Since $\delta Q_{ij} = 0$, equation (3.15), from equation (3.10) we have that

$$\delta \mathcal{F} = \int_V \frac{\partial f}{\partial Q_{ij,k}} \delta Q_{ij,k} \, dV,$$

which is

$$\delta \mathcal{F} = \int_V \frac{\partial f}{\partial Q_{ij,k}} \Big(\frac{\partial Q_{ij}}{\partial r^*_k} - \frac{\partial Q_{ij}}{\partial r_k} \Big) \, dV \tag{3.17}$$

and substituting equation (3.16) into (3.17) we get

$$\delta \mathcal{F} = - \int_V \frac{\partial f}{\partial Q_{ij,k}} Q_{ij,m} u_{m,k} \, dV \, .$$

We need to constrain ourselves to incompressible fluids ($\nabla \cdot \mathbf{u} = 0$), so we introduce a Lagrange multiplier p (the pressure) to account for the incompressibility. The variation of the free energy with respect to $\delta \mathbf{r}$ is then re-written using the Lagrange multiplier as

$$\delta \mathcal{F} = \int_V \Big(- \frac{\partial f}{\partial Q_{ij,k}} Q_{ij,m} u_{m,k} - p \delta_{mk} u_{m,k} \Big) \, dV \, . \tag{3.18}$$

We define the tensors

$$\begin{aligned} \Pi^k_{ij} &= -\frac{\delta f}{\delta Q_{ij,k}} = -\frac{\partial f}{\partial Q_{ij,k}} \, , & (3.19) \\ \sigma^d_{ij} &= \Pi^i_{lm} Q_{lm,j} \, , & (3.20) \end{aligned}$$

and

$$\sigma^r_{ij} = \sigma^d_{ij} - p \delta_{ij} \, . \tag{3.21}$$

Here the tensors $\boldsymbol{\sigma}^d$ and $\boldsymbol{\sigma}^r$ are the distortion stress and reversible viscous stress respectively. Introducing this notation into the variation of $\mathcal{F}$, equation (3.18), we have

$$\delta \mathcal{F} = \int_V \sigma^r_{ji} u_{i,j} \, dV \, . \tag{3.22}$$

Finally the rate of change with respect to time of the kinetic energy is given by

$$\frac{1}{2} \frac{D}{Dt} \int_V \rho v_i v_i \, dV = \int_V \rho v_i \frac{D}{Dt} v_i \, dV = \int_V \sigma_{ji,j} v_i \, dV \, , \tag{3.23}$$

where we have used the linear momentum equation (3.1).
By integrating by parts the right hand side of equation (3.23) we obtain

$$\int_V \sigma_{ji,j} v_i \, dV = \int_\Sigma \sigma_{ji} v_i \, d\Sigma_j - \int_V \sigma_{ji} v_{i,j} \, dV \, . \tag{3.24}$$

The combination of equations (3.23) and (3.24) gives

$$\frac{1}{2} \frac{D}{Dt} \int_V \rho v_i v_i \, dV = \int_\Sigma \sigma_{ji} v_i \, d\Sigma_j - \int_V \sigma_{ji} v_{i,j} \, dV \, . \tag{3.25}$$

Then, the variation in $\mathcal{F}$ with respect to time has contributions from the change in the free energy with respect to changes in the order parameter, equation (3.14), contributions from the change with respect to material deformations, (3.22), and contributions from the variation of the kinetic energy, equation (3.25). Therefore we can calculate the rate of change of the free energy with respect to time to obtain

$$\dot{\mathcal{F}} = - \int_V \left[H_{ij}^{[st]} \dot{Q}_{ij} + \left(\sigma_{ji} - \sigma_{ji}^r \right) v_{i,j} \right] dV + \int_\Sigma \sigma_{ji,j} v_i \, d\Sigma_j \, .$$

If we substitute this expression into (3.7), ignore the surface integrals and equate the volume integrals we obtain the following equation

$$\int_V T\vartheta \, dV = \int_V \left[H_{ij}^{[st]} \dot{Q}_{ij} + \left(\sigma_{ji} - \sigma_{ji}^r \right) v_{i,j} \right] dV \, ,$$

which is valid for any arbitrary volume V, therefore we can omit the integrals and we have an expression for the entropy production

$$T\vartheta = H_{ij}^{[st]} \dot{Q}_{ij} + \hat{\sigma}_{ji} v_{i,j} \, , \tag{3.26}$$

where $\hat{\boldsymbol{\sigma}} = \boldsymbol{\sigma} - \boldsymbol{\sigma}^r$ is the irreversible part of the stress tensor. We manipulate this expression by decomposing every tensor A_{ij} as $A_{ij} = A_{ij}^{[st]} + A_{ij}^{[a]} + A_{kk}\delta_{ij}/3$ where $A_{ij}^{[st]}$ is the symmetric and traceless part of the tensor and $A_{ij}^{[a]}$ is the antisymmetric part of the tensor to obtain

$$T\vartheta = H_{ij}^{[st]} \dot{Q}_{ij} + \hat{\sigma}_{ij}^{[st]} D_{ij}^{[t]} - \hat{\sigma}_{ij}^{[a]} W_{ij} \, , \tag{3.27}$$

where $\mathbf{D}$ and $\mathbf{W}$ are the symmetric and antisymmetric part, respectively, of the velocity gradient field. The script $[t]$ indicates the traceless part of a tensor.

We re-write the entropy production (3.26) employing a different choice of tensors and so we consider the property that the free energy is invariant under rigid body rotations. Consider then a rotation of a small angle $|\boldsymbol{\omega}|$. The variations $\delta\mathbf{r}$ and $\delta\mathbf{Q}$ are given by

$$\delta r_i = u_i = \epsilon_{ijk} \omega_j r_k \, , \tag{3.28}$$

$$\delta Q_{ij} = \epsilon_{ilm} \omega_l Q_{mj} + \epsilon_{jlm} \omega_l Q_{im} \, . \tag{3.29}$$

Using a similar argument to that used before, equations (3.10) and (3.22), we have that the variation of $\mathcal{F}$ under infinitesimal rotation is given by

$$\delta\mathcal{F} = \int_V \left[\sigma_{ij}^r u_{j,i} + \frac{\partial f^{[st]}}{\partial Q_{ij}} \delta Q_{ij} + \frac{\partial f^{[st]}}{\partial Q_{ij,k}} \delta Q_{ij,k} \right] dV \, ,$$

where we have that $\boldsymbol{\sigma}^r$ is given by equation (3.21). Here we are using the Lagrange multipliers to account for the constrains of having a symmetric and traceless order parameter and an incompressible fluid. Substituting equations (3.28) and (3.29) into $\delta\mathcal{F}$ we obtain

$$\begin{aligned}\delta\mathcal{F} &= \int_V \left[\epsilon_{lij}\omega_l\sigma^r_{ij} + \frac{\partial f^{[st]}}{\partial Q_{ij}}\left(\epsilon_{ilm}\omega_l Q_{mj} + \epsilon_{jlm}\omega_l Q_{im}\right)\right] dV \\ &+ \int_V \frac{\partial f^{[st]}}{\partial Q_{ij,k}}\left[\epsilon_{ilm}\omega_l Q_{mj} + \epsilon_{jlm}\omega_l Q_{im}\right]_{,k} dV\,. \qquad (3.30)\end{aligned}$$

The substitution of equation (3.19) into the definition of the molecular field (3.13) yields

$$\frac{\partial f^{[st]}}{\partial Q_{ij}} = -H^{[st]}_{ij} - \left(\Pi^{k[st]}_{ij}\right)_{,k}\,.$$

We employ this expression to simplify equation (3.30) to obtain

$$\begin{aligned}\delta\mathcal{F} &= \int_V \left[\epsilon_{lij}\omega_l\sigma^r_{ij} - H^{[st]}_{ij}\left(\epsilon_{ilm}\omega_l Q_{mj} + \epsilon_{jlm}\omega_l Q_{im}\right)\right] dV \\ &- \int_V \left[\Pi^{k[st]}_{ij}\left(\epsilon_{ilm}\omega_l Q_{mj} + \epsilon_{jlm}\omega_l Q_{im}\right)\right]_{,k} dV\,. \qquad (3.31)\end{aligned}$$

The free energy is invariant to rotations therefore $\delta\mathcal{F} = 0$ and the integration of the last term of equation (3.31) yields

$$\begin{aligned}&\int_V \left(\epsilon_{kij}\omega_k\sigma^r_{ij} - \epsilon_{ikj}\omega_k H^{[st]}_{im} Q_{jm} - \epsilon_{jki}\omega_k H^{[st]}_{mj} Q_{mi}\right) dV \\ &= \int_\Sigma \left(\epsilon_{ikj}\omega_k \Pi^{l[st]}_{im} Q_{jm} + \epsilon_{jki}\omega_k \Pi^{l[st]}_{mj} Q_{mi}\right) d\Sigma_l\,.\end{aligned}$$

Since this equation is valid for every $\boldsymbol{\omega}$ we can re-write it as

$$\int_V \epsilon_{kij}\left(\sigma^r_{ij} + H^{[st]}_{im} Q_{mj} - Q_{im} H^{[st]}_{mj}\right) dV = \int_\Sigma \epsilon_{kij}\left(Q_{im}\Pi^{l[st]}_{mj} - \Pi^{l[st]}_{im} Q_{mj}\right) d\Sigma_l\,. \quad (3.32)$$

We will now consider the total applied torque in the absence of flow, which is equal to the rate of change of the angular momentum. From this relationship we will obtain an equation in terms of the order tensor parameter, the molecular field and the irreversible stress tensor, which will provides us with a new expression for the entropy production and a choice of forces and fluxes.

The rate of change of the angular momentum by definition is

$$\dot{L}_i = \frac{D}{Dt}\int_V (\mathbf{r} \times \rho\mathbf{v})_i\, dV\,. \qquad (3.33)$$

The total applied torque in the absence of external fields accounts for the torques due to external stresses acting at the surface

$$\int_\Sigma \epsilon_{kij} r_i \sigma_{lj}\, d\Sigma_l\,, \qquad (3.34)$$

and for the torques on the director tensor at the surface of the volume

$$\int_\Sigma \epsilon_{kij}\left(\Pi^{l[st]}_{im}Q_{mj} - Q_{im}\Pi^{l[st]}_{mj}\right)\,d\Sigma_l\,. \tag{3.35}$$

Then the total applied torque given by equations (3.34) and (3.35) must balance the rate of change of the angular momentum (3.33), which yields

$$\frac{D}{Dt}\int_V \epsilon_{kij}r_i\rho v_j\,dV = \int_\Sigma \epsilon_{kij}\left(r_i\sigma_{lj} + \Pi^{l[st]}_{im}Q_{mj} - Q_{im}\Pi^{l[st]}_{mj}\right)\,d\Sigma_l\,. \tag{3.36}$$

The left-hand-side can be simplified by using the linear momentum equation (3.1) and integrating by parts

$$\begin{aligned}\frac{D}{Dt}\int_V \epsilon_{kij}r_i\rho v_j\,dV &= \int_V \epsilon_{kij}r_i\sigma_{lj,l}\,dV\\ &= \int_\Sigma \epsilon_{kij}r_i\sigma_{lj}\,d\Sigma_l - \int_V \epsilon_{kij}\sigma_{ij}\,dV\end{aligned}$$

and substituting this equation into (3.36) we obtain the following relationship

$$\int_\Sigma \epsilon_{kij}\left(Q_{im}\Pi^{l[st]}_{mj} - \Pi^{l[st]}_{im}Q_{mj}\right)\,d\Sigma_l = \int_V \epsilon_{kij}\sigma_{ij}\,dV\,.$$

This equation can be combined with the relationship expressed in (3.32) to give

$$\int_V \epsilon_{kij}\left(\sigma^r_{ij} + H^{[st]}_{im}Q_{mj} - Q_{im}H^{[st]}_{mj}\right)\,dV = \int_V \epsilon_{kij}\sigma_{ij}\,dV\,.$$

The above expression is valid for an arbitrary volume V, therefore the integrands must be equal, and in this equation we can use the definition of irreversible stress, $\hat{\boldsymbol{\sigma}} = \boldsymbol{\sigma} - \boldsymbol{\sigma}^r$, the tensor equation $\epsilon_{kij}A_{ij} = \epsilon_{kij}A^{[a]}_{ij}$ and the fact that $\epsilon_{kij}A_{ij} = \epsilon_{kij}B_{ij}$ implies $A^{[a]}_{ij} = B^{[a]}_{ij}$ for any tensors $\mathbf{A}$ and $\mathbf{B}$, to obtain a relationship between the anti-symmetric part of the irreversible stress, the tensor order parameter and the molecular field tensor

$$\hat{\sigma}^{[a]}_{ij} = H^{[st]}_{im}Q_{mj} - Q_{im}H^{[st]}_{mj}\,. \tag{3.37}$$

We substitute this equation into the expression for the entropy production (3.27) to obtain

$$\begin{aligned}T\vartheta &= H^{[st]}_{ij}\dot{Q}_{ij} + \hat{\sigma}^{[st]}_{ij}D^{[t]}_{ij} - \hat{\sigma}^{[a]}_{ij}W_{ij}\\ &= H^{[st]}_{ij}\dot{Q}_{ij} + \hat{\sigma}^{[st]}_{ij}D^{[t]}_{ij} - H^{[st]}_{im}Q_{mj}W_{ij} + Q_{im}H^{[st]}_{mj}W_{ij}\\ &= H^{[st]}_{ij}(\dot{Q}_{ij} - W_{im}Q_{mj} + Q_{im}W_{mj}) + \hat{\sigma}^{[st]}_{ij}D^{[t]}_{ij}\,.\end{aligned}$$

Simplifying and using tensor notation we derived the expression

$$T\vartheta = \mathbf{H}^{[st]}\!:\!\mathbf{K} + \hat{\boldsymbol{\sigma}}^{[st]}\!:\!\mathbf{D}^{[t]}\,, \tag{3.38}$$

where

$$\mathbf{K} = \dot{\mathbf{Q}} - (\mathbf{WQ} - \mathbf{QW}) \tag{3.39}$$

represents the rate of change of the director with respect to the background fluid.
In the expression for the entropy production, equation (3.38) we identify $\mathbf{D}^{[t]}$ and $\mathbf{H}^{[st]}$ as the forces, and $\hat{\boldsymbol{\sigma}}^{[st]}$ and $\mathbf{K}$ as their conjugates fluxes [42]. We assume we are close to equilibrium and therefore we can express the fluxes as linear equations in the forces

$$\begin{aligned}
\hat{\sigma}^{[st]}_{ij} &= L_{ijkl} D^{[t]}_{kl} + M_{ijkl} H^{[st]}_{kl} \,, \\
K_{ij} &= M'_{ijkl} D^{[t]}_{kl} + L'_{ijkl} H^{[st]}_{kl} \,,
\end{aligned}$$

where the transport coefficient tensors $\mathbf{L}$, $\mathbf{M}$, $\mathbf{L}'$ and $\mathbf{M}'$ must verify the Onsager reciprocity relations [51]

$$L_{ijkl} = L_{klij} \,, \tag{3.40}$$

$$L'_{ijkl} = L'_{klij} \,, \tag{3.41}$$

$$M_{ijkl} = -M'_{klij} \,. \tag{3.42}$$

The symmetric and traceless character of $\hat{\boldsymbol{\sigma}}^{[st]}$ and $\mathbf{K}$ implies the following relations between the transport coefficient tensors

$$M_{iikl} = M'_{iikl} = L_{iikl} = L'_{iikl} = 0 \tag{3.43}$$

and

$$M_{ijkl} = M_{jikl} \,, \quad M'_{ijkl} = M'_{jikl} \,, \tag{3.44}$$

$$L_{ijkl} = L_{jikl} \,, \quad L'_{ijkl} = L'_{jikl} \,. \tag{3.45}$$

The transport tensors are expansions in terms of the unit tensor $\mathbf{I}$ and the order parameter $\mathbf{Q}$, but assuming small values of the order parameter and vicinity to the isotropic nematic temperature an expansion to the linear order in $\mathbf{Q}$ should be enough for our purposes. The expansion to the linear order in $\mathbf{Q}$ the transport coefficients, such that they verify the Onsager relationships (3.40)-(3.42), and the traceless and symmetric conditions (3.43)-(3.45) yields

$$\begin{aligned}
L_{ijkl} &= \beta_3 \left(\delta_{ik}\delta_{jl} - \frac{1}{3}\delta_{ij}\delta_{kl} \right) + \beta_4 \left(Q_{ik}\delta_{jl} + \delta_{ik}Q_{jl} - \frac{2}{3}\delta_{ij}Q_{kl} \right) \,, \\
M_{ijkl} &= -\beta_1 \left(\delta_{ik}\delta_{jl} - \frac{1}{3}\delta_{ij}\delta_{kl} \right) - \beta_5 \left(Q_{ik}\delta_{jl} + \delta_{ik}Q_{jl} - \frac{2}{3}\delta_{ij}Q_{kl} \right) \,, \\
M'_{ijkl} &= \beta_1 \left(\delta_{ik}\delta_{jl} - \frac{1}{3}\delta_{ij}\delta_{kl} \right) + \beta_5 \left(Q_{ik}\delta_{jl} + \delta_{ik}Q_{jl} - \frac{2}{3}\delta_{ij}Q_{kl} \right) \,. \\
L'_{ijkl} &= \frac{1}{\beta_2} \left(\delta_{ik}\delta_{jl} - \frac{1}{3}\delta_{ij}\delta_{kl} \right) + \frac{1}{\beta_6} \left(Q_{ik}\delta_{jl} + \delta_{ik}Q_{jl} - \frac{2}{3}\delta_{ij}Q_{kl} \right) \,.
\end{aligned}$$

These transport tensors give the following tensor equations for the antisymmetric part of the irreversible stress and the tensor **K**

$$\begin{aligned}\hat{\boldsymbol{\sigma}}^{[st]} &= \beta_3 \mathbf{D}^{[t]} + \beta_4 \left\{ \mathbf{Q}\mathbf{D}^{[t]} + \mathbf{D}^{[t]}\mathbf{Q} - \frac{2}{3}(\mathbf{D}^{[t]} : \mathbf{Q})\mathbf{I} \right\} \\ &\quad - \beta_1 \mathbf{H}^{[st]} - \beta_5 \left\{ \mathbf{Q}\mathbf{H}^{[st]} + \mathbf{H}^{[st]}\mathbf{Q} - \frac{2}{3}(\mathbf{H}^{[st]} : \mathbf{Q})\mathbf{I} \right\}, \end{aligned} \tag{3.46}$$

$$\begin{aligned}\mathbf{K} &= \beta_1 \mathbf{D}^{[t]} + \beta_5 \left\{ \mathbf{Q}\mathbf{D}^{[t]} + \mathbf{D}^{[t]}\mathbf{Q} - \frac{2}{3}(\mathbf{D}^{[t]} : \mathbf{Q})\mathbf{I} \right\} \\ &\quad + \frac{1}{\beta_2} \mathbf{H}^{[st]} + \frac{1}{\beta_6} \left\{ \mathbf{Q}\mathbf{H}^{[st]} + \mathbf{H}^{[st]}\mathbf{Q} - \frac{2}{3}(\mathbf{H}^{[st]} : \mathbf{Q})\mathbf{I} \right\}. \end{aligned} \tag{3.47}$$

Here $\boldsymbol{\sigma}^{[st]}$ and $\mathbf{H}^{[st]}$ have dimension of energy per unit volume, $\mathbf{D}^{[t]}$ and **K** have dimension of frequency and therefore β_1 and β_5 are dimensionless coefficients while β_2, β_3, β_4 and β_6 have dimension of viscosity.

However, using the expansion to the zeroth order will be enough for our purposes of studying the dynamics of a nematic liquid crystal under flow. Therefore combining the zeroth order term of equation (3.47) with the definition of the flux **K**, equation (3.39), we obtain the equation of motion of the order parameter

$$\dot{\mathbf{Q}} = \mathbf{W}\mathbf{Q} - \mathbf{Q}\mathbf{W} + \beta_1 \mathbf{D}^{[t]} + \frac{1}{\beta_2}\mathbf{H}^{[st]} . \tag{3.48}$$

This equation together with the linear momentum equation (3.1) and the incompressibility condition (3.2) are the governing equations of our model. In the linear momentum equation

$$\rho \frac{D\mathbf{v}}{Dt} = \nabla \cdot \boldsymbol{\sigma}^T ,$$

we have that the stress tensor can be decomposed as

$$\boldsymbol{\sigma} = \boldsymbol{\sigma}^d + \hat{\boldsymbol{\sigma}}^{[st]} + \hat{\boldsymbol{\sigma}}^{[a]} - p\mathbf{I} .$$

Here p is the pressure, $\boldsymbol{\sigma}^d$ is the distortion stress tensor given by equation (3.20), $\hat{\boldsymbol{\sigma}}^{[st]}$ is the symmetric and traceless part of the irreversible stress tensor , equation (3.37), and $\hat{\boldsymbol{\sigma}}^{[a]}$ the antisymmetric part of the irreversible stress, given by the zeroth order term of equation (3.46). Then

$$\sigma^d_{ij} = -\frac{\delta F}{\delta Q_{kl,i}} Q_{kl,j} , \tag{3.49}$$

$$\hat{\boldsymbol{\sigma}}^{[st]} = \beta_3 \mathbf{D}^{[t]} - \beta_1 \mathbf{H}^{[st]} , \tag{3.50}$$

$$\hat{\boldsymbol{\sigma}}^{[a]} = \mathbf{H}^{[st]}\mathbf{Q} - \mathbf{Q}\mathbf{H}^{[st]} . \tag{3.51}$$

3.2 Leslie-Ericksen theory

Leslie-Ericksen theory [5, 6, 7, 8, 9] is the classical theory that describes the dynamics for the director $\mathbf{n}$ in a general flow field. The theory assumes local equilibrium and a uniaxial nematic state. We briefly introduce the governing equations for the study of small deformations in an incompressible nematic as derived by de Gennes [1].
The equation for the dynamics of the vector field is

$$\dot{\mathbf{n}} = \boldsymbol{\omega} \times \mathbf{n} + \frac{1}{\gamma_1}\mathbf{h} + \lambda \mathbf{D}\mathbf{n}\,, \tag{3.52}$$

where $\boldsymbol{\omega}$ is the vorticity vector $\boldsymbol{\omega} = \nabla \times \mathbf{v}$, γ_1 has dimensions of viscosity, λ is a dimensionless parameter ratio of viscosities and the molecular field $\mathbf{h}$ is defined by

$$\mathbf{h} = -\frac{\delta f}{\delta \mathbf{n}}\,. \tag{3.53}$$

Here f is the total distortion free energy density of the system.
The linear momentum equation is given by

$$\rho \frac{D\mathbf{v}}{Dt} = \nabla \cdot \boldsymbol{\sigma}^T\,,$$

where the stress tensor is defined by

$$\begin{aligned}
\boldsymbol{\sigma} &= \boldsymbol{\sigma}^d + \hat{\boldsymbol{\sigma}}^{[s]} + \hat{\boldsymbol{\sigma}}^{[a]} - p\mathbf{I}\,, && (3.54)\\
\boldsymbol{\sigma}^d &= -\frac{\delta f}{\delta \mathbf{G}}\mathbf{G}^T\,, && (3.55)\\
\hat{\boldsymbol{\sigma}}^{[s]} &= 2\nu_2 \mathbf{D} + 2(\nu_3 - \nu_2)\left(\mathbf{D}(\mathbf{n}\otimes\mathbf{n}) + (\mathbf{n}\otimes\mathbf{n})\mathbf{D}\right) \\
&\quad + 2(\nu_1 + \nu_2 - 2\nu_3)\left(\mathbf{D} : (\mathbf{n}\otimes\mathbf{n})\right)(\mathbf{n}\otimes\mathbf{n}) \\
&\quad - \frac{1}{2}\lambda\left(\mathbf{h}\otimes\mathbf{n} + \mathbf{n}\otimes\mathbf{h}\right)\,, && (3.56)\\
\hat{\boldsymbol{\sigma}}^{[a]} &= (\mathbf{h}\otimes\mathbf{n})^{[a]}\,, && (3.57)
\end{aligned}$$

Here, in the equation for $\boldsymbol{\sigma}^d$, the tensor $\mathbf{G}$ is $\mathbf{G} = (\nabla \mathbf{n})^T$ and in the equation for $\hat{\boldsymbol{\sigma}}^{[s]}$ the constants ν_1, ν_2 and ν_3 are viscosity coefficients.
The incompressibility condition is

$$\nabla \cdot \mathbf{v} = 0\,. \tag{3.58}$$

3.3 Correspondence between Leslie-Ericksen and Landau-de Gennes theories

We are interested in making a comparison between the Leslie-Ericksen (LE) and Olmsted-Goldbart (OG) theories that will enable us to interpret our results in terms of the widely used LE theory.

The LE theory concerns a uniaxial theory of a nematic liquid crystal. Therefore in order to make a correspondence with the OG theory which allows for a biaxial state we must restrict it to the uniaxial case and so set S_2 to zero in the tensor order parameter $\mathbf{Q}$ given in equation (2.3). Hence the order parameter is of the form

$$\mathbf{Q} = \frac{3}{2}S_1(\mathbf{n}\otimes\mathbf{n} - \frac{1}{3}\mathbf{I})\,. \tag{3.59}$$

Using the definitions of the molecular field, (3.53) and (3.13), and the definition of the order parameter (3.59), we obtain

$$\begin{aligned} h_i &= -\frac{\delta f}{\delta n_i}\,, \\ h_i &= -\frac{\delta f}{\delta Q_{jk}}\frac{\delta Q_{jk}}{\delta n_i} \\ &= 3S_1 H_{jk}(n_k\delta_{ji} + n_j\delta_{ki})/2 \\ &= 3S_1 H^{[s]}_{ij} n_j \\ &= 3S_1 H^{[st]}_{ij} n_j + S_1 \mathrm{tr}(\mathbf{H}) n_i\,. \end{aligned}$$

And written in tensor notation this yields

$$\mathbf{h} = 3S_1\mathbf{H}^{[st]}\mathbf{n} + S_1\mathrm{tr}(\mathbf{H})\mathbf{n}. \tag{3.60}$$

Contracting this equation with $\mathbf{n}$ gives

$$S_1\mathrm{tr}(\mathbf{H}) = \mathbf{h}\cdot\mathbf{n} - 3S_1\mathbf{H}^{[st]}:(\mathbf{n}\otimes\mathbf{n})\,. \tag{3.61}$$

The tensor $\mathbf{H}$ is assumed to have the symmetric traceless part

$$\mathbf{H}^{[st]} = \frac{1}{3S_1}(\mathbf{h}\otimes\mathbf{n} + \mathbf{h}\otimes\mathbf{n}) - K\mathbf{I}\,, \tag{3.62}$$

where $K = 2(\mathbf{h}\cdot\mathbf{n})/9S_1$. In fact, this definition of the molecular field tensor satisfies equation (3.60). Inserting the expression for $\mathbf{H}^{[st]}$ (3.62), into the right hand side of (3.60) using equation (3.61) gives

$$\begin{aligned} & 3S_1\left[\frac{1}{3S_1}(\mathbf{h}\otimes\mathbf{n} + \mathbf{n}\otimes\mathbf{h}) - \frac{2}{9S_1}(\mathbf{h}\cdot\mathbf{n})\mathbf{I}\right]\mathbf{n} \\ & \quad + (\mathbf{h}\cdot\mathbf{n})\mathbf{n} - 3S_1\left[(\frac{1}{3S_1}(\mathbf{h}\otimes\mathbf{n} + \mathbf{n}\otimes\mathbf{h}) - \frac{2}{9S_1}(\mathbf{h}\cdot\mathbf{n})(\mathbf{n}\otimes\mathbf{n})\right]\mathbf{n} \\ = {} & \mathbf{h} + (\mathbf{h}\cdot\mathbf{n})\mathbf{n} - \frac{2}{3} + (\mathbf{h}\cdot\mathbf{n})\mathbf{n} + (\mathbf{h}\cdot\mathbf{n})\mathbf{n} - 2(\mathbf{h}\cdot\mathbf{n})\mathbf{n} + \frac{2}{3}(\mathbf{h}\cdot\mathbf{n})\mathbf{n} \\ = {} & \mathbf{h}\,, \end{aligned}$$

as required.

The correspondence between the coefficients is found, initially, by using the zeroth order expansion of the transport tensors in the OG theory. Using the definition of the order parameter (3.59) and the relationship between the molecular fields (3.60), the symmetric traceless viscous stress in the OG theory (3.50) is

$$\hat{\boldsymbol{\sigma}}^{[st]} = \beta_3 \mathbf{D}^{[t]} - \frac{\beta_1}{3S_1}(\mathbf{h}\otimes\mathbf{n} + \mathbf{n}\otimes\mathbf{h}) + \frac{2\beta_1}{9S_1}(\mathbf{h}\cdot\mathbf{n})\mathbf{I}. \tag{3.63}$$

In the LE theory, the corresponding tensor $\hat{\boldsymbol{\sigma}}^{[st]}$ (3.56) is given by

$$\begin{aligned} \hat{\boldsymbol{\sigma}}^{[st]} &= 2\nu_2\mathbf{D}^{[t]} + 2(\nu_3 - \nu_2)(\mathbf{D}^{[t]}(\mathbf{n}\otimes\mathbf{n}) + (\mathbf{n}\otimes\mathbf{n})\mathbf{D}^{[t]}) \\ &\quad + 2(\nu_1 + \nu_2 - 2\nu_3)(\mathbf{D}^{[t]} : (\mathbf{n}\otimes\mathbf{n}))(\mathbf{n}\otimes\mathbf{n}) \\ &\quad - \frac{1}{2}\lambda(\mathbf{h}\otimes\mathbf{n} + \mathbf{n}\otimes\mathbf{h}) \\ &\quad - \frac{1}{3}\Big(2(\nu_1 - \nu_2)(\mathbf{D}^{[t]} : (\mathbf{n}\otimes\mathbf{n})) - \lambda(\mathbf{h}\cdot\mathbf{n})\Big)\mathbf{I}. \end{aligned} \tag{3.64}$$

Comparing equations (3.63) and (3.64) we deduce that

$$\beta_1 = \frac{3S_1}{2}\lambda\,, \tag{3.65}$$

$$\beta_3 = 2\nu_2\,, \tag{3.66}$$

where λ and β_1 are dimensionless parameters and ν_2 and $\beta_3$are viscosity parameters. The contraction of equation (3.48) with $\mathbf{n}$ together with the relationship (3.60) yield

$$\begin{aligned} \dot{\mathbf{Q}}\mathbf{n} &= \mathbf{W}\mathbf{Q}\mathbf{n} - \mathbf{Q}\mathbf{W}\mathbf{n} + \beta_1\mathbf{D}^{[t]}\mathbf{n} \\ &\quad + \frac{1}{\beta_2}\Big[\frac{1}{3S_1}(\mathbf{h}\otimes\mathbf{n} + \mathbf{n}\otimes\mathbf{h}) - \frac{2}{9S_1}(\mathbf{h}\cdot\mathbf{n})\mathbf{I}\Big]\mathbf{n}. \end{aligned}$$

Noting that $\mathbf{n}$ is a unit vector so that $\mathbf{n}\cdot\dot{\mathbf{n}} = 0$ and using the definition of $\mathbf{Q}$, we obtain

$$\begin{aligned} \frac{3}{2}S_1\dot{\mathbf{n}} &= \frac{3}{2}S_1\Big(\mathbf{W}\mathbf{n} - (\mathbf{W}\mathbf{n}\cdot\mathbf{n})\mathbf{n}\Big) + \beta_1\mathbf{D}^{[t]}\mathbf{n} \\ &\quad + \frac{1}{3S_1\beta_2}\Big(\mathbf{h} + (\mathbf{h}\cdot\mathbf{n})\mathbf{n}\Big) - \frac{2}{9S_1\beta_2}(\mathbf{h}\cdot\mathbf{n})\mathbf{n}. \end{aligned} \tag{3.67}$$

Employing the definition of the vorticity

$$\mathbf{W}\mathbf{n} = \boldsymbol{\omega}\times\mathbf{n}\,,$$

equation (3.67) becomes

$$\dot{\mathbf{n}} = \boldsymbol{\omega}\times\mathbf{n} + \frac{2}{9S_1^2\beta_2}\mathbf{h} + \frac{2\beta_1}{3S_1}\mathbf{D}^{[t]}\mathbf{n} + \frac{2}{27S_1^2\beta_2}(\mathbf{h}\cdot\mathbf{n})\mathbf{n}.$$

Comparing coefficients with the director motion equation in the LE theory, (3.52), gives in addition

$$\beta_2 = \frac{2\gamma_1}{9S_1^2}. \tag{3.68}$$

where γ_1 is a rotational viscosity in the LE model.

The relationships between the coefficients are given by equations (3.65), (3.66) and (3.68). However the relationships between the coefficients are calculated for the value of the uniaxial order parameter before the re-scaling (2.9). Once the re-scaling is done and dropping bars, the correspondence between the coefficients in the LE and OG models is

$$\begin{aligned} \beta_1 &= \frac{-\widetilde{B}\lambda}{3} S_1 \,, && (3.69) \\ \beta_3 &= 2\nu_2 \,, && (3.70) \\ \beta_2 &= \frac{9\gamma_1}{2\widetilde{B}^2 S_1^2} \,. && (3.71) \end{aligned}$$

There is only correspondence between three of the coefficients in both theories. However, if the transport tensors are expanded to a higher order, then the correspondence can be extended between more parameters. For example, using the equation for the order parameter and the relationship between the molecular fields, equations (3.59) and (3.60), the following expressions are obtained

$$\begin{aligned} \mathbf{Q}\mathbf{H}^{[st]} + \mathbf{H}^{[st]}\mathbf{Q} - \frac{2}{3}(\mathbf{H}^{[st]} : \mathbf{Q})\mathbf{I} &= \frac{1}{6}(\mathbf{h} \otimes \mathbf{n} + \mathbf{n} \otimes \mathbf{h}) \\ &\quad + \frac{1}{3}(\mathbf{h} \cdot \mathbf{n})(\mathbf{n} \otimes \mathbf{n}) - \frac{2}{9}(\mathbf{h} \cdot \mathbf{n})\mathbf{I} \qquad (3.72) \end{aligned}$$

and

$$\begin{aligned} \mathbf{Q}\mathbf{D}^{[t]} + \mathbf{D}^{[t]}\mathbf{Q} - \frac{2}{3}(\mathbf{D}^{[t]} : \mathbf{Q})\mathbf{I} &= \frac{3S_1}{2}\Big[\mathbf{D}^{[t]}(\mathbf{n} \otimes \mathbf{n}) + (\mathbf{n} \otimes \mathbf{n})\mathbf{D}^{[t]}\Big] \\ &\quad - S_1\mathbf{D}^{[t]} - S_1\Big[\mathbf{D}^{[t]} : (\mathbf{n} \otimes \mathbf{n})\Big]\mathbf{I} \,. \qquad (3.73) \end{aligned}$$

Therefore the first order expansion of the symmetric traceless part of the viscous tensor, (3.46), in terms of $\mathbf{D}^{[t]}$, $\mathbf{n}$, and $\mathbf{h}$, is given by

$$\begin{aligned} \hat{\boldsymbol{\sigma}}^{[st]} &= (\beta_3 - S_1\beta_4)\mathbf{D}^{[t]} + \frac{3}{2}S_1\beta_4\Big(\mathbf{D}^{[t]}(\mathbf{n} \otimes \mathbf{n}) + (\mathbf{n} \otimes \mathbf{n})\mathbf{D}^{[t]}\Big) \\ &\quad - \frac{\beta_5}{3}(\mathbf{h} \cdot \mathbf{n})(\mathbf{n} \otimes \mathbf{n}) - \Big(\frac{\beta_1}{3S_1} + \frac{\beta_5}{6}\Big)(\mathbf{h} \otimes \mathbf{n} + \mathbf{n} \otimes \mathbf{h}) \\ &\quad - \frac{1}{3}\Big(3S_1\beta_4\mathbf{D}^{[t]} : (\mathbf{n} \otimes \mathbf{n}) - \frac{2\beta_1}{3S_1}(\mathbf{h} \cdot \mathbf{n}) - \frac{2\beta_5}{3}(\mathbf{h} \cdot \mathbf{n})\Big)\mathbf{I} \,. \end{aligned}$$

Comparing with (3.64) gives

$$\begin{aligned} 2\nu_2 &= \beta_3 - S_1\beta_4 \,, && (3.74) \\ 2(\nu_3 - \nu_2) &= \frac{3}{2}S_1\beta_4 \,, && (3.75) \\ \lambda &= \frac{2\beta_1}{3S_1} + \frac{\beta_5}{3} \,. && (3.76) \end{aligned}$$

Further relations can be found from the flux conjugate equations, (3.39) and (3.47). Using the form for $\mathbf{Q}$ in (3.59) in equation (3.39) gives

$$\mathbf{K} = \frac{3S_1}{2}\left(\mathbf{n}\otimes\dot{\mathbf{n}} + \dot{\mathbf{n}}\otimes\mathbf{n} - (\boldsymbol{\omega}\times\mathbf{n})\otimes\mathbf{n} - \mathbf{n}\otimes(\boldsymbol{\omega}\times\mathbf{n})\right). \tag{3.77}$$

Expressing the flux (3.47) in terms of $\mathbf{D}^{[t]}$, $\mathbf{n}$, and $\mathbf{h}$, using equations (3.72) and (3.73), shows that

$$\begin{aligned}\mathbf{K} \;=\; & \Big(\frac{1}{3S_1\beta_2} + \frac{1}{6\beta_6}\Big)(\mathbf{h}\otimes\mathbf{n} + \mathbf{n}\otimes\mathbf{h}) + (\beta_1 - S_1\beta_5)\mathbf{D}^{[t]} \\ & + \frac{3\beta_5 S_1}{2}\Big(\mathbf{D}^{[t]}(\mathbf{n}\otimes\mathbf{n}) + (\mathbf{n}\otimes\mathbf{n})\mathbf{D}^{[t]}\Big) + \frac{1}{3\beta_6}(\mathbf{h}\cdot\mathbf{n})(\mathbf{n}\otimes\mathbf{n}) \\ & - \frac{1}{3}\Big(\frac{2}{3S_1\beta_2}(\mathbf{h}\cdot\mathbf{n}) + \frac{2}{3\beta_6}(\mathbf{h}\cdot\mathbf{n}) + 3S_1\beta_5\mathbf{D}^{[t]}:(\mathbf{n}\otimes\mathbf{n})\Big)\mathbf{I}. \end{aligned} \tag{3.78}$$

Equating (3.77) and (3.78) and multiplying by $\mathbf{n}$ yields

$$\begin{aligned}\dot{\mathbf{n}} \;=\; & (\boldsymbol{\omega}\times\mathbf{n}) + \Big(\frac{2}{9S_1^2\beta_2} + \frac{1}{9S_1\beta_6}\Big)\mathbf{h} + \Big(\frac{2\beta_1}{3S_1} + \frac{\beta_5}{3}\Big)\mathbf{D}^{[t]}\mathbf{n} \\ & + \Big(\frac{2}{27S_1^2\beta_2} + \frac{5}{27S_1\beta_6}\Big)(\mathbf{h}\cdot\mathbf{n})\mathbf{n} + \frac{2\beta_5}{3}\Big(\mathbf{D}^{[t]}:(\mathbf{n}\otimes\mathbf{n})\Big)\mathbf{n}.\end{aligned}$$

Finally, comparing this expression with the LE expression (3.52), the following relation is found

$$\frac{1}{\gamma_1} = \frac{2}{9S_1^2\beta_2} + \frac{1}{9S_1\beta_6}. \tag{3.79}$$

Therefore, in the first order expansion, four relations may be found: equations (3.74), (3.75), (3.76), (3.79). However an expression for $(\nu_1 + \nu_2 - 2\nu_3)$ cannot be derived and it is necessary to go to a higher order expansion of the transport tensors for its determination. Expressing these relationships with the re-scaled uniaxial order parameter (2.9) and dropping bars

$$\begin{aligned} 2\nu_2 &= \beta_3 + \frac{2\widetilde{B}}{9}S_1\beta_4\,, \\ 2(\nu_3 - \nu_2) &= -\frac{\widetilde{B}}{3}S_1\beta_4\,, \\ \lambda &= -\frac{3\beta_1}{\widetilde{B}S_1} + \frac{\beta_5}{3}\,, \\ \frac{1}{\gamma_1} &= \frac{9}{2\widetilde{B}^2S_1^2\beta_2} - \frac{1}{2\widetilde{B}S_1\beta_6}\,. \end{aligned}$$

Chapter 4

Bifurcation theory

In this chapter we summarise the concepts and tools of bifurcation theory [54, 55, 56, 57] that will be employed in the subsequent chapters of this thesis.

This study does not pretend to be a detailed account on nonlinear dynamics and bifurcation theory but a short introduction on the character of the changes of an orbit of a dynamical system depending on its parameters, as well as the methods necessary for this study.

Firstly we describe the bifurcations of simple differential equations and subsequently we introduce centre of manifold theory and normal form reduction, that will allow us to explain the dynamical behaviour and bifurcation set of more complicated dynamical systems.

Secondly we describe bifurcations of periodic orbits and global bifurcations.

4.1 Equilibrium points: stability and bifurcations

We consider a general autonomous differential system

$$\dot{\mathbf{x}} = \mathbf{f}(\mathbf{x})\,, \tag{4.1}$$

where $\mathbf{x} \in \mathbb{R}^n$ and $\mathbf{f} : A \in \mathbb{R}^n \to \mathbb{R}^n$ is a smooth function on some open set A in $\mathbb{R}^n$.

The point $\mathbf{x} = \mathbf{x}_0$ is said to be an equilibrium solution or steady state of the system (4.1) if $\mathbf{f}(\mathbf{x}_0) = 0$.

A solution of the system $\mathbf{x}_0(t)$ is said to be stable if given $\epsilon > 0$, there exists $\delta = \delta(\epsilon) > 0$, such that for any other solution $\mathbf{y}(t)$ satisfying $||\mathbf{x}_0(t_0) - \mathbf{y}(t_0)|| < \delta$, then

$||\mathbf{x}_0(t) - \mathbf{y}(t)|| < \epsilon$ for $t > t_0$ and $t_0 \in \mathbb{R}$.

When the solution $\mathbf{x}_0(t)$ is stable if there exists $\bar{\epsilon} > 0$ such that for any other solution $\mathbf{y}(t)$ satisfying $||\mathbf{x}_0(t_0) - \mathbf{y}(t_0)|| < \bar{\epsilon}$, then $||\mathbf{x}_0(t) - \mathbf{y}(t)|| \to 0$ as $t \to \infty$, then $\mathbf{x}_0(t)$ is said to be an asymptotically stable solution.

In order to determine the stability of the equilibrium solution we linearise system (4.2) about the steady state to obtain

$$\dot{\overline{\mathbf{x}}} = \mathbf{M}\overline{\mathbf{x}}\,,$$

where $\overline{\mathbf{x}} = \mathbf{x} - \mathbf{x}_0$ and $\mathbf{M} = \mathrm{D}_x\mathbf{f}(\mathbf{x}_0)$, is the differential of $\mathbf{f}$ with respect to $\mathbf{x}$ evaluated at $\mathbf{x}_0$. When all the eigenvalues of $\mathbf{M}$ have real negative part, then the equilibrium point $\mathbf{x}_0$ is stable, it is unstable otherwise.

We now consider a system depending on parameters

$$\dot{\mathbf{x}} = \mathbf{f}(\mathbf{x}\,,\boldsymbol{\alpha})\,, \tag{4.2}$$

where $\mathbf{x} \in \mathbb{R}^n$ and $\boldsymbol{\alpha} \in \mathbb{R}^k$ is the parameter of the system. We say that the point $(\mathbf{x}_0\,,\boldsymbol{\alpha}_0)$ is an equilibrium of the system (4.2) when $\mathbf{f}(\mathbf{x}_0\,,\boldsymbol{\alpha}_0) = 0$, and the equilibrium is stable when all the eigenvalues of $\mathbf{M} = \mathrm{D}_x\mathbf{f}(\mathbf{x}_0,\ \boldsymbol{\alpha}_0)$ have negative real part, it is unstable otherwise.

If all the eigenvalues of $\mathbf{M}$ have non-zero real part, then the point is said to be hyperbolic and for $\boldsymbol{\alpha}$ sufficiently close to $\boldsymbol{\alpha}_0$ the stability of the equilibrium points is the same than that of $(\mathbf{x}_0,\ \boldsymbol{\alpha}_0)$. However, if the equilibrium point is nonhyperbolic, i.e. at least one eigenvalue has real part zero, then an array of different behaviours occur in a neighbourhood of the equilibrium point. Bifurcation theory aims to give a systematic classification of the equilibrium points local to a nonhyperbolic equilibrium point, as well as an account of the behaviour of the periodic orbits of a dynamical system.

4.1.1 Local Bifurcations of equilibria

In this section we only regard those bifurcations that arise in this this thesis.

In order to describe the different types of bifurcations we use the smallest dimension of the differential equation and the minimum number of parameters necessary for such bifurcation to occur. In this thesis the bifurcations will normally occur in higher dimensions but centre manifold theory and normal form reduction, explained below, will allow us to express our problem in terms of simpler lower dimensional system.

The local bifurcation of equilibria occurs in a neighbourhood of a nonhyperbolic equilibrium point and as we have already seen, nonhyperbolic equilibrium points are those steady states that have some eigenvalues with real part zero. Thus we consider three different cases of nonhyperbolic systems: that with a single zero eigenvalue, a conjugate pair of pure imaginary eigenvalues or a double zero eigenvalue of the linearised system.

Single zero eigenvalue

In order to describe the bifurcation corresponding to this case it is enough to consider a one dimensional system depending in one parameter only,

$$\dot{x} = f(x, \alpha),$$

where $x \in \mathbb{R}$ and $\alpha \in \mathbb{R}$. We assume $(x,\, \alpha) = (x_0,\, \alpha_0)$ is the equilibrium point and therefore

$$f(x_0,\, \alpha_0) = 0\,. \tag{4.3}$$

The condition for the equilibrium point to be nonhyperbolic is

$$\frac{\partial f}{\partial x}(x_0,\, \alpha_0) = 0\,. \tag{4.4}$$

Depending on other additional conditions the nonhyperbolic equilibrium point with will be of one of the following types:

Limit point bifurcation:

An example of a limit point occurring at $(x_0,\, \alpha_0)$ is plotted in figure 4.1. Here we observe that for values of $\alpha < \alpha_0$ there are no equilibrium points, at $\alpha = \alpha_0$ the limit point occurs and the curve of equilibrium points, which exists for $\alpha \geq \alpha_0$ is tangent to this axis. For values of the parameter larger than α_0 two equilibrium points coexist, one stable and one unstable. The bifurcation occurring at the limit point is also called a saddle-node bifurcation. The conditions on the vector field f for the existence of a limit point are

$$\begin{aligned} \frac{\partial f}{\partial \alpha}(x_0,\, \alpha_0) &\neq 0\,, & (4.5)\\ \frac{\partial^2 f}{\partial \alpha^2}(x_0,\, \alpha_0) &\neq 0\,, & (4.6) \end{aligned}$$

together with (4.3) and (4.4). Conditions (4.5) and (4.6) imply that, locally to the point of the single zero eigenvalue the bifurcation diagram is similar to that shown in figure 4.1.

Transcritical bifurcation:

Figure 4.2 shows an example of a transcritical bifurcation. Here we observe that two curves of equilibria pass through the bifurcation point, both curves exist at both sides

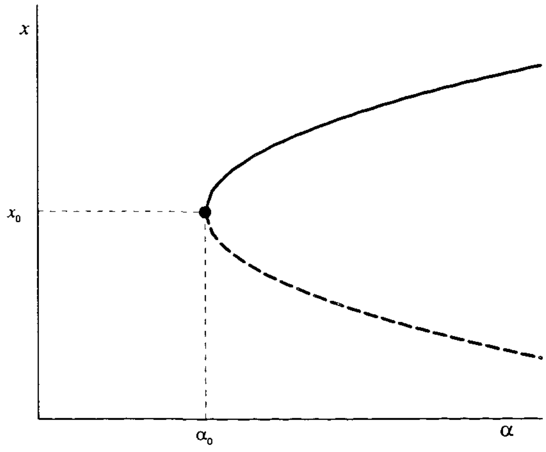

Figure 4.1: Bifurcation diagram local to a limit point occurring at $(x_0,\, \alpha_0)$. The dashed lines indicate unstable states, while solid lines indicate stable solutions.

of $\alpha = \alpha_0$ and the branches swap stability at $\alpha = \alpha_0$. The conditions on the vector field f in order to have a transcritical bifurcation are

$$\begin{aligned} \frac{\partial f}{\partial \alpha}(x_0,\, \alpha_0) &= 0\,, \\ \frac{\partial^2 f}{\partial x^2}(x_0,\, \alpha_0) &\neq 0\,, \\ \frac{\partial^2 f}{\partial x \partial \alpha}(x_0,\, \alpha_0) &\neq 0\,, \end{aligned}$$

together with the conditions (4.3) and (4.4). Any transcritical bifurcation occurring in a one dimensional system is locally equivalent to that shown in figure 4.2. If the transcritical bifurcation occurs at a higher dimension, then we would apply centre of manifold theory and normal form reduction in order to get a one dimensional system depending in one parameter.

Pitchfork bifurcation:

A pitchfork bifurcation is shown in figure 4.3, where we observe that two branches of equilibrium points pass through the nonhyperbolic point $(x_0,\, \alpha_0)$. One of the branches lies on both sides of $\alpha = \alpha_0$, and changes stability at this point, while the other, which is tangent to the bifurcation point, lies only on one side of $\alpha = \alpha_0$ and its stability remains unchanged, so that for $\alpha \geq \alpha_0$ the system has two stable equilibrium points. The conditions on f for the equilibrium point to be a pitchfork bifurcation are

$$\begin{aligned} \frac{\partial f}{\partial \alpha}(x_0,\, \alpha_0) &= 0\,, \\ \frac{\partial^2 f}{\partial x^2}(x_0,\, \alpha_0) &= 0\,, \\ \frac{\partial^2 f}{\partial x \partial \alpha}(x_0,\, \alpha_0) &\neq 0\,, \\ \frac{\partial^3 f}{\partial x^3}(x_0,\, \alpha_0) &\neq 0\,, \end{aligned} \tag{4.7}$$

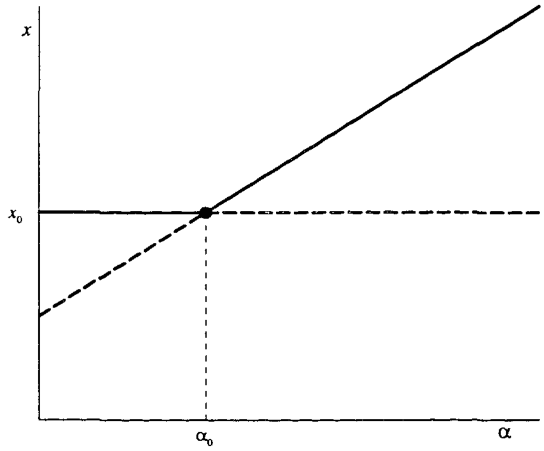

Figure 4.2: Bifurcation diagram local to a transcritical bifurcation occurring at $(x, \alpha) = (x_0, \alpha_0)$. Solid lines indicate stable states while dashed lines indicate unstable states.

together with conditions (4.3) and (4.4).

The stability of the branches shown in figures 4.1, 4.2 and 4.3 is only relevant for the one-dimensional case.

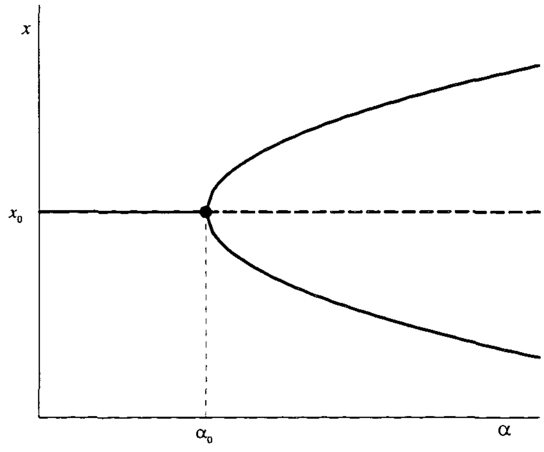

Figure 4.3: Bifurcation diagram local to a pitchfork bifurcation occurring at $(x, \alpha) = (x_0, \alpha_0)$. Solid lines indicate stable states while dashed lines indicate unstable states.

Pure imaginary conjugate pair of eigenvalues

The simplest bifurcation resulting from a pure imaginary conjugate pair of eigenvalues is called a Hopf bifurcation. In order to have such bifurcation we need a two dimensional system depending on a one dimensional parameter

$$\dot{\mathbf{x}} = \mathbf{f}(\mathbf{x}, \alpha),$$

with $\mathbf{x} \in \mathbb{R}^2$ and $\alpha \in \mathbb{R}$, such that the point $(\mathbf{x}_0 , \alpha_0)$ is the equilibrium point where the matrix $\mathrm{D}_x\mathbf{f}(\mathbf{x}_0 , \alpha_0)$ has a pure imaginary conjugate pair of eigenvalues. The phase portrait of this system is similar to that shown in figure 4.4. Here we plot the orbits in the neighbourhood of the equilibrium point $\mathbf{x}_0 = (x_0, y_0)$. For parameters smaller than α_0 the system presents one stable equilibrium point marked with a cross in the figure, while for eigenvalues larger than the critical α_0 the equilibrium point becomes unstable but a stable limit cycle (periodic orbit) appears surrounding the equilibrium point, i.e., a time dependent solution emerges from the Hopf bifurcation.

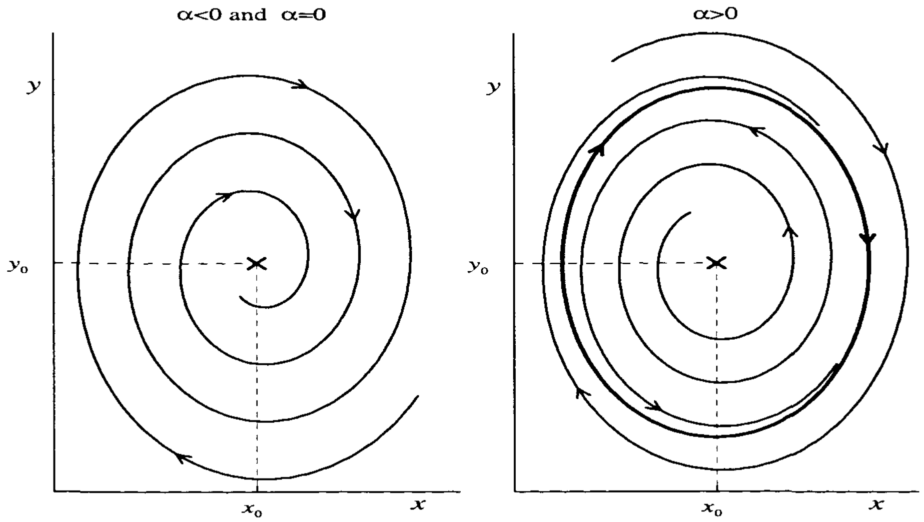

Figure 4.4: Sketch of the phase portrait of a system for values near a purely imaginary complex conjugate pair of eigenvalues. The left figure shows the equilibrium stable point, and on the right hand side figure we observe that the limit point becomes unstable and appears a limit cycle, which is the closed loop in the left figure.

Double zero eigenvalue

The simplest system that can produce a double zero eigenvalue is a two dimensional system depending on a two dimensional parameter

$$\dot{\mathbf{x}} = \mathbf{f}(\mathbf{x}\boldsymbol{\alpha}),$$

where $\mathbf{x} \in \mathbb{R}^2$ and $\boldsymbol{\alpha} \in \mathbb{R}^2$. The point $(\mathbf{x}_0, \boldsymbol{\alpha}_0)$ is said to be a Takens-Bogdanov bifurcation when $\mathrm{D}_x\mathbf{f}(\mathbf{x}_0, \boldsymbol{\alpha}_0)$ has a double zero eigenvalue. This bifurcation can be understood as the collision of a limit point and a Hopf bifurcation.

In the next section we will derive the normal form of the Takens-Bogdanov bifurcation and in appendix B we give a complete account of the bifurcation set in the neighbourhood of a Takens-Bogdanov bifurcation.

4.2 Simplifications of dynamical systems

In the previous section we described the bifurcations for the smallest possible dimension of the system and of the parameter space. Centre of manifold theory will allow us to find invariant manifolds on which a larger system locally behaves as the smaller one that we have already described.

Moreover, two systems

$$\dot{\mathbf{x}} = \mathbf{f}(\mathbf{x}, \boldsymbol{\alpha}),$$
$$\dot{\mathbf{y}} = \mathbf{g}(\mathbf{y}, \boldsymbol{\lambda}),$$

where $\mathbf{x}, \mathbf{y} \in \mathbb{R}^n$ and $\boldsymbol{\alpha}, \boldsymbol{\lambda} \in \mathbb{R}^k$ are said to be topologically equivalent in the parameter dependent open sets $U_\alpha \in \mathbb{R}^n$, $V_\lambda \in \mathbb{R}^n$ if there exists a homeomorphism of the parameter space

$$\rho : \mathbb{R}^k \to \mathbb{R}^k, \text{ such that } \rho(\mathbf{0}) = \mathbf{0},$$

and a parameter-dependent homeomorphism

$$h_\alpha : \mathbb{R}^n \to \mathbb{R}^n, \text{ such that } h_\alpha(U_\alpha) = V_{\rho(\alpha)} \text{ and } h_\alpha(0) = 0,$$

so that for every $\boldsymbol{\alpha}$, h_α transforms orbits of U_α into orbits of $V_{\rho(\alpha)}$ preserving the time direction.

When two systems are topologically equivalent their bifurcation diagrams are also equivalent.

Therefore, if we find local to an equilibrium point, a system topologically equivalent to a given one, such that the new system is simpler this will facilitate the analysis of the bifurcation diagram. This procedure is called the normal form reduction.

4.2.1 Centre of Manifold Theory

Our next task is to simplify the system by finding a centre of manifold such that the dynamical behaviour of the original system, restricted to the centre of manifold, is described by the dynamics of a simpler system.

The idea that lies behind centre of manifold theory is related to the fact that every linear system has invariant subspaces

$$\begin{aligned}\mathrm{E^s} = \mathrm{span}\{&\text{Eigenvectors corresponding to}\\ &\text{eigenvalues with negative real part}\}\end{aligned}$$

$$\begin{aligned}\mathrm{E^u} = \mathrm{span}\{&\text{Eigenvectors corresponding to}\\ &\text{eigenvalues with positive real part}\},\end{aligned}$$

$$\begin{aligned}\mathrm{E^c} = \mathrm{span}\{&\text{Eigenvectors corresponding to}\\ &\text{eigenvalues with zero real part}\}.\end{aligned}$$

Then, an orbit starting in $\mathrm{E^s}$ goes to zero as $t \to \infty$ (stable), while an orbit starting at $\mathrm{E^u}$ is unbounded as $t \to \infty$. Therefore, if $\mathrm{E^u} = \emptyset$ the stability of the system can be determined by studying the system restricted to $\mathrm{E^c}$. Therefore, in order to explain the centre of manifold theory we re-write system (4.2) as

$$\dot{\mathbf{y}} = \mathbf{F}(\mathbf{y},\, \boldsymbol{\lambda}), \tag{4.8}$$

where $\mathbf{y} = \mathbf{x} - \mathbf{x}_0 \in \mathbb{R}^n$ and $\boldsymbol{\lambda} = \boldsymbol{\alpha} - \boldsymbol{\alpha}_0 \in \mathbb{R}^k$, so that $\mathbf{F}(\mathbf{0},\, \mathbf{0}) = 0$. Then, assuming $\mathbf{F}$ to be a smooth function in a open set about the origin, we can write system (4.8) as

$$\dot{\mathbf{y}} = \mathbf{A}\mathbf{y} + \mathbf{G}(\mathbf{y},\, \boldsymbol{\lambda}), \tag{4.9}$$

where $\mathbf{A} = \mathrm{D}_y\mathbf{F}(\mathbf{0},\, \mathbf{0})$ is a $n \times n$ matrix and

$$\begin{aligned}\mathbf{G}(\mathbf{y},\, \boldsymbol{\lambda}) &= \mathrm{D}_\lambda\mathbf{F}(\mathbf{0},\, \mathbf{0})\boldsymbol{\lambda} + \frac{1}{2}\mathrm{D}_{yy}\mathbf{F}(\mathbf{0},\, \mathbf{0})\mathbf{y}^2 + \frac{1}{2}\mathrm{D}_{\lambda\lambda}\mathbf{F}(\mathbf{0},\, \mathbf{0})\boldsymbol{\lambda}^2\\ &\quad + \mathrm{D}_{\lambda y}\mathbf{F}(\mathbf{0},\, \mathbf{0})\boldsymbol{\lambda}\mathbf{y} + \text{ higher order terms},\end{aligned}$$

so that $\mathbf{G}(\mathbf{0},\, \mathbf{0}) = \mathbf{0}$ and $\mathrm{D}_y\mathbf{G}(\mathbf{0},\, \mathbf{0}) = \mathbf{0}$.

If we consider that the matrix $\mathbf{A}$ has eigenvalues $\sigma_1, \ldots, \sigma_p$ with zero real part and $\sigma_{p+1}, \ldots, \sigma_n$ with negative real part, then, exists an invertible $n \times n$ matrix $\mathbf{P}$, non-unique, such that

$$\mathbf{P}^{-1}\mathbf{A}\mathbf{P} = \left(\begin{array}{c|c} \mathbf{B} & \mathbf{0} \\ \hline \mathbf{0} & \mathbf{C} \end{array}\right),$$

where $\mathbf{B}$ is an $p \times p$ matrix and $\mathbf{C}$ is a $(n-p) \times (n-p)$ matrix. Thus, we can re-write system (4.9) as

$$\dot{\mathbf{u}} = \mathbf{B}\mathbf{u} + \mathbf{g}_1(\mathbf{u},\, \mathbf{v},\, \boldsymbol{\lambda}), \tag{4.10}$$

$$\dot{\mathbf{v}} = \mathbf{C}\mathbf{v} + \mathbf{g}_2(\mathbf{u},\, \mathbf{v},\, \boldsymbol{\lambda}), \tag{4.11}$$

where $\mathbf{u} \in \mathbb{R}^p$, $\mathbf{v} \in \mathbb{R}^{n-p}$ and the functions

$$\mathbf{g}_1 : B_1 \in \mathbb{R}^p \times \mathbb{R}^{n-p} \times \mathbb{R}^k \to \mathbb{R}^p$$

and

$$\mathbf{g}_2 : B_2 \in \mathbb{R}^p \times \mathbb{R}^{n-p} \times \mathbb{R}^k \to \mathbb{R}^{n-p}$$

satisfy $\mathbf{g}_i(\mathbf{0},\, \mathbf{0}) = \mathbf{0}$, and $\mathrm{D}_u\mathbf{g}_i(\mathbf{0},\, \mathbf{0}) = \mathbf{0}$, with $i = \{1,\, 2\}$. Here $(\mathbf{u},\, \mathbf{v})^T = \mathbf{P}^{-1}\mathbf{y}$ and $(\mathbf{g}_1,\, \mathbf{g}_2)^T = \mathbf{P}^{-1}\mathbf{G}$. Thus, there exists a centre of manifold given by

$$\begin{aligned} W^c_{loc}(0) &= \Big\{(\mathbf{u},\, \mathbf{v},\, \boldsymbol{\lambda}) \in \mathbb{R}^p \times \mathbb{R}^{n-p} \times \mathbb{R}^k :\ \mathbf{v} = \mathbf{h}(\mathbf{u},\, \boldsymbol{\lambda}), \\ &\qquad ||\mathbf{u}|| < \epsilon,\ ||\boldsymbol{\lambda}|| < \bar{\epsilon},\ \mathbf{h}(\mathbf{0},\, \mathbf{0}) = \mathbf{0},\ D_u\mathbf{h}(\mathbf{0},\, \mathbf{0}) = \mathbf{0}\Big\} \end{aligned}$$

for $\epsilon \in \mathbb{R}^+$ and $\bar{\epsilon} \in \mathbb{R}^+$ sufficiently small. The dynamical behaviour of the system (4.10)-(4.11) restricted to the centre of manifold is given by

$$\dot{\mathbf{w}} = \mathbf{B}\mathbf{w} + \mathbf{g}_1\left(\mathbf{w},\, \mathbf{h}(\mathbf{w}, \boldsymbol{\lambda}),\, \boldsymbol{\lambda}\right),\ \ \mathbf{w} \in \mathbb{R}^p\,, \tag{4.12}$$

for sufficiently small $||(\mathbf{w},\, \boldsymbol{\lambda})||$. So that the dynamics near the origin of system (4.12), explain the dynamics of system (4.10)-(4.11), and hence we have the dynamical behaviour of system (4.9) in the neighbourhood of $\mathbf{y} = \mathbf{0}$ and ultimately the behaviour of the dynamical system (4.2) about the point $(\mathbf{x},\, \boldsymbol{\alpha}) = (\mathbf{x}_0,\, \boldsymbol{\alpha}_0)$. Therefore, analysing a system of a smaller dimension (4.12), we can understand the behaviour of systems of higher dimensions (4.2).

4.2.2 Normal Forms

The theory of normal form reduction consists of finding, locally to an equilibrium point, invertible changes of coordinates, invertible changes of parameters and direction-preserving time parameterizations so that they allow us to express the system in a simpler form. Therefore, normal form reduction is a problem-dependent technique and, furthermore, for the same equilibrium point we can derive several normal forms. We will illustrate the idea of normal form reduction by finding the Bogdanov reduction local to a Takens-Bogdanov bifurcation as explained by Kuznetsov [56].

Normal form reduction local to a Takens Bogdanov bifurcation

We consider a two dimensional system

$$\dot{\mathbf{x}} = \mathbf{f}(\mathbf{x},\, \boldsymbol{\alpha}) \tag{4.13}$$

where $\mathbf{x} \in \mathbb{R}^2$, $\boldsymbol{\alpha} \in \mathbb{R}^2$ and at $(\mathbf{x}, \boldsymbol{\alpha}) = (\mathbf{0}, \mathbf{0})$ the system has a double zero eigenvalue. Then, as done for the centre of manifold theory we can re-write system (4.13) as

$$\dot{\mathbf{x}} = \mathbf{A}\mathbf{x} + \mathbf{F}(\mathbf{x}, \boldsymbol{\alpha}), \tag{4.14}$$

where we assume

$$\mathbf{A} = \mathrm{D}_x\mathbf{f}(\mathbf{0}, \mathbf{0}) \neq \mathbf{0} \tag{4.15}$$

and

$$\mathbf{F}(\mathbf{x}, \boldsymbol{\alpha}) = \mathbf{f}(\mathbf{x}, \boldsymbol{\alpha}) - \mathbf{A}\mathbf{x} = \mathrm{O}(\|\mathbf{x}^2\|).$$

Then, exists a nonsingular matrix $\mathbf{P}$, non unique, such that

$$\mathbf{J} = \mathbf{P}^{-1}\mathbf{A}\mathbf{P} = \begin{pmatrix} 0 & 1 \\ 0 & 0 \end{pmatrix}.$$

Here $\mathbf{J}$ is called the Jordan canonical form of the matrix $\mathbf{A}$. Then, introducing a new set of variables

$$\mathbf{y} = \mathbf{P}^{-1}\mathbf{x}$$

and calling

$$\mathbf{G}(\mathbf{y}, \boldsymbol{\alpha}) = \mathbf{P}^{-1}\mathbf{F}(\mathbf{P}\mathbf{y}, \boldsymbol{\alpha}),$$

system (4.14) becomes

$$\dot{y}_1 = y_2 + G_1(y_1, y_2, \boldsymbol{\alpha}), \tag{4.16}$$

$$\dot{y}_2 = G_2(y_1, y_2, \boldsymbol{\alpha}), \tag{4.17}$$

where, the functions $G_i(y_1, y_2, \boldsymbol{\alpha})$, $i = \{1, 2\}$, can be expanded about $\mathbf{y} = \mathbf{0}$ as

$$\begin{aligned} G_i(y_1, y_2, \boldsymbol{\alpha}) &= a_{00}^{(i)}(\boldsymbol{\alpha}) + a_{10}^{(i)}(\boldsymbol{\alpha})y_1 + a_{01}^{(i)}(\boldsymbol{\alpha})y_2 + \frac{1}{2}a_{20}^{(i)}(\boldsymbol{\alpha})y_1^2 \\ &\quad + \frac{1}{2}a_{02}^{(i)}(\boldsymbol{\alpha})y_2^2 + a_{11}^{(i)}(\boldsymbol{\alpha})y_1y_2 + \mathrm{O}\left(\|\mathbf{y}\|^3\right), \end{aligned}$$

where

$$a_{00}^{(i)}(\mathbf{0}) = a_{10}^{(i)}(\mathbf{0}) = a_{01}^{(i)}(\mathbf{0}) = 0.$$

with $i = \{1, 2\}$.

Then we introduce the following change of variables

$$\begin{aligned} u_1 &= y_1, \\ u_2 &= y_2 + G_1(y_1, y_2, \boldsymbol{\alpha}), \end{aligned}$$

that is an invertible transformation mapping the origin into itself and then, system (4.16)-(4.17) can be re-written as

$$\dot{u}_1 = u_2, \tag{4.18}$$

$$\dot{u}_2 = H_2(u_1, u_2, \boldsymbol{\alpha}), \tag{4.19}$$

where the right hand side of equation (4.19) can be expanded as

$$\begin{aligned} H_2(u_1,u_2,\boldsymbol{\alpha}) &= h_{00}(\boldsymbol{\alpha}) + h_{10}(\boldsymbol{\alpha})u_1 + h_{01}(\boldsymbol{\alpha})u_2 + \frac{1}{2}h_{20}(\boldsymbol{\alpha})u_1^2 \\ &\quad + \frac{1}{2}h_{02}(\boldsymbol{\alpha})u_2^2 + h_{11}(\boldsymbol{\alpha})u_1u_2 + \mathrm{O}\left(||\mathbf{u}||^3\right) . \end{aligned}$$

Here the coefficients satisfy

$$h_{00}(\mathbf{0}) = h_{10}(\mathbf{0}) = 0$$

and

$$\begin{aligned} h_{20}(\mathbf{0}) &= a_{20}^{(2)}(\mathbf{0}) , \\ h_{02}(\mathbf{0}) &= a_{02}^{(2)}(\mathbf{0}) + 2a_{11}^{(1)}(\mathbf{0}) , \\ h_{11}(\mathbf{0}) &= a_{20}^{(1)}(\mathbf{0}) + a_{11}^{(2)}(\mathbf{0}) . \end{aligned}$$

We now shift the variables by introducing the new set

$$\begin{aligned} v_1 &= u_1 + \sigma(\boldsymbol{\alpha}) , \\ v_2 &= u_2 , \end{aligned}$$

and then the system (4.18)-(4.19) can be re-written as

$$\begin{aligned} \dot{v}_1 &= v_2 , && (4.20) \\ \dot{v}_2 &= h_{00} - h_{10}\sigma + \mathrm{O}(\sigma^2) + \left[h_{10} - h_{20}\sigma + \mathrm{O}(\sigma^2)\right] v_1 \\ &\quad + \left[h_{01} - h_{11}\sigma + \mathrm{O}(\sigma^2)\right] v_2 + \frac{1}{2}\left[h_{20} + \mathrm{O}(\sigma)\right] v_1^2 \\ &\quad + \frac{1}{2}\left[h_{02} + \mathrm{O}(\sigma)\right] v_2^2 + \left[h_{11} + \mathrm{O}(\sigma)\right] v_1v_2 + \mathrm{O}\left(||\mathbf{v}||^3\right) . && (4.21) \end{aligned}$$

Assuming that

$$h_{11}(\mathbf{0}) = a_{20}^{(1)}(\mathbf{0}) + a_{11}^{(2)}(\mathbf{0}) \neq 0 , \qquad (4.22)$$

and imposing the coefficient of v_2 to be zero, we find that for $||\boldsymbol{\alpha}||$ sufficiently small, by the implicit function theorem, exists a function

$$\sigma(\boldsymbol{\alpha}) \approx \frac{h_{01}(\boldsymbol{\alpha})}{h_{11}(\boldsymbol{\alpha})} ,$$

which makes the coefficient zero, and hence (4.20)-(4.21) yields

$$\begin{aligned} \dot{v}_1 &= v_2 , && (4.23) \\ \dot{v}_2 &= k_{00}(\boldsymbol{\alpha}) + k_{10}(\boldsymbol{\alpha})v_1 + \frac{1}{2}k_{20}(\boldsymbol{\alpha})v_1^2 \\ &\quad + \frac{1}{2}k_{02}(\boldsymbol{\alpha})v_2^2 + k_{11}(\boldsymbol{\alpha})v_1v_2 + \mathrm{O}\left(||\mathbf{v}||^3\right) , && (4.24) \end{aligned}$$

where

$$k_{00}(\mathbf{0}) = k_{10}(\mathbf{0}) = 0$$

and

$$\begin{aligned} k_{20}(\mathbf{0}) &= h_{20}(\mathbf{0}), \\ k_{02}(\mathbf{0}) &= h_{02}(\mathbf{0}), \\ k_{11}(\mathbf{0}) &= h_{11}(\mathbf{0}), \end{aligned}$$

We now re-parameterize the system by introducing a new time scale

$$\bar{t} = \frac{1}{1+\rho(\boldsymbol{\alpha})v_1} t,$$

where $\rho(\boldsymbol{\alpha})$ is a smooth function of the parameters. With respect to the new time scale system (4.23)-(4.24) becomes

$$\begin{aligned} \dot{v}_1 &= (1+\rho v_1)v_2, && (4.25) \\ \dot{v}_2 &= k_{00} + (k_{10}+\rho k_{00})v_1 + \frac{1}{2}(k_{20}+2\rho k_{10})v_1^2 \\ &\quad + \frac{1}{2}k_{02}v_2^2 + k_{11}v_1v_2 + \mathrm{O}\left(\|\mathbf{v}\|^3\right), && (4.26) \end{aligned}$$

where the dot indicates a derivative with respect to $\bar{t}$.
We introduce the new set of variables

$$\begin{aligned} w_1 &= v_1, \\ w_2 &= v_2 + \rho(\boldsymbol{\alpha})v_1v_2, \end{aligned}$$

which maps the origin into itself for any $\rho(\boldsymbol{\alpha})$. Then, from equations (4.25) and (4.26), we obtain

$$\begin{aligned} \dot{w}_1 &= w_2 && (4.27) \\ \dot{w}_2 &= k_{00} + [k_{10}+\rho k_{00}]\, w_1 + \frac{1}{2}[k_{20}+2\rho k_{10}]\, w_1^2 \\ &\quad + \frac{1}{2}[k_{02}+2\rho]\, w_2^2 + k_{11}w_1w_2 + \mathrm{O}\left(\|\mathbf{w}\|^3\right), && (4.28) \end{aligned}$$

hence, in order to set the coefficient of w_2 to zero, we define

$$\rho(\boldsymbol{\alpha}) = -\frac{1}{2}k_{02}(\boldsymbol{\alpha}),$$

and substituting this expression into the system (4.27)-(4.28), we obtain

$$\begin{aligned} \dot{w}_1 &= w_2 && (4.29) \\ \dot{w}_2 &= \mu_{00}(\boldsymbol{\alpha}) + \mu_{10}(\boldsymbol{\alpha})w_1 + \mu_{20}(\boldsymbol{\alpha})w_1^2 \\ &\quad + \mu_{12}(\boldsymbol{\alpha})w_1w_2 + \mathrm{O}\left(\|\mathbf{w}\|^3\right), && (4.30) \end{aligned}$$

where

$$
\begin{aligned}
\mu_{00}(\boldsymbol{\alpha}) &= k_{00}(\boldsymbol{\alpha}), \\
\mu_{10}(\boldsymbol{\alpha}) &= k_{10}(\boldsymbol{\alpha}) - \frac{1}{2}k_{00}(\boldsymbol{\alpha})k_{02}(\boldsymbol{\alpha}), \\
\mu_{20}(\boldsymbol{\alpha}) &= \frac{1}{2}\left(k_{20}(\boldsymbol{\alpha}) - k_{02}(\boldsymbol{\alpha})k_{10}(\boldsymbol{\alpha})\right), \\
\mu_{11}(\boldsymbol{\alpha}) &= k_{11}(\boldsymbol{\alpha}).
\end{aligned}
$$

Assuming

$$\mu_{20}(\mathbf{0}) = \frac{1}{2}k_{20}(\mathbf{0}) = \frac{1}{2}h_{20}(\mathbf{0}) = \frac{1}{2}a_{20}^{(2)}(\mathbf{0}) \neq 0 \tag{4.31}$$

for $||\boldsymbol{\alpha}||$ sufficiently small we can define a new time scale

$$\hat{t} = \left|\frac{\mu_{11}(\boldsymbol{\alpha})}{\mu_{20}(\boldsymbol{\alpha})}\right| \bar{t}$$

which is well defined, since from equation (4.22) we have that $\mu_{11}(\mathbf{0}) \neq 0$. Moreover we can introduce a new set of variables

$$
\begin{aligned}
\eta_1 &= \frac{\mu_{20}(\boldsymbol{\alpha})}{\mu_{11}^2(\boldsymbol{\alpha})} w_1, \\
\eta_2 &= \operatorname{sign}\left(\frac{\mu_{11}(\boldsymbol{\alpha})}{\mu_{20}(\boldsymbol{\alpha})}\right) \frac{\mu_{20}^2(\boldsymbol{\alpha})}{\mu_{11}^3(\boldsymbol{\alpha})} w_2,
\end{aligned}
$$

and hence system (4.29)-(4.30) yields

$$\dot{\eta}_1 = \eta_2, \tag{4.32}$$

$$\dot{\eta}_2 = \xi_1(\boldsymbol{\alpha}) + \xi_2(\boldsymbol{\alpha})\eta_1 + \eta_1^2 + s\eta_1\eta_2 + \mathrm{O}\left(||\boldsymbol{\eta}||\right), \tag{4.33}$$

where

$$
\begin{aligned}
\xi_1(\boldsymbol{\alpha}) &= \frac{\mu_{11}^4(\boldsymbol{\alpha})}{\mu_{20}^3(\boldsymbol{\alpha})}\mu_{00}(\boldsymbol{\alpha}), \\
\xi_2(\boldsymbol{\alpha}) &= \frac{\mu_{11}^2(\boldsymbol{\alpha})}{\mu_{20}^2(\boldsymbol{\alpha})}\mu_{10}(\boldsymbol{\alpha}),
\end{aligned}
$$

with $\xi_1(\mathbf{0}) = \xi_2(\mathbf{0}) = 0$ and

$$s = \operatorname{sign}\left(\frac{\mu_{11}(\mathbf{0})}{\mu_{20}(\mathbf{0})}\right).$$

In order to have that (4.32)-(4.33) is the normal form of the original system (4.13) we need to prove that the change of parameters is regular near the origin, i.e. defining the matrix

$$\Xi_{ij} = \frac{\partial \xi_i}{\partial \alpha_j}(\mathbf{0})$$

then the regularity condition is given by $\det(\Xi) = 0$, which assuming conditions (4.22) and (4.31) hold, is equivalent to the regularity of the map

$$(\mathrm{x}, \boldsymbol{\alpha}) \to (\mathbf{f}(\mathrm{x}, \boldsymbol{\alpha}), \operatorname{tr}(\mathrm{D}_x\mathbf{f}(\mathrm{x}, \boldsymbol{\alpha})), \det(\mathrm{D}_x\mathbf{f}(\mathrm{x}, \boldsymbol{\alpha}))) \tag{4.34}$$

at $(\mathbf{x}, \boldsymbol{\alpha}) = (\mathbf{0}, \mathbf{0})$.

Therefore, we have proved that when a system (4.13) with a double zero eigenvalue at $(\mathbf{x}, \boldsymbol{\alpha}) = (\mathbf{0}, \mathbf{0})$ verifies conditions (4.15), (4.22), (4.31) and (4.34), then the system is equivalent, locally to the Takens-Bogdanov bifurcation, to its normal form reduction, given by (4.32)-(4.33).

In section 5.3.2.1 of this thesis we will apply this normal form to our problem, while in appendix B we describe the bifurcation set of the normal form given by (4.32)-(4.33).

Other normal forms

The Takens -Bogdanov normal form is a complicated example, however other cases are easier to derive. These are normal forms of the bifurcations that we have described above

- The normal form local to a limit point occurring at $(x, \alpha) = (0, 0)$ is given by
$$\dot{x} = \pm\alpha + x^2 + \mathrm{O}\left(|x|^3\right) .$$
- The normal form local to a transcritical bifurcation is given by
$$\dot{x} = \pm\alpha x + x^2 + \mathrm{O}\left(|x|^3\right) .$$
- The normal form close to a pitchfork bifurcation is given by
$$\dot{x} = \pm\alpha x + x^3 + \mathrm{O}\left(|x|^4\right) .$$
- The normal form of a Hopf bifurcation is given by
$$\begin{aligned} \dot{x} &= \mu_1 x - \mu_2 y + (\nu_1 x - \nu_2 y)(x^2 + y^2) + \mathrm{O}\left(\|\mathbf{x}\|^5\right) , \\ \dot{y} &= \mu_2 x + \mu_1 y + (\nu_2 x + \nu_1 y)(x^2 + y^2) + \mathrm{O}\left(\|\mathbf{x}\|^5\right) , \end{aligned} \tag{4.35}$$
where $\mu_i = \mu_i(\alpha)$ and $\nu_i = \nu_i(\alpha)$, $i = \{1, 2\}$.

4.3 Bifurcation of periodic solutions

In this chapter we introduce the concept of Poincaré maps and Floquet multipliers that allow us to explain the stability of a periodic orbit, as well as to classify its bifurcations.

We also introduce in this section the description of global bifurcations of periodic orbits.

4.3.1 Poincaré maps

We consider the system

$$\dot{\mathbf{x}} = \mathbf{f}(\mathbf{x}), \tag{4.36}$$

where $\mathbf{x} \in \mathbb{R}^n$ and $\mathbf{f} : A \in \mathbb{R}^n \to \mathbb{R}^n$ is a smooth function. Assuming L_0 is a periodic orbit (limit cycle) of the system (4.36), which passes through $\mathbf{x}_0$, we can consider an hyperplane, Σ, orthogonal to L_0 at $\mathbf{x}_0$. Then, any orbit passing through Σ close to $\mathbf{x}_0$ returns to a point on Σ, $\tilde{\mathbf{x}}$, and we can define the Poincaré map associated to L_0 as

$$\mathbf{x} \mapsto \tilde{\mathbf{x}} = P(\mathbf{x}).$$

This map is well defined and it satisfies that $\mathbf{x}_0$ is a fixed point of the map ($\mathbf{x}_0 = P(\mathbf{x}_0)$. Introducing a local set of coordinates on Σ, $\boldsymbol{\xi} = (\xi_1, \ldots, \xi_{n-1})$, such that $\mathbf{x}_0$ is the origin of coordinates, $\boldsymbol{\xi} = \mathbf{0}$, we can define a map

$$P : \mathbb{R}^{n-1} \mapsto \mathbb{R}^{n-1},$$

that transforms $\boldsymbol{\xi}$ corresponding to $\mathbf{x}$ into $\tilde{\boldsymbol{\xi}}$ corresponding to $\tilde{\mathbf{x}}$, and so that the origin is a fixed point of the system $P(\mathbf{0}) = \mathbf{0}$.

A fixed point of a map is said to be stable when the eigenvalues of the matrix $\mathbf{M} = \mathrm{D}_{\xi}P(\mathbf{0})$, $\sigma_1, \ldots, \sigma_n - 1$, the so-called Floquet multipliers, verify $|\sigma_i| < 1$, $i = \{1, \ldots, n\}$. And the stability of the limit cycle L_0 coincides with that of the fixed point $\boldsymbol{\xi} = \mathbf{0}$.

When any of the eigenvalues of the system has modulus one, then the fixed point (or the periodic orbit) is said to be hyperbolic, and as done for the equilibrium points, we can study the bifurcations of a parameter-dependent system local to a hyperbolic point.

4.3.2 Classification of local bifurcations of periodic orbits

Considering the bifurcations of the Poincaré map associated to the limit cycle L_0 of the system

$$\dot{\mathbf{x}} = \mathbf{f}(\mathbf{x}, \boldsymbol{\alpha}),$$

occurring at $\boldsymbol{\alpha} = \boldsymbol{\alpha}_0$, we can classify the bifurcations of the periodic orbits as follows

- Limit point. When the Poincaré map has a Floquet multiplier $\sigma_k = 1$, then the bifurcation is called a limit point, due to the analogy with the limit point bifurcation of continuum systems as described above.

- Period doubling bifurcation. This case occurs when one of the Floquet multipliers verifies $\sigma_k = -1$. Figure 4.5 shows two orbits of a system occurring before and after a period doubling bifurcation and we can observe that the period has been, indeed, doubled.
- Neimark-Sacker bifurcation. This occurs when a complex conjugate pair of eigenvalues has modulus one. Since such a bifurcation will not arise in this thesis we will not give it any further consideration.

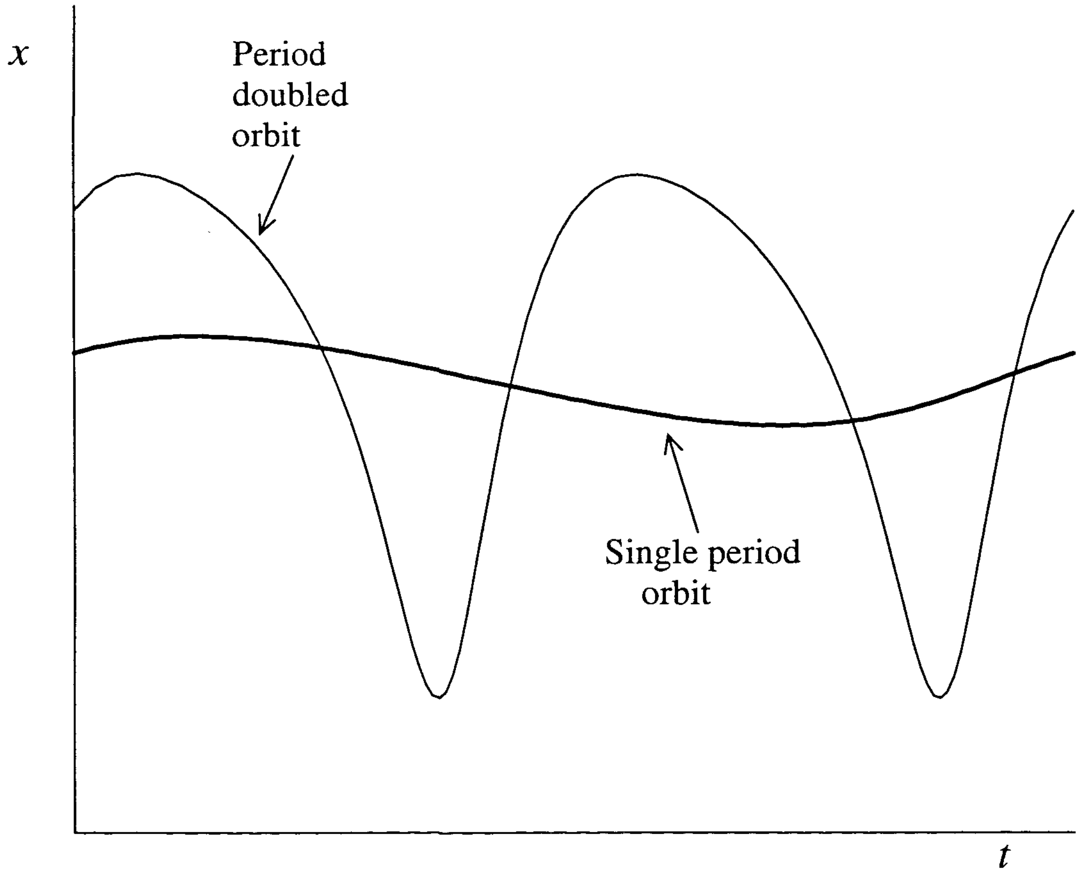

Figure 4.5: Two orbits of a system occurring before and after a period doubling bifurcation.

To study the bifurcation of periodic solutions we used the continuation and bifurcation software AUTO97 [58]. However, the computation of the linearized Poincaré map and of the Floquet multipliers can occasionally be inaccurate, due to the proximity of the eigenvalues to the unit circle.

4.3.3 Global Bifurcations

In this thesis we only consider two different types of global bifurcations: a saddle homoclinic bifurcation and a saddle-node homoclinic bifurcation. Sketches of the phase portraits of the evolution of the bifurcation as the parameter of the system is changed are plotted in figures 4.6 and 4.7 for the saddle and saddle-node cases respectively.

Figure 4.6a) shows the phase portrait for values of the parameter greater than the critical value at which the bifurcation exists. The system exhibits a saddle bifurcation, labelled S in the figure and an attractor limit cycle. As the parameter is decreased the limit cycle gets larger, until eventually the limit cycle collides with the saddle point at the critical value of the parameter. A saddle homoclinic bifurcation (SHB), shown in figure 4.6b), exists for the critical value of the parameter. For this value of the parameter the limit cycle is an homoclinic orbit, i.e. the period is infinite. For smaller values of the parameter the limit cycle no longer exists and only a single saddle point (S) remains, as shown in figure 4.6c).

The saddle-node homoclinic bifurcation is shown in figure 4.7. Here we observe that for values of the parameter larger than the critical one, the system presents a saddle point (S) and a stable node (SN) in a loop, figure 4.7a). As the value of the parameter decreases the equilibrium points come closer together, merging at a critical value of the parameter, at which a saddle-node homoclinic bifurcation (SNHB) occurs, as seen in figure 4.7b). For even smaller values of the parameter, only a limit cycle remains as an attractor of the system, figure 4.7c). In both examples we could reverse the succession of events as the parameter decreases.

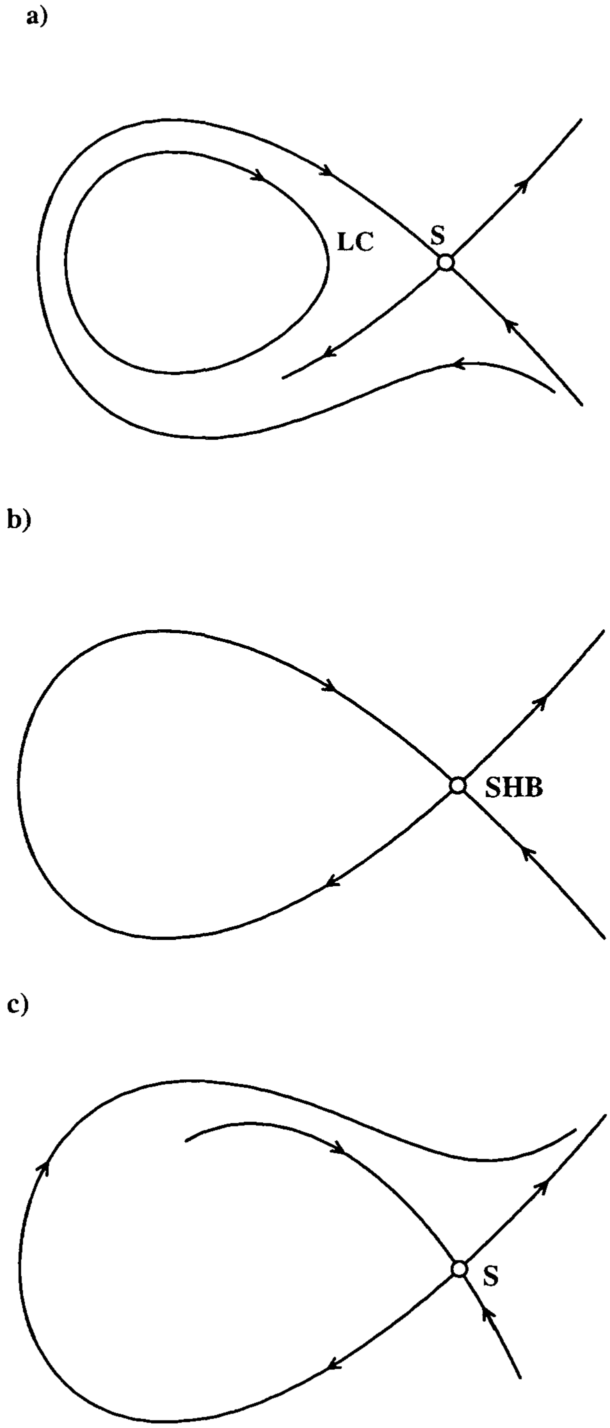

Figure 4.6: Sketch of the phase portrait of a saddle homoclinic bifurcation. Figure a) shows a saddle (S) and a stable limit cycle (LC). As the parameter changes the diameter of the limit cycle increases until we have a saddle homoclinic bifurcation (SHB) shown in figure b). And as the parameter changes only the saddle point remains (S), as seen in figure c)

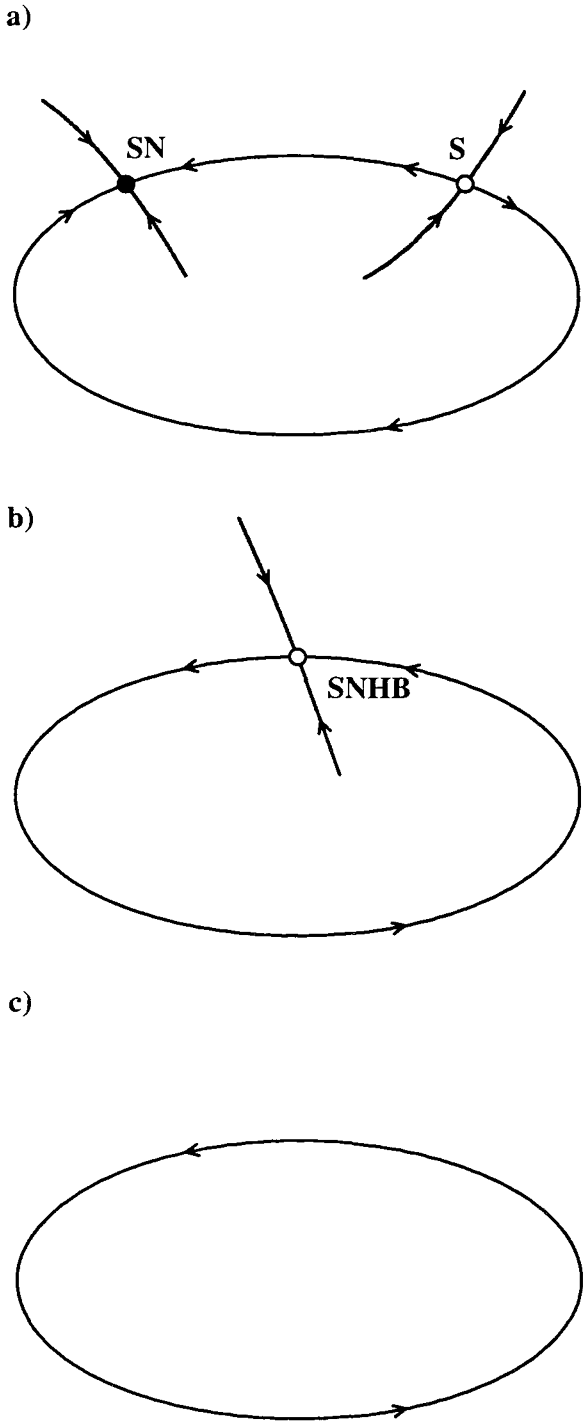

Figure 4.7: Sketch of the phase portrait of a saddle-node homoclinic bifurcation. Figure a) shows a saddle (S) and a stable node in a loop. As the parameter changes the equilibrium points get closer together until they merge forming a saddle-node homoclinic bifurcation (SNHB) shown in figure b). And as we change the parameter the only attractor left is a limit cycle as seen in figure c)

Chapter 5

The two dimensional problem

Our task in this chapter is to accomplish full understanding of the behaviour of a uniform homogeneous nematic liquid crystal under a shear flow in terms of both the temperature and the shear rate of the system for the case where two of the vectors of the local basis $\{\mathbf{n}, \mathbf{m}, \mathbf{l}\}$ are considered to be in the shear plane and, as a result of this restriction, the preferred direction of alignment will either be in the shear plane or in a direction perpendicular to it.

Steady state solutions when no flow is present describe the isotropic and uniaxial nematic state while the introduction of flow gives a complex array of different steady states and time dependent solutions.

5.1 Governing Equations

The governing equations of the Olmsted and Goldbart theory (OG), [41, 40], for the dynamics of a liquid crystal were presented in section 3.1. The model comprises the linear momentum equation (3.1), the incompressibility condition (3.2) and the equation for the evolution of the order tensor (3.48), which may be written as

$$\dot{\mathbf{Q}} = \mathbf{W}\mathbf{Q} - \mathbf{Q}\mathbf{W} + \beta_1 \mathbf{D}^{[t]} + \frac{1}{\beta_2}\mathbf{H}^{[st]}, \tag{5.1}$$

where the tensor

$$\mathbf{H} = -\frac{\delta f}{\delta \mathbf{Q}},$$

is the molecular field. Here f is the total free energy density of the system that can be decomposed into a distortion (Frank) free energy density, f_g, and bulk (Landau) free energy density, f_b. The distortion free energy density is given in terms of the gradient of $\mathbf{Q}$ by

$$f_g = \frac{1}{2}L_1 Q_{jk,i}Q_{jk,i} + \frac{1}{2}L_2 Q_{ik,i}Q_{jk,j}\,,$$

where L_1 and L_2 are the elastic constants. The bulk free energy density can be written in terms of the invariants of $\mathbf{Q}$, ($\mathrm{tr}(\mathbf{Q}^2)$ and $\mathrm{tr}(\mathbf{Q}^3)$) by the expansion (2.7)

$$f_b = \frac{1}{2}A\mathrm{tr}(\mathbf{Q}^2) + \frac{1}{3}B\mathrm{tr}(\mathbf{Q}^3) + \frac{1}{4}C\mathrm{tr}(\mathbf{Q}^2)^2\,.$$

Here A is a linear function of the temperature and B and C are assumed to be constants.

For simplicity, in our study we consider a system with a velocity field $\mathbf{v} = Dy\,\mathbf{i}$, where $\mathbf{i}$ is the unit vector in the x-direction, D is the constant strain rate and we look for homogeneous solutions of the system, i.e., spatially uniform states where $\mathbf{Q}$ is independent of position. The linear momentum equation (3.1) and the incompressibility condition (3.2) are automatically satisfied and equation (5.1) can be written as

$$\dot{\mathbf{Q}} = \mathbf{W}\mathbf{Q} - \mathbf{Q}\mathbf{W} + \beta_1\mathbf{D}^{[t]} - \frac{1}{\beta_2}\Big[A\mathbf{Q} + B\mathbf{Q}^2 + C\mathrm{tr}(\mathbf{Q}^2)\mathbf{Q} - \frac{B}{3}\mathrm{tr}(\mathbf{Q}^2)\mathbf{I}\Big]. \qquad (5.2)$$

We non-dimensionalise this equation by introducing the quantities

$$\tau = \frac{A}{C}\,, \quad \widehat{\mathbf{W}} = \frac{1}{D}\mathbf{W}\,, \quad \widehat{\mathbf{D}}^{[t]} = \frac{1}{D}\mathbf{D}^{[t]}\,,$$

with the non-dimensional time given by $\bar{t} = Ct/\beta_2$, and the non-dimensional strain rate by $\delta = D\beta_2/C$. Hence the dimensionless form of (5.2) is

$$\dot{\mathbf{Q}} = \delta\Big(\widehat{\mathbf{W}}\mathbf{Q} - \mathbf{Q}\widehat{\mathbf{W}} + \beta_1\widehat{\mathbf{D}}^{[t]}\Big) - \tau\mathbf{Q} - \widetilde{B}\mathbf{Q}^2 - \mathrm{tr}(\mathbf{Q}^2)\mathbf{Q} + \frac{\widetilde{B}}{3}\mathrm{tr}(\mathbf{Q}^2)\mathbf{I}, \qquad (5.3)$$

where $\widetilde{B} = B/C$, δ is the dimensionless strain rate and τ the dimensionless temperature. The homogeneous states depend on the value of the kinetic coefficient β_1 and the ratio of the Landau constants $\widetilde{B}$. A negative value of $\widetilde{B}$ gives a conventional nematic state.

Throughout this chapter we consider the two dimensional case and therefore $\mathbf{n}$ and $\mathbf{m}$ are confined to the shear plane as shown in the configuration scheme in figure 5.1. In this situation the number of variables reduces to three: the two order parameters, S_1 and S_2, and θ, the angle that $\mathbf{n}$ subtends to $\mathbf{i}$. The appropriate re-scaling, which sets the dimensionless isotropic-nematic transition temperature and the corresponding dimensionless uniaxial order parameter both to unity in the absence of flow was given by the relations (2.8)-(2.10)

$$\begin{aligned} \bar{\tau} &= 27\tau/\widetilde{B}^2\,, \\ \bar{S}_1 &= -9S_1/2\widetilde{B}\,, \\ \bar{S}_2 &= -3S_2/2\widetilde{B}\,. \end{aligned}$$

Dropping bars, the three independent components of the tensor equation (5.3) with respect to the $\{\mathbf{n}\,,\mathbf{m}\,,\mathbf{l}\}$ basis yields the nonlinear dynamical system

$$\begin{aligned}
\dot{S}_1 &= -\frac{9\beta_1}{4\widetilde{B}}\delta\sin 2\theta - \frac{\widetilde{B}^2}{27}\left[\tau S_1 - 3(S_1^2 - 3S_2^2) + 2S_1(S_1^2 + 3S_2^2)\right], && (5.4)\\
\dot{S}_2 &= \frac{3\beta_1}{4\widetilde{B}}\delta\sin 2\theta - \frac{\widetilde{B}^2}{27}\left[\tau S_2 + 6S_1S_2 + 2S_2(S_1^2 + 3S_2^2)\right], && (5.5)\\
\dot{\theta} &= \frac{\delta}{2}\left[\frac{3\beta_1\cos 2\theta}{\widetilde{B}(S_2 - S_1)} - 1\right]. && (5.6)
\end{aligned}$$

These equations are invariant under $\delta \to -\delta$, $\theta \to -\theta$ changes and, without loss of generality, we can therefore restrict ourselves to the case $\delta \geq 0$.

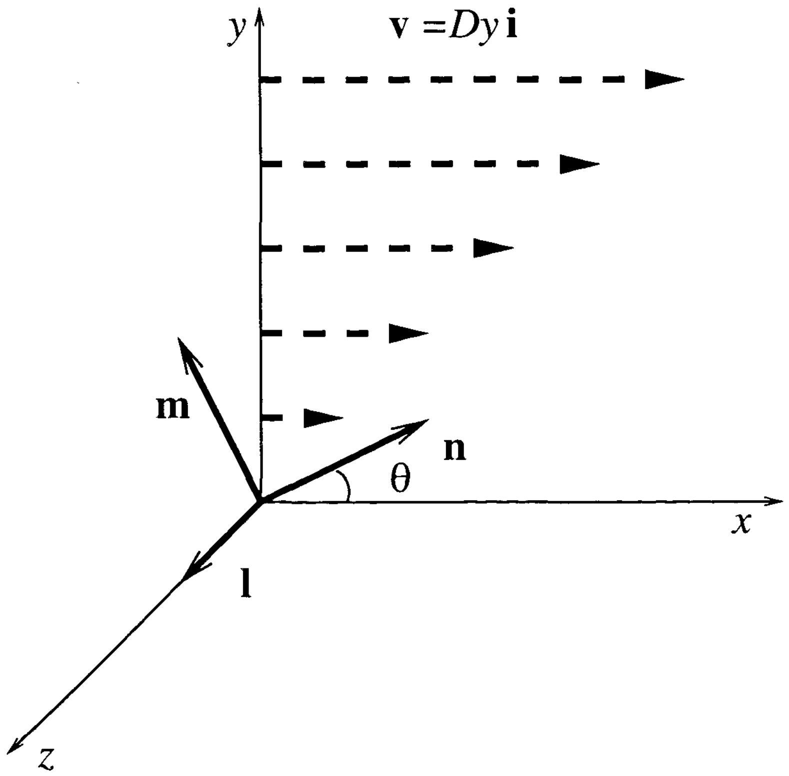

Figure 5.1: The local basis $\{\mathbf{n},\mathbf{m},\mathbf{l}\}$ is plotted with respect to the Cartesian coordinate axis. The unit vectors $\mathbf{n}$ and $\mathbf{m}$ are in the xy-plane and θ is the angle between $\mathbf{n}$ and the x axis. The vector field $\mathbf{v} = Dy\mathbf{i}$ is the velocity field associated to the shear flow, where $\mathbf{i}$ is the unit vector in the x-direction.

5.2 Classification of the solution branches

We expect the behaviour of the system to be substantially different for small and large values of the strain rate. With this in mind we analyse the system under weak flow in order to achieve a qualitative classification of the different solution branches. A detailed study of every solution branch will be done in subsequent sections, where we have found numerical solutions of the system and perform asymptotic expansions to clarify and confirm the numerical results.

5.2.1 Absence of flow: $\delta = 0$

We will first determine the homogeneous and stationary states of the system (5.4)-(5.6) in the situation when there is no flow acting on the system, i.e. $\delta = 0$. Under this restriction the third equation of the system, (5.6), is trivially satisfied and θ is undetermined. The remaining equations (5.4) and (5.5) that determine the stationary state are

$$\begin{aligned}
&\tau S_1 - 3(S_1^2 - 3S_2^2) + 2S_1(S_1^2 + 3S_2^2) = 0 \ , \\
&\tau S_2 + 6S_1S_2 + 2S_2(S_1^2 + 3S_2^2) = 0 \ ,
\end{aligned}$$

whose solutions, the bulk equilibrium states, equations (2.11) and (2.12), have been discussed in chapter 2 and are displayed in figure 2.4. For the sake of clarity we re-call that the solutions are

- an isotropic solution with $S_1 = S_2 = 0$ for every τ,
- a uniaxial nematic branch with $S_2 = 0$, $S_1 = \frac{3}{4} \pm \frac{1}{4}\sqrt{9 - 8\tau}$. with **n** as the distinguished direction,
- a uniaxial nematic branches with $S_2 = -S_1$, $S_1 = -\frac{3}{8} \pm \frac{1}{8}\sqrt{9 - 8\tau}$. with **m** as the distinguished direction,
- a uniaxial nematic branches with $S_2 = S_1$, $S_1 = -\frac{3}{8} \pm \frac{1}{8}\sqrt{9 - 8\tau}$. with **l** as the distinguished direction.

5.2.2 Small strain rate, $0 < \delta \ll 1$

We now consider the presence of flow in the system. For definiteness we set the material parameters to the constant values $\beta_1 = 0.9$ and $\widetilde{B} = -1.2$, which are typical values for MBBA [41]. The steady state solutions of the system (5.4)-(5.6) were found by using the bifurcation and continuation software package AUTO97 [58]. For $\delta = 4.0 \times 10^{-3}$ four different solution branches were found. However they correspond to only two physically distinct states. The four branches form two pairs, each pair being different representations of the same physical state, the distribution function in each of the two equivalent branches is the same, but with either $\mathbf{n}$ or $\mathbf{m}$ as the distinguished direction in the shear plane. In figure 5.2 each plot shows the solution for the case without flow and the two solution branches which are physically equivalent. Figure 5.2a shows the evolution of the state of the liquid crystal from a high temperature paranematic state (P) ($S_1 \approx 0$, $S_2 \approx 0$) to a nematic state (N) which aligns to the flow direction as the temperature decreases. At lower temperatures the liquid crystal adopts a disk-like distribution function (D) in the shear plane. Solution branches in figure 5.2b connect a low temperature paranematic state (P) to a disk like distribution fuction (D) in the xz-plane to a low temperature elongated nematic distribution in the z-direction, the so-called log-rolling state (LR). These two different states will be the subject of a more detailed study in sections 5.3 and 5.4. As the two solution branches in each plot represent the same physical state we will focus our attention on the solution branch which has S_1 positive in its paranematic state. The corresponding branches in figures 5.2a and 5.2b will be termed IPN (In-Plane Nematic) branch and LRN (Log-Rolling Nematic) branch respectively.

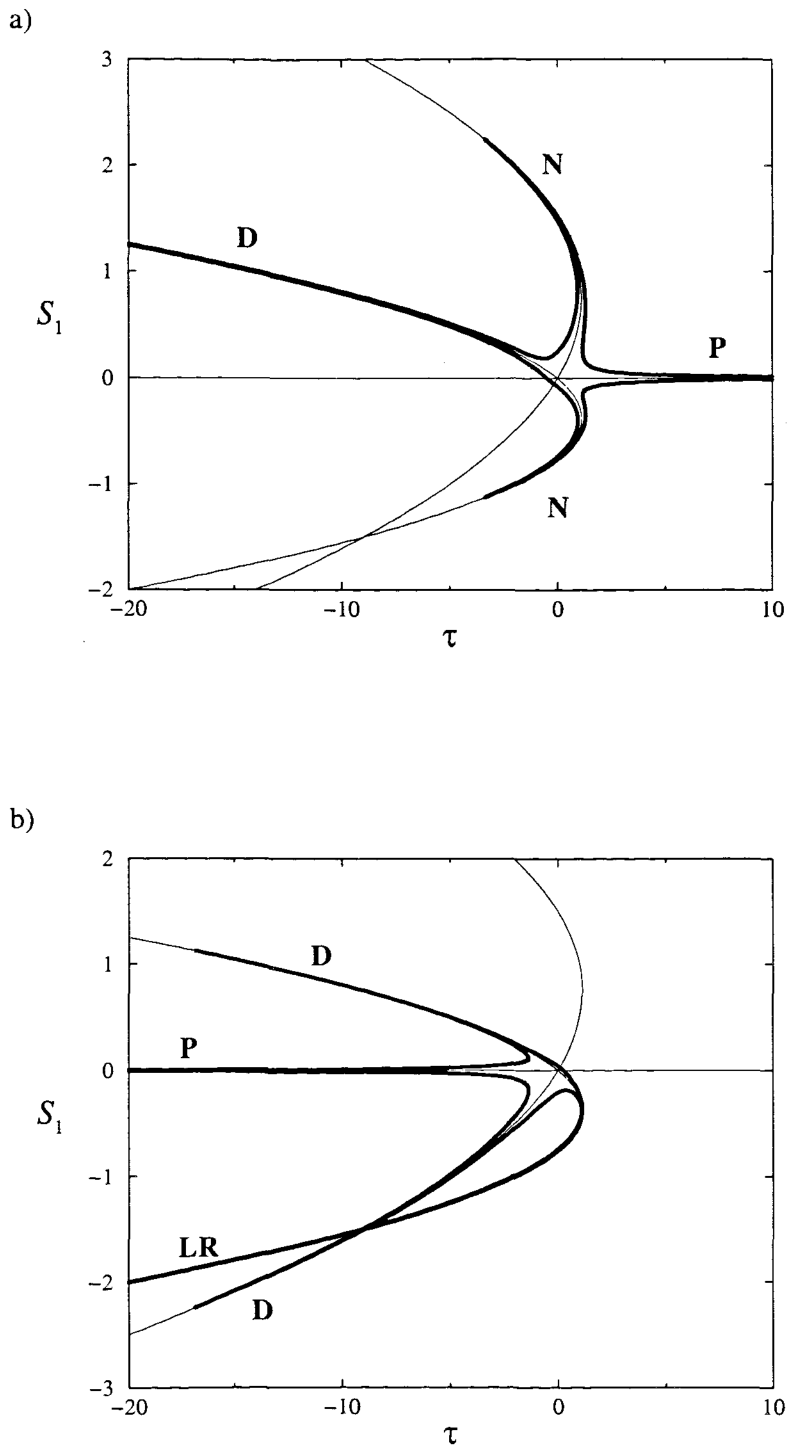

Figure 5.2: Bold solid lines in both diagrams are solutions of the steady form of the system (5.4)-(5.6) for a fixed value of the dimensionless strain rate parameter, $\delta = 4.0 \times 10^{-3}$, and fixed values of the material parameters, $\beta_1 = 0.9$ and $\widetilde{B} = -1.2$. Thin solid lines correspond to the solutions without flow. Figure a) displays the pair of two physically equivalent solution branches which connect a high temperature paranematic state (P) to a low temperature disk-like distribution (D). Figure b) shows the two physically equivalent solution branches which connect a low temperature paranematic state (P) to a log-rolling state (LR).

5.3 The In-Plane Nematic Branch

In this section we analyse the behaviour of IPN Branch as the strain rate is varied. We identify the existence of a Takens-Bogdanov point in the underlying bifurcation structure of the system which organises the different steady states and time dependent solutions. The time dependent solutions fall into two classes; tumbling and wagging.

5.3.1 Small strain rate

In figure 5.3 we display the IPN Branch for a small value of the dimensionless strain rate, $\delta = 4.512960 \times 10^{-3}$. A regular perturbation analysis in δ about the isotropic branch $S_1 = S_2 = 0$, for a fixed positive value of τ, say τ^*, gives the following expression for the paranematic state

$$\begin{aligned} S_1 &\approx -\frac{3^5\beta_1}{4\widetilde{B}^3\tau^*}\delta + \mathrm{O}(\delta^2)\,, \\ S_2 &\approx \frac{3^4\beta_1}{4\widetilde{B}^3\tau^*}\delta + \mathrm{O}(\delta^2)\,, \\ \theta &\approx \frac{\pi}{4} - \frac{3^3}{2\widetilde{B}^2\tau^*}\delta + \mathrm{O}(\delta^2)\,, \end{aligned}$$

as $\delta \to 0$. Thus the director is aligned at approximately $\pi/4$ for a very small shear rate, which is the characteristic behaviour for isotropic solutions. The above expansions are singular as τ goes to zero, i.e. as the supercooling limit, $\tau = S_1 = S_2 = 0$, is approached. A consistent expansion about this point is performed in Appendix A. In figure 5.3 the linearly stable states are plotted with a solid line, unstable states use dashed lines. The linear stability of the solutions has been calculated using AUTO97 with respect to in-plane perturbances.

At high temperatures a stable paranematic state exists with the director aligned at approximately $\pi/4$ to the x-axis (denoted by P in figure 5.3). As the temperature decreases the uniaxial order parameter S_1 increases and the system evolves into a weak uniaxial state with the director angle decreasing. At a sufficiently low temperature this branch loses stability at the limit point LP1. The portion of IPN Branch between the temperatures τ_1 and τ_2 associated with LP1 and LP2 represents an unstable uniaxial state for which the order parameter increases with increasing temperature. A fully developed stable nematic state exists at temperatures between LP2 and LP3 with S_1 increasing and θ decreasing with decreasing temperature (denoted by N in figure 5.3). This state loses stability at LP3. At this point θ has a small negative value, the

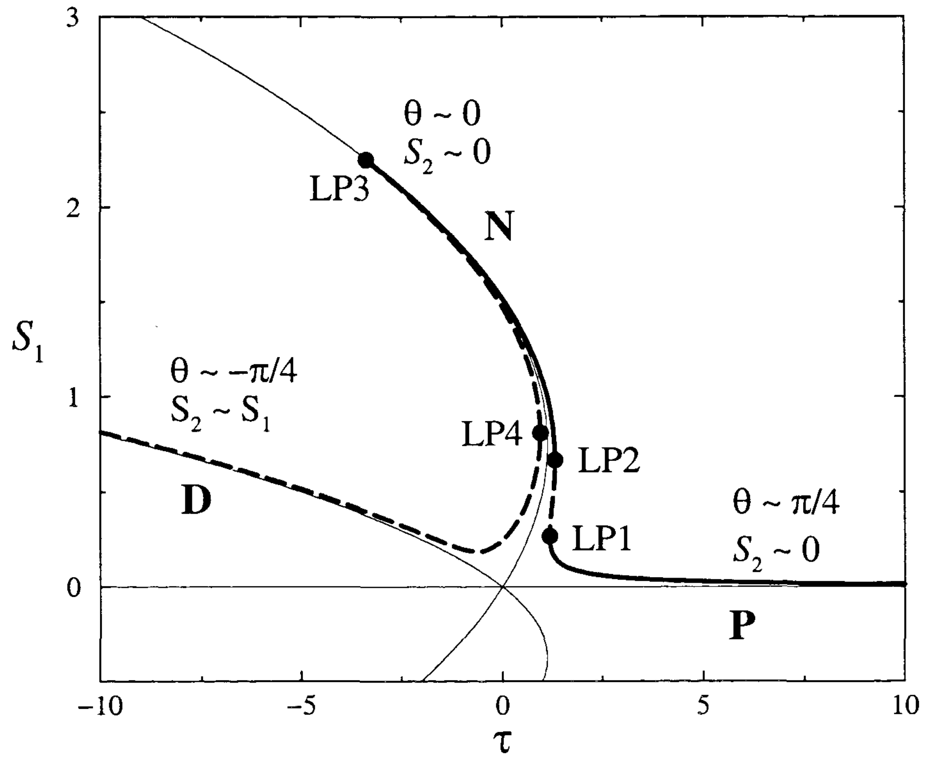

Figure 5.3: The bold line is the solution of the stationary form of the system (5.4)-(5.6) plotted in the $(\tau,\ S_1)$-plane for a fixed value of the dimensionless strain rate $\delta = 4.512960 \times 10^{-3}$ and fixed values of the material parameters $\beta = 0.9$ and $\widetilde{B} = -1.2$. Solid lines are linearly stable states while dashed lines are linearly unstable states. This solution branch links a stable paranematic state (P) with a stable quasi uniaxial nematic state which aligns in flow (N) to an unstable in-plane disk-like distribution (D). The labelled solid dots are limit points. LP1 has $(\tau, S_1) = (1.178625, 0.267008)$, LP2 occurs at $(\tau, S_1) = (1.314420, 0.667175)$, LP3 has $(\tau, S_1) = (-3.375223, 2.249976)$ and LP4 has $(\tau, S_1) = (0.952480, 0.8090584)$.

director being fully aligned ($\theta = 0$) at a slightly higher temperature. In fact it is simple to show that the point where $\theta = S_2 = 0$ is given by $\tau = \tau^* = -9\beta_1(1 + 2\beta_1/\widetilde{B})/\widetilde{B}$, $S_1 = S_1^* = -3\beta_1/\widetilde{B}$ which is independent of δ and therefore represents a fixed point for IPN Branch.

We now conduct a regular perturbation expansion in δ in the vicinity of this fixed point. We put

$$S_1 = S_1^* + S_1^{(2)}\delta^2 + \mathrm{O}(\delta^3)\ , \quad S_2 = S_2^{(2)}\delta^2 + \mathrm{O}(\delta^3)\, ,$$
$$\tau = \tau^* + \tau^{(2)}\delta^2 + \mathrm{O}(\delta^3)\ , \quad \theta = \theta^{(1)}\delta + \mathrm{O}(\delta^2)\, ,$$

and expand the steady state form of equations (5.4)-(5.6), we find at $\mathrm{O}(\delta^2)$ that

$$\begin{aligned}
&\theta^{(1)} = -\frac{2}{3}\widetilde{B}^2 S_2^{(2)}\ ,\\
&S_2^{(2)} = \frac{-3 - \sqrt{9 + 96\beta_1\widetilde{B}^3 S_1^{(2)}}}{16\beta_1\widetilde{B}^3}\ ,\\
&\widetilde{B}\tau^{(2)} - 3S_1^{(2)}(4\beta_1 + \widetilde{B}) + 27\widetilde{B}S_2^{(2)} = 0\ .
\end{aligned}$$

The nearby limit point LP3 satisfies $\partial S_1/\partial\tau = \infty$, which from the above equations gives that LP3 is given by

$$S_1^{(2)} = 3\frac{10\widetilde{B}^2 - 2\beta_1^2 - \beta_1\widetilde{B}}{4\widetilde{B}^3\beta_1(4\beta_1 + \widetilde{B})^2}, \tag{5.7}$$

$$S_2^{(2)} = -\frac{3}{16\beta_1\widetilde{B}^3}\left(1 + 9\left|\frac{\widetilde{B}}{4\beta_1 + \widetilde{B}}\right|\right), \tag{5.8}$$

$$\theta^{(1)} = \frac{1}{8\beta_1\widetilde{B}}\left(1 + 9\left|\frac{\widetilde{B}}{4\beta_1 + \widetilde{B}}\right|\right). \tag{5.9}$$

This analysis and the numerical results from AUTO97 in both (δ, S_1)-plane and (τ, S_1)-space are shown in figures 5.4a and 5.4b respectively. The agreement of the numerical and analytical results is excellent in the vicinity of the fixed point of the system.

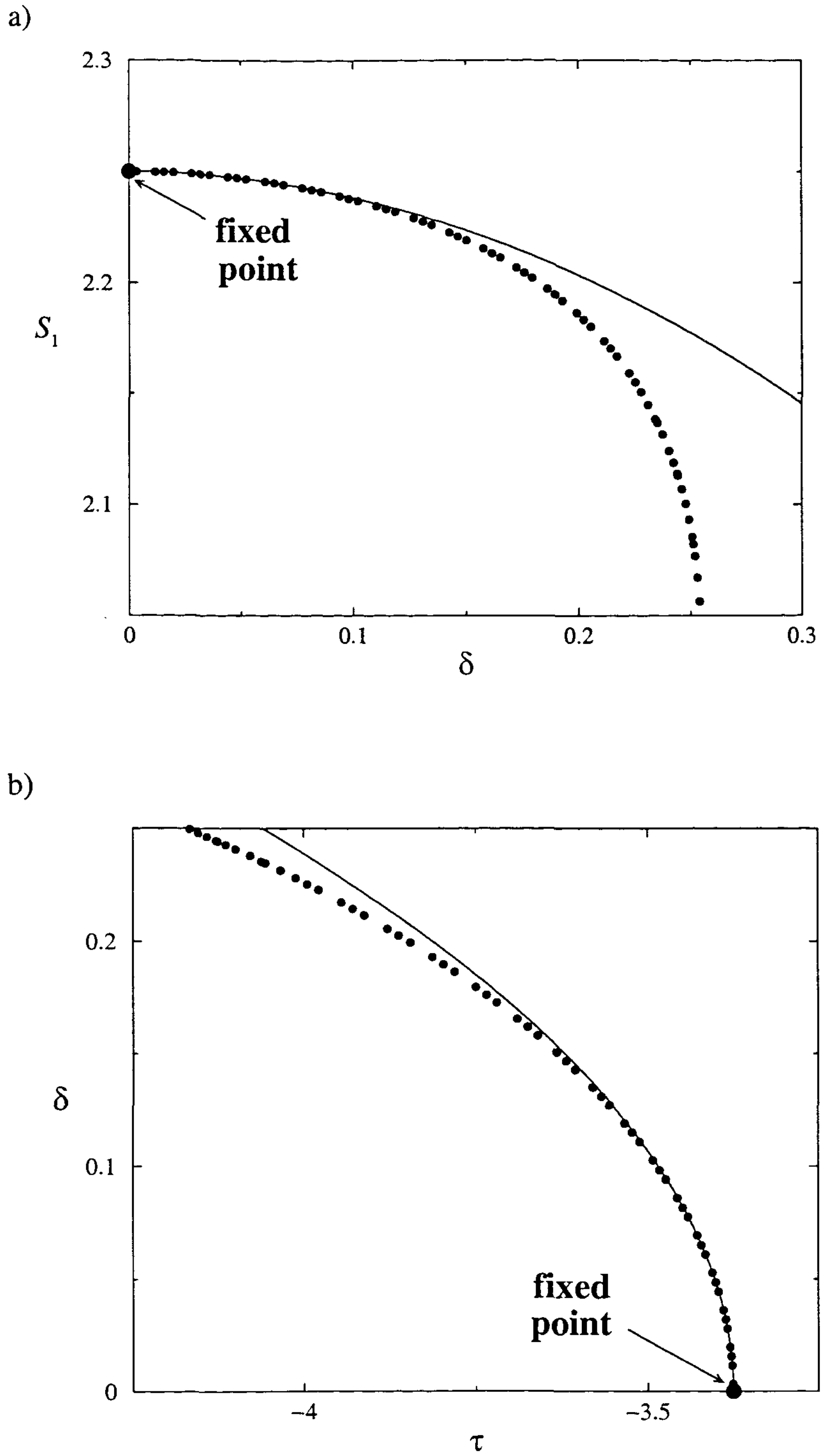

Figure 5.4: Comparison of analytical expressions obtained from system (5.7)-(5.9) and numerical results for the limit point LP3 near the fixed point of the system $\theta = S_2 = 0$, $S_1^* = -3\beta_1/\widetilde{B}$, $\tau^* = -9\beta_1(1 + 2\beta_1/\widetilde{B})\widetilde{B}$. The solid lines are the asymptotic results while the solid dots are the numerical results calculated using AUTO97. Figure a) shows the comparison on the (δ, S_1)-space and figure b) on the (τ, δ)-space. The values of the material parameters are $\beta_1 = 0.9$, $\widetilde{B} = -1.2$.

5.3.1.1 Regular perturbation of the nematic state. Tumbling regime

In the previous section we found that the existence of LP3 results in no steady state near the upper nematic branch when δ is small and $\tau < \tau_3$. To investigate this state of affairs more closely, and also to provide a more general analysis of the system in the presence of a small strain we conduct a perturbation analysis in small δ about the uniaxial nematic branch ($S_2 = 0$) when $\delta = 0$ which allows for time dependent behaviour.

Let the uniaxial nematic branch in the absence of flow be denoted by $S_1^{(n)} = (3 + \sqrt{9 - 8\tau})/4$, $S_2^{(n)} = 0$ with $\tau < 9/8$. We introduce two time scales; the order one time scale $T_0 = t$ and a long time scale $T_1 = \delta t$. We make the regular expansion

$$\begin{aligned} S_1 &= S_1^{(n)} + \delta S_1^{(1)}(T_0\,, T_1)\,, &(5.10)\\ S_2 &= \delta S_2^{(1)}(T_0\,, T_1)\,, &(5.11)\\ \theta &= \theta^{(0)}(T_0\,, T_1) + \delta\theta^{(1)}(T_0\,, T_1)\,. &(5.12)\end{aligned}$$

At leading order the time dependent governing equations give that $\partial\theta^{(0)}/\partial T_0 = 0$ and so $\theta^{(0)}(T_0\,, T_1) = \theta^{(0)}(T_1)$. At first order in δ we obtain the dynamical system

$$\begin{aligned} \frac{\partial S_1^{(1)}}{\partial T_0} &= \frac{-9\beta_1}{4\widetilde{B}}\sin 2\theta^{(0)} - k_1 S_1^{(1)}\,, &(5.13)\\ \frac{\partial S_2^{(1)}}{\partial T_0} &= \frac{3\beta_1}{4\widetilde{B}}\sin 2\theta^{(0)} - k_2 S_2^{(1)}\,, &(5.14)\\ \frac{\partial\theta^{(1)}}{\partial T_0} &= \frac{-1}{2}\left(\frac{3\beta_1\cos 2\theta^{(0)}}{\widetilde{B}S_1^{(n)}} + 1\right) - \frac{\partial\theta^{(0)}}{\partial T_1}, &(5.15)\end{aligned}$$

where $k_1 = \widetilde{B}^2\Big(\tau - 6S_1^{(n)} + 6(S_1^{(n)})^2\Big)/27$ and $k_2 = \widetilde{B}^2\Big(\tau + 6S_1^{(n)} + 2(S_1^{(n)})^2\Big)/27$, are positive constants. Integrating equations (5.13), (5.14) and (5.15) we get

$$\begin{aligned} S_1^{(1)} &= A(T_1)e^{-k_1T_0} - \frac{9\beta_1}{4\widetilde{B}k_1}\sin 2\theta^{(0)}\,, &(5.16)\\ S_2^{(1)} &= B(T_1)e^{-k_2T_0} + \frac{3\beta_1}{4\widetilde{B}k_2}\sin 2\theta^{(0)} &(5.17)\\ \theta^{(1)} &= -T_0\left[\frac{1}{2}\left(\frac{3\beta_1\cos 2\theta^{(0)}}{\widetilde{B}S_1^{(n)}} + 1\right) + \frac{\partial\theta^{(0)}}{\partial T_1}\right] + C(T_1), &(5.18)\end{aligned}$$

where $A(T_1)$, $B(T_1)$ and $C(T_1)$ are functions of T_1 alone. We require that θ_1 is bounded for our procedure to be valid and hence we obtain the solvability condition

$$\frac{\partial\theta^{(0)}}{\partial T_1} + \frac{1}{2}\left(\frac{3\beta_1\cos 2\theta^{(0)}}{\widetilde{B}S_1^{(n)}} + 1\right) = 0, \qquad (5.19)$$

which governs the leading order evolution of θ.

We now discuss the solutions of equation (5.19) and without loss of generality we assume that $\beta_1/\widetilde{B}$ is negative (which is the case for the numerical results given above). When $S_1^{(n)} < -3\beta_1/\widetilde{B}$ equation (5.19) has two distinct equilibrium solutions in the interval $(-\pi/2,\ \pi/2)$, $\theta = \pm\theta_0$, where $\theta_0 = [\arccos(-S_1^{(n)}\widetilde{B}/3\beta_1)]/2$. The positive solution being stable and the negative solution unstable. If $S_1^{(n)} > -3\beta_1/\widetilde{B}$, then $\partial\theta^{(0)}/\partial T_1$ is always negative and so $\theta^{(0)}$ continuously decreases with T_1. This we term the tumbling state as it corresponds to continual rotation of the director. The period of rotation from $-\pi/2$ to $\pi/2$ is

$$T = \frac{-2\pi\widetilde{B}S_1^{(n)}}{\delta\sqrt{\widetilde{B}^2\left(S_1^{(n)}\right)^2 - 9\beta_1^2}}\,. \tag{5.20}$$

We observe that the period of rotation becomes infinite as $S_1^{(n)} \to -3\beta_1/\widetilde{B}$.

Equation (5.19) can be solved directly in this case to give

$$\theta^{(0)}(T_1) = \arctan\left\{\frac{\sqrt{\widetilde{B}^2 S_1^{n^2} - 9\beta_1^2}}{3\beta_1 - \widetilde{B}S_1^n}\tan\left[\frac{\sqrt{\widetilde{B}^2 S_1^{n^2} - 9\beta_1^2}}{\widetilde{B}S_1^n}\left(\frac{T_1}{2} + K\right)\right]\right\}, \tag{5.21}$$

where K is a constant of integration.

A comparison of the analytical expressions (5.16), (5.17) and (5.21) for S_1, S_2 and θ respectively with a direct numerical integration of the time dependent governing equations (5.4)-(5.6) is given in figures 5.5-5.7. The numerical integration employed the initial conditions $S_1(0) = S_1^{(n)}$, $S_2(0) = 0$, $\theta(0) = -\pi/4$, $\tau = -5$ and $\delta = 10^{-3}$, with $S_1^{(n)} = 2.5$. The coefficients $A(T_1)$ and $B(T_1)$ of the transient part of the solutions for $S_1^{(1)}$ and $S_2^{(1)}$, respectively were approximated by $A(T_1) = A(0)$ and $B(T_1) = B(0)$. The numerical values of $A(0)$, $B(0)$ and K were determined by setting $S_1^{(1)}(0,0) = 0$, $S_2^{(1)}(0,0) = 0$ and $\theta^{(0)}(0,0) = -\pi/4$.

Figure 5.5 compares numerical and analytical results of the tumbling state for θ over a time interval $2T$, figure 5.6a shows the analytical and numerical results of the periodic solution for S_1 on the long time scale, figure 5.6b shows the initial transient behaviour of the solutions over a much shorter time interval. Figure 5.7 shows similar comparisons for S_2. We see that there is excellent agreement between the numerical and analytical results.

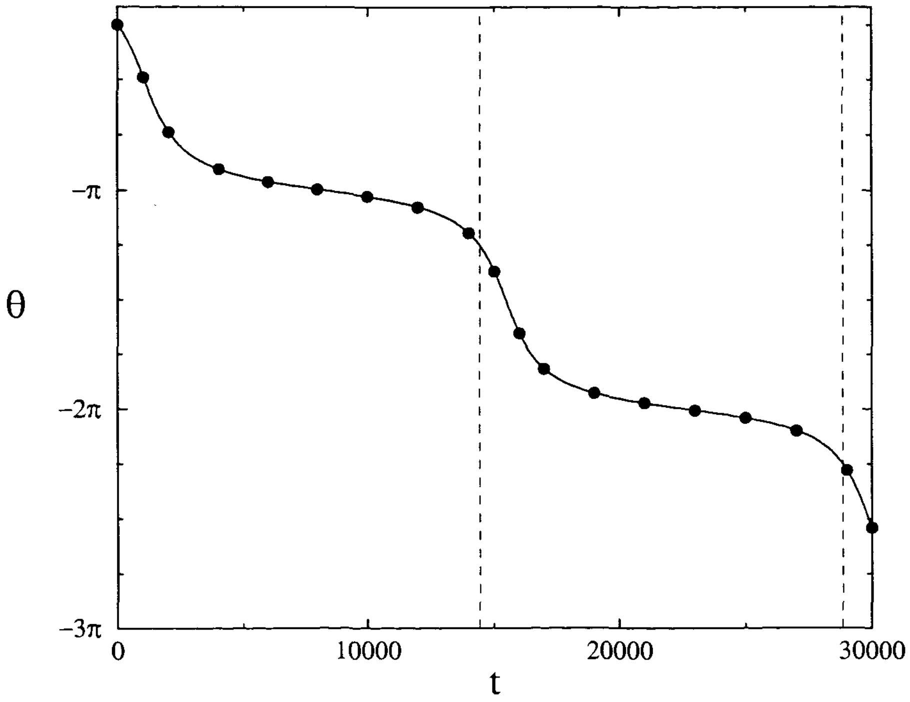

Figure 5.5: The solid line displays the analytical form for θ given by (5.21) when tumbling occurs, while the dots represent the numerical results. The dashed vertical lines mark the analytical expression for the tumbling time period T, given by (5.20). The parameters are $\beta_1 = 0.9$, $\widetilde{B} = -1.2$, $\delta = 10^{-3}$ and $\tau = -5$.

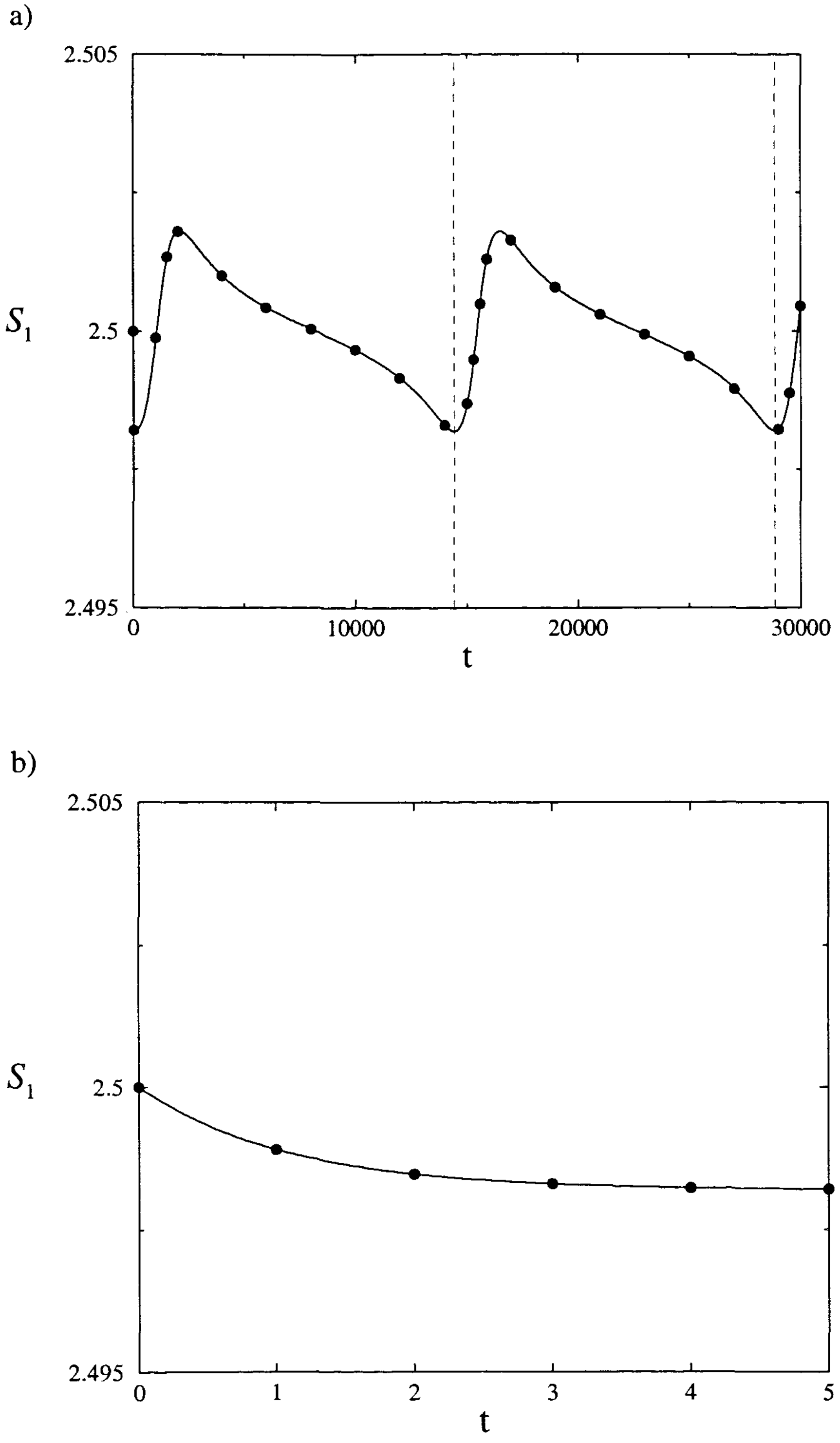

Figure 5.6: In both plots the solid line represents the analytical expression for S_1 given by (5.10) and (5.16) in the tumbling state and the dots represent the results of numerical time integration of the initial value problem. Figure a) corresponds to the long time scale with vertical dashed lines indicating the analytical expression for the time period, T, given by (5.20). Figure b) shows the same results on a shorter time scale where the transient part of the solution is significant.

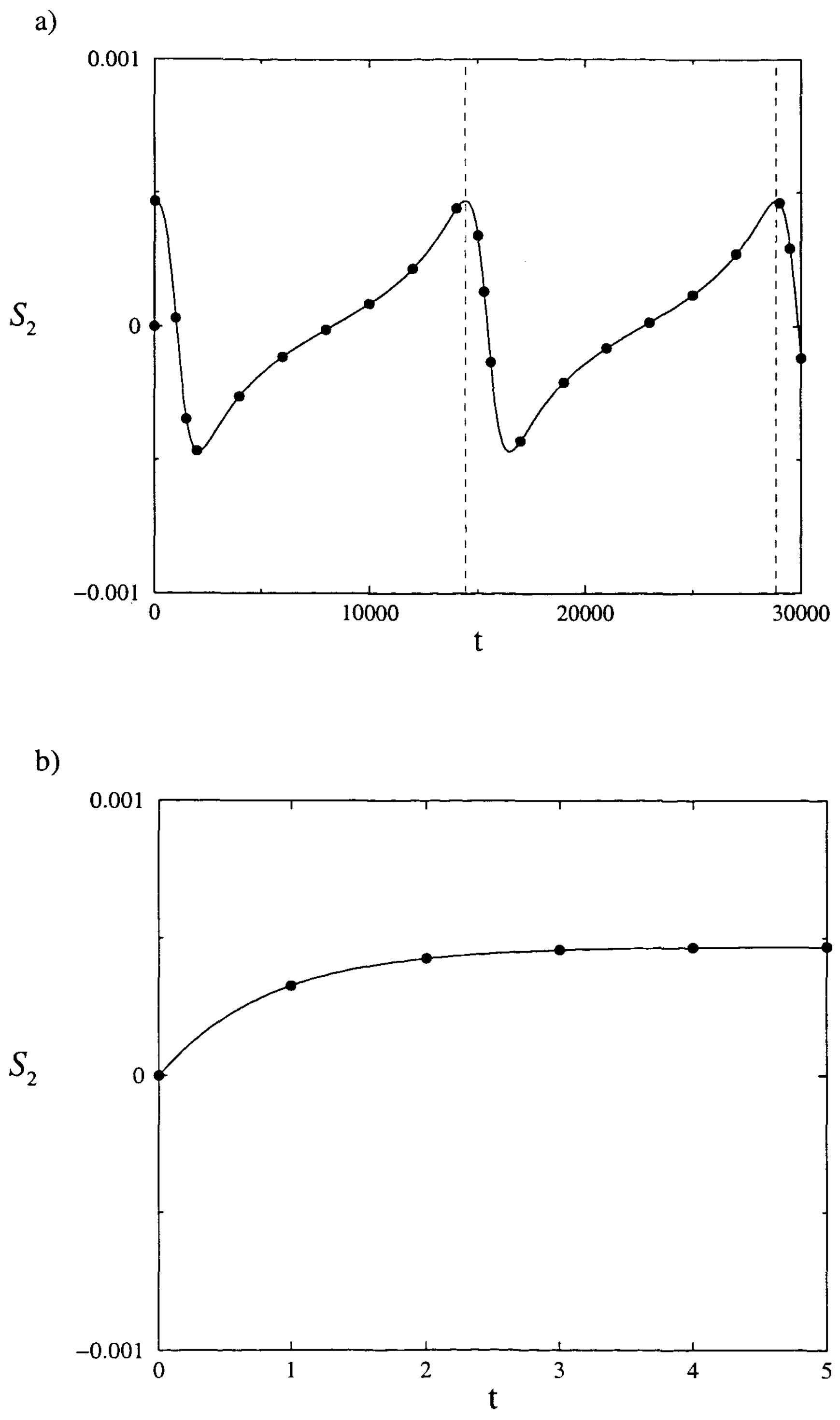

Figure 5.7: In both plots the solid line represents the analytical expression for S_2 given by (5.11) and (5.17) in the tumbling state and the dots represent the results of numerical time integration of the initial value problem. Figure a) corresponds to the long time scale with vertical dashed lines indicating the analytical expression for the time period, T, given by (5.20). Figure b) shows the same results on a shorter time scale where the transient part of the solution is significant.

5.3.1.2 Correspondence of the prediction of tumbling between the Leslie-Ericksen and Landau-de Gennes theories

In order to establish a correspondence between the prediction of tumbling in the Leslie-Ericksen and Olmsted-Goldbart theories we need to re-write the equation for the evolution of the director vector in the Leslie-Ericksen theory, equation (3.52), for the planar homogeneous case: the director is given by $\mathbf{n} = (\cos\theta, \, ,\sin\theta, \, 0)$, and the molecular field, $\mathbf{h}$, is zero since the distortion free energy of a homogeneous system is zero. Then, considering a velocity field $\mathbf{v} = \delta y \mathbf{i}$, the two independent components of equation (3.52) are

$$\begin{aligned} \dot{\theta}\sin\theta &= -\frac{\delta}{2}(1+\lambda)\sin\theta\,, & (5.22) \\ \dot{\theta}\cos\theta &= -\frac{\delta}{2}(1-\lambda)\cos\theta\,. & (5.23) \end{aligned}$$

Multiplying equation (5.22) by $\sin\theta$, equation (5.23) by $\cos\theta$ and adding the resulting equations, we obtain an expression for the evolution of the director angle

$$\dot{\theta} = -\frac{\delta}{2}\left(1 - \lambda\cos 2\theta\right)\,, \tag{5.24}$$

where we re-call that the parameter λ is a ratio of viscosities, and its correspondence with the Olmsted-Goldbart theory is $\lambda = 3\beta_1/\widetilde{B}S_1$, equation (3.69).

When $|\lambda| \geq 1$ the steady states of equation (5.24) are $\theta = \pm\theta_0$, where $\theta_0 = [\arccos(1/\lambda)]/2$. This corresponds to the case $|S_1| \leq -3\beta_1/\widetilde{B}$ in the Olmsted and Goldbart theory and we have shown in the previous section, that the equilibrium solution is approximated by $\theta_0 = [\arccos(-S_1\widetilde{B}/3\beta_1)]/2$ and substituting λ into this equation, it corresponds to the solution found by the Leslie-Ericksen model. Therefore both theories predict the same steady state alignment for correspondent values of the material parameters.

Equation (5.24) predicts tumbling when $|\lambda| < 1$ and given equation (3.69) for the relationship between OG and LE coefficients, this leads to predict tumbling when $|S_1| > -3\beta_1/\widetilde{B}$, as shown in section 5.3.1.1. Therefore there is a direct correspondence between the predictions of tumbling in the LE and OG theories.

The tumbling behaviour has been extensively studied theoretically for liquid-crystalline polymers (LCP) and low molecular weight nematics (LMW) by using Doi's and LE theories respectively. Tumbling for LCP at low shear rates has been predicted by Marrucci and Maffettone [28] in the two dimensional case and extended to the third dimension by Larson [29], Larson and Öttinger [30] and Faraoni et al. [32]. Farhoudi and Rey [45] predicted also tumbling at low shear rates using a tensorial theory similar to ours but for lyotropic polymers. Predictions of tumbling nematics using LE theory have been done by several authors [22, 15, 11, 12, 18] and experiments done by Srinivasarao and Berry [25] and Burghardt and Fuller [23, 24] with LCP and by Cladis and Torza [14] with LMW nematics corroborate the LE predictions for the tumbling regime, while Maryurama et al. [36] found excellent agreemen between their experimental evidence of tumbling and the predictions obtained by using Doi's theory.

5.3.2 Increasing the strain rate. Wagging solutions

For a small strain rate we have found that the steady solution given by IPN Branch links a paranematic stable state at high temperatures with an in-plane stable nematic state and an unstable in-plane disk-like distribution at low temperatures. In the previous section we showed that for values of the uniaxial order parameter larger than $S_1 = -3\beta_1/\widetilde{B}$ there exists a stable tumbling state.

We now investigate IPN Branch as δ is increased. This is done numerically and the results are shown in figure 5.8. For a small value of the strain rate, given by curve (a), the solution branch has four limit points LP1, LP2, LP3, and LP4. For large values of δ, LP1 and LP2 merge leaving LP3 and LP4 as shown by curve (b) and the paranematic and nematic states are linked as a continuously stable branch. For a larger value of the strain rate LP3 and LP4 merge and a Hopf bifurcation point (HB) exists as shown by curve (c). The Hopf bifurcation corresponds to a pure imaginary pair of eigenvalues of the linearised problem. The time periodic solutions emanating from HB will be called wagging solutions as in particular θ is periodic and the director therefore wags backwards and forwards. In figure 5.9 we display the dependence of θ on time in the wagging regime. Experimental evidence of director wagging at intermediate shear rates has been found for lyotropic liquid crystals and the results agree with the predictions of Doi's theory [36]

We have used AUTO97 to compute the locus of the limit points on IPN Branch as τ and δ are varied. The results are shown in figure 5.10. We observe that two limit points coincide at critical values of the strain rate $\delta^{c1} = 7.964190 \times 10^{-3}$ and $\delta^{c2} = 2.545934 \times 10^{-1}$ associated to dimensionless temperatures $\tau^{c1} = 1.484079$ and $\tau^{c2} = -4.211501$. In figure 5.11 we show the locus of the HB on IPN Branch as the parameters vary, together with the previously described locus of the limit points. We observe that the HB points terminate at a limit point in a manner that is characteristic of the presence of a so-called Takens-Bogdanov point [57]. The critical strain rate and temperature associated to this point is given by $(\delta^{\mathrm{TB}}, \tau^{\mathrm{TB}}) = (1.921104 \times 10^{-1}, -3.358297)$. In the next section we rigorously show that this is indeed a Takens-Bogdanov point (TB).

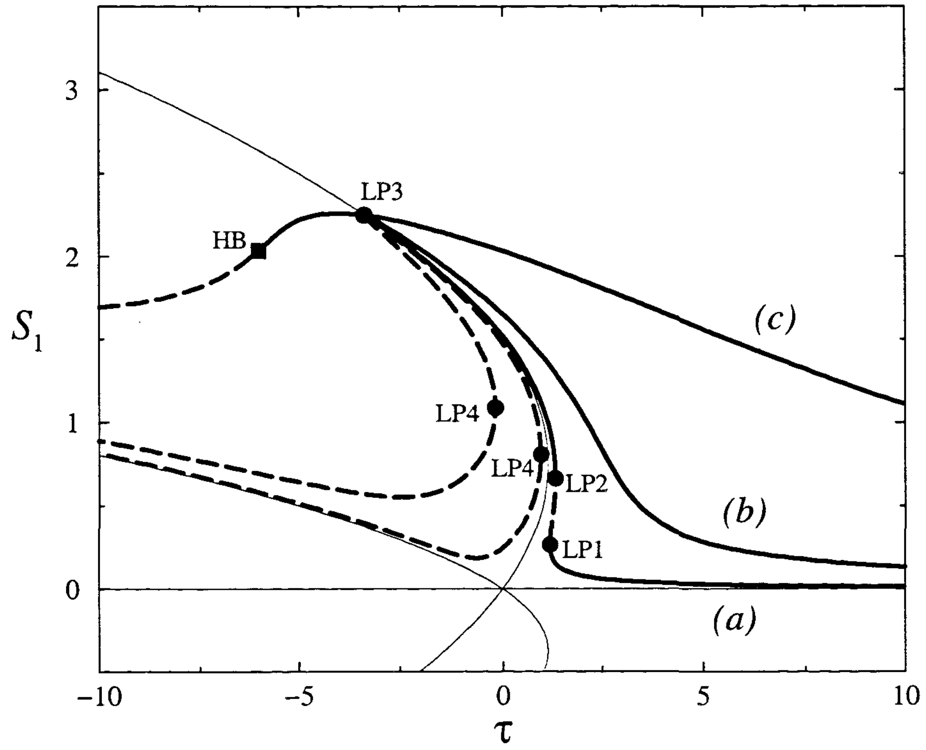

Figure 5.8: Plot of S_1 against the dimensionless temperature for different values of δ calculated using AUTO97. The thin lines correspond to the case without flow, while bold lines are solution branches for different values of the strain rate with the material parameters $\beta = 0.9$, and $\widetilde{B} = -1.2$. Branches (a), (b) and (c) correspond to $\delta = 4.512960 \times 10^{-3}$, $\delta = 4.051649 \times 10^{-2}$ and $\delta = 4.120275 \times 10^{-1}$, respectively. Solid bold curves are linearly stable states are plotted with solid line while dashed bold curves are linearly unstable. The solid dots indicate limit points LP1, LP2, LP3. and LP4. The square symbol in branch (c) represents a Hopf bifurcation point.

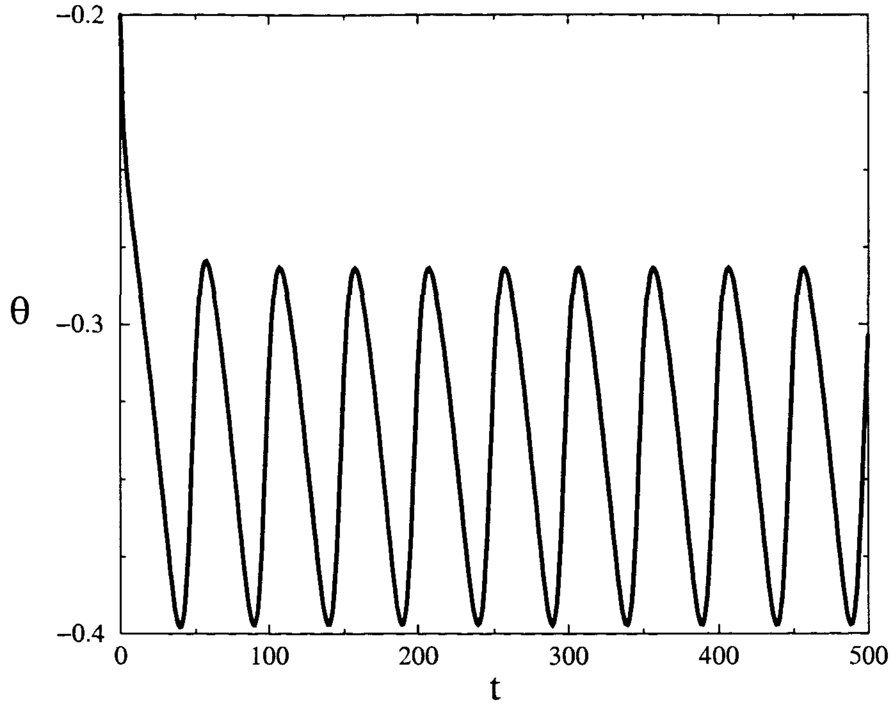

Figure 5.9: θ as a function of time for a wagging solution. This solution was computed directly from the time dependent governing equations for $\tau = -4.5$, $\delta = 0.27$, $\beta_1 = 0.9$, $\widetilde{B} = -1.2$.

We now summarise the behaviour of IPN Branch as δ increases:

- $0 < \delta < \delta^{c1}$. IPN Branch has four limit points LP1, LP2, LP3 and LP4. As τ increases LP1 and LP2 move together as do LP3 and LP4. Curve (*a*) in figure 5.8 shows this case.
- $\delta = \delta^{c1}$. Limit points LP1 and LP2 coincide. The stable nematic and paranematic states become directly connected.
- $\delta^{c1} < \delta < \delta^{TB}$. LP3 and LP4 continue to move closer as δ increases. Curve (*b*) in figure 5.8 shows this case.
- $\delta = \delta^{TB}$. A Takens-Bogdanov point forms; the genesis of the HB branch.
- $\delta^{TB} < \delta < \delta^{c2}$. The HB point on IPN Branch lies between LP3 and LP4 which continue to move closer as δ increases.
- $\delta = \delta^{c2}$. The limit points LP3 and LP4 coincide.
- $\delta > \delta^{c2}$. IPN Branch represents a continuous evolution from a stable high temperature paranematic state to a lower temperature stable nematic state which

becomes unstable to a stable wagging mode at sufficient low temperatures. Curve (*c*) in figure 5.8 shows this case.

In section 5.3.1.1 we have shown the existence of a tumbling state for small values of δ. In the next section we investigate the relationship between the wagging and tumbling regimes by conducting a local analysis near the Takens-Bogdanov point.

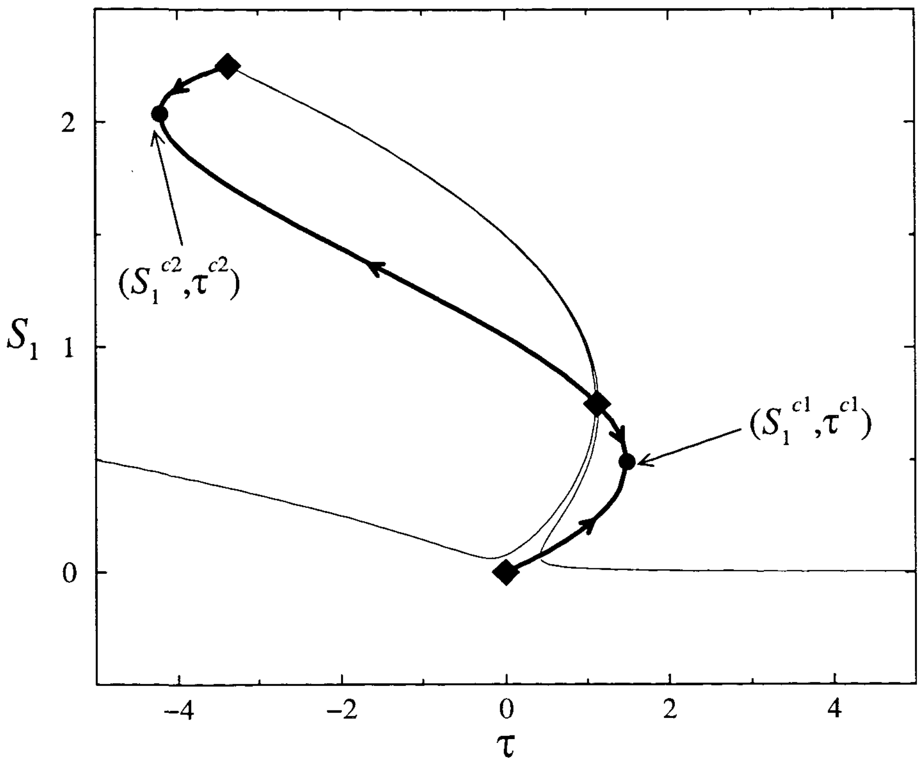

Figure 5.10: The bold line indicates the locus of the four limit points on IPN Branch, computed by AUTO97 for material parameters $\beta = 0.9$, $\widetilde{B} = -1.2$. The solid dots correspond to the coincidence of a pair of limit points at which S_1, τ and δ have values $(S_1^{c1}, \tau^{c1}, \delta^{c1}) = (0.4924527, 1.484079, 7.964190\times10^{-3})$ and $(S_1^{c2}, \tau^{c2}, \delta^{c2}) = (2.036373, -4.211501, 0.2545934)$. The diamond symbols correspond to $\delta = 0$ and the arrows indicate the direction of δ increasing. The thin line is IPN Branch for $\delta = 4.812671 \times 10^{-4}$.

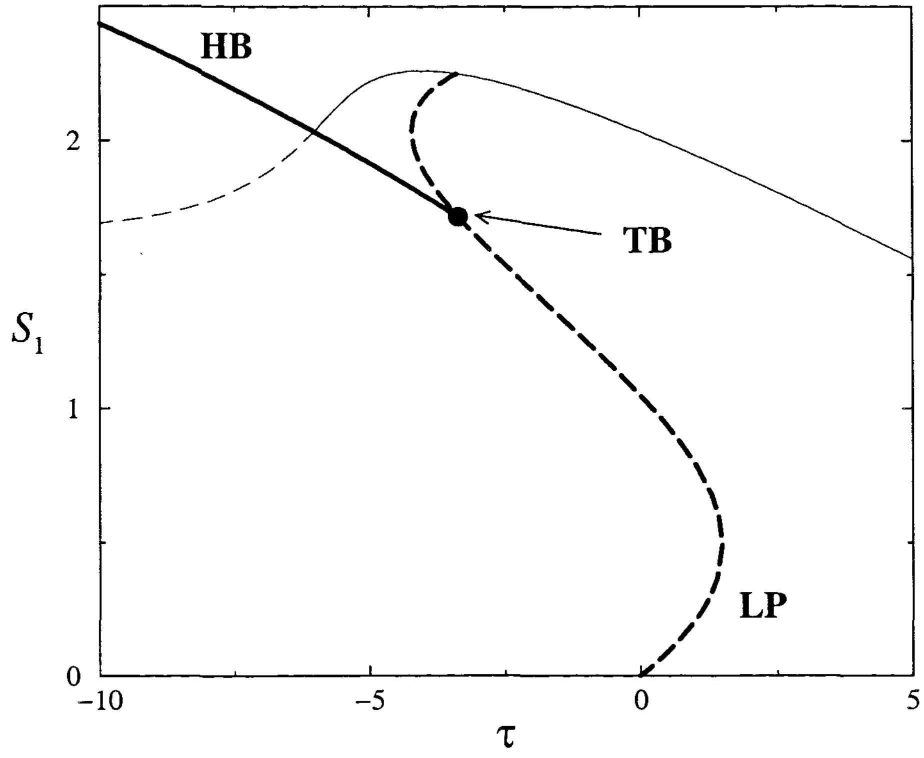

Figure 5.11: The bold dashed line is the locus of the limit points LP1, LP2, LP3 and LP4. The bold solid line is the locus of the Hopf Bifurcation point. The Takens-Bogdanov bifurcation point is labelled as TB. The thin solid line is IPN Branch with $\delta = 4.120275 \times 10^{-1}$. The solid part of this curve represents linearly stable state and the dashed portion is linearly unstable.

5.3.2.1 Local analysis about the Takens-Bogdanov bifurcation

In this section we conduct a local analysis about the putative Takens-Bogdanov point using centre of manifold reduction, Wiggins [55], and normal forms, Kuznetsov [56]. We will show that the local form of the system is indeed that of a Takens-Bogdanov point as we conjectured earlier. We will use this normal form to obtain an analytical expression for the locus of the HB points near the Takens-Bogdanov point.
To proceed we write the dynamical system (5.4)-(5.6) in vector notation as

$$\dot{\mathbf{x}} = \mathbf{G}(\mathbf{x}, \boldsymbol{\alpha}), \tag{5.25}$$

where $\mathbf{x} = (S_1, S_2, \theta)^T$, $\boldsymbol{\alpha} = (\tau, \delta)$ and $\mathbf{G} = (G_1, G_2, G_3)^T$, with

$$\begin{aligned} G_1(\mathbf{x}, \boldsymbol{\alpha}) &= \frac{-9\beta_1\delta}{4\widetilde{B}}\sin 2\theta - \frac{\widetilde{B}^2}{27}\left(\tau S_1 - 3\left(S_1^2 - 3S_2^2\right) + 2S_1\left(S_1^2 + 3S_2^2\right)\right), \\ G_2(\mathbf{x}, \boldsymbol{\alpha}) &= \frac{3\beta_1\delta}{4\widetilde{B}}\sin 2\theta - \frac{\widetilde{B}^2}{27}\left(\tau S_2 + 6S_1S_2 + 2S_2\left(S_1^2 + 3S_2^2\right)\right), \\ G_3(\mathbf{x}, \boldsymbol{\alpha}) &= \frac{\delta}{2}\left(\frac{3\beta_1\cos 2\theta}{\widetilde{B}\left(S_2 - S_1\right)} - 1\right). \end{aligned}$$

We will define the matrix $\mathbf{A}(\mathbf{x}, \boldsymbol{\alpha})$ as $\nabla\mathbf{G}$. In order to determine the location of the TB point we exploit the fact that it corresponds to a double zero eigenvalue of the linearised system. This requires

$$\mathbf{G}(\mathbf{x}, \boldsymbol{\alpha}) = \mathbf{0}, \tag{5.26}$$

$$\det(\mathbf{A}) = 0, \tag{5.27}$$

$$\operatorname{tr}(\mathbf{A}^2) - [\operatorname{tr}(\mathbf{A})]^2 = 0. \tag{5.28}$$

Equation (5.26) is the condition for the TB to be an equilibrium point of the system and equations (5.27) and (5.28) are the conditions of a double zero eigenvalue of the linearised system. We have solved (5.26)-(5.28) numerically using Newton's method for material parameters $\widetilde{B} = -1.2$ and $\beta_1 = 0.9$ and found that the TB point occurs at

$$\begin{aligned} &(S_1^{\mathrm{TB}},\, S_2^{\mathrm{TB}},\, \theta^{\mathrm{TB}}) = (1.71710090,\, 0.10979754,\, -0.38754572), \\ &(\tau^{\mathrm{TB}},\, \delta^{\mathrm{TB}}) = (-3.35829676,\, 0.19211037). \end{aligned}$$

At the TB point the system is characterised by its Jacobian having a double zero eigenvalue and a negative real eigenvalue. We now employ centre of manifold theory [55] in order to reduce the dimension of the system by one. The governing equations (5.25) may be expressed as

$$\dot{\tilde{\mathbf{x}}} = \mathbf{J}\tilde{\mathbf{x}} + \mathbf{f}(\tilde{\mathbf{x}},\, \tilde{\boldsymbol{\alpha}}), \tag{5.29}$$

where

$$\mathbf{J} = \begin{pmatrix} 0 & 1 & 0 \\ 0 & 0 & 0 \\ 0 & 0 & -\sigma \end{pmatrix}$$

is the Jordan canonical form of the matrix $\mathbf{A}(\mathbf{x}^{\mathrm{TB}}, \boldsymbol{\alpha}^{\mathrm{TB}})$, i.e. there exists a nonsingular matrix $\mathbf{P}$ such that $\mathbf{J} = \mathbf{P}^{-1}\mathbf{A}(\mathbf{x}^{\mathrm{TB}}, \boldsymbol{\alpha}^{\mathrm{TB}})\mathbf{P}$ and $-\sigma$ is the negative real eigenvalue at the TB point. We define $\tilde{\mathbf{x}} = \mathbf{P}^{-1}(\mathbf{x} - \mathbf{x}^{\mathrm{TB}})$ and $\tilde{\boldsymbol{\alpha}} = \boldsymbol{\alpha} - \boldsymbol{\alpha}^{\mathrm{TB}}$ such that $(\tilde{\mathbf{x}}, \tilde{\boldsymbol{\alpha}}) = (\mathbf{0}, \mathbf{0})$ is the TB equilibrium point for system (5.25) and $\mathbf{f}(\mathbf{0}, \mathbf{0}) = \mathbf{0}$.

The matrix $\mathbf{P}$ is not unique but for the TB point considered here by using Maple we get that

$$\mathbf{P} = \begin{pmatrix} 0.92048568 & -1.92735701 & 0.42957483 \\ -0.17684878 & 0.20188146 & 0.90250308 \\ 0.34846897 & 1.17552137 & -0.03088137 \end{pmatrix}$$

and $-\sigma = -0.7270212781$, with $\mathbf{f}(\tilde{\mathbf{x}}, \tilde{\boldsymbol{\alpha}}) = (f_1(\tilde{\mathbf{x}}, \tilde{\boldsymbol{\alpha}}), f_2(\tilde{\mathbf{x}}, \tilde{\boldsymbol{\alpha}}), f_3(\tilde{\mathbf{x}}, \tilde{\boldsymbol{\alpha}}))^T$, where

$$\begin{aligned}
f_1(\tilde{\mathbf{x}}, \tilde{\boldsymbol{\alpha}}) &= -0.05603713\tilde{\tau} - 0.84569753\tilde{\delta} \\
&\quad -0.23200404\tilde{x}_1^2 - 0.31623843\tilde{x}_2^2 - 0.48932781\tilde{x}_3^2 \\
&\quad +0.81465209\tilde{x}_1\tilde{x}_2 + 0.09012070\tilde{x}_1\tilde{x}_3 + 0.08366450\tilde{x}_2\tilde{x}_3 \\
&\quad -0.03333882\tilde{\tau}\tilde{x}_1 + 0.06744928\tilde{\tau}\tilde{x}_2 - 0.00177192\tilde{\tau}\tilde{x}_3 \\
&\quad +0.60167518\tilde{\delta}\tilde{x}_1 + 3.98115195\tilde{\delta}\tilde{x}_2 + 0.07241004\tilde{\delta}\tilde{x}_3 + \mathrm{O}\left(\|(\tilde{\mathbf{x}}, \tilde{\boldsymbol{\alpha}})\|^3\right), \\
f_2(\tilde{\mathbf{x}}, \tilde{\boldsymbol{\alpha}}) &= 0.01605824\tilde{\tau} + 0.25629498\tilde{\delta} \\
&\quad +0.04977576\tilde{x}_1^2 + 0.25777010\tilde{x}_2^2 + 0.13688443\tilde{x}_3^2 \\
&\quad -0.58284702\tilde{x}_1\tilde{x}_2 - 0.04975475\tilde{x}_1\tilde{x}_3 + 0.13202622\tilde{x}_2\tilde{x}_3 \\
&\quad +0.00992748\tilde{\tau}\tilde{x}_1 - 0.01984410\tilde{\tau}\tilde{x}_2 - 0.00087977\tilde{\tau}\tilde{x}_3 \\
&\quad -0.18234218\tilde{\delta}\tilde{x}_1 + 0.35381189\tilde{\delta}\tilde{x}_2 + 0.07858567\tilde{\delta}\tilde{x}_3 + \mathrm{O}\left(\|(\tilde{\mathbf{x}}, \tilde{\boldsymbol{\alpha}})\|^3\right), \\
f_3(\tilde{\mathbf{x}}, \tilde{\boldsymbol{\alpha}}) &= -0.02106123\tilde{\tau} + 0.21310205\tilde{\delta} \\
&\quad +0.03219880\tilde{x}_1^2 - 0.10827009\tilde{x}_2^2 - 0.51901235\tilde{x}_3^2 \\
&\quad -0.19341224\tilde{x}_1\tilde{x}_2 - 0.51455631\tilde{x}_1\tilde{x}_3 + 1.23478206\tilde{x}_2\tilde{x}_3 \\
&\quad +0.00169732\tilde{\tau}\tilde{x}_1 + 0.00572571\tilde{\tau}\tilde{x}_2 - 0.05348375\tilde{\tau}\tilde{x}_3 \\
&\quad -0.15161238\tilde{\delta}\tilde{x}_1 - 0.34578930\tilde{\delta}\tilde{x}_2 + 0.02410906\tilde{\delta}\tilde{x}_3 + \mathrm{O}\left(\|(\tilde{\mathbf{x}}, \tilde{\boldsymbol{\alpha}})\|^3\right),
\end{aligned}$$

where $\tilde{\tau} = \tau - \tau^{\mathrm{TB}}$ and $\tilde{\delta} = \delta - \delta^{\mathrm{TB}}$.

From the theory for the existence of centre of manifold theory as presented by Wiggins [55] and explained in chapter 4 we deduce that local to the TB point the centre of manifold of our system is

$$W_{loc}^{c}(0) = \Big\{(\tilde{x}_1, \tilde{x}_2, \tilde{x}_3, \tilde{\boldsymbol{\alpha}}) \in \mathbb{R} \times \mathbb{R} \times \mathbb{R} \times \mathbb{R}^2 : \ \tilde{x}_3 = h(\tilde{x}_1, \tilde{x}_2, \tilde{\boldsymbol{\alpha}}),$$

$$\|(\tilde{x}_1,\, \tilde{x}_2)\| < \epsilon,\ \|\tilde{\boldsymbol{\alpha}}\| < \bar{\epsilon},\ h(0,\,0,\,\mathbf{0}) = 0,\ Dh(0,\,0,\,\mathbf{0}) = 0\Big\}$$

for $\epsilon \in \mathbb{R}^+$ and $\bar{\epsilon} \in \mathbb{R}^+$ sufficiently small. Thus we have that local to the TB point

$$\tilde{x}_3 = h(\tilde{x}_1,\, \tilde{x}_2,\, \tilde{\boldsymbol{\alpha}}) \tag{5.30}$$

and

$$\dot{\tilde{x}}_3 = -\sigma + f_3\left(\tilde{x}_1, \tilde{x}_2, h(\tilde{x}_1,\, \tilde{x}_2,\, \tilde{\boldsymbol{\alpha}}),\, \tilde{\boldsymbol{\alpha}}\right) . \tag{5.31}$$

Then, differentiating equation (5.30) and substituting into (5.31) we get

$$\frac{\partial h}{\partial \tilde{x}_1}\dot{\tilde{x}}_1 + \frac{\partial h}{\partial \tilde{x}_2}\dot{\tilde{x}}_2 = -\sigma + f_3\,,$$

whence we obtain

$$\frac{\partial h}{\partial \tilde{x}_1}(\tilde{x}_2 + f_1) + \frac{\partial h}{\partial \tilde{x}_2} f_2 + \sigma - f_3 = 0\,. \tag{5.32}$$

If we assume that $h(\tilde{x}_1,\, \tilde{x}_2,\, \tilde{\boldsymbol{\alpha}})$ has the form

$$\begin{aligned} h(\tilde{x}_1,\, \tilde{x}_2,\, \tilde{\boldsymbol{\alpha}}) \ &= \ a_\tau \tilde{\tau} + a_\delta \tilde{\delta} + a_{\tau\tau}\tilde{\tau}^2 + a_{\delta\delta}\tilde{\delta}^2 \\ &\quad + a_{11}\tilde{x}_1^2 + a_{22}\tilde{x}_2^2 + a_{12}\tilde{x}_1\tilde{x}_2 \\ &\quad + a_{\tau 1}\tilde{\tau}\tilde{x}_1 + a_{\tau 2}\tilde{\tau}\tilde{x}_2 + a_{\delta 1}\tilde{\delta}\tilde{x}_1 \\ &\quad + a_{\delta 2}\tilde{\delta}\tilde{x}_2 + a_{\tau\delta}\tilde{\tau}\tilde{\delta} + \mathrm{O}\left(\|(\tilde{x}_1,\, \tilde{x}_2,\, \tilde{\boldsymbol{\alpha}})\|^3\right)\,, \end{aligned}$$

and we substitute it into (5.32), equating the coefficients to zero, for the given TB point we have

$$\begin{aligned} h(\tilde{x}_1,\, \tilde{x}_2,\, \tilde{\boldsymbol{\alpha}}) \ &= \ -0.02896921\tilde{\tau} + 0.29311667\tilde{\delta} \\ &\quad + 0.00758882\tilde{\tau}^2 - 0.09524118\tilde{\delta}^2 \\ &\quad + 0.04428867\tilde{x}_1^2 + 0.38458253\tilde{x}_2^2 - 0.38786977\tilde{x}_1\tilde{x}_2 \\ &\quad - 0.03823235\tilde{\tau}\tilde{x}_1 + 0.14079898\tilde{\tau}\tilde{x}_2 + 0.17622414\tilde{\delta}\tilde{x}_1 \\ &\quad + 0.45773572\tilde{\delta}\tilde{x}_2 + 0.08023596\tilde{\tau}\tilde{\delta} + \mathrm{O}\left(\|(\tilde{x}_1,\, \tilde{x}_2,\, \tilde{\boldsymbol{\alpha}})\|^3\right)\,. \end{aligned} \tag{5.33}$$

Thus on the centre of manifold (5.25) reduces to

$$\dot{\tilde{x}}_1 \ = \ \tilde{x}_2 + g_1(\tilde{x}_1,\, \tilde{x}_2,\, \tilde{\boldsymbol{\alpha}})\,, \tag{5.34}$$

$$\dot{\tilde{x}}_2 \ = \ g_2(\tilde{x}_1,\, \tilde{x}_2,\, \tilde{\boldsymbol{\alpha}})\,, \tag{5.35}$$

where g_1 and g_2 are nonlinear functions of $\tilde{x}_1$ and $\tilde{x}_2$, such that $g_1(0,\, 0,\, \mathbf{0}) = g_2(0,\, 0,\, \mathbf{0}) = 0$. In particular with the expression for h (5.33) and the given TB point we have

$$\begin{aligned} g_1(\tilde{x}_1,\, \tilde{x}_2,\, \tilde{\boldsymbol{\alpha}}) \ &= \ -0.05603713\tilde{\tau} - 0.84569753\tilde{\delta} \\ &\quad - 0.00035932\tilde{\tau}^2 - 0.02081717\tilde{\delta}^2 \\ &\quad - 0.23200404\tilde{x}_1^2 - 0.31623843\tilde{x}_2^2 + 0.81465209\tilde{x}_1\tilde{x}_2 \\ &\quad - 0.03594954\tilde{\tau}\tilde{x}_1 + 0.06502558\tilde{\tau}\tilde{x}_2 + 0.62809106\tilde{\delta}\tilde{x}_1 \\ &\quad + 4.00567541\tilde{\delta}\tilde{x}_2 + 0.00569308\tilde{\tau}\tilde{\delta} + \mathrm{O}\left(\|(\tilde{x}_1,\, \tilde{x}_2,\, \tilde{\boldsymbol{\alpha}})\|^3\right)\,, \end{aligned}$$

and

$$\begin{aligned} g_2(\tilde{x}_1,\, \tilde{x}_2,\, \tilde{\boldsymbol{\alpha}}) &= 0.01605824\tilde{\tau} + 0.25629498\tilde{\delta} \\ &\quad +0.00014036\tilde{\tau}^2 + 0.03479552\tilde{\delta}^2 \\ &\quad +0.04977576\tilde{x}_1^2 + 0.25777010\tilde{x}_2^2 - 0.58284702\tilde{x}_1\tilde{x}_2 \\ &\quad +0.01136883\tilde{\tau}\tilde{x}_1 - 0.02366879\tilde{\tau}\tilde{x}_2 - 0.19692613\tilde{\delta}\tilde{x}_1 \\ &\quad +0.39251098\tilde{\delta}\tilde{x}_2 - 0.00485911\tilde{\tau}\tilde{\delta} + \mathrm{O}\left(\|(\tilde{x}_1,\, \tilde{x}_2,\, \tilde{\boldsymbol{\alpha}})\|^3\right) , \end{aligned}$$

We now follow the derivation of the standard normal form as described by Kuznetsov [56]. Our system (5.29) satisfies all the nondegenerancy conditions explained in chapter 4.2.2 and given by equations (4.15), (4.22), (4.31) and (4.34). Hence we deduce that there exist smooth invertible variable transformations of the independent variable, parameters and time which together reduce system (5.34)-(5.35) to its Bogdanov normal form representation

$$\dot{\eta}_1 = \eta_2 \,, \tag{5.36}$$

$$\dot{\eta}_2 = \xi_1(\tilde{\boldsymbol{\alpha}}) + \xi_2(\tilde{\boldsymbol{\alpha}})\eta_1 + \eta_1^2 - \eta_1\eta_2 + \mathrm{O}(\|\boldsymbol{\eta}^3\|) \,. \tag{5.37}$$

For the TB point considered here we implemented the normal form procedure using Maple to find that

$$\begin{aligned} \xi_1(\tilde{\boldsymbol{\alpha}}) &= 1.2010091\Big[0.01605824\tilde{\tau} + 0.0256294498\tilde{\delta} + 0.00014036\tilde{\tau}^2 \\ &\quad -0.0048591\tilde{\delta}\tilde{\tau} + 0.03479552\tilde{\delta}^2\Big]\Big[0.0497757 \\ &\quad +0.08318996\tilde{\tau} + 0.03136086331\tilde{\delta} + 0.00006228\tilde{\tau}^2 \\ &\quad +0.00114555\tilde{\delta}\tilde{\tau} - 0.01796682\tilde{\delta}^2\Big]^{-3} \end{aligned}$$

and

$$\begin{aligned} \xi_2(\tilde{\boldsymbol{\alpha}}) &= 1.0959056\Big[-0.24978414\tilde{\tau} - 0.567286662\tilde{\delta} - 0.00020860\tilde{\tau}^2 \\ &\quad +0.00414283\tilde{\delta}\tilde{\tau} - 0.0205619979\tilde{\delta}^2\Big]\Big[0.0497757 \\ &\quad +0.08318996\tilde{\tau} + 0.03136086331\tilde{\delta} + 0.00006228\tilde{\tau}^2 \\ &\quad +0.00114555\tilde{\delta}\tilde{\tau} - 0.01796682\tilde{\delta}^2\Big]^{-3} \end{aligned}$$

with $\tilde{\tau} = \tau - \tau^{\mathrm{TB}}$ and $\tilde{\delta} = \delta - \delta^{\mathrm{TB}}$. It is not difficult to verify that the TB point corresponds to $\xi_1 = \xi_2 = 0$ and in Appendix B we show that the locus of the Hopf Bifurcation corresponds to the curve

$$\mathrm{HB} = \{(\xi_1,\, \xi_2) :\; \xi_1(\tilde{\boldsymbol{\alpha}}) = 0,\; \xi_2(\tilde{\boldsymbol{\alpha}}) < 0\} \,. \tag{5.38}$$

In figure 5.12 this analytical result is compared with the numerical locus of the Hopf Bifurcation obtained by using AUTO97. The numerical results are plotted with points, while the local analytical result (5.38) is drawn with a solid line. From the Hopf bifurcation periodic orbits are generated, the stable limit cycle, that eventually breaks down at a global bifurcation, namely a saddle homoclinic bifurcation (SHB). In appendix B we show that locally to the TB point it has the following representation

$$\mathrm{SHB} = \left\{(\xi_1, \xi_2) : \ \xi_1 + \frac{6}{25}\xi_2^2 = 0, \ \xi_2 < 0\right\}. \tag{5.39}$$

The comparison of this analytical result with the numerical locus of the homoclinic bifurcation computed with AUTO97 by fixing an "infinite" period of the orbits is shown in figure 5.13 where the numerical solution is plotted with points while the analytical result is shown by a solid line. The agreement of the numerical and analytical results is excellent in both cases as shown in figures 5.12 and 5.13.

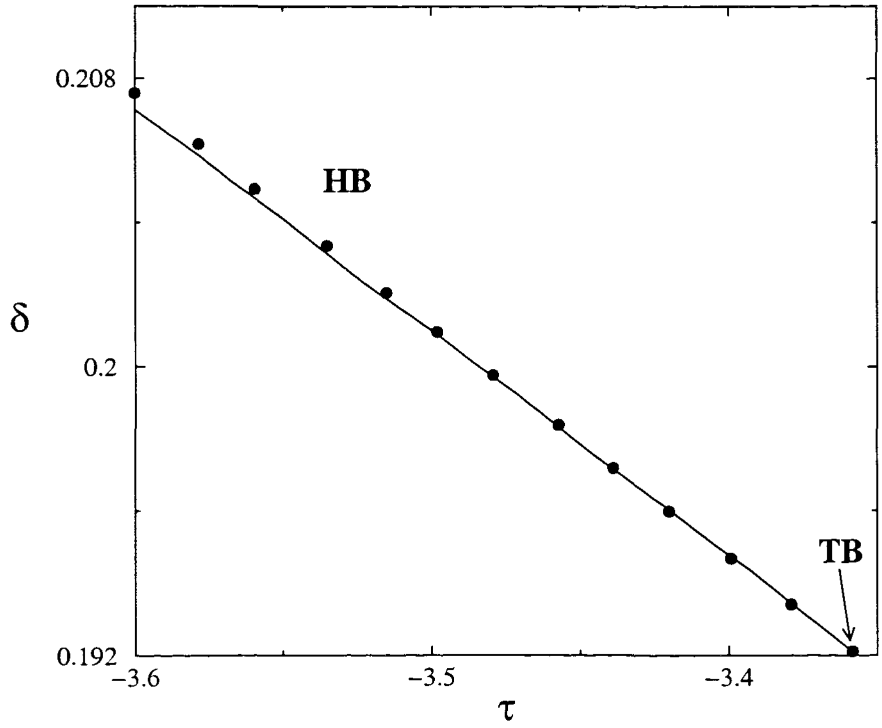

Figure 5.12: A comparison of the locus of the Hopf bifurcation point near the TB point given by the analytical result (5.38) and numerical computation with AUTO97. The solid line is the local analytical result and the points are the numerical result.

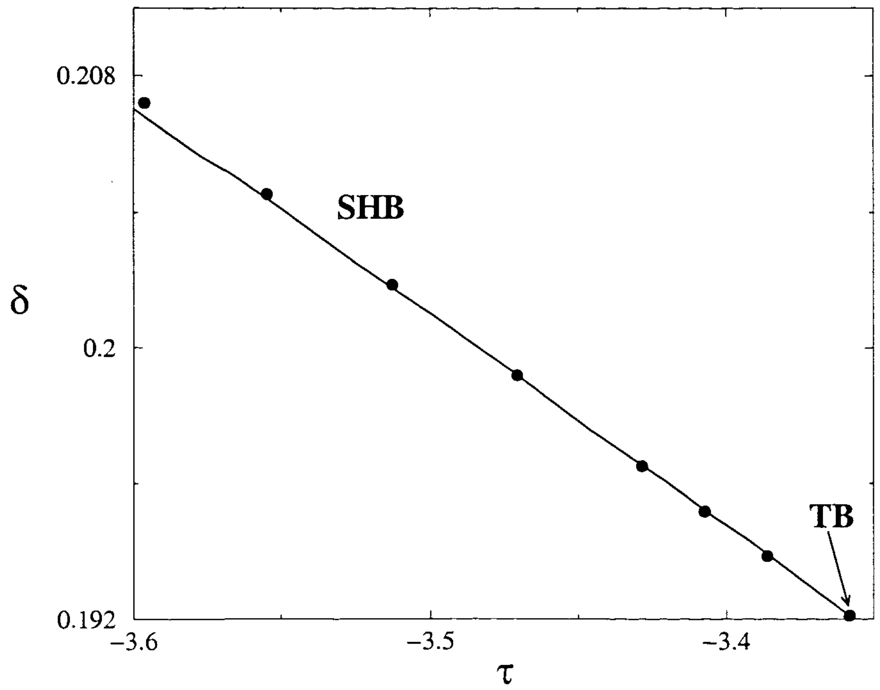

Figure 5.13: A comparison of the locus of the saddle homoclinic bifurcation point near the TB point given by the analytical result (5.39) and numerical computation with AUTO97. The solid line is the local analytical result and the points are the numerical result.

5.3.3 The relationship between tumbling and wagging: A new set of variables

We now investigate the relation between the two time dependent states. It turns out that essential to this is the observation that the one branch of HB points terminates when $S_1 = S_2$, which corresponds to a singularity of the governing equations. Figure 5.14 shows the steady state for $\delta = 4.120275 \times 10^{-1}$ by a bold curve and the locus of the maximum of S_1 of the wagging solution by a dotted curve in (τ, S_1)-space. This locus of wagging solutions ends when one of the wagging orbits reaches the singularity point. Two of the wagging orbits are shown in figure 5.15 in the (S_1, S_2) plane. The orbit for $\tau = -6.53864$ attains $S_1 = S_2$. For larger values of τ we were unable to compute wagging orbits for this value of δ. The singularity of the system at $S_1 = S_2$ represents the boundary between the tumbling and wagging states.

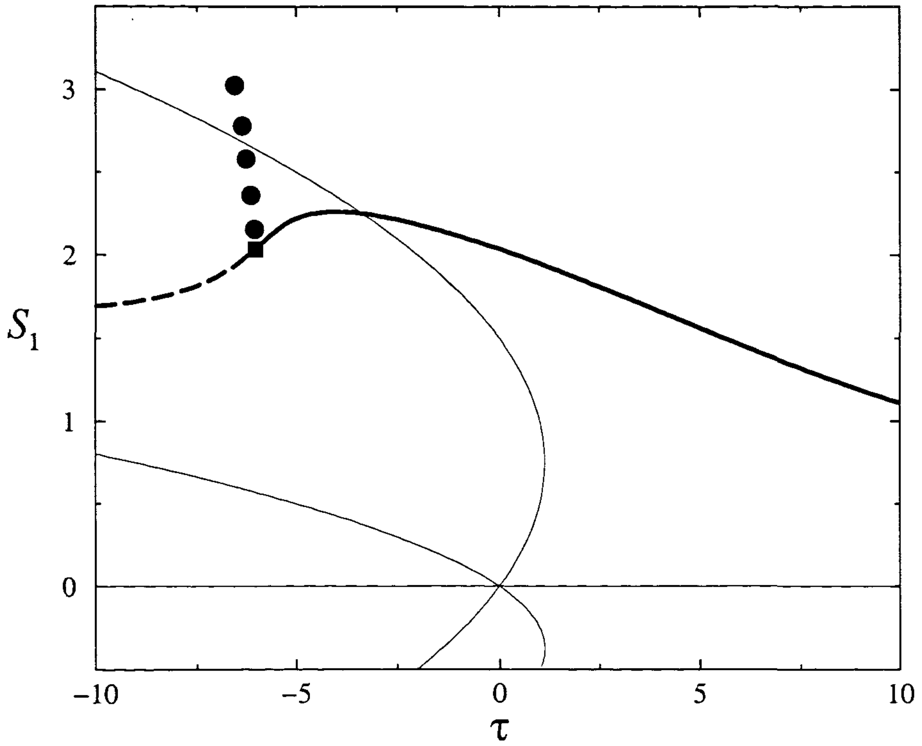

Figure 5.14: The bold line is the steady state for $\delta = 4.120275 \times 10^{-1}$ and the square point in this branch is the Hopf bifurcation (HB) from where periodic solutions emerge. The points are the continuation in τ of the periodic orbits plotting the maximum of S_1 against the dimensionless temperature. The locus of the wagging orbits finishes when $S_1 \approx S_2$.

The relationship between tumbling and wagging states is more conveniently investi-

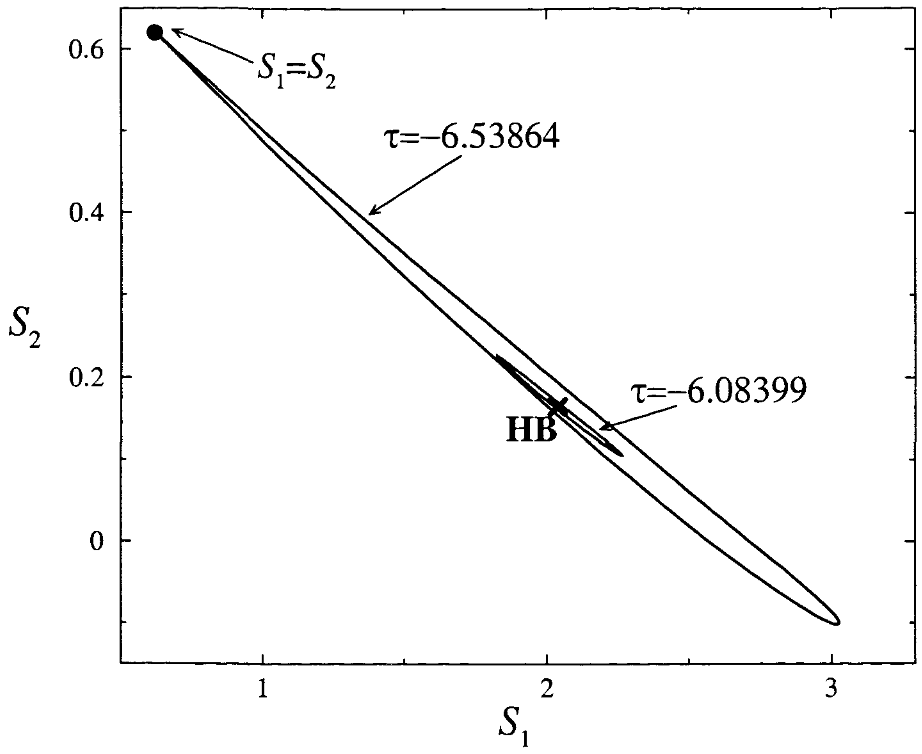

Figure 5.15: Two of the wagging orbits for $\delta = 4.120275 \times 10^{-1}$ are plotted in the $(S_1,\ S_2)$-plane. The orbit with $\tau = -6.53864$ attains $S_1 = S_2$. It is the last orbit computed by AUTO97 with the given value of δ. The cross is the Hopf bifurcation point (HB) from where the periodic orbits originate.

gated in a new set of independent variables defined by

$$\mathbf{Q} = \begin{pmatrix} \eta + \sqrt{3}\mu & \sqrt{3}\nu & 0 \\ \sqrt{3}\nu & \eta - \sqrt{3}\mu & 0 \\ 0 & 0 & -2\eta \end{pmatrix}$$

where $\mathbf{Q}$ is the order tensor parameter associated with our system. These new variables do not depend on a basis associated with the rotating director director but on a fixed Cartesian frame. In addition the system is not singular expressed in terms of the new variables $(\mu,\ \nu,\ \eta)$.

The Landau free energy density of the system (2.7) may be expressed in these new variables as

$$f_b = 3A(\mu^2 + \nu^2 + \eta^2) + 2B\eta(3\mu^2 + 3\nu^2 - \eta^2) + 9C(\mu^2 + \nu^2 + \eta^2)^2.$$

An appropriate re-scaling of the dimensionless tensor equation (5.3) such that the homogeneous steady planar isotropic-nematic transition temperature and the corresponding new variables are set to unity is

$$\bar{\tau} \ = \ \frac{27}{\tilde{B}^2}\tau,$$

$$\begin{aligned}
\bar{\mu} &= -\frac{18}{\widetilde{B}}\mu, \\
\bar{\nu} &= -\frac{18}{\widetilde{B}}\nu, \\
\bar{\eta} &= -\frac{18}{\widetilde{B}}\eta.
\end{aligned}$$

The relationship between these variables with the re-scaled scalar order parameters, S_1 and S_2, and the angle θ is given by

$$\begin{aligned}
\bar{\mu} &= \sqrt{3}(S_1 - S_2)\cos 2\theta, \\
\bar{\nu} &= \sqrt{3}(S_1 - S_2)\sin 2\theta, \\
\bar{\eta} &= S_1 + 3S_2.
\end{aligned}$$

We re-scale the Landau free energy density by $\bar{f}_b = 3^6 C^3 f_b / B^4$ to obtain

$$\bar{f}_b = \frac{\bar{\tau}}{4}\left(\bar{\mu}^2 + \bar{\nu}^2 + \bar{\eta}^2\right) - \frac{1}{4}\bar{\eta}\left(3\bar{\mu}^2 + 3\bar{\nu}^2 - \bar{\eta}^2\right) + \frac{1}{16}\left(\bar{\mu}^2 + \bar{\nu}^2 + \bar{\eta}^2\right)^2,$$

which is rotationally invariant with respect to $\bar{\mu}$ and $\bar{\nu}$.

Dropping the overbars the three independent components of the re-scaled homogeneous system (5.3) are

$$\begin{aligned}
\dot{\mu} &= \delta\nu - \mathcal{B}\frac{\partial f_b}{\partial \mu}, && (5.40) \\
\dot{\nu} &= \delta(d_0 - \mu) - \mathcal{B}\frac{\partial f_b}{\partial \nu}, && (5.41) \\
\dot{\eta} &= -\mathcal{B}\frac{\partial f_b}{\partial \eta}, && (5.42)
\end{aligned}$$

where the new material parameters are $\mathcal{B} = 2\widetilde{B}^2/27$ and $d_0 = -3\sqrt{3}\beta_1/\widetilde{B}$.

The steady state solutions of the system (5.40)-(5.42) in the absence of flow ($\delta = 0$) are

- An isotropic state solution $\mu = \nu = \eta = 0$ for all values of τ.
- A uniaxial nematic solution, with an in-plane director given by $\tau = 3\eta - 2\eta^2$ and $\eta^2 = (\mu^2 + \nu^2)/3$ (which represents a cone in (μ, ν, η)-space).
- A uniaxial nematic solution with the out-of plane as distinguished direction, where $\tau = -\eta(\eta + 3)/2$ and $\mu = \nu = 0$.

When $\delta \neq 0$ steady states were computed with AUTO97. The results are shown in figures 5.16, 5.17 and 5.18, where the IPN branch is shown for several values of the strain rate for material parameters $\widetilde{B} = -1.2$ and $\beta_1 = 0.9$. Figure 5.16 shows the variable μ plotted against the dimensionless temperature τ for different values of the strain rate. In curve (a) $\delta = 4.512960 \times 10^{-3}$, in (b) $\delta = 4.509332 \times 10^{-2}$ and in (c) $\delta = 4.581803 \times 10^{-1}$. The solid lines represent linearly stable states, while the dashed lines are unstable states. The solid dots are limit points, and the square marks the Hopf bifurcation. Figure 5.17 shows the same curves in the (τ, ν)-plane, and figure 5.18 shows them in the (τ, η)-plane. As expected in this new set of variables the underlying bifurcation structure is the same as that found using the original variables.

The system (5.40)-(5.42) may be conveniently expressed in the form

$$\dot{\mathbf{x}} = -[\mathcal{B}\nabla f + \delta \mathbf{A}(\mathbf{x})] \; ,$$

where $\mathbf{x} = \mu\mathbf{e_1} + \nu\mathbf{e_2} + \eta\mathbf{e_3}$, $\{\mathbf{e_1}, \mathbf{e_2}, \mathbf{e_3}\}$ is an orthonormal basis and

$$\mathbf{A}(\mathbf{x}) = \mathbf{e_3} \times (\mathbf{x} - d_0\mathbf{e_1}).$$

Thus we see the system is the superposition of a gradient flow, with a potential f, and a rotation about $d_0\mathbf{e_1}$, with angular velocity δ. As we observed above f is rotationally invariant with respect to μ and ν, i.e., about the $\mathbf{e_3}$-axis, hence $\partial f/\partial\eta = 0$ and $\nabla f = |\nabla f|\mathbf{e_r}$ where $\mathbf{e_r}$ is the radial unit vector in the (μ, ν)-plane. Thus $\mathbf{x}$ may be expressed as $\mathbf{x} = r\mathbf{e_r} + \eta\mathbf{e_3}$ and the steady states are given by

$$\mathcal{B}|\nabla f|\mathbf{e_r} + \delta\mathbf{e_3} \times (\mathbf{x} - d_0\mathbf{e_1}) = \mathbf{0},$$

which may be solved to yield

$$\begin{aligned} r &= d_0 \cos\theta, \\ \sin\theta &= -\frac{\mathcal{B}|\nabla f|}{\delta d_0} \; , \\ \frac{\partial f}{\partial \eta} &= 0, \end{aligned}$$

where θ is the angle that $\mathbf{e_r}$ forms with $\mathbf{e_1}$. Thus we see that the steady state solutions lie on the surface of the cylinder given by $\nu^2 + (\mu - d_0/2)^2 = d_0^2/4$. The numerical calculations confirm this analysis. In figure 5.19 the solution curve for $\delta = 4.512960 \times 10^{-3}$ is plotted in the (μ, ν)-plane and it is found to be coincident with the circle $\nu^2 + (\mu - d_0/2)^2 = d_0^2/4$. Thus we deduce that when $\mu < 0$ or $\mu > d_0$ then a stationary state cannot exist but rather time dependent behaviour, such as tumbling or wagging. When the strain rate is larger than δ^{TB} there is a Hopf bifurcation from where the periodic orbits emanate. The continuation from the Hopf bifurcation of the locus of the orbits in τ, with a fixed strain rate was done using AUTO97. In figure 5.20, for a value $\delta = 4.581803 \times 10^{-1}$, the periodic orbits for different values of the dimensionless temperature are shown in the (μ, ν)-plane. The orbits that are not surrounding the axis $(\mu,\ \nu) = (0,\ 0)$, verify that the angle $\theta = \tan^{-1}(\nu/\mu)$ is bounded and therefore these are wagging orbits. When the periodic orbits are surrounding the η-axis, then the director angle θ is unbounded and these are tumbling orbits. Therefore, with this sets of variables is possible to continue from wagging to tumbling without the discontinuity that appeared expressing the problem with respect to the the local frame of reference. However, the singularity of the system gives us an easier way to determined numerically the boundary between tumbling and wagging solutions.

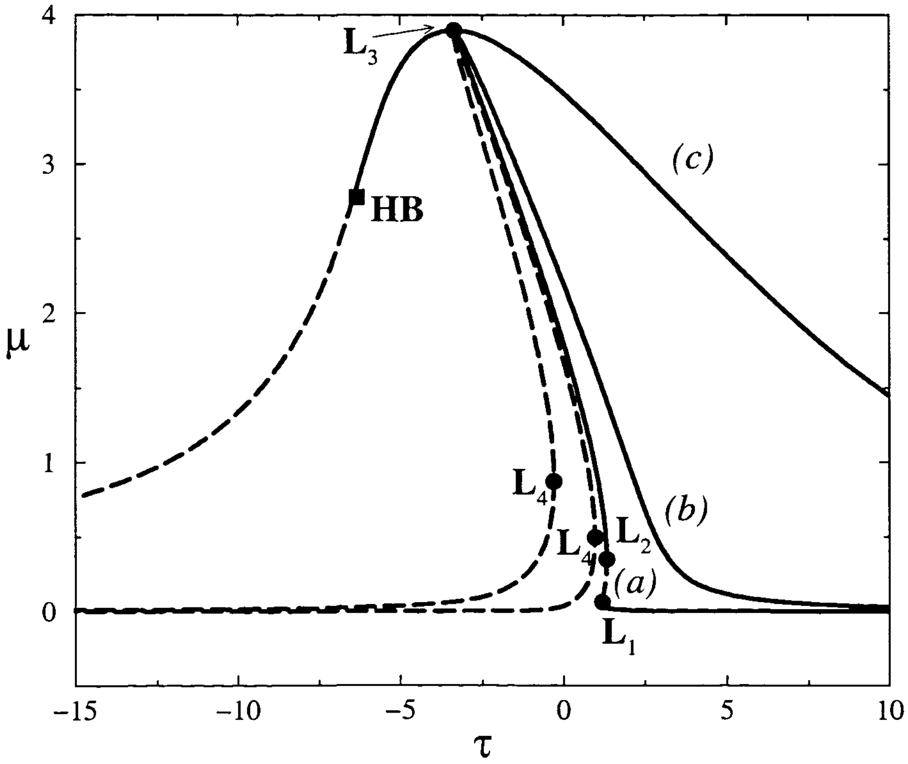

Figure 5.16: The IPN branch of the system (5.40)-(5.42) for several values of the strain rate and values of the material parameters $\widetilde{B} = -1.2$, $\beta = 0.9$. The curves are plotted in the (τ, μ)-plane. In curve (a) $\delta = 4.512960 \times 10^{-3}$, in (b) $\delta = 4.509332 \times 10^{-2}$ and in (c) $\delta = 4.581803 \times 10^{-1}$. The solid curves represent steady stable states, while dashed lines are unstable steady states. The solid dots in the plot L_1, L_2, L_3 and L_4 correspond to the limit points LP1, LP2, LP3 and LP4 respectively, while the square corresponds to a Hopf bifurcation (HB).

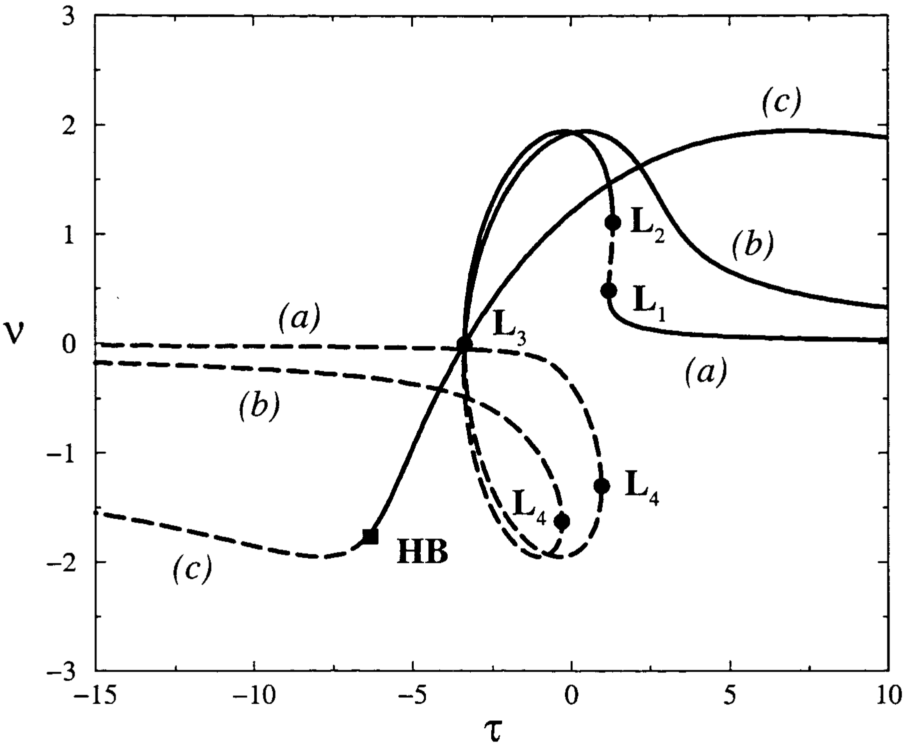

Figure 5.17: The IPN Branch of the system (5.40)-(5.42) plotted for several values of the strain rate and values of the material parameters $\widetilde{B} = -1.2$, $\beta = 0.9$. The curves are plotted in the (τ, ν)-plane. In curve (a) $\delta = 4.512960 \times 10^{-3}$, in (b) $\delta = 4.509332 \times 10^{-2}$ and in (c) $\delta = 4.581803 \times 10^{-1}$. The solid curves represent steady stable states, while dashed lines are unstable steady states. The solid dots in the plot L$_1$, L$_2$, L$_3$ and L$_4$ correspond to the limit points LP1, LP2, LP3 and LP4 respectively, while the square corresponds to a Hopf bifurcation (HB).

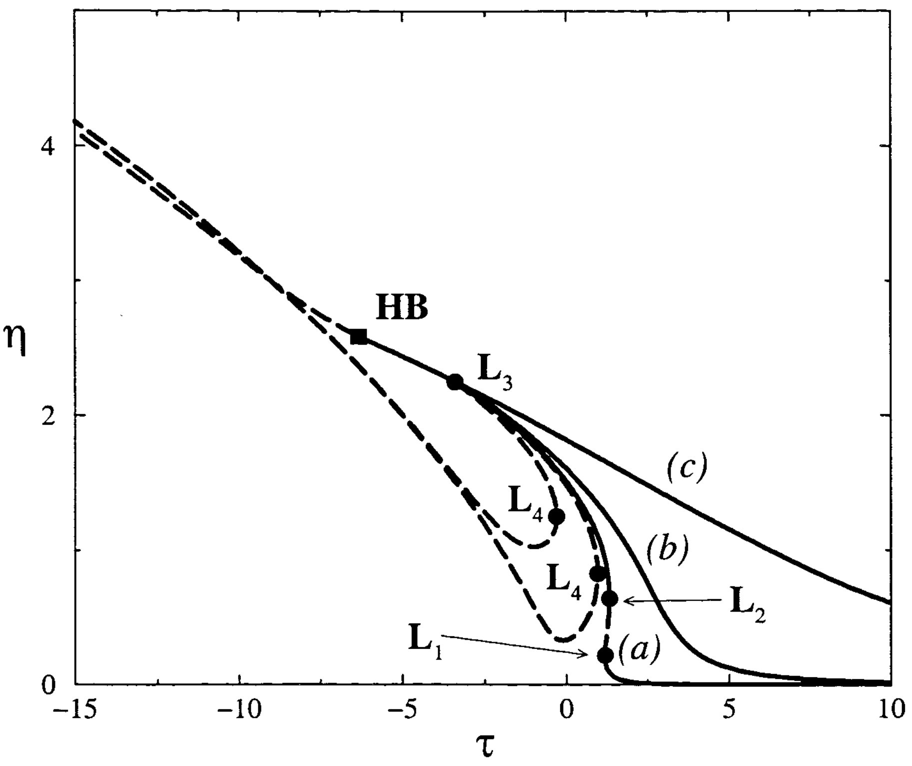

Figure 5.18: The IPN Branch of the system (5.40)-(5.42) for several values of the strain rate and values of the material parameters $\widetilde{B} = -1.2$, $\beta = 0.9$. The curves are plotted in the (τ, η)-plane. In curve (a) $\delta = 4.512960 \times 10^{-3}$, in (b) $\delta = 4.509332 \times 10^{-2}$ and in (c) $\delta = 4.581803 \times 10^{-1}$. The solid curves represent steady stable states, while dashed lines are unstable steady states. The solid dots in the plot L_1, L_2, L_3 and L_4 correspond to the limit points LP1, LP2, LP3 and LP4 respectively while the square corresponds to a Hopf bifurcation (HB).

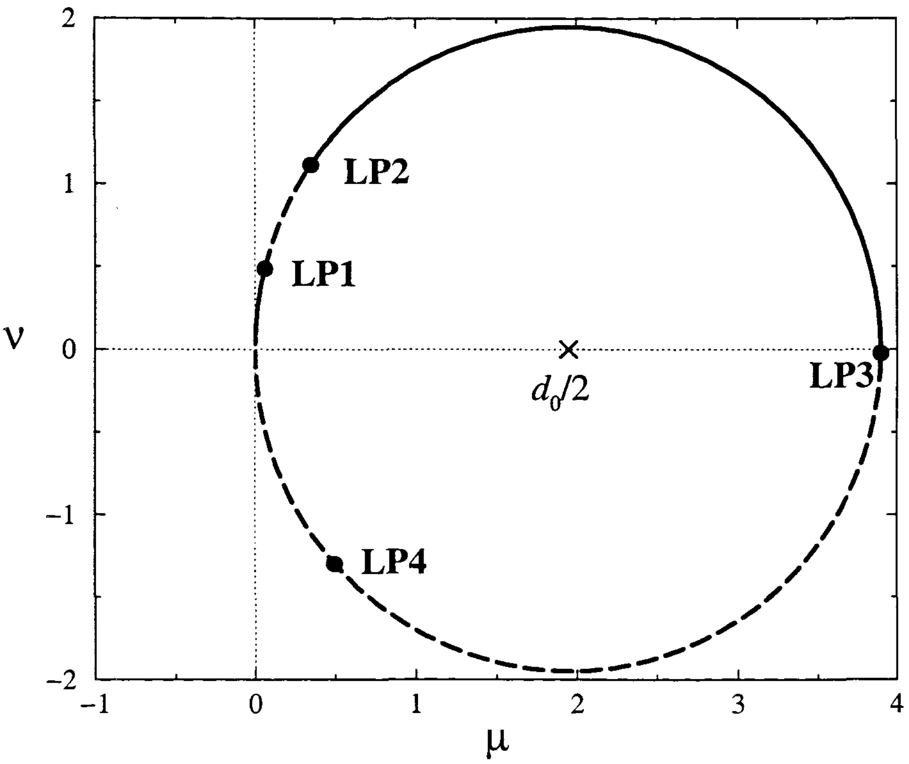

Figure 5.19: IPN Branch computed using AUTO97 for a value of $\delta = 4.512960 \times 10^{-3}$ in the (μ, ν)-plane which lies on the circumference $\nu^2 + (\mu - d_0/2)^2 = d_0^2/4$. Solid lines are linearly stable states and dashed lines linearly unstable states. The solid dots are the limit points.

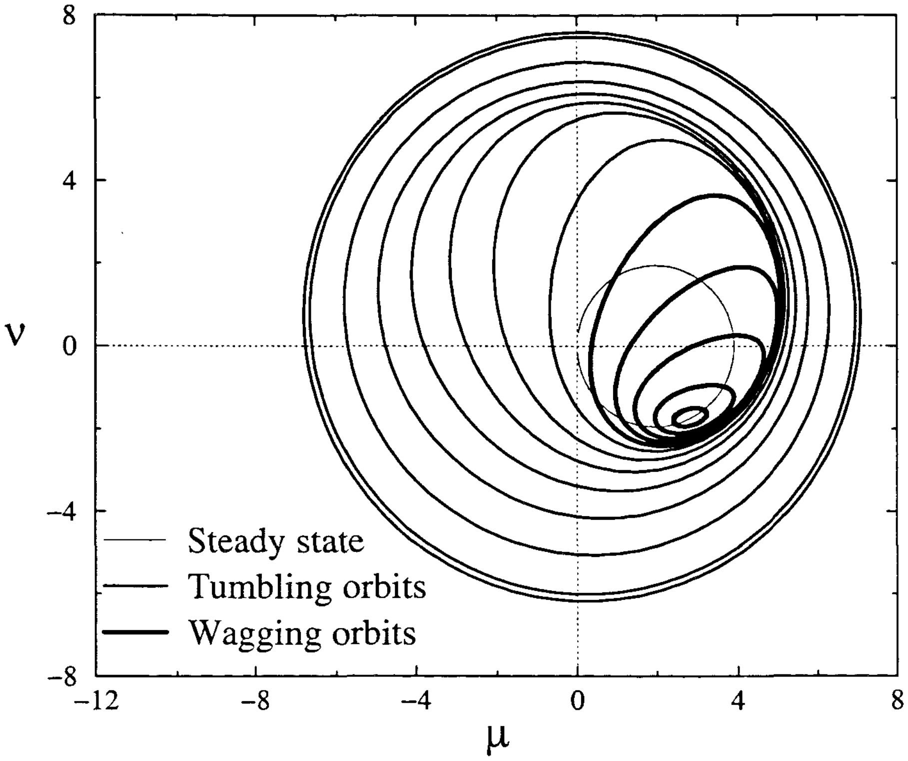

Figure 5.20: Periodic orbits for a fixed value of the strain rate $\delta = 4.581803 \times 10^{-1}$ as temperature decreases. The longer the perimeter of the orbits, the lower the temperature. Those orbits which does not contain the origin are tumbling orbits, while the others are wagging orbits.

5.4 The Log-Rolling Nematic Branch

In this section we analyse the behaviour of the Log-Rolling Nematic Branch (LRN) as we increase the strain rate. We also perform an analysis of the solution branches for very large values of the dimensionless strain rate, δ, in order to confirm the numerical evidence of the existence of a limit solution curve.

5.4.1 Small and intermediate strain rate

Figure 5.21 shows the LRN Branch for a fixed value of the strain rate $\delta = 4.313060 \times 10^{-3}$, with material parameters $\widetilde{B} = -1.2$ and $\beta_1 = 0.9$. In this figure the linearly stable states are plotted with solid lines while dashed lines indicate the linearly unstable states. The computation of this branch and its stability has been done using the software AUTO97.

At very low temperatures an unstable paranematic state (labelled P in figure 5.21) exists with the director at an angle of approximately $-\pi/4$ with respect to the x-axis. As temperature starts to decrease at τ_1 the temperature associated to the limit point LP1, the angle θ increases and for temperatures between τ_1 and τ_2 (associated to LP2), the system adopts an unstable disk-like nematic distribution in the xz-plane. The system passes through a fully aligned unstable disk-like state with $\theta = 0$, $S_1 = -S_2 = -3b/2$, where $b = \beta_1/\widetilde{B}$, at a temperature $\tau = 9b(1-2b)$. This occurs close to τ_2 the temperature associated to the limit point LP2. The portion of solution branch between the limit points LP2 and LP3 represents an unstable disk-like distribution in the xz plane (labelled D in figure 5.21) that evolves at the limit point LP3 into a stable elongated nematic state with the z-axis as preferred direction: the so-called log-rolling state (labelled LR in the figure).

As the strain rate is increased the limit points LP1 and LP2 come closer together and merge for a critical value of the strain rate $\delta^c = 0.6668743$, with associated temperature $\tau^c = -17.65580$ as shown in figure 5.22. We also observe that at $(\tau^{\mathrm{TB}}, \delta^{\mathrm{TB}}) = (-16.97717, 0.5824285)$ a Takens-Bogdanov bifurcation occurs, from where a branch of Hopf bifurcations originates (labelled HB in figure 5.22). The locus of the limit point LP3 presents a vertical asymptote on the (τ, δ)-space at $\tau = \tau^v$, with the order parameters S_1 and S_2, and the angle θ approaching S_1^v, S_2^v and θ^v as $\delta \to \infty$. The behaviour of the solution branches and their limit points and Hopf bifurcations for very large strain rate will be studied in next section. In figure 5.23 the LRN Branch is plotted for different values of the strain rate. Summarising its behaviour as δ increases we have

- $0 < \delta < \delta^{TB}$. The IPN branch has three limit points, LP1, LP2 and LP3. LP1 and LP2 move closer together as δ is increased. The only stable solution is the log-rolling state. Curve (a) in figure 5.23 is an example of this situation.
- $\delta = \delta^{TB}$. A Takens-Bogdanov bifurcation appears generating a branch of Hopf bifurcations.
- $\delta^{TB} < \delta < \delta^c$. The LRN branch presents three limit points and a Hopf bifurcation between LP1 and LP2. The limit points LP1 and LP2 move closer together as δ is increased.
- $\delta = \delta^c$. The two limit points LP1 and LP2 coincide.
- $\delta > \delta^c$. The branches present only one limit point, LP3, and a Hopf bifurcation.

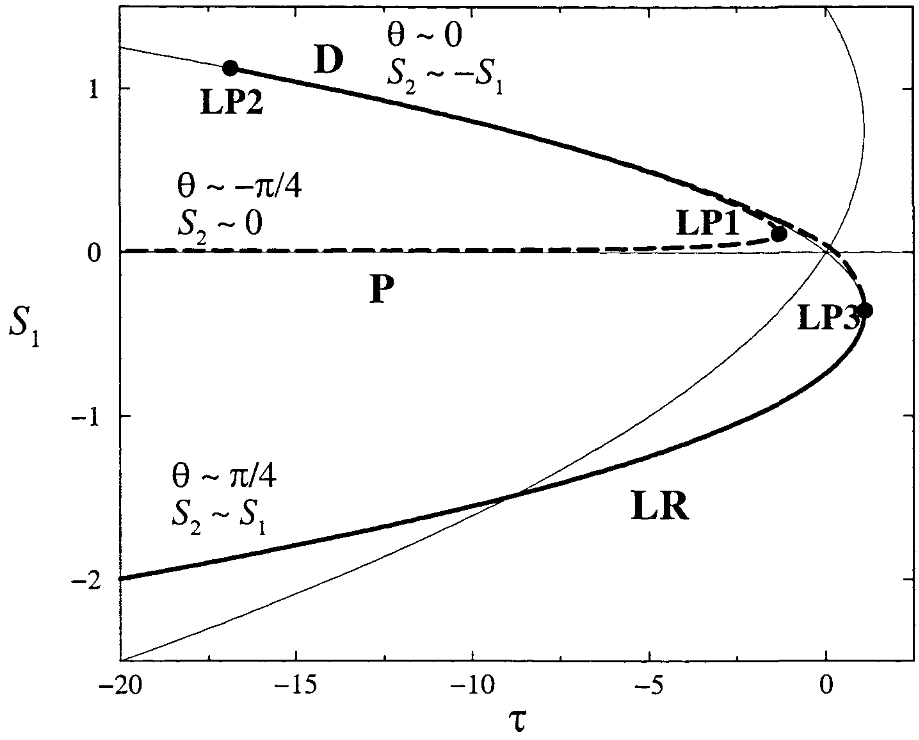

Figure 5.21: Steady state solution branch computed with a fixed value of the dimensionless strain rate $\delta = 4.313060 \times 10^{-3}$ and values of the material parameters $\widetilde{B} = -1.2$ and $\beta_1 = 0.9$. Linearly stable states are plotted with solid lines and linearly unstable states with dashed lines and the labelled points are limit points. This solution branch links an unstable paranematic state (P) to an unstable disk-like distribution in the xz-plane (D), to a elongated out-of-plane distribution in the z-direction, the so-called log-rolling state (LR).

This behaviour is shown in branch (*b*) of figure 5.23. As the strain rate is increased the solutions approach a limit branch: curve (*c*) in figure 5.23.

For the LRN Branch a local study about the Takens-Bogdanov bifurcation, similar to that done for the IPN Branch in section 5.3.2.1, is unnecessary, since both the Takens-Bogdanov point and the Hopf bifurcation occur on unstable states of the LRN Branch and therefore they are physically irrelevant. However, from the numerical calculations we observe that the solution approaches a limit branch as $\delta \rightarrow \infty$. In order to corroborate this result and find an analytical expression for the limit curve we perform an analysis for very large strain rates.

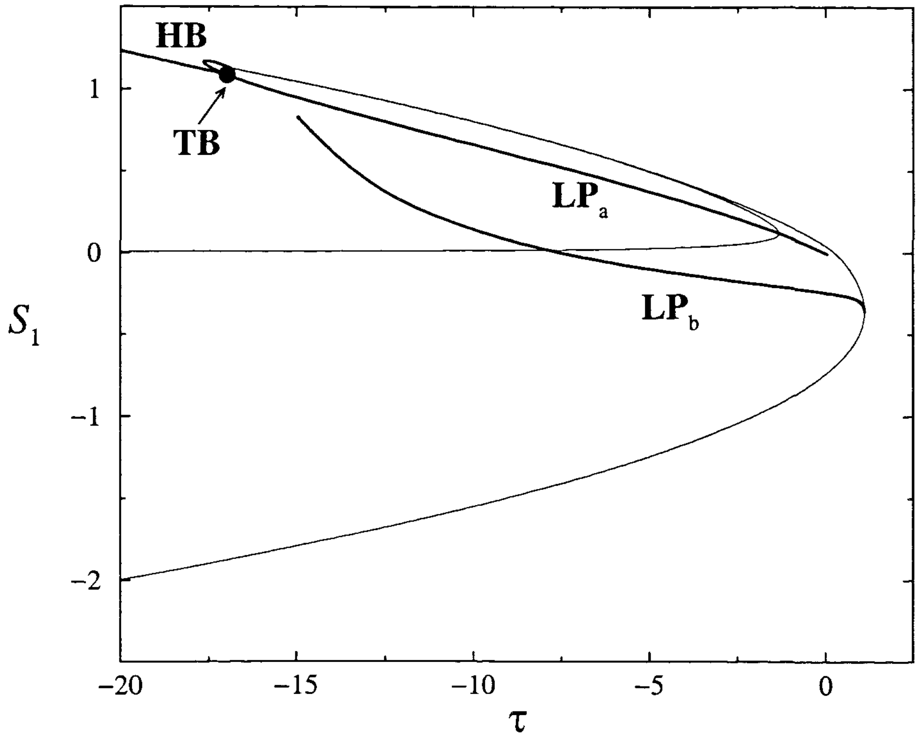

Figure 5.22: The bold solid lines lines labelled $\mathrm{LP_a}$ and $\mathrm{LP_b}$ in the figure are the locus of the limit points computed with AUTO97 using the material parameters $\widetilde{B} = -1.2$ and $\beta_1 = 0.9$. The curve $\mathrm{LP_a}$ is the locus of the limit points LP1 and LP2 that collide at $(\tau^c, \delta^c) = (-17.65580, 0.5824285)$. Curve $\mathrm{LP_b}$ is the locus of the limit point LP3. The solid point TB is the Takens-Bogdanov bifurcation from where a branch of Hopf bifurcations (HB) generates.

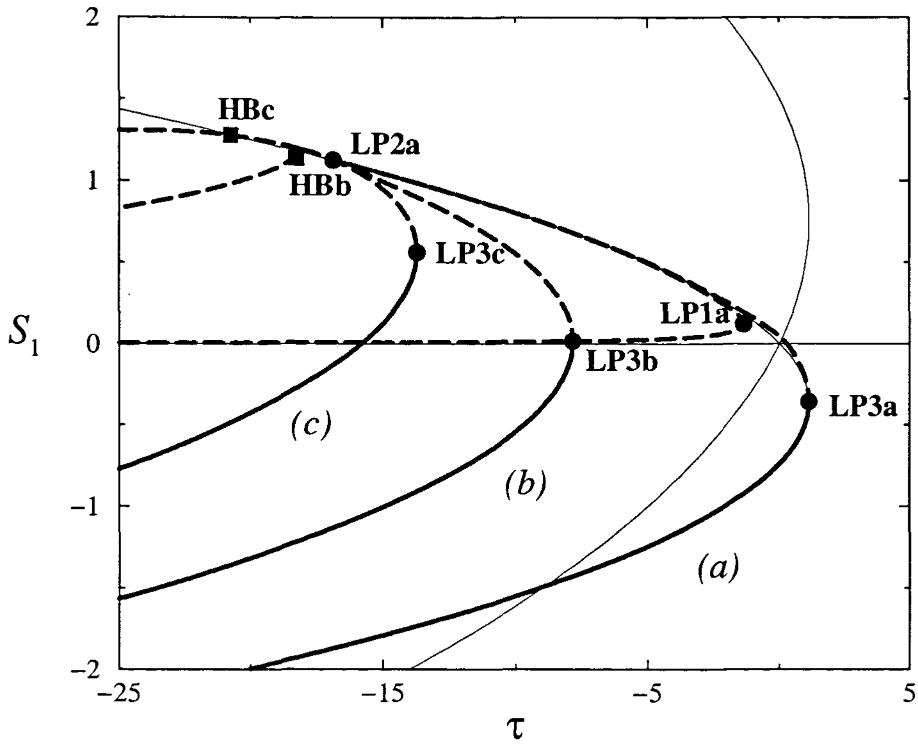

Figure 5.23: Plot of S_1 against τ for different values of the strain rate. The thin solid lines correspond to the case without flow and the bold solid lines are solutions for different values of δ and with material parameters $\widetilde{B} = -1.2$ and $\beta_1 = 0.9$. Curves (a), (b) and (c) correspond to $\delta = 4.313060 \times 10^{-3}$, $\delta = 0.7384020$ and $\delta = 1.88521099$, respectively. Solid bold lines represent the stable states and dashed lines are the linearly unstable states. The solid points are the limit points of the different branches. The square symbols are the Hopf bifurcation points of branches (b) and (c).

5.4.2 Very large strain rate. $\delta \to \infty$

Given the limiting behaviour observed in the numerically computed LRN branch for large δ we analyse the behaviour of the steady state solutions of system (5.4)-(5.6) for a very large value of the strain rate. We define $\epsilon = \delta^{-1}$ and re-write the steady form of the system as

$$\begin{aligned}
\frac{9\beta_1}{4\widetilde{B}}\sin 2\theta &= -\frac{\widetilde{B}^2}{27}\left(\tau S_1 - 3S_1^2 + 9S_2^2 + 2S_1\left(S_1^2 + 3S_2^2\right)\right)\epsilon\,, \\
\frac{3\beta_1}{4\widetilde{B}}\sin 2\theta &= \frac{\widetilde{B}^2}{27}\left(\tau S_2 + 6S_1S_2 + 2S_2\left(S_1^2 + 3S_2^2\right)\right)\epsilon\,, \\
\frac{3\beta_1}{\widetilde{B}}\cos 2\theta &= S_2 - S_1\,.
\end{aligned}$$

We perform a regular expansion of this system in ϵ, with

$$S_1 = x_0 + x_1\epsilon + \mathrm{O}(\epsilon^2), \quad S_2 = y_0 + y_1\epsilon + \mathrm{O}(\epsilon^2), \quad \theta = z_0 + z_1\epsilon + \mathrm{O}(\epsilon^2), \tag{5.43}$$

as $\epsilon \to 0$. This gives to order ϵ^0

$$z_0 = 0\,, \tag{5.44}$$

$$x_0 = y_0 - 3b\,, \tag{5.45}$$

where $b = \beta_1/\widetilde{B}$. At $\mathrm{O}(\epsilon)$ we obtain

$$x_1 = y_1\,, \tag{5.46}$$

$$z_1 = -\frac{2\widetilde{B}^4 b}{243}\left(\tau x_0 - 3x_0^2 + 9y_0^2 + 2x_0\left(x_0^2 + 3y_0^2\right)\right) \tag{5.47}$$

$$\tau = -\frac{32x_0^3 + 24(1+9b)x_0^2 + 108b(1+5b)x_0 + 81b^2(1+6b)}{4x_0 + 9b}\,. \tag{5.48}$$

For very large δ ($\epsilon \ll 1$) we approximate S_1 and S_2 by x_0 and y_0, respectively, then (5.48) provides the equation of solution branches IPN and LRN in the (τ, S_1)-space when $\delta \to \infty$. The line $S_1 = -9b/4$ is the horizontal asymptote which separates both solution branches. Substituting equation (5.45) into (5.48) we obtain an expression for the solution branches in the (τ, S_2)-space

$$\tau = -\frac{32S_2^3 + 24(1-3b)S_2^2 + 36b(3b-1)S_2 - 27b^2(1+2b)}{4S_2 - 3b}\,. \tag{5.49}$$

The solid lines in figure 5.24 are the solution branches in the (τ, S_1)-space for $\delta \to \infty$ and the dots are the numerical results obtained by computing, using AUTO97, the IPN and LRN branches with $\delta = 10^3$. Solid dots represent the linearly stable states and the white dots are the linearly unstable states. The square symbols in figure

5.24 are the Hopf bifurcation points of the IPN branch (HB1) and the LRN branch labelled HB2, the diamond is the limit point LP3 of the LRN Branch. There is clearly excellent agreement between the asymptotic results and numerical computations. The limit point LP3 and the Hopf Bifurcations, HB1 and HB2, can also be calculated analytically for very large values of the strain rate.

To find the limit point and the Hopf bifurcation requires linearising the dynamical system about the steady state, hence the points at which the linearised system has one zero eigenvalue are limit points while those points where the linearised system presents a pure imaginary pair of eigenvalues are Hopf bifurcations.

We consider $(S_1^*,\, S_2^*,\, \theta^*)$ a steady state solution and define

$$\mathrm{x} = (x,\, y,\, z)^T = (S_1 - S_1^*,\, S_2 - S_2^*,\, \theta - \theta^*)^T$$

and a new time scale $T = \delta t$. The linearised form of the dynamical system (5.4)-(5.6) can be written as

$$\dot{\mathrm{x}} = \mathbf{M}\mathrm{x}\,, \tag{5.50}$$

where the matrix $\mathbf{M}$ is

$$\begin{pmatrix} -a\epsilon f_{1,1}^* & -a\epsilon f_{1,2}^* & -\frac{9}{2}b\cos 2\theta^* \\ -a\epsilon f_{2,1}^* & -a\epsilon f_{2,2}^* & \frac{3}{2}b\cos 2\theta^* \\ \frac{3b\cos 2\theta^*}{2(S_2^*-S_1^*)^2} & -\frac{3b\cos 2\theta^*}{2(S_2^*-S_1^*)^2} & -\frac{3b\sin 2\theta^*}{(S_2^*-S_1^*)} \end{pmatrix}.$$

Here $\epsilon = \delta^{-1}$, $a = \widetilde{B}^2/27$, $b = \beta_1/\widetilde{B}$ and the functions f_1 and f_2 are given by

$$f_1 = \tau S_1 - 3S_1^2 + 9S_2^2 + 2S_1(S_1^2 + 3S_2^2)\,,$$

and

$$f_2 = \tau S_2 + 6S_1S_2 + 2S_2(S_1^2 + 3S_2^2)\,.$$

The subscript 1 or 2 after the comma indicates partial derivative with respect to S_1 and S_2 respectively, and the asterisk indicates evaluation of the function at the steady state solution $(S_1^*,\, S_2^*,\, \theta^*)$. We consider a regular expansion of the steady state solution in terms of ϵ given by equations (5.43) that verifies relationships (5.44)-(5.48). We now perform a regular expansion of the system (5.50) to obtain

$$\dot{\mathrm{x}} = (\mathbf{M}_0 + \epsilon\mathbf{M}_1)\mathrm{x} + O(\epsilon^2)\,,$$

where

$$\mathbf{M}_0 = \begin{pmatrix} 0 & 0 & -\frac{9}{2}b \\ 0 & 0 & \frac{3}{2}b \\ \frac{1}{6b} & -\frac{1}{6b} & 0 \end{pmatrix},$$

and

$$\mathbf{M}_1 = \begin{pmatrix} -af_{1,1}^0 & -af_{1,2}^0 & 0 \\ -af_{2,1}^0 & -af_{2,2}^0 & 0 \\ 0 & 0 & -2z_1 \end{pmatrix}.$$

Here the superscript 0 indicates evaluation of the functions at (x_0, y_0, z_0). However, from equation (5.47) we have $z_1 = -6a^2bf_1^0$ and therefore, using (5.45) and (5.48), $\mathbf{M}_1$ can be written in terms of x_0 and the two material constants a and b only.
The characteristic equation of the linearised system is

$$\det\Big(\mathbf{M}_0 + \epsilon\mathbf{M}_1 - \lambda\mathbf{I} + \mathrm{O}(\epsilon^2)\Big) = 0\,, \tag{5.51}$$

where the eigenvalue λ can also be expanded in terms of ϵ as follows

$$\lambda = \lambda_0 + \lambda_1\epsilon + \mathrm{O}(\epsilon^2)\,.$$

Performing an expansion of the characteristic equation (5.51) in powers of ϵ we obtain

$$\lambda_0(\lambda_0^2 + 1) + g(\lambda_0,\, \lambda_1,\, x_0)\epsilon + \mathrm{O}(\epsilon^2) = 0\,, \tag{5.52}$$

where the function g is given by

$$\begin{aligned} g(\lambda_0,\, \lambda_1,\, x_0) \;=\; & \Big\{243ab^3(3+4\lambda_0^2) + 162ab^2(1-3\lambda_0^2) + (9b+4x_0)(1+3\lambda_0^2)\lambda_1 \\ & +108ab^2(9+10\lambda_0^2)x_0 + 12a(9b+2x_0)(1-5\lambda_0^2)x_0 \\ & +16a(27b+4x_0)(1+\lambda_0^2)x_0^2\Big\}\Big\{4x_0+9b\Big\}^{-1} \end{aligned}$$

At leading order (5.52) gives that λ_0 is 0, $\pm i$. Hence there are three eigenvalues given by

$$\begin{aligned} \lambda^{(1)} &= \lambda_1^{(1)}\epsilon + \mathrm{O}(\epsilon^2)\,, \\ \lambda^{(2)} &= i + \lambda_1^{(2)}\epsilon + \mathrm{O}(\epsilon^2)\,, \\ \lambda^{(3)} &= -i + \lambda_1^{(3)}\epsilon + \mathrm{O}(\epsilon^2)\,. \end{aligned}$$

The values $\lambda_1^{(1)}$, $\lambda_1^{(2)}$ and $\lambda_1^{(3)}$ are given from the form of $g(\lambda_0,\, \lambda_1,\, x_0)$. We consider each in turn

- The eigenvalue $\lambda^{(1)}$ has $\lambda_0^{(1)} = 0$ and from the characteristic equation, (5.52), we obtain the condition for $\lambda^{(1)}$; $g(0,\, \lambda_1^{(1)},\, x_0) = 0$ from which we find

$$\lambda_1^{(1)} = -a\frac{81b^2(9b+2) + 108b(9b+1)x_0 + 24(18b+1)x_0^2 + 64x_0^3}{4x_0+9b}\,. \tag{5.53}$$

A limit point occurs when $\lambda^{(1)}$ is zero. Therefore we substitute $\lambda_1^{(1)} = 0$ in equation (5.53) and solve for x_0. We use the relationships (5.44), (5.45) and (5.48), to find that the limit point is given by

$$(\tau^L;\, S_1^L,\, S_2^L,\, \theta^L) = (-14.972954;\, 0.8292514,\, -1.4207485,\, 0) + (O)(\delta^{-1})\,,$$

as $\delta \to \infty$

- For the eigenvalues $\lambda^{(2)}$ and $\lambda^{(3)}$, $\lambda_0 = \pm i$, respectively. Therefore, proceeding as before, the equations $g(i,\, \lambda_1^{(2)}, x_0) = g(-i,\, \lambda_1^{(3)}, x_0) = 0$ provide expressions for $\lambda^{(k)}$, with $k = \{2,\, 3\}$. Thus, the relationship between $\lambda_1^{(k)}$ and x_0 is given by

  $$\lambda_1^{(k)} = -a\frac{9\left[9b^2(3b-8) + 12b(b-6)x_0 - 16x_0^2\right]}{2(4x_0 + 9b)}\,.$$

  At the Hopf bifurcation the linearised system has a pair of pure imaginary eigenvalues, therefore imposing $\lambda_1^{(k)} = 0$ defines the Hopf bifurcation points. Substituting this condition into the above equation and solving for values of the material parameters $a = 16/3$ and $b = -3/4$ we obtain two solution for x_0. Employing the relationships (5.44), (5.45) and (5.48) we have that, when $\delta \to \infty$, the Hopf bifurcations occur at

  $$(\tau^{H1};\, S_1^{H1},\, S_2^{H1},\, \theta^{H1}) = (-21.08088508;\, 1.297687237,\, -0.952312763,\, 0)\,,$$
  $$(\tau^{H2};\, S_1^{H2},\, S_2^{H2},\, \theta^{H2}) = (-10.71794304;\, 2.499187763,\, 0.249187763,\, 0)\,,$$

  where the script $H1$ corresponds to the Hopf bifurcation HB1 of the IPN branch and $H2$ to HB2 of the LRN branch. These values are in excellent agreement with the numerical results shown in figure 5.24.

From the above results we can also predict the linear stability of the system and confirm the results obtained by employing AUTO97 and shown in figure 5.24. When $S_1 < S_1^L$ then the system has a real negative eigenvalue and a conjugate pair with negative real part, therefore the system is linearly stable. At $S_1 = S_1^L$ the real eigenvalue passes through zero and thus for $S_1^L < S_1 < S_1^{H1}$ the real eigenvalue is positive and the system is unstable. At $S_1 = S_1^{H1}$ the complex pair of eigenvalues crosses the imaginary axis, from negative to positive values and the system remains unstable. The horizontal asymptote occurs at $S_1 = -9b/4$ and the real eigenvalue changes sign as also does the real part of the complex conjugate pair, therefore for $-9b/4 < S_1 < S_1^{H2}$ the real eigenvalue is negative and the complex conjugate pair has negative real part, thus the system is stable. However at $S_1 = S_1^{H2}$ the system changes its stability because at the Hopf bifurcation the complex pair crosses the imaginary axis from negative to positive and the system becomes unstable.

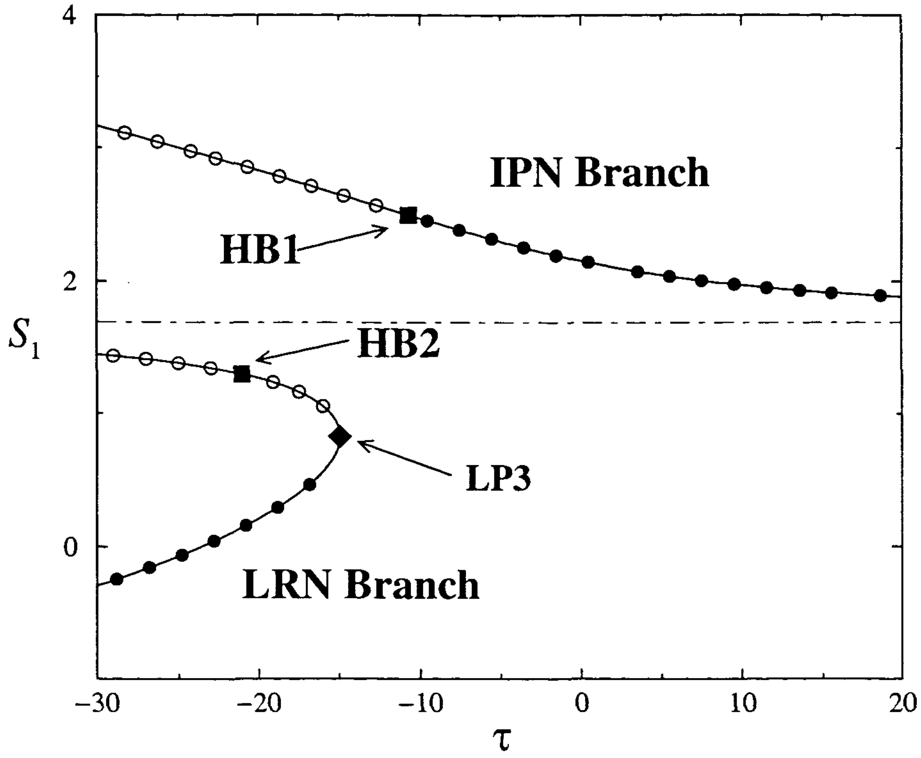

Figure 5.24: The solid line represents the analytical locus of the solution branches for $\delta \to \infty$. The points are the numerical results obtained by computing solution branches IPN and LRN for a fixed value of the dimensionless strain rate $\delta = 10^3$. The solid points are linearly stable states and the white points represent linearly unstable states. The dot-dashed line is the horizontal asymptote $S_1 = -9b/4$. The square symbols are the Hopf bifurcation points and the diamond symbol is the limit point of the LRN Branch.

5.5 The state diagram for the two dimensional case

In this section we summarise the behaviour of a liquid crystal in a shear flow for the two dimensional case. We have used AUTO97 to produce the state diagram shown in figure 5.25. Here we show in the (τ, δ)-space the locus of limit points, Hopf bifurcations and the boundary between tumbling and wagging for the two dimensional case, as explained in sections 5.3 and 5.4. In figure 5.25 the solid lines are the loci of the limit points LP1, LP2, LP3 and LP4 of the IPN Branch, the dashed line is the locus of the Hopf Bifurcation in the IPN Branch, and the dotted line is the locus of the boundary between the tumbling and the wagging state, the latter is not a feature of the bifurcation diagram but of the period of the orbits, as explained in section 5.3.3. The bold solid line is the locus of LP3 of the LRN Branch. All these loci divide the parameter space in six different regions where the liquid crystal behaves as follows

- $\boxed{1}$ The only stable state in this region is the in-plane flow-aligning nematic state of the IPN Branch. For very low strain rates this nematic phase is called paranematic state.

- $\boxed{2}$ This is a very small region which is shown in detail on section (a) of figure 5.25. It is bounded by the locus of the limit points LP1 and LP2 of the IPN Branch.

    - $\boxed{2\text{i}}$ Inside region 2, and to the right of the bold solid line two stable states co-exist: the nematic and paranematic phases of the IPN Branch.

    - $\boxed{2\text{ii}}$ This region is to the left of the bold solid line, and therefore the two stable in-plane nematic phases from the IPN Branch co-exist with the log-rolling state from the LRN Branch.

    - $\boxed{2\text{iii}}$ The stable solutions are those of the previous region: the in-plane paranematic and nematic phases and the log-rolling state. Crossing from region 2ii to 2iii different unstable states are generated, however the stable phases remain the same.

- $\boxed{3}$ There are two stable states in this area: the in-plane nematic state, from IPN Branch and the log-rolling state.

- $\boxed{4}$ This region is delimited by the locus of limit points LP3 and LP4 of IPN Branch. It is subdivided in three sub-regions, that are shown on section (b) of figure 5.25. The log-rolling state is a stable phase on every sub-region that we are describing here

- $\boxed{\text{4i}}$ The phase portrait for parameter values within this region accounts for an unstable node (disk-like distribution), a stable node (in-plane nematic phase) and a saddle, thus the only physically relevant solution is the in-plane nematic state.

- $\boxed{\text{4ii}}$ The phase portrait of this region accounts for a unstable node and two stable nodes. One of them evolves into a centre on the locus of the Hopf bifurcation, dashed line of figure 5.25), generating the periodic solutions that will appear on the following sub-region. The selection of one of the stable states by the system is determined by the initial conditions.

- $\boxed{\text{4iii}}$ This region is bounded to the right by the locus of the Hopf bifurcation from where the time dependent periodic solutions on this sub-region generate. This stable limit cycles co-exist with the in-plane nematic state. The period of the time dependent solutions increases as we approach the left boundary, the saddle homoclinic bifurcation, where the period is infinite and the limit cycle breaks down, leaving on the sub-region 4i the stable and unstable nodes and the saddle point mentioned above.

$\boxed{5}$ From crossing from region 4i to region 5 time-dependent solutions are generated. This occurs on the boundary between both regions through a saddle-node homoclinic bifurcation, that has been explained in section 4.3.3.

$\boxed{6}$ This is the small region where the liquid crystal is wagging. For more details on the relationship between tumbling and wagging see sections 5.3.2 and 5.3.3.

It is important to remark that the Hopf Bifurcation and the limit point of the LRN Branch both present vertical asymptotes in the $(\tau,\ \delta)$-space as predicted by the large δ analysis. In figure 5.26 the Hopf Bifurcation branch (HB) and the limit point (LR) are plotted simultaneously with the vertical asymptotes found analytically in section 5.4.2. A similar bifurcation diagram has been described by Chaubal et al. [33] using the Hinch and Leal closure of the Doi's model for liquid crystal polymers (LCP), and also by Maffettone et al. using their own closure of Doi's model [34]. Their results are qualitatively similar to ours in terms of the control parameters of their system: the Maier-Saupe nematic potential (the intensity) and the shear rate. Subsequently Maffettone and Crescitelli [31] described the bifurcation diagram for the exact Doi's model, finding similar results to those of the previous references, however, their study does not account for the log-rolling regime, which is an out-of plane feature of the two-dimensional case.

Our analysis of the dynamics of a liquid crystal under a shear flow shows that the

Landau-de Gennes model captures the behaviour of a liquid crystal under shear flow in the two dimensional case observed experimentally [36], and it is comparable to similar analysis done for lyotropic liquid crystal polymers [31, 29, 45, 34, 33].

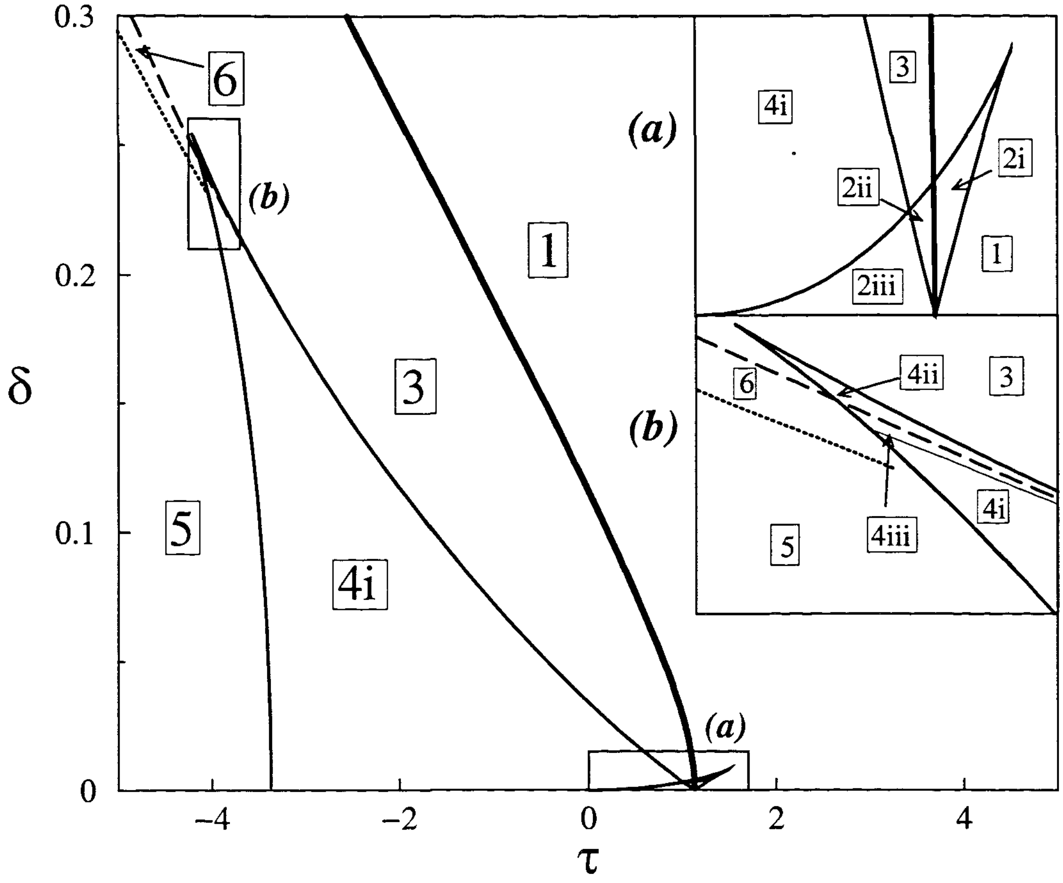

Figure 5.25: The solid line is the locus in the (τ, δ)-space of the limit points LP1, LP2, LP3, and LP4 of the IPN Branch, the bold solid line is the locus of the limit point LP3 of the LRN Branch. The dashed line is the locus of the Hopf-Bifurcation branch of IPN and the dotted line is the boundary between tumbling and wagging regimes. The behaviour of the liquid crystals in the different labelled regions is explained in detail on the text.

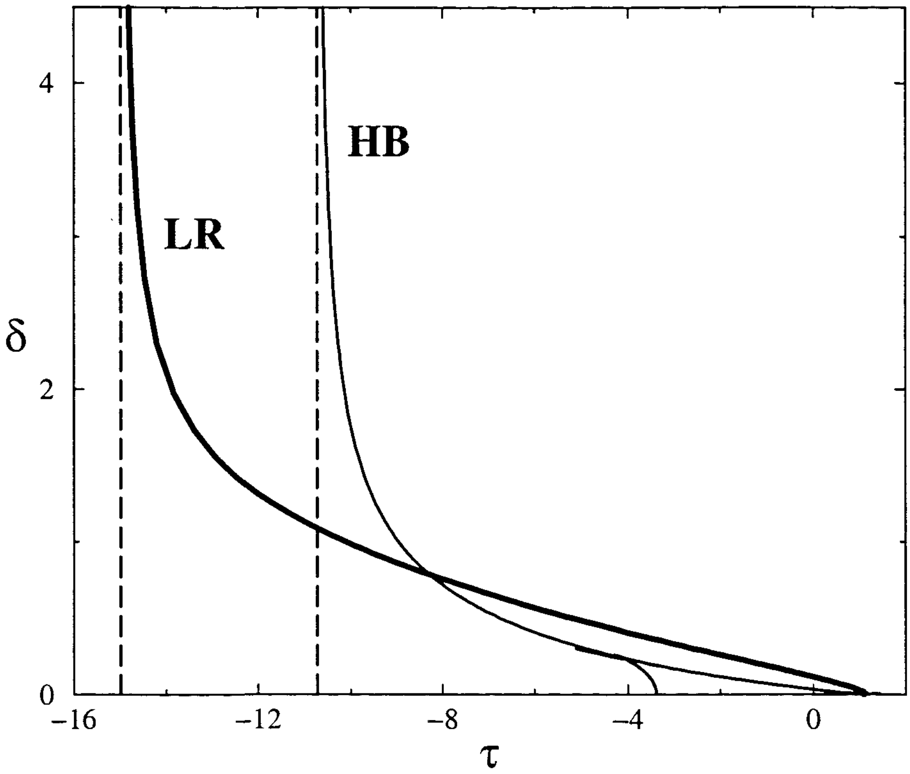

Figure 5.26: The solid line (HB) is the locus of the Hopf-bifurcation of our system, while the bold solid line (LR) is the locus of the boundary of the log-rolling state. The dashed lines are the analytical values of the vertical asymptotes calculated on section 5.4.2.

Chapter 6

A nematic liquid crystal under a general flow

In this chapter we consider the effects of a general planar homogeneous flow on the dynamics of a nematic liquid crystal and explain the effects of the strain and the vorticity on the behaviour of a liquid crystal in the two dimensional case. The strain favours the alignment of the liquid crystal with the flow, while vorticity favours the time dependent tumbling state. A similar analysis was done by Chaubal et al. [33] in order to compare different closure approximations of the Doi model for the dynamics of liquid crystalline polymers.

6.1 Decomposition of the flow into strain and vorticity

The velocity gradient of a shear flow is given by $\mathbf{L}_0 = \mathbf{D}_0 + \mathbf{W}_0$, where the strain tensor $\mathbf{D}_0$ is

$$\mathbf{D}_0 = \frac{\delta}{2}\begin{pmatrix} 0 & 1 & 0 \\ 1 & 0 & 0 \\ 0 & 0 & 0 \end{pmatrix},$$

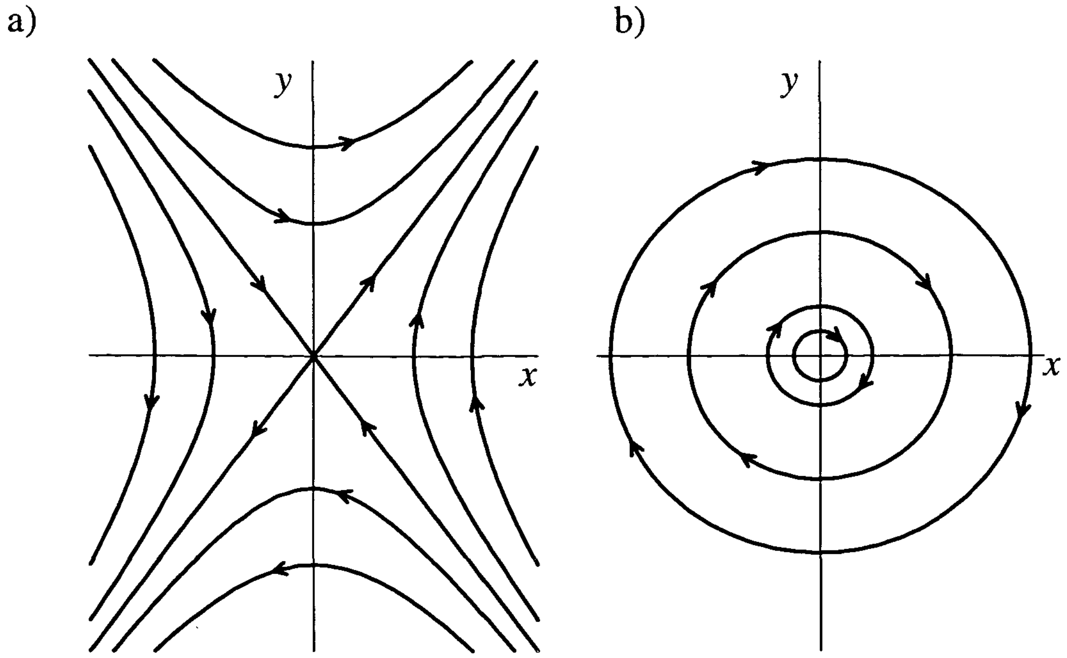

Figure 6.1: Planar homogeneous flows. Figure a) corresponds to a flow with $0 < \alpha < 1$, where the magnitude of the strain rate exceeds that of the vorticity. Figure b) represents a flow with $-1 < \alpha < 0$, where the vorticity is larger than the strain rate.

and the vorticity tensor is given by

$$\mathbf{W}_0 = \frac{\delta}{2}\begin{pmatrix} 0 & 1 & 0 \\ -1 & 0 & 0 \\ 0 & 0 & 0 \end{pmatrix}.$$

A general planar homogeneous flow is described by the following velocity gradient

$$\mathbf{L}_\alpha = (1+\alpha)\mathbf{D}_0 + (1-\alpha)\mathbf{W}_0\,, \tag{6.1}$$

with $|\alpha| \leq 1$, where $\alpha = 0$ corresponds to the shear flow, $\alpha = -1$ to the absence of strain in the flow, and $\alpha = 1$ to the absence of vorticity in the flow. For $0 < \alpha < 1$ the magnitude of the strain rate exceeds that of the vorticity and the flow is qualitatively similar to that shown in figure 6.1a). When $-1 < \alpha < 0$ (figure 6.1b)) the magnitude of the vorticity exceeds that of the strain rate. The velocity field associated to the flow described by (6.1) is

$$\mathbf{v} = \delta(y\mathbf{i} + \alpha x\mathbf{j})\,, \tag{6.2}$$

where $\mathbf{i}$ and $\mathbf{j}$ are the unit vectors in the x and y direction respectively.

We model the behaviour of a nematic liquid crystal under a general flow by using the model described in chapter 3 and given by the momentum equation, (3.1), the incompressibility condition (3.2) and an equation for the dynamics of the order tensor parameter, equation (3.48). Considering the velocity field (6.2) the linear momentum equation, (3.1), is not satisfied when $\alpha \neq 0$, since the divergence of the stress tensor is zero but the material derivative of the velocity is given by

$$\frac{D\mathbf{v}}{Dt} = \alpha(x,\, y,\, 0)^T\,,$$

which is zero only when $\alpha = 0$. However, an analysis of the equation of the evolution of the order parameter, (3.48), will provide understanding of the influence of the strain rate and the vorticity in the dynamics of the system.

We consider then the non-dimensionalised form of the equation for the motion of the order parameter given by (5.3), with $\mathbf{Q} = 3S_1(\mathbf{n}\otimes\mathbf{n} - \mathbf{I}/3)/2 + S_2(\mathbf{m}\otimes\mathbf{m} - \mathbf{l}\otimes\mathbf{l})/2$, equation (2.6), and the liquid crystal confined to a planar configuration as shown in figure 5.1. We re-scale the equation by using (2.8)-(2.10) and considering a planar homogeneous flow, (6.1), equation (5.3) can be re-written in components as follows

$$\begin{aligned}
\dot{S}_1 &= -\frac{9\delta\beta_1}{4\widetilde{B}}(1+\alpha)\sin 2\theta \\
&\quad -\frac{\widetilde{B}^2}{27}\left(\tau S_1 - 3S_1^2 + 9S_2^2 + 2S_1(S_1^2 + 3S_2^2)\right)\,, &(6.3)\\
\dot{S}_2 &= \frac{3\delta\beta_1}{4\widetilde{B}}(1+\alpha)\sin 2\theta \\
&\quad -\frac{\widetilde{B}^2}{27}\left(\tau S_2 + 6S_1S_2 + 2S_2(S_1^2 + 3S_2^2)\right)\,, &(6.4)\\
\dot{\theta} &= \frac{\delta}{2}\left(3\beta_1(1+\alpha)\frac{\cos 2\theta}{\widetilde{B}(S_2 - S_1)} - 1 + \alpha\right)\,. &(6.5)
\end{aligned}$$

When $\alpha = 0$ this system corresponds to (5.4)-(5.6), and its solutions have been studied in chapter 5. A similar analysis with $\alpha \in [-1,\, 1]$ will help to understand the influence of vorticity and strain rate in the dynamics of a liquid crystal.

6.1.1 Pure vorticity. $\alpha = -1$

When $\alpha = -1$ the correspondent velocity gradient is $L_{-1} = 2W_0$, and therefore the flow only accounts for vorticity. The system (6.3)-(6.5) re-writes as

$$\begin{aligned}
\dot{S}_1 &= -\frac{\widetilde{B}^2}{27}\left(\tau S_1 - 3S_1^2 + 9S_2^2 + 2S_1(S_1^2 + 3S_2^2)\right)\,, &(6.6)\\
\dot{S}_2 &= -\frac{\widetilde{B}^2}{27}\left(\tau S_2 + 6S_1S_2 + 2S_2(S_1^2 + 3S_2^2)\right)\,, &(6.7)\\
\dot{\theta} &= -\delta\,. &(6.8)
\end{aligned}$$

The steady state solutions of this system in the absence of flow, i.e., $\delta = 0$, correspond to those found for the case $\alpha = 0$. They have been explained in detail in section 5.2.1 and shown in figure 2.4. Summarising, the stable states are

(a) an isotropic state with $S_1 = S_2 = 0$ and positive dimensionless temperature, τ. The distribution function in this state is an sphere as shown in figure 6.2(a);

(b) an elongated uniaxial nematic state with in-plane preferred direction occurring when $\tau < 9/8$. It is shown in figure 6.2(b). This state has two different representations corresponding to the selection of $\mathbf{n}$ or $\mathbf{m}$ as distinguished directions;

(c) an elongated uniaxial nematic state with the preferred direction perpendicular to the shear plane. An sketch of the distribution function is shown in figure 6.2(c). This is the so-called log-rolling state and occurs for values of τ smaller than 9/8.

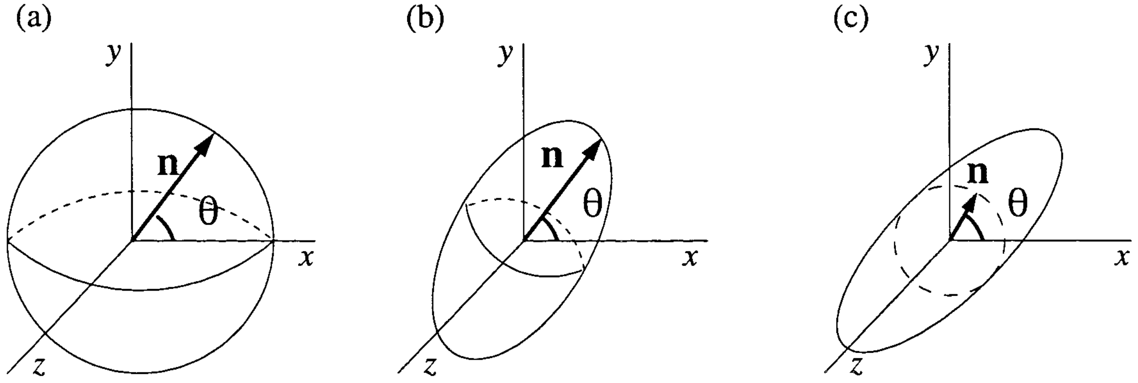

Figure 6.2: Figure (a) represents the distribution function of the isotropic state. It is invariant under rotations of the director vector $\mathbf{n}$. Figure (b) represents the distribution function of the in-plane nematic state. When θ decreases the liquid crystal tumbles. Figure (c) is the distribution function of the log-rolling state, which is invariant under rotations in the xy-plane.

In these three stable solutions the director angle θ remains undetermined.

When the flow is introduced in the system, i.e. $\delta \neq 0$, the system (6.6)-(6.8) decouples into a two dimensional system in S_1 and S_2, with steady states described above, and a equation for the angle θ, (6.8). When $\delta \neq 0$, the latter equation does not provide any stationary state, and the only possible solution is a time dependent tumbling state with the director angle θ decreasing continuously on time. However, for the isotropic and log-rolling states rotations of the director vector $\mathbf{n}$ do not change the steady states since their distribution functions are both invariant under rotations in the xy-plane, as it can be seen in figures 6.2(a) and 6.2(c). The rotation of the in-plane nematic, figure 6.2(b), produces the tumbling solutions. The state diagram for the case $\alpha = -1$, figure 6.3, shows three vertical bands with different behaviours: when $\tau > 9/8$ the only stable state is the isotropic state. When $0 < \tau < 9/8$ the isotropic state coexists with a log-rolling state and a in-plane tumbling state. For negative τ the isotropic state loses its stability and the only stable solutions are the log-rolling and the tumbling states. Thus the vorticity favours the appearance of the tumbling regime for $\tau < 9/8$.

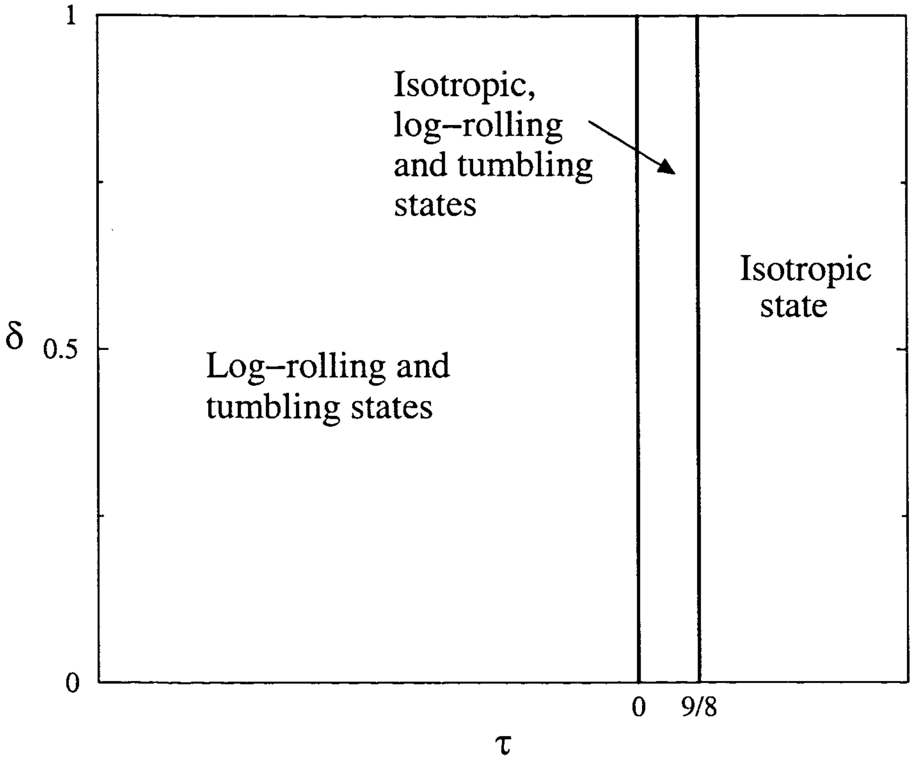

Figure 6.3: Steady state in the case $\alpha = -1$. The parameter space is divided in three vertical bands with different stable states in each one of them.

6.1.2 Pure strain. $\alpha = 1$

When $\alpha = 1$ the flow consists of a pure strain and the velocity gradient is given by $\mathbf{L}_1 = 2\mathbf{D}_0$. For this value of α the system (6.3)-(6.5) becomes

$$\dot{S}_1 = -\frac{9\delta\beta_1}{2\widetilde{B}}\sin 2\theta - \frac{\widetilde{B}^2}{27}\left(\tau S_1 - 3S_1^2 + 9S_2^2 + 2S_1(S_1^2 + 3S_2^2)\right), \tag{6.9}$$

$$\dot{S}_2 = \frac{3\delta\beta_1}{2\widetilde{B}}\sin 2\theta - \frac{\widetilde{B}^2}{27}\left(\tau S_2 + 6S_1S_2 + 2S_2(S_1^2 + 3S_2^2)\right), \tag{6.10}$$

$$\dot{\theta} = \frac{3\delta\beta_1}{\widetilde{B}(S_2 - S_1)}\cos 2\theta\,. \tag{6.11}$$

When there is no flow present in the system, i.e. $\delta = 0$, the steady states are those described in the previous section. When $\delta \neq 0$ we obtain, from equation (6.11), that the steady state solution satisfies $\cos 2\theta = 0$ and hence $\theta = \pm\pi/4$. Figure 6.4 shows the solution branches in the $(\tau,\, S_1)$-space for a fixed value of the strain rate $\delta = 5 \times 10^{-3}$. These branches have been computed using AUTO97 for values of the material parameter $\widetilde{B} = -1.2$ and $\beta = 0.9$. We observe the existence of four physically distinctive solution branches (two for $\theta = \pi/4$ and two for $\theta = -\pi/4$) that have been labelled in figure 6.4 as N,YDL, ZDL and LR.

- The solution branch labelled as N in the figure links a stable paranematic state at positive temperatures to a stable in-plane nematic solution that remains stable as $\tau \to -\infty$. Along this branch θ is constant and equal to $\pi/4$;
- the solution YDL links, as S_1 increases, an unstable nematic state to an unstable disk-like distribution function in the xy-plane. The angle θ is $-\pi/4$ along this branch. Due to its instability this solution branch is physically irrelevant.
- Along the ZDL branch $\theta = -\pi/4$. This solution links, as S_1 increases, two unstable states: a paranematic state to a disk-like distribution in the xz-plane;
- finally the LR branch links an unstable disk-like distribution to the stable log-rolling state. On this branch $\theta = \pi/4$.

We observe in the state diagram, figure 6.5 that the only stable states are a log-rolling state and the in-plane nematic state aligning at a $\pi/4$ angle with the horizontal axis.

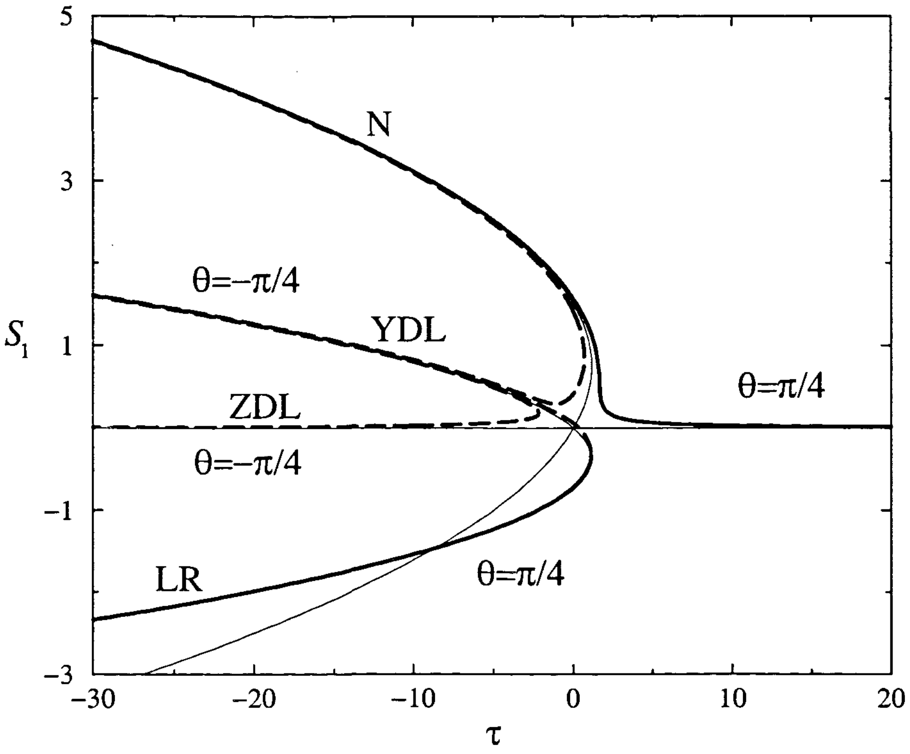

Figure 6.4: Solution branches of the system (6.9)-6.11) for a fixed value of the strain rate $\delta = 5. \times 10^{-3}$. In this case there is no vorticity present in the system. The four branches N, ZDL, YDL, and LR have been computed using AUTO97 for values of the material parameters $\widetilde{B} = -1.2$, $\beta_1 = 0.9$. Solid lines indicate stable states and dashed lines linearly unstable states.

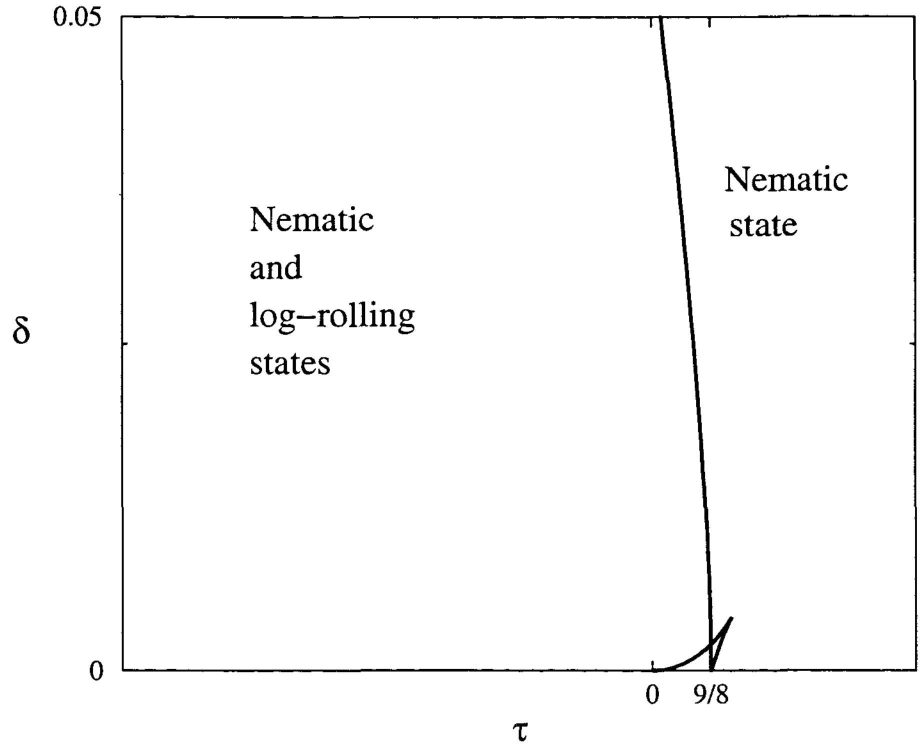

Figure 6.5: State diagram for the case $\alpha = 1$. The vertical line marks the origin of the log-rolling state. The small region is a region where a paranematic and a flow aligning nematic state co-exist.

6.1.3 The influence of strain rate and vorticity

We consider now the parameter $\alpha \in (-1, 1)$ and study the behaviour of the solution branches as α varies. The analysis of the solutions in the shear flow case, $\alpha = 0$, shows the relevance of the existence of a fixed point solution on the IPN branch to determine the location in the system of time dependent behaviour for very small strain rate: see section 5.3.1.1. Therefore, extending this result to the $\alpha \in (-1,\ 1)$ case, we calculate the fixed point of the system by substituting $\theta = S_2 = 0$ in (6.3)-(6.5) and find that it occurs at

$$\tau = \tau^* = \frac{9\beta_1(\alpha+1)}{\widetilde{B}^2(\alpha-1)}\left(\widetilde{B}(\alpha-1) - 2\beta_1(\alpha+1)\right),\ S_1 = S_1^* = \frac{3\beta_1(\alpha+1)}{\widetilde{B}(\alpha-1)},$$

with $\tau^* = 3S_1^* - 2(S_1^*)^2$ and $S_1^* > 0$. The behaviour of τ^* and S_1^* depending on α is shown in figure 6.6 for values of the material parameters $\beta_1 = 0.9$ and $\widetilde{B} = -1.2$. We distinguish two regions of behaviour: when $-1 < \alpha \leq -1/2$, the fixed point of the system occurs on $S_1^* = (3 - \sqrt{9 - 8\tau^*})/4$, while when $-1/2 \leq \alpha < 1$ it occurs on $S_1^* = (3 + \sqrt{9 - 8\tau^*})/4$. We will study the solution branches for $\alpha = -0.6$ and $\alpha = 0.6$ as representative behavior for the cases $0 < \alpha \leq -1/2$ and $-1/2 < \alpha < 1$, respectively.

6.1.3.1 Solutions for $\alpha = -0.6$

For $\alpha = -0.6$ and values of the material parameters $\beta_1 = 0.9$ and $\widetilde{B} = -1.2$ there are two physically different solution branches, as also occurs for $\alpha = 0$: the IPN branch, where the steady stable solution is an in-plane nematic-state and the LRN Branch where the stable solution is the log-rolling nematic state. These branches, computed using AUTO97 are shown in figures 6.7a) and 6.7b), respectively. Figure 6.7a) shows the IPN Branch for two different values of the shear rate: branch (a) has been computed with $\delta = 10^{-2}$, while curve (b) has $\delta = 10^{-1}$. The IPN branch represents the in-plane nematic state at positive values of τ. This curve has two limit points, L$_1$ and L$_2$, as can be seen in curve (a) of figure 6.7a). As δ increases these limit points come closer together to eventually merge at a critical value of the strain rate $\delta^c = 1.286372 \times 10^{-2}$. For larger values of the strain rate a Hopf bifurcation is created from where periodic solutions originate, curve (b) of figure 6.7a) is an example of this behaviour. The locus of the limit points and the Hopf bifurcation of the IPN branch is shown in figure 6.8. The existence of a Takens-Bogdanov bifurcation is observed here, and it occurs at $(\tau^{\mathrm{TB}}, \delta^{\mathrm{TB}}) = (1.150255, 1.255476 \times 10^{-2})$.

Figure 6.7b) shows the LRN branch for values of the strain rate $\delta = 10^{-2}$ in branch (a) and $\delta = 10^{-1}$ in branch (b). This branch is qualitatively similar to the LRN branch in the shear flow case, that has been described in detail in section 5.4. The limit point L_3 determines the beginning of the stable log-rolling state.

The state diagram for $\alpha = -0.6$ is shown in figure 6.9. Here we can distinguish seven regions of behaviour of the nematic liquid crystal.

$\boxed{1}$ In this region the only stable state is the in-plane paranematic state;

$\boxed{2}$ this small region can be seen in the blow-up of figure 6.9. It is bounded by the locus of L_2 and L_1 of IPN branch, however the only stable state of this region is the in-plane paranematic state as in region 1;

$\boxed{3}$ this region is to the left of the limit point L_3 of the log-rolling branch, labelled LR in the figure. Thus the paranematic state co-exists with the log-rolling state;

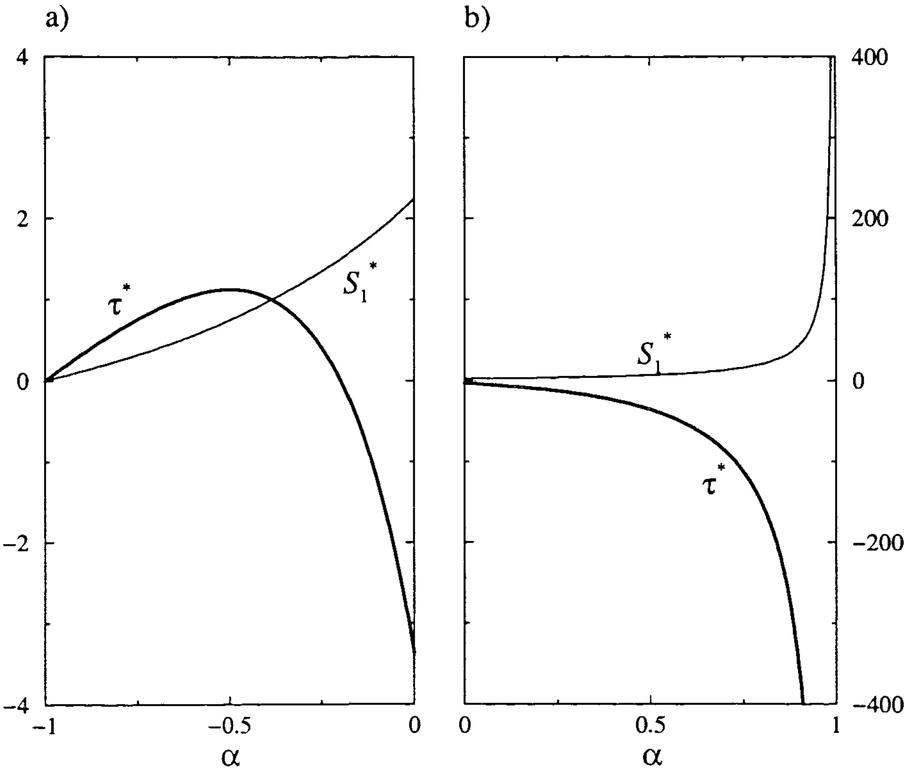

Figure 6.6: Locus of the fixed point of the system for different values of α. Figure a) shows the locus of the dimensionless temperature and uniaxial order parameter at the fixed point, τ^* and S_1^* respectively, for $-1 \leq \alpha \leq 0$. Figure b) represents the values of τ^* and S_1^* the fixed point for $0 \leq \alpha \leq 1$.

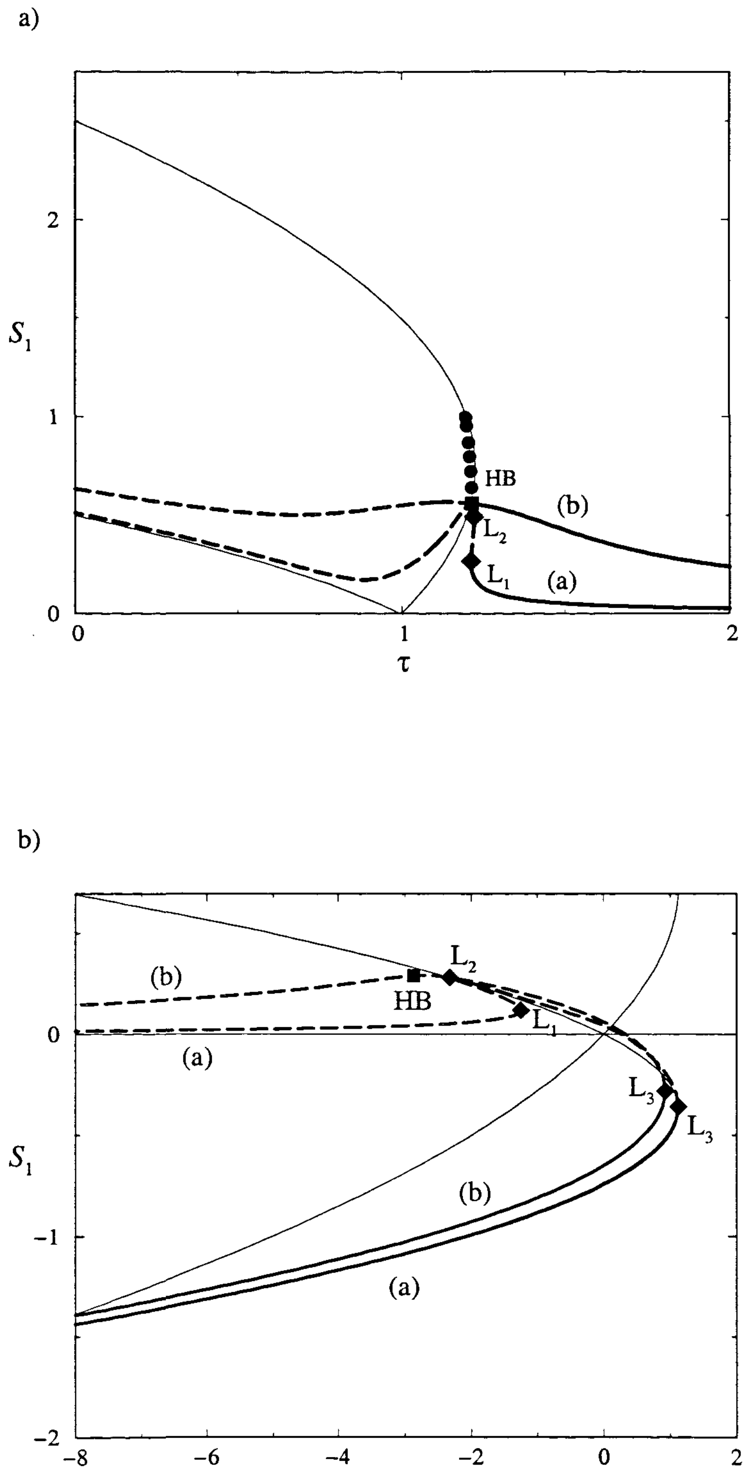

Figure 6.7: Solution branches computed using AUTO97 for values of the material parameters $\widetilde{B} = -1.2$ and $\beta = 0.9$. Figure a) shows the IPN branch and figure b) the LRN branch. The curves have been calculated for fixed values of the strain rate: $\delta = 10^{-2}$ in curve (a), and $\delta = 10^{-1}$ in curve (b). The solid lines indicate stable states and the dashed lines unstable states. The solid circles in figure a) are the time dependent periodic solutions. The diamonds are limit points and the square points mark Hopf-bifurcations.

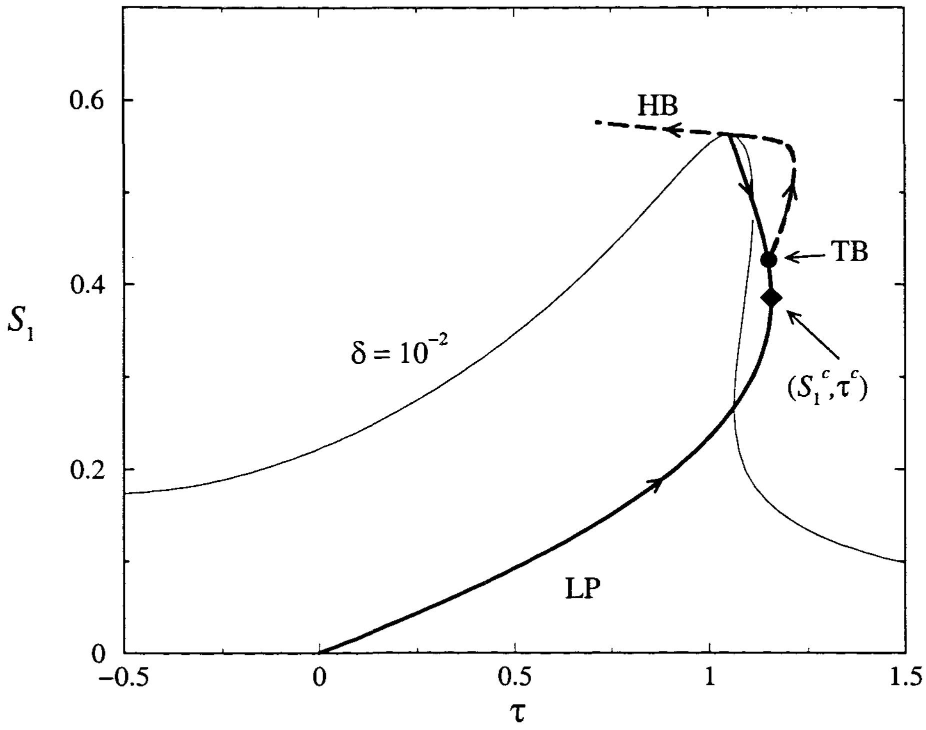

Figure 6.8: The locus of the limit points L_1 and L_2 of the IPN branch with $\alpha = -0.6$ is plotted with a thick solid line. The dashed line is the locus of the Hopf Bifurcation. The solid point marks the Takens-Bogdanov bifurcation and the diamond corresponds the point where the two limit points merge. The thin line is the IPN branch for a fixed strain rate $\delta = 10^{-2}$. The arrows indicate the direction of increasing δ. The material parameters are $\widetilde{B} = -1.2$ and $\beta_1 = 0.9$.

$\boxed{4}$ in this region the paranematic state co-exists with time dependent orbits (tumbling/wagging states). For values of δ smaller than δ^{TB} the periodic solution generates at a saddle-node bifurcation occurring at L_2, while for $\delta \geq \delta^{\mathrm{TB}}$ the periodic solutions originate at the Hopf bifurcations (branch labelled HB in the figure);

$\boxed{5}$ in this region the stable states described in region 4 exist together with the log-rolling state from the LRN branch;

$\boxed{6}$ the tumbling/wagging states are the stable solutions here since the paranematic state loses its stability at the Hopf Bifurcation from where the periodic solutions originate. The boundary between tumbling and wagging has not been computed for this value of α, however the behaviour is similar to that described in 5.3.3 for the shear flow case;

$\boxed{7}$ this region accounts for the same stable states as region 6, together with the log-rolling state.

6.1.4 Solutions for $\alpha = 0.6$

When $\alpha > -0.5$ the behaviour of the liquid crystal is qualitatively similar to that of the shear flow case $\alpha = 0$, but when $-0.5 < \alpha < 0$ the fixed point of the system occurs at higher temperatures than for the shear flow case while when $0 < \alpha < 1$ it occurs at lower temperatures.

Figure 6.10 shows the two physically distinctive solution branches of the system (6.3)-(6.5) computed using values of the parameters $\alpha = 0.6$, $\beta_1 = 0.9$ and $\widetilde{B} = -1.2$.

Figure 6.10a) shows the IPN branch for values of the shear rate $\delta = 1.0$ and $\delta = 10.0$. It is observed that higher shear rates than in the shear flow case are necessary for the appearance of a Hopf-bifurcation. In particular the Takens-Bogdanov bifurcation occurs at $(\tau^{\mathrm{TB}}, \delta^{\mathrm{TB}}) = (-1.356096 \times 10^2, 5.237895)$.

Figure 6.10b) shows the LRN branch computed with a fixed strain rate $\delta = 0.1$. The limit point L_3 marks the beginning of the log-rolling state.

A physical description of the IPN and LRN branches has been previously given for the shear flow case in sections 5.3 and 5.4, respectively.

Figure 6.11 shows the state diagram for $\alpha = 0.6$, which is qualitatively similar to the state diagram when $\alpha = 0$, shown in figure 5.25 of section 5.5, but in figure 6.11 the region of multistability near the origin is not noticeable since it occurs for very small

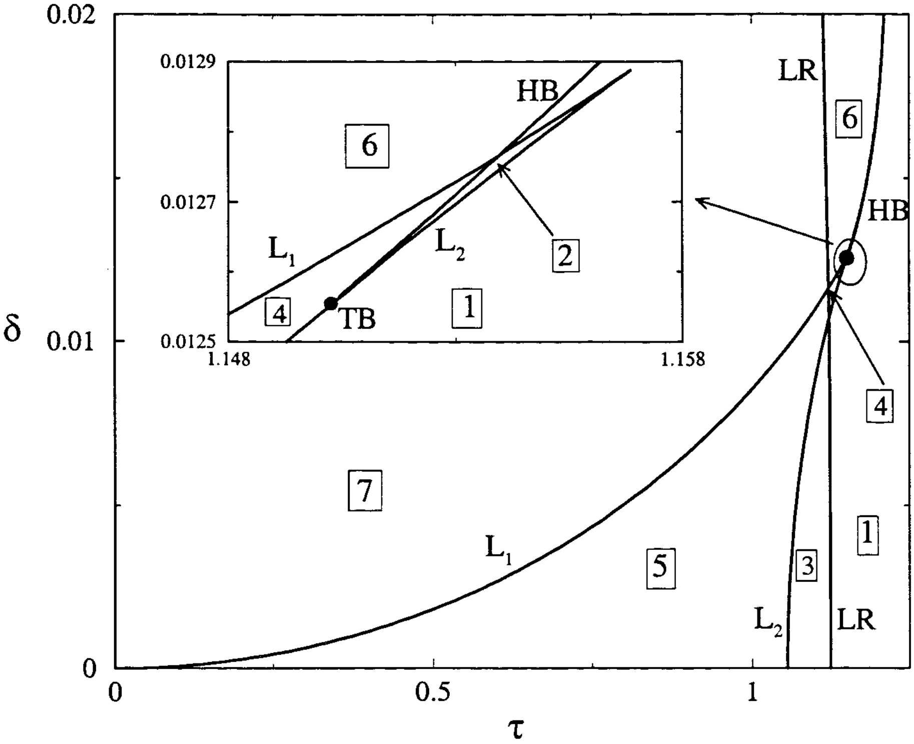

Figure 6.9: State diagram for $\alpha = -0.6$ and values of the material parameters $\widetilde{B} = -1.2$ and $\beta = 0.9$. The stable states in every region are described in the text. The inset figure is a blow-up of the circled region. The L_1 and L_2 branches determine the locus of the limit points of the IPN branch. The branch labelled HB is the locus of the Hopf bifurcation of the IPN branch and its Takens-Bogdanov bifurcation is labelled as TB. The locus of the limit point L_3 of the LRN branch is labelled LR.

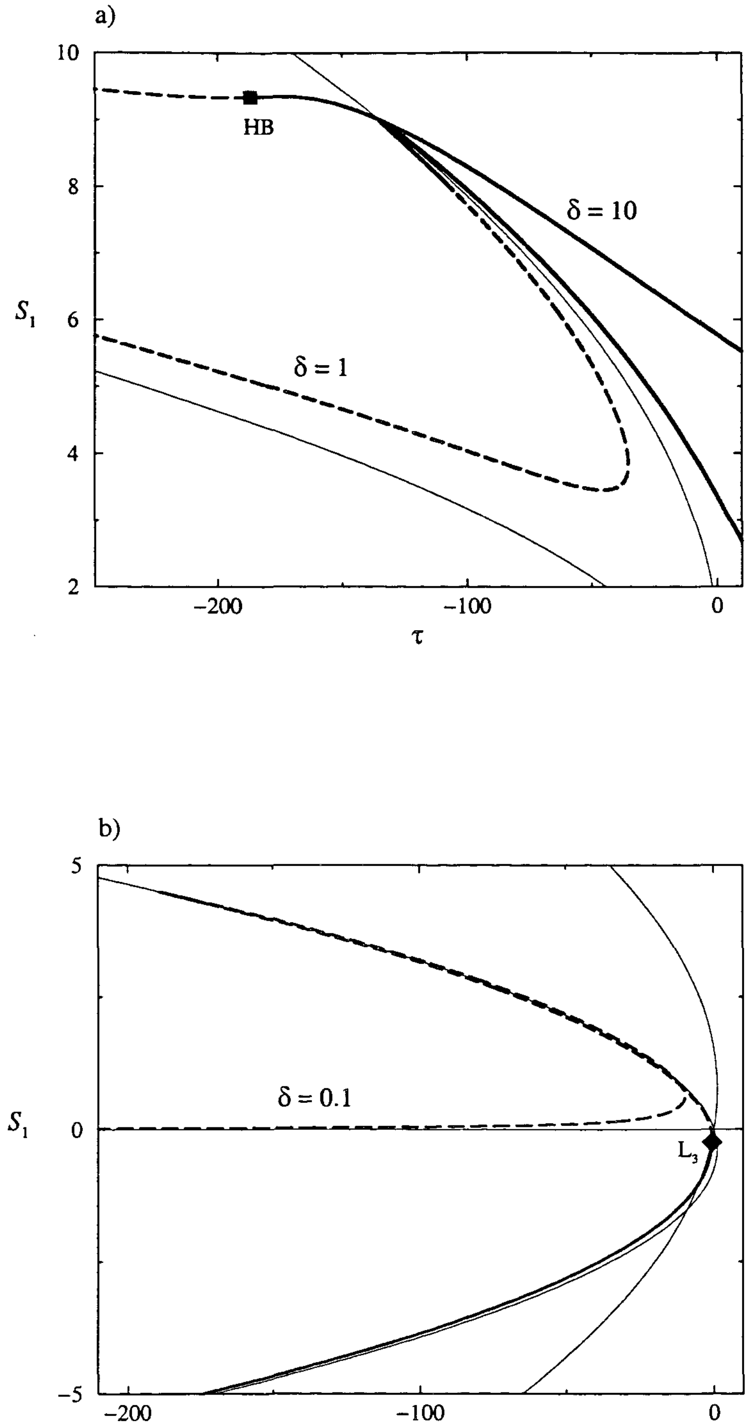

Figure 6.10: Figure a) shows the IPN solution branch computed for strain rates $\delta = 1.0$ and $\delta = 10$. The solid square in this figure marks a Hopf bifurcation (HB) from where periodic solutions originate. Figure b) shows the LRN solution branch for $\delta = 0.1$, and the diamond point is the limit point L_3, that indicates the beginning of the log-rolling solution. Solid lines in the figures indicate stable states while dashed lines are unstable solutions. The material parameters are $\beta = 0.9$ and $\widetilde{B} = -1.2$.

values of the strain rate. In this case we have not computed the locus of the homoclinic bifurcation nor the tumbling/waging boundary, but they could be calculated as done in the $\alpha = 0$ case.

From the results shown in this chapter of the computations of the solution branches of

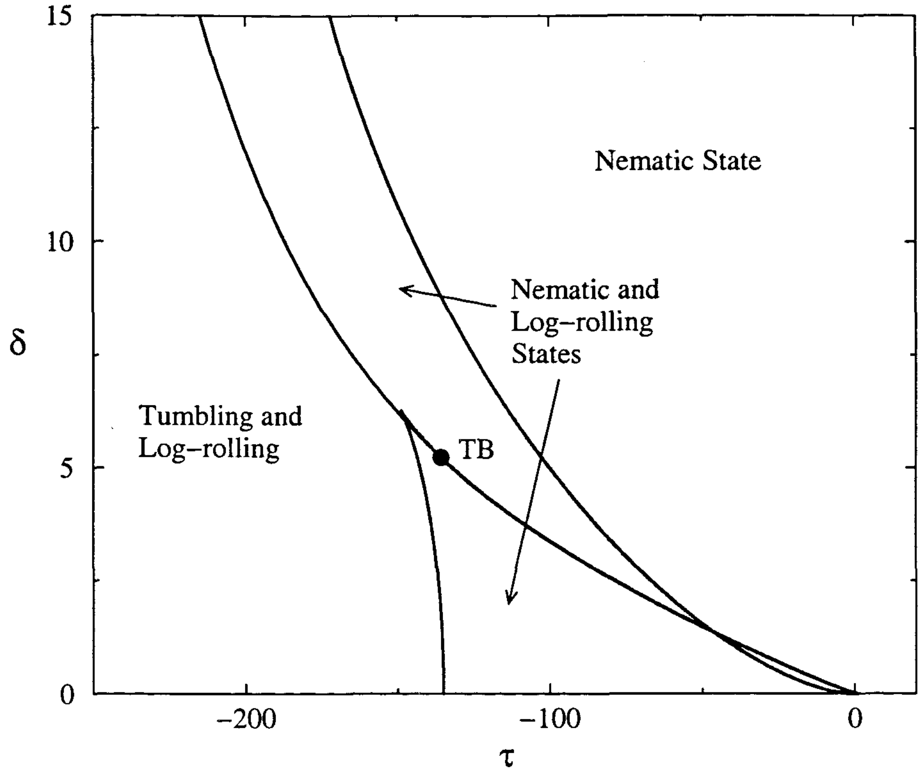

Figure 6.11: State diagram for $\alpha = 0.6$ and values of the material parameters $\widetilde{B} = -1.2$ and $\beta = 0.9$. The solid point indicates the Takens-Bogdanov bifurcation.

the system (6.3)-(6.5) for different values of α, we conclude that the prevalence of strain rate over vorticity in the planar homogeneous flow favours the in-plane nematic state over the time dependent regimes of a liquid crystal, while a flow with stronger vorticity allows the appearance of tumbling and wagging solutions at lower temperatures. The aligment of a nematic liquid crystal for pure strain rate occurs at a $\pi/4$ angle with respect to the positive x-axis and when the type of flown is changed, the strain will favour the aligment of the system always at an angle close to $\pi/4$. The existence of a stable log-rolling nematic state is independent of the type of planar homogeneous flow.

Chapter 7

The three dimensional problem

In this section we give a detailed description of the behaviour of a liquid crystal in a shear flow allowing for three dimensional behaviour.. The steady states are the in-plane nematic state and the log-rolling solution, which is only stable for very small values of the shear rate. We also show in this chapter that the only steady out-of-plane solution of this model are anomalous continua of equilibria, which shows that the Landau-de Gennes theory is structurally unstable [49].
The time dependent states are the so-called tumbling, wagging and kayaking solutions which exist in different regions of the parameter space.

7.1 Governing equations

We will consider a three dimensional system so that the director of the liquid crystal may lie out of the shear plane. Therefore the distribution function will be described by the two scalar order parameters, S_1 and S_2, and the three angles which determine the principle directions of the distribution function with respect to the Cartesian coordinates, or, otherwise, by the five independent components of the order tensor parameter. For simplicity in this chapter we write the order tensor parameter with respect to the Cartesian frame of reference as

$$\mathbf{Q} = \begin{pmatrix} q_1 & q_3 & q_4 \\ q_3 & q_2 & q_5 \\ q_4 & q_5 & -q_1 - q_2 \end{pmatrix} .$$

As done for the two dimensional case in chapter 5, we consider a homogeneous nematic liquid crystal under a shear flow with an associated velocity field given by $\mathbf{v} = Dy\,\mathbf{i}$ ($D > 0$), and model the behaviour of the nematic liquid crystal by using the Landau-de Gennes theory described previously in section 3.1. Considering this configuration the incompressibility condition (3.2) and the linear momentum equation (3.1) are automatically satisfied, while the dimensionless equation for the dynamics of the order parameter, (5.3), can be re-scaled by

$$\begin{aligned} \overline{\mathbf{Q}} &= -\frac{18}{\widetilde{B}}\mathbf{Q}\,, & (7.1)\\ \bar{\tau} &= \frac{27}{\widetilde{B}^2}\tau\,, & (7.2) \end{aligned}$$

which sets the isotropic-nematic transition temperature to the unity. Dropping the overlines the independent components of the tensor equation, (5.3), are

$$\begin{aligned} \dot{q}_1 &= \delta q_3 - \frac{\widetilde{B}^2}{162}\left[6\tau q_1 - 3(q_1^2 + q_3^2 + q_4^2) + 6(q_2^2 + q_5^2 + q_1 q_2) + q_1\kappa\right]\,, & (7.3)\\ \dot{q}_2 &= -\delta q_3 - \frac{\widetilde{B}^2}{162}\left[6\tau q_2 - 3(q_2^2 + q_3^2 + q_5^2) + 6(q_1^2 + q_4^2 + q_1 q_2) + q_2\kappa\right]\,, & (7.4)\\ \dot{q}_3 &= \frac{\delta}{2}\left(q_2 - q_1 - 18\frac{\beta_1}{\widetilde{B}}\right) - \frac{\widetilde{B}^2}{162}\left[6\tau q_3 - 9(q_1 q_3 + q_2 q_3 + q_4 q_5) + q_3\kappa\right]\,, & (7.5)\\ \dot{q}_4 &= \frac{\delta}{2}q_5 - \frac{\widetilde{B}^2}{162}\left[6\tau q_4 - 9(q_3 q_5 - q_2 q_4) + q_4\kappa\right]\,, & (7.6)\\ \dot{q}_5 &= -\frac{\delta}{2}q_4 - \frac{\widetilde{B}^2}{162}\left[6\tau q_5 - 9(q_3 q_4 - q_1 q_5) + q_5\kappa\right]\,, & (7.7) \end{aligned}$$

where $\kappa = q_1^2 + q_2^2 + q_3^2 + q_4^2 + q_5^2 + q_1 q_2$.

When $q_4 = q_5 = 0$ the three dimensional case reduces to two dimensions, and we can establish a correspondence between $\{q_1,\, q_2,\, q_3\}$ and the sets of variables described in sections 5.1 and 5.3.3: $\{S_1,\, S_2,\, \theta\}$ and $\{\eta,\, \mu,\, \nu\}$, respectively. The relationships are

$$\begin{aligned} q_1 &= \eta + \sqrt{3}\mu = S_1(1 + 3\cos 2\theta) + 3S_2(1 - \cos 2\theta)\,, & (7.8)\\ q_2 &= \eta - \sqrt{3}\mu = S_1(1 - 3\cos 2\theta) + 3S_2(1 + \cos 2\theta)\,, & (7.9)\\ q_3 &= \sqrt{3}\nu = 3(S_1 - S_2)\sin 2\theta\,. & (7.10) \end{aligned}$$

7.2 Steady state solutions

In this section we compute the steady solutions of the three dimensional system (7.3)-(7.7) and analytically corroborate some of the results.

7.2.1 Description of the solution branches

Figure 7.1 shows the steady state solution of the system (7.3)-(7.7) computed using the continuation software AUTO97 and values of the material parameters $\beta_1 = 0.9$, $\widetilde{B} = -1.2$. The steady states solutions have been continued from initial data obtained from the two-dimensional case with a fixed value of the strain rate $\delta = 0.1$. The main diagram of figure 7.1 shows the solution branch in the (τ, q_1)-space. Here we observe two solution branches quantitatively equal to the in-plane solutions IPN and LRN described in chapter 5 and two *vertical lines*, OP_1 and OP_2, connecting the in-plane solutions at the branch points BP_1-BP_3 and BP_2-BP_4, respectively.

For large values of the dimensionless temperature, τ, the paranematic state , labelled IP in the figure, is the only steady stable state. It evolves, as τ decreases, to the stable in-plane nematic state, labelled IN. However, in contrast with the two dimensional case, the stable state does not loses its stability at the limit point LP3, labelled L_3 in figure 7.1, but at the branch point BP_1, which occurs at a slightly higher temperature than L_3.

A continuum of equilibria of undetermined stability, OP_1, emanates from the branch point BP_1 and it is displayed in the figure with a thick solid line. This is an anomalous out-of-plane solution constituted of limit points connecting the two dimensional solution branches, IPN and LRN at the branch points BP_1 and BP_3. The existence of the BP_3 bifurcation in the LRN branch implies that the log-rolling nematic state, stable in the two dimensional case, loses its stability in the three dimensional case for this value of the strain rate.

Between the limit points L_3 and L_4, of the in-plane branch, the temperature increases but after L_4 it decreases. At a lower value of τ a new branch point, BP_2 exists from which a degenerate locus of limit points emerges. Although not apparent in figure 7.1 this is in fact a *vertical line* in (τ, q_1)-space, OP_2, joining BP_2 and BP_4.

The inset diagram of figure 7.1, shows that the two degenerate solutions are ellipses in the (q_4, q_1)-space and therefore they are out-of plane solutions ($q_4 \neq 0$). In a subsequent section we will show that these are, in fact, the only steady out-of-plane solutions that the system presents [49].

The two dimensional steady solutions, described in chapter 5, are solutions of the three dimensional case, however the stability may vary when a third dimension is introduced into the system. Then, as seen for the two dimensional case, as we increase the strain rate, the limit points L_3 and L_4 come closer together and at a critical point they coincide. This behaviour can be seen in figure 5.10.

In the three dimensional case a Takens-Bogdanov point also exists for values of the

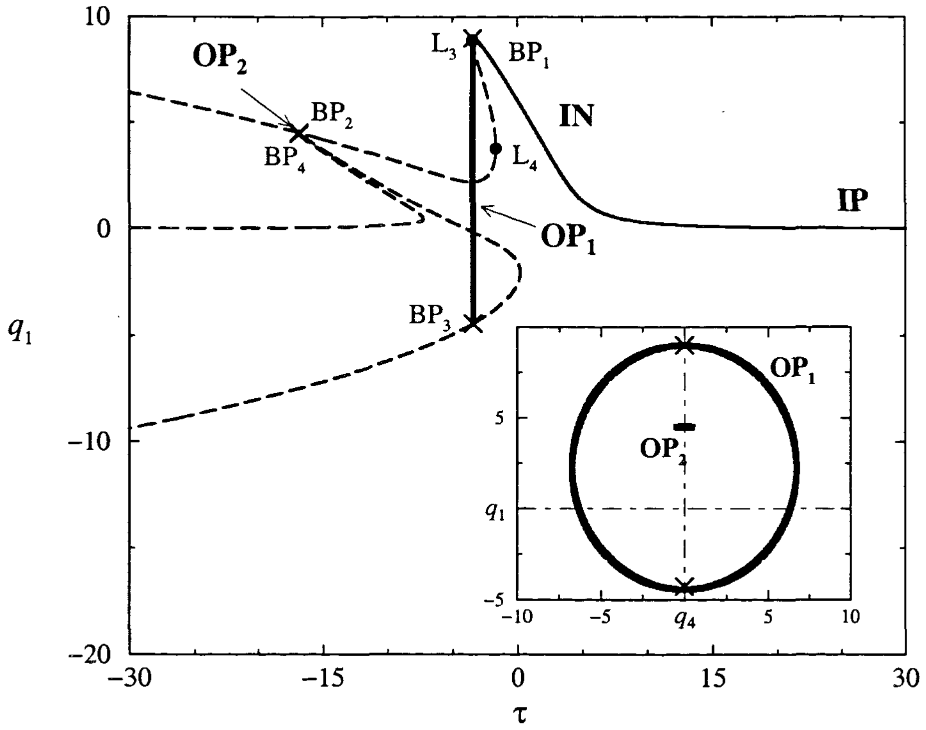

Figure 7.1: The steady state solution branches of the system (7.3)-(7.7) computed with a fixed value of the dimensionless strain rate $\delta = 0.1$ and values of the material parameters $\widetilde{B} = -1.2$ and $\beta_1 = 0.9$. Linearly stable states are plotted with thin solid lines. These are the in-plane paranematic state, labelled as IP, and the in-plane nematic state (IN). The linearly unstable states are plotted with thin dashed lines. The solid dots L_3 and L_4 are limit points. The crosses are branch points (BP) from where the degenerate solutions, plotted with thick solid lines, emanate. These are shown in the $(q_4,\, q_1)$-space in the inset diagram of the figure.

dimensionless temperature and strain rate, $(\tau^{\mathrm{TB}}, \delta^{\mathrm{TB}}) = (-3.35829676, 0.19211037)$, see figure 5.11, however, it occurs on a unstable branch and therefore the centre of manifold theory and normal form reduction applied in section 5.3.2.1 is not relevant when the director of the liquid crystal is allowed to move out of the shear plane. From figure 5.11 we also recall that from the Takens-Bogdanov point a locus of Hopf bifurcations originates, so that for values of the strain rate larger than δ^{TB} the IPN branch will present a Hopf bifurcation also in the three dimensional case.

In the next section we will perform an analytical and numerical study of the branch point BP_1 and of the anomalous solutions, in order to complete the state diagram for the three dimensional case.

In order to understand the behaviour of the three dimensional system we compute solution branches for larger values of the dimensionless strain rate.

Figure 7.2 shows the solution branch with $\delta = 0.6$, and comparing this diagram with figure 7.1 we observe that as δ increases the out-of-plane solution branches, OP_1 and OP_2, come closer together along the τ axis. The behaviour of these out-of-plane solutions for $\delta = 0.6$ is shown in figure 7.3 in different variable sub-spaces.

As the strain rate is increased we observe that, after a critical value of the strain rate, $\delta = 0.72$, the out-of-plane degenerate solutions disappear and the planar solution branches detach from each other so that the nematic state is the only stable solution, since the log-rolling state remains unstable as δ is increased. Figure 7.4 is an example of this behaviour. Here the solution branches for $\delta = 0.8$ are shown in the (τ, q_1)-space. We observe that the only stable solution, plotted with a solid line, loses its stability at the Hopf bifurcation. For this value of δ the system does not present any out-of-plane solution and the log-rolling state is unstable.

The solution branches shown in this section have an unstable log-rolling solution, however for very small strain rates there exists a Hopf bifurcation on the log-rolling branch that makes the log-rolling solution stable. Figure 7.5 shows the solution of the system (7.3)-(7.7) computed for a fixed strain rate $\delta = 3 \times 10^{-3}$, and here we observe the Hopf bifurcation, (HB), which stabilises the log-rolling branch.

This stability for very small values of the strain rate of the log-rolling state has also been observed using Doi's theory: Larson and Öttinger [30] obtained the stability employing simulation techniques, while Faraoni et. al. [32] employed continuation and bifurcation theory to find a similar result.

We observed this phenomena for strain rates smaller than $\delta \approx 3.5 \times 10^{-3}$, however, a computation of the locus of the Hopf bifurcation of the log-rolling branch was not possible using AUTO97, due to the computational sensitivity of this bifurcation to small changes in the strain rate.

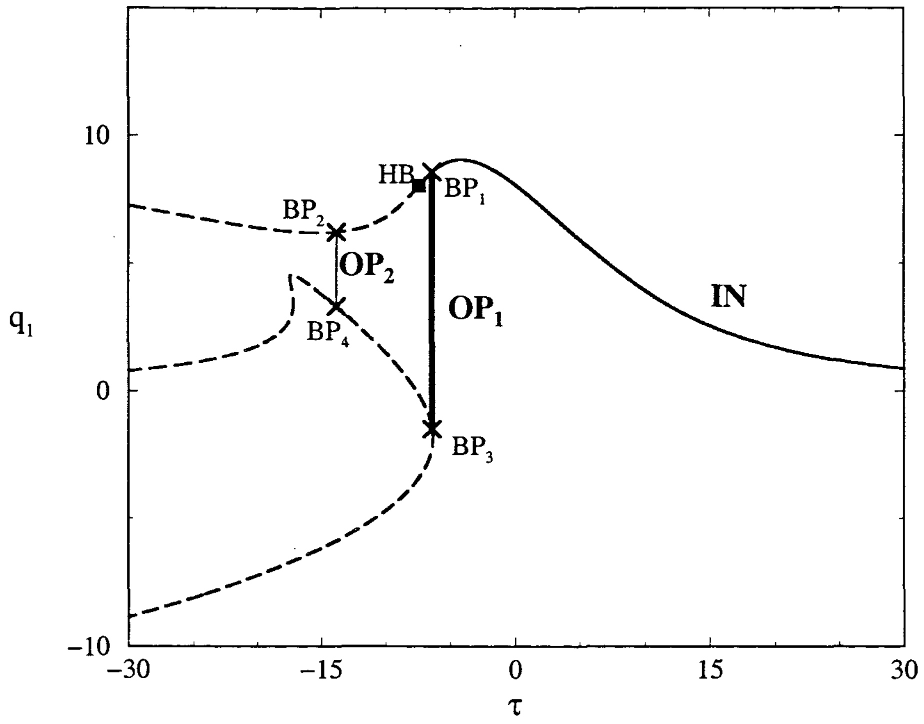

Figure 7.2: Steady state solutions of the system (7.3)-(7.7) computed with a fixed value of the dimensionless strain rate $\delta = 0.6$ and values of the material parameters $\widetilde{B} = -1.2$ and $\beta_1 = 0.9$. The stable in-plane nematic state is plotted with a thin solid line and labelled IN. The crosses are branch points (BP) from where the out-of-plane anomalous solutions, OP_1 and OP_2, originate. The solid square marks the locus of the Hopf-bifurcation.

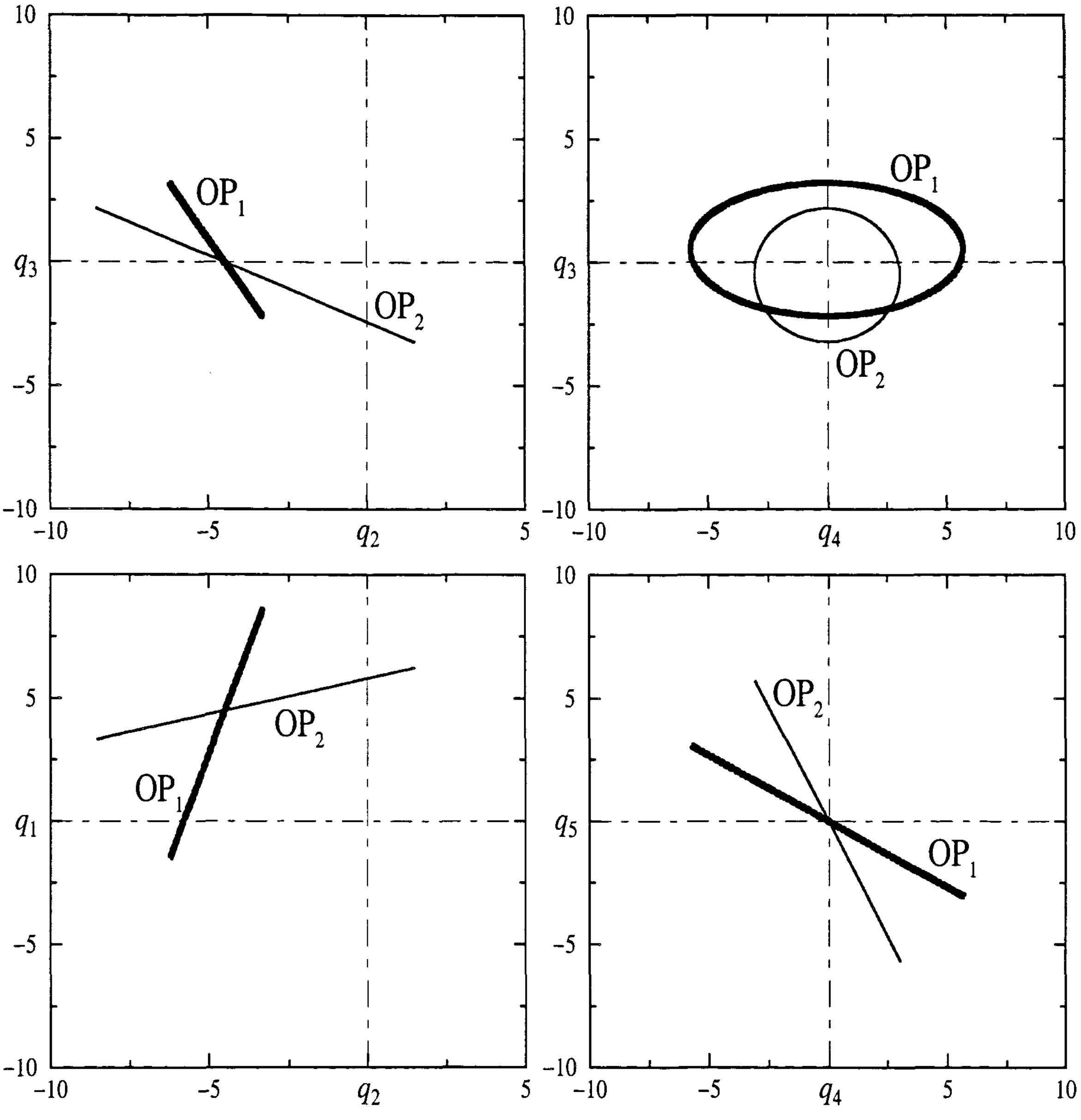

Figure 7.3: The out-of-plane solutions, OP$_1$ and OP$_2$, are shown here in different variable spaces. They have been computed for a fixed strain rate $\delta = 0.6$ and parameter values $\beta_1 = 0.9$ and $\widetilde{B} = -1.2$.

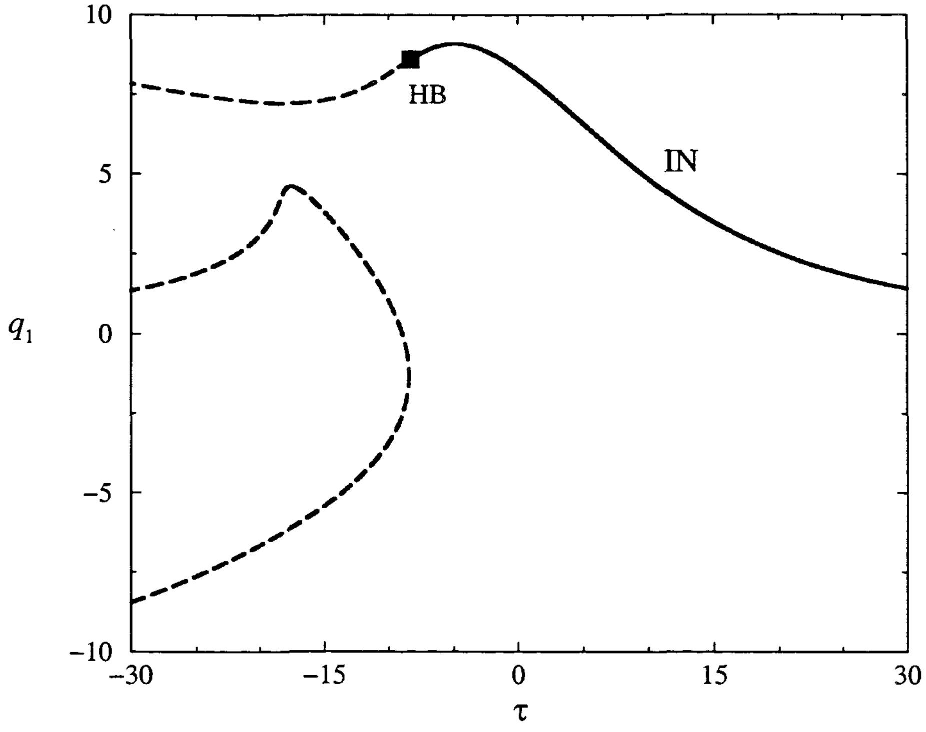

Figure 7.4: Solution branches computed using AUTO97 for a fixed value of the strain rate $\delta = 0.8$ and values of the material parameters $\beta_1 = 0.9$ and $\widetilde{B} = -1.2$. The stable states are plotted with a solid line while unstable states are plotted with dashed line. The only stable solution is the in-plane nematic state (IN). The solid square marks the Hopf bifurcation (HB).

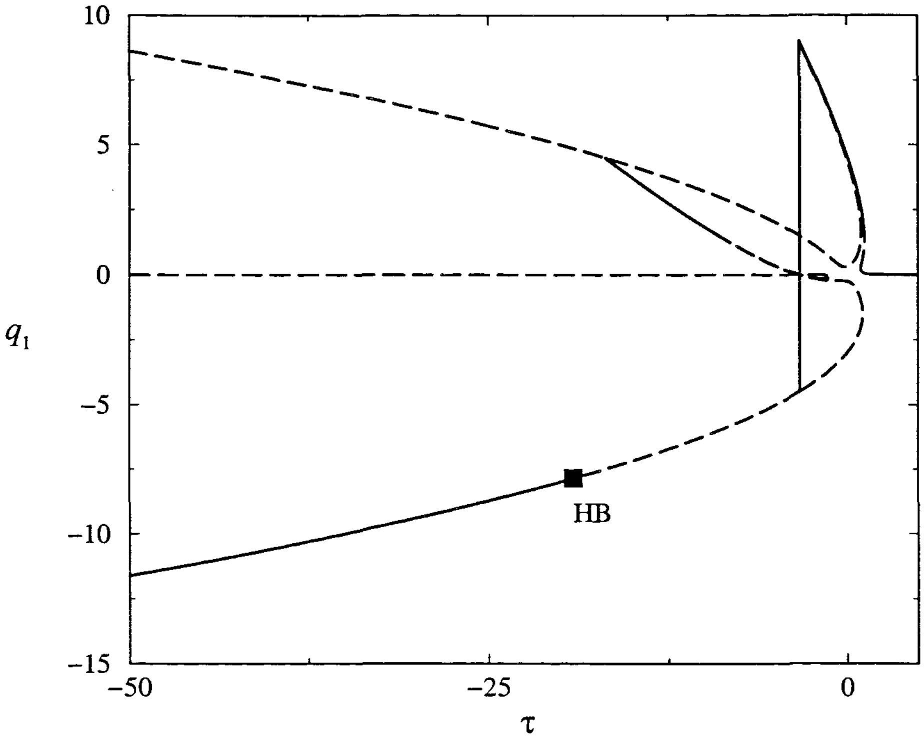

Figure 7.5: Solution branches computed using AUTO97 for a fixed value of the strain rate $\delta = 3 \times 10^{-3}$ and values of the material parameters $\beta_1 = 0.9$ and $\widetilde{B} = -1.2$. The Hopf bifurcation (HB) occurring on the log-rolling branch stabilises this solution.

7.2.2 Analysis of the out-of-plane steady solutions

Figure 7.3 suggests linear dependence between some of the variables in the out-of-plane solutions. This motivates the search for an analytical expression for the locus of the branch points as well as equations for the out of plane solutions. To proceed, we write the steady form of system (7.3)-(7.7) in vector form

$$\mathbf{f}(q_1, q_2, q_3, q_4, q_5; \tau, \delta) = \mathbf{0}\,, \tag{7.11}$$

where the five components of the vector $\mathbf{f}$ are given by the right hand side of equations (7.3)-(7.7). A branch point must satisfy that the Jacobian of the system evaluated at the branch point is zero, therefore in order to find the branch point of the system we solve the system constituted by the steady state conditions (7.11) and the equation $\det(\nabla \mathbf{f}) = 0$. We used the mathematical software MAPLE to obtain the following relationships

$$\begin{aligned}
q_1 &= \frac{1}{k} q_3 - 6\frac{\beta_1}{\widetilde{B}}\,, && (7.12)\\
q_2 &= k q_3 + 6\frac{\beta_1}{\widetilde{B}}\,, && (7.13)\\
q_4^2 &= \frac{9\beta_1^2}{\widetilde{B}^2(k^2+1)^3}(9k^4 + 14k^2 + 9) \\
&\quad - \frac{k^2+1}{k^2}\left(q_3 + 3k\frac{\beta_1}{\widetilde{B}}\frac{(k^2-1)}{(k^2+1)}\right)^2\,, && (7.14)\\
q_5 &= k q_4\,, && (7.15)\\
\tau &= -\frac{9\beta_1\left(k^2(2\beta_1 - \widetilde{B}) + 2\beta_1 + \widetilde{B}\right)}{\widetilde{B}^2(k^2+1)}\,, && (7.16)
\end{aligned}$$

where $k = k(\delta)$ is solution of the equation $3\delta k^2 - 4\beta_1 \widetilde{B} k + 3\delta = 0$. Then, substituting $k(\delta)$ into (7.16), squaring and simplifying we obtain

$$\left(\frac{27}{2\widetilde{B}^2}\right)^2 \delta^2 + (\tau + 2\mathcal{A})^2 = 9\mathcal{A}\,, \tag{7.17}$$

where $\mathcal{A} = (3\beta_1/\widetilde{B})^2$. Equation (7.17) provides an analytical expression for the locus of the branch points in the parameter space. This locus can also be found numerically by using the continuation software AUTO97. Figure 7.6 shows the analytical solution plotted with a solid line and the numerical results with solid dots. Here we observe that the agreement between numerical and analytical calculations is excellent.

From equation (7.17) we obtain that for $\delta > |2\beta_1/3\widetilde{B}|$ ($\delta > 0.72$ when $\beta_1 = 0.9$ and $\widetilde{B} = -1.2$) the system does not exhibit the branch points nor the anomalous solutions observed in figures 7.1 and 7.2.

Chillingworth, Vicente Alonso and Wheeler [49] gave a geometric explanation for these phenomena that we describe in the next section.

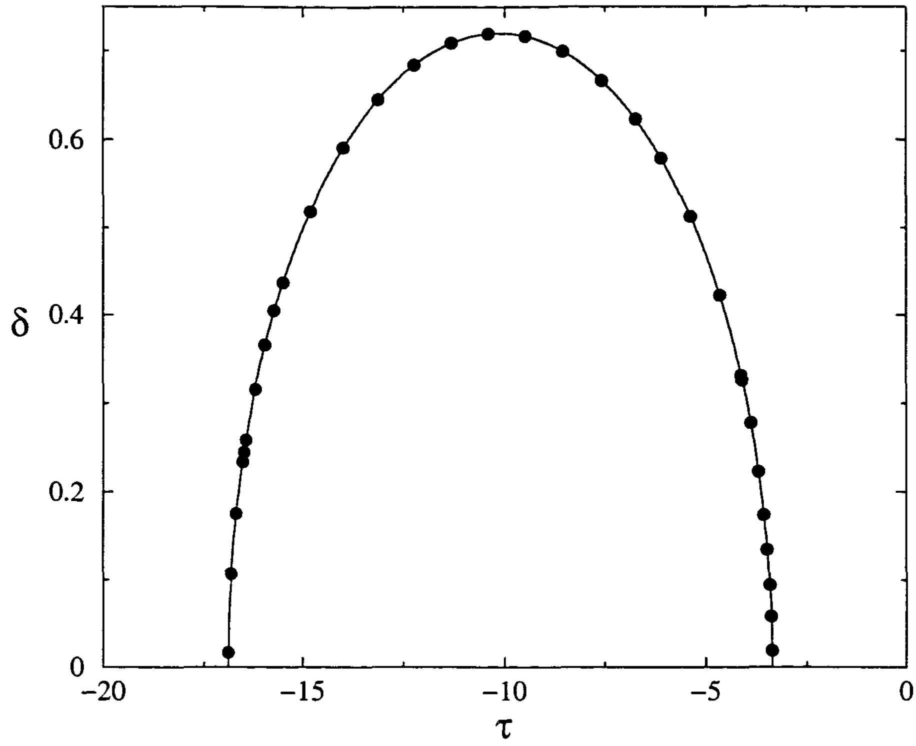

Figure 7.6: The locus of the branch points plotted in the parameter space. The solid line is the analytical result given by (7.17) with values of the material parameters $\beta_1 = 0.9$ and $\widetilde{B} = -1.2$. The solid dots are the numerical calculations for the same values of the material parameters.

Geometry of the out-of-plane solutions

We consider V the five dimensional space of the 3×3 symmetric and traceless matrices where we define the inner product $\langle \mathbf{P}, \mathbf{Q} \rangle = \mathrm{tr}(\mathbf{Q}^T\mathbf{P})$, with $\mathbf{P}, \mathbf{Q} \in V$.

We re-write the dimensionless equation of the motion of the order parameter, (5.3), re-scaled by (7.1)-(7.2) as

$$\dot{\mathbf{Q}} = \delta A(\mathbf{Q}) - \frac{\widetilde{B}^2}{162}\nabla f(\mathbf{Q}), \tag{7.18}$$

where $\mathbf{Q} \in V$, $A(\mathbf{Q}) = \widehat{\mathbf{W}}\mathbf{Q} - \mathbf{Q}\widehat{\mathbf{W}} - 18\beta_1\widehat{\mathbf{D}}^{[t]}/\widetilde{B}$, and $f(\mathbf{Q})$ is the dimensionless and re-scaled form of the Landau free energy density, given by

$$f(\mathbf{Q}) = 3\tau\mathrm{tr}(\mathbf{Q}^2) - 3\mathrm{tr}(\mathbf{Q}^3) + \frac{1}{8}[\mathrm{tr}(\mathbf{Q}^2)]^2 .$$

The function f is invariant under the action of the orthogonal group $G = \mathrm{O}(3)$, which acts on V by $\mathbf{R} \cdot \mathbf{Q} = \mathbf{R}\mathbf{Q}\mathbf{R}^T$, $\mathbf{R} \in G$, $\mathbf{Q} \in V$ (see section 5.3.3), thus the gradient of $f(\mathbf{Q})$, given by

$$\nabla f(\mathbf{Q}) = 3\mathrm{tr}(\mathbf{Q}^2)\mathbf{I} + \left(6\tau + \frac{1}{2}\mathrm{tr}(\mathbf{Q}^2)\right)\mathbf{Q} - 9\mathbf{Q}^2 ,$$

is G-equivariant, i.e. $\nabla f(\mathbf{R} \cdot \mathbf{Q}) = \mathbf{R} \cdot \nabla f(\mathbf{Q})$, for all $\mathbf{R} \in G$ and all $\mathbf{Q} \in V$.

The orbit of $\mathbf{Q}$ under the action of G is defined by $GQ = \{\mathbf{R} \cdot \mathbf{Q} \, , \; \mathbf{R} \in G\}$. In order to find the tangent space of the orbit GQ at $\mathbf{Q}$, $T_{\mathbf{Q}}$, we write $\mathbf{R} \in G$ as $\mathbf{R} = \exp(\mathbf{W})$, where $\mathbf{W} \in Skew$ and $Skew$ is the space of the 3×3 anti-symmetric matrices. We consider the path based on $\mathbf{Q}$, $t \mapsto \exp(t\mathbf{W}) \cdot \mathbf{Q}$, and the tangent space at $\mathbf{Q}$ is given by

$$\left.\frac{d}{dt}\exp(t\mathbf{W}) \cdot \mathbf{Q}\right|_{t=0} = \mathbf{W}\mathbf{Q} - \mathbf{Q}\mathbf{W} = [\mathbf{W}, \, \mathbf{Q}] \, ,$$

where $\mathbf{W} \in Skew$ and $[\,\cdot, \, \cdot\,]$ denotes the Lie brackets. Hence, we can write $T_{\mathbf{Q}} = \{[\mathbf{W}, \, \mathbf{Q}], \; \mathbf{W} \in Skew\}$.

Since $\nabla f(\mathbf{Q})$ is G-equivariant, then it is orthogonal to $T_{\mathbf{Q}}$ for every $\mathbf{Q} \in V$, and then

$$\langle \nabla f(\mathbf{Q}), \, [\mathbf{W}, \, \mathbf{Q}] \rangle = 0 \, , \quad \text{for every } \mathbf{W} \in Skew \text{ and every } \mathbf{Q} \in V \, . \tag{7.19}$$

When $\mathbf{Q}$ is an equilibrium solution we obtain, from equation (7.18), $\nabla f(\mathbf{Q}) = \delta \mathbf{A}$, where $\mathbf{A} = A(\mathbf{Q})$. Substituting this into (7.19) yields

$$\langle \mathbf{A}, \, [\mathbf{W}, \, \mathbf{Q}] \rangle = 0 \, , \; \text{for every } \mathbf{W} \in Skew \, .$$

However, $\langle \mathbf{A}, \, [\mathbf{W}, \, \mathbf{Q}] \rangle = \langle [\mathbf{A}, \, \mathbf{Q}], \, \mathbf{W} \rangle$, thus $[\mathbf{A}, \, \mathbf{Q}]$ is orthogonal to every $\mathbf{W} \in Skew$ and hence $[\mathbf{A}, \, \mathbf{Q}]$ is symmetric. But since both $\mathbf{A}$ and $\mathbf{Q}$ are symmetric $[\mathbf{A}, \, \mathbf{Q}]$ is anti-symmetric, and so we have that $[\mathbf{A}, \, \mathbf{Q}]$ must be zero, thus $\mathbf{A}\mathbf{Q} = \mathbf{Q}\mathbf{A}$. Therefore if $\mathbf{Q} \in V$ is an equilibrium solution it must be on the set $\mathcal{N}$, which is given by

$$\mathcal{N} = \{\mathbf{Q} \in V : \, A(\mathbf{Q}) \text{ conmutes with } \mathbf{Q}\} \, .$$

Considering $\mathbf{Q}$ re-scaled by (7.1), $\mathcal{N}$ is then described by the system

$$\frac{1}{2}\mathrm{tr}(\mathbf{Q}^2) = 3(q_1 q_2 - q_3^2) - 18\frac{\beta_1}{\widetilde{B}}(q_1 - q_2) \, , \tag{7.20}$$

$$q_3 q_4 = q_1 q_5 + 6\frac{\beta_1}{\widetilde{B}} q_5 \, , \tag{7.21}$$

$$q_3 q_5 = q_2 q_4 - 6\frac{\beta_1}{\widetilde{B}} q_4 \, . \tag{7.22}$$

When $q_4 = q_5 = 0$ we get $\mathcal{C} : \, 4q_3^2 + (q_2 - q_1 - 9\beta_1/\widetilde{B})^2 = (9\beta_1/\widetilde{B})^2$, and using the relationships between the different sets of variables (7.8)-(7.10), we obtain the locus of the steady solution described on section 5.3.3 for the planar case.

We designate $\widetilde{\mathcal{N}} = \mathcal{N} \setminus \mathcal{C}$ the locus of the solution with $(q_4,\, q_5) \neq (0,\, 0)$.

When $q_4 q_5 \neq 0$, multiplying equations (7.21) and (7.22) and dividing the result by $q_4 q_5$, we obtain

$$q_1 q_2 - q_3^2 = \left(6\frac{\beta_1}{\widetilde{B}}\right)^2 + 6\frac{\beta_1}{\widetilde{B}}(q_1 - q_2)$$

and substituting this into equation (7.20) we get $\operatorname{tr}(\mathbf{Q}^2) = 6^3\beta_1^2/\widetilde{B}^2$.

When $q_4 = 0$ and $q_5 \neq 0$, from equations (7.21) we have $q_3 = 0$ and from (7.22) we obtain $q_1 = -6\beta_1/\widetilde{B}$. Substituting into (7.20) gives again $\operatorname{tr}(\mathbf{Q}^2) = 2\beta_1^2/3$. Similarly, for the case $q_5 = 0$ and $q_4 \neq 0$ we also obtain $\operatorname{tr}(\mathbf{Q}^2) = 6^3\beta_1^2/\widetilde{B}^2$. Therefore, every equilibrium solution with non-zero out-of-plane component verifies $\operatorname{tr}(\mathbf{Q}^2) = 6^3\beta_1^2/\widetilde{B}^2$, and hence the steady form of equation (7.18) restricted to $\widetilde{\mathcal{N}}$ can be written as

$$\delta A(\mathbf{Q}) - 4\beta_1^2\mathbf{I} - \left(\frac{\widetilde{B}^2}{27}\tau + \frac{2}{3}\beta_1^2\right)\mathbf{Q} + \frac{\widetilde{B}^2}{18}\mathbf{Q}^2 = \mathbf{0}\,.$$

The out-of-plane components of this system are

$$\begin{aligned} \frac{\delta}{2}q_5 - \left(\frac{\widetilde{B}^2}{27}\tau + \frac{2}{3}\beta_1^2\right)q_4 + \frac{\widetilde{B}^2}{18}\left(q_3q_5 - q_2q_4\right) &= 0\,, \\ -\frac{\delta}{2}q_4 - \left(\frac{\widetilde{B}^2}{27}\tau + \frac{2}{3}\beta_1^2\right)q_5 + \frac{\widetilde{B}^2}{18}\left(q_3q_4 - q_1q_5\right) &= 0\,. \end{aligned}$$

Here using equations (7.21) and (7.22) we obtain

$$\frac{\delta}{2}q_5 - \left(\frac{\widetilde{B}^2}{27}\tau + \frac{2}{3}\beta_1^2 + \frac{1}{3}\beta_1\widetilde{B}\right)q_4 = 0\,, \tag{7.23}$$

$$-\frac{\delta}{2}q_4 - \left(\frac{\widetilde{B}^2}{27}\tau + \frac{2}{3}\beta_1^2 - \frac{1}{3}\beta_1\widetilde{B}\right)q_5 = 0\,. \tag{7.24}$$

Non-trivial solutions of this system only exist when the Jacobian of the system is zero, i.e.

$$\begin{vmatrix} -\frac{\widetilde{B}^2}{27}\tau - \frac{2}{3}\beta_1^2 - \frac{1}{3}\beta_1\widetilde{B} & \frac{\delta}{2} \\ -\frac{\delta}{2} & -\frac{\widetilde{B}^2}{27}\tau - \frac{2}{3}\beta_1^2 + \frac{1}{3}\beta_1\widetilde{B} \end{vmatrix} = 0\,.$$

Therefore the system presents out-of-plane solutions when

$$\frac{\delta^2}{4} + \left(\frac{\widetilde{B}^2}{27}\tau + \frac{2}{3}\beta_1^2\right)^2 = \frac{1}{9}\beta_1^2\widetilde{B}^2\,, \tag{7.25}$$

which coincides with (7.17). Solving the homogeneous system (7.23)-(7.24) for the case when equation (7.25) holds we obtain that the out-of-plane solutions must be in the set

$$\begin{aligned}\mathcal{H} \;=\; &\Big\{\mathbf{Q}\in V:\ (q_4,\,q_5)\neq(0,\,0)\,,\\ &\quad q_5 = kq_4,\ k=\frac{2\widetilde{B}^2\tau+36\beta_1^2+18\beta_1\widetilde{B}}{27\delta}\Big\}\,,\end{aligned}$$

Therefore all the out-of-plane solutions must lie on the set $\widetilde{\mathcal{N}}\cap\mathcal{H}$ which is given by

$$\begin{aligned}\widetilde{\mathcal{N}}\cap\mathcal{H} \;=\; &\Big\{\mathbf{Q}\in V:\ (q_4,\,q_5)\neq(0,\,0)\,,\\ &\frac{1}{2}\mathrm{tr}(\mathbf{Q}^2)=3(q_1q_2-q_3^2)-18\frac{\beta_1}{\widetilde{B}}(q_1-q_2)\,,\\ &q_3q_4=q_1q_5+6\frac{\beta_1}{\widetilde{B}}q_5\,,\\ &q_3q_5=q_2q_4-6\frac{\beta_1}{\widetilde{B}}q_4\,.\\ &q_5=\frac{2\widetilde{B}^2\tau+36\beta_1^2+18\beta_1\widetilde{B}}{27\delta}q_4,\quad\text{with}\\ &\frac{\delta^2}{4}+\left(\frac{\widetilde{B}^2}{27}\tau+\frac{2}{3}\beta_1^2\right)^2=\frac{1}{9}\beta_1^2\widetilde{B}^2\Big\}\,.\end{aligned}$$

Moreover, by direct substitution into (7.3)-(7.7) we can prove that any $\mathbf{Q}\in\widetilde{\mathcal{N}}\cap\mathcal{H}$ is indeed an equilibrium solution of the full three dimensional system and hence we deduce that $\mathbf{Q}\in V$ is an out-of-plane steady solution of the three dimensional system if and only if it is an element of $\widetilde{\mathcal{N}}\cap\mathcal{H}$. This set, found through geometric arguments coincides with the relationships (7.12)-(7.17) obtained by solving the steady state system subject to the branch point condition. The degenerate character of the out-of-plane solutions described in this section shows that the Landau-de Gennes model as described in chapter 3 is structurally unstable [49].

7.2.3 Very large strain rate

Similarly to the planar case, numerical evidence suggests a limiting behaviour of the system when $\delta\to\infty$. We will perform an analysis that will confirm this behaviour and will also corroborate that the log-rolling solution is, indeed, unstable for large values of the strain rate. We consider the steady form of system (7.3)-(7.7), and defining $\epsilon=\delta^{-1}$ we perform a regular expansion in ϵ, with $q_i=q_i^{(0)}+\epsilon q_i^{(1)}+O(\epsilon^2)$ $i\in\{1,\,2,\ldots,\,5\}$ as $\epsilon\to 0$. To order zero in epsilon we obtain

$$q_2^{(0)}=q_1^{(0)}+18b\,, \tag{7.26}$$

$$q_3^{(0)}=q_4^{(0)}=q_5^{(0)}=0\,, \tag{7.27}$$

where $b = \beta_1/\widetilde{B}$. To $O(\epsilon)$ we have

$$
\begin{aligned}
q_2^{(1)} &= q_1^{(1)}\,, && (7.28)\\
q_4^{(1)} &= q_5^{(1)} = 0\,, && (7.29)\\
q_3^{(1)} &= \frac{\widetilde{B}}{162}\Big[6\tau q_1^{(0)} - 3(q_1^{(0)})^2 + 6(q_2^{(0)})^2 + 6q_1^{(0)}q_2^{(0)} \\
&\quad + (q_1^{(0)})^3 + (q_1^{(0)})^2 q_2^{(0)} + q_1^{(0)}(q_2^{(0)})^2\Big]\,, && (7.30)\\
\tau &= -\frac{(q_1^{(0)})^3 + 3(1+9b)(q_1^{(0)})^2 + 54b(1+5b)q_1^{(0)} + 162(1+6b)b^2}{2q_1^{(0)} + 18b}\,. && (7.31)
\end{aligned}
$$

When $\delta \to \infty$, then $\epsilon \to 0$ and therefore we can approximate q_i by $q_i^{(0)}$ and equation (7.31) provides the solution branches when $\delta \to \infty$ in the $(\tau,\, q_1)$-space. This solution presents a horizontal asymptote at $q_1 = -9b$ ($q_1 = 6.75$ when $\beta_1 = 0.9$ and $\widetilde{B} = -1.2$). Substituting equation (7.26) into (7.31) we obtain an approximation of the solution branch in the $(\tau,\, q_2)$-space. Figure 7.7 shows the analytical and numerical solutions in the $(\tau,\, q_1)$-space. Here the analytical result, given by (7.31), is plotted with a solid line for values of the material parameters $\beta_1 = 0.9$ and $\widetilde{B} = -1.2$. Numerical solutions for the same value of the material parameters and a strain rate $\delta = 10^3$ are plotted with dots. Solid dots indicate stable states while white dots indicate linearly unstable states. Here we observe that the agreement between the numerical and analytical results is excellent.

An analysis of the full dynamical system, (7.3)-(7.7), will confirm the numerical stability found using AUTO97 and is shown in figure 7.7.

Considering q_i^*, $i \in \{1, \ldots, 5\}$ the equilibrium solution of the system (7.3)-(7.7), and defining $x_i = q_i - q_i^*$, $i \in \{1, \ldots, 5\}$, and a new time scale $T = \delta t$, then the linearised form of the system is given by

$$
\dot{\mathbf{x}} = \mathbf{M}\mathbf{x}\,, \tag{7.32}
$$

where $\mathbf{x} = (x_1, \ldots, x_5)^T$ and

$$
\mathbf{M} = \begin{pmatrix}
-a\epsilon f_{1,1}^* & -a\epsilon f_{1,2}^* & 1 - a\epsilon f_{1,3}^* & -a\epsilon f_{1,4}^* & -a\epsilon f_{1,5}^* \\
-a\epsilon f_{2,1}^* & -a\epsilon f_{2,2}^* & -1 - a\epsilon f_{2,3}^* & -a\epsilon f_{2,4}^* & -a\epsilon f_{2,5}^* \\
-\frac{1}{2} - a\epsilon f_{3,1}^* & \frac{1}{2} - a\epsilon f_{3,2}^* & -a\epsilon f_{3,3}^* & -a\epsilon f_{3,4}^* & -a\epsilon f_{3,5}^* \\
-a\epsilon f_{4,1}^* & -a\epsilon f_{4,2}^* & -a\epsilon f_{4,3}^* & -a\epsilon f_{4,4}^* & \frac{1}{2} - a\epsilon f_{4,5}^* \\
-a\epsilon f_{5,1}^* & -a\epsilon f_{5,2}^* & -a\epsilon f_{5,3}^* & -\frac{1}{2} - a\epsilon f_{5,4}^* & -a\epsilon f_{5,5}^*
\end{pmatrix}.
$$

Here $\epsilon = \delta^{-1}$, $a = \widetilde{B}/162$ and $f_{i,j}$ denotes the partial derivative of f_i with respect to q_j, where the functions are given by

$$
f_1 = 6\tau q_1 - 3(q_1^2 + q_3^2 + q_4^2) + 6(q_2^2 + q_5^2 + q_1 q_2) + q_1\kappa,
$$

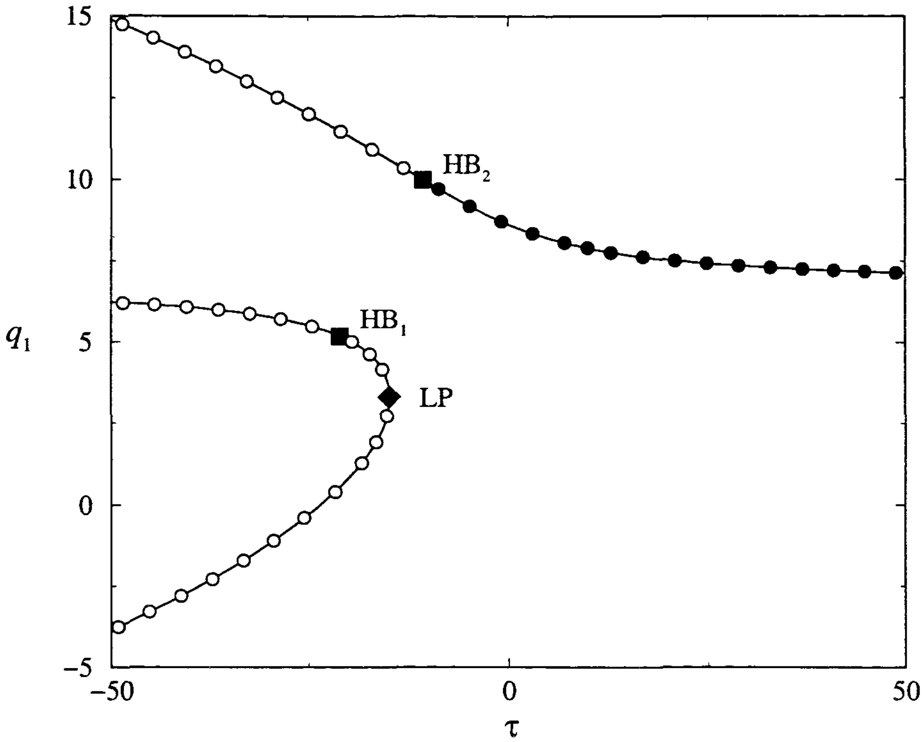

Figure 7.7: The dots are the numerical solution branches in the (τ, q_1)-space computed for $\delta = 10^3$ and values of the material parameters $\widetilde{B} = -1.2$, $\beta_1 = 0.9$. Solid dots denote the stable state and white dots unstable solutions. The square symbols mark the Hopf bifurcations (HB) and the diamond the limit point (LP). The solid line is the analytical solution given by (7.31).

$$
\begin{aligned}
f_2 &= 6\tau q_2 - 3(q_2^2 + q_3^2 + q_5^2) + 6(q_1^2 + q_4^2 + q_1 q_2) + q_2 \kappa, \\
f_3 &= 6\tau q_3 - 9(q_1 q_3 + q_2 q_3 + q_4 q_5) + q_3 \kappa, \\
f_4 &= 6\tau q_4 - 9(q_3 q_5 - q_2 q_4) + q_4 \kappa, \\
f_5 &= 6\tau q_5 - 9(q_3 q_4 - q_1 q_5) + q_5 \kappa,
\end{aligned}
$$

with $\kappa = q_1^2 + q_2^2 + q_3^2 + q_4^2 + q_5^2 + q_1 q_2$. The asterisk indicates evaluation of the function at the steady state solution.

We now consider the expansion of the steady state solution given by $q_i = q_i^{(0)} + \epsilon q_i^{(1)} + \mathrm{O}(\epsilon^2)$, as $\epsilon \to 0$, such that verify equations (7.26)-(7.31). Thus, the expansion of the system (7.32) is given by

$$
\dot{\mathbf{x}} = (\mathbf{M}_0 + \epsilon \mathbf{M}_1)\mathbf{x} + \mathrm{O}(\epsilon^2),
$$

where

$$
\mathbf{M}_0 = \begin{pmatrix}
0 & 0 & 1 & 0 & 0 \\
0 & 0 & -1 & 0 & 0 \\
-\frac{1}{2} & \frac{1}{2} & 0 & 0 & 0 \\
0 & 0 & 0 & 0 & \frac{1}{2} \\
0 & 0 & 0 & -\frac{1}{2} & 0
\end{pmatrix},
$$

and

$$
\mathbf{M}_1 = \begin{pmatrix}
-af_{1,1}^{(0)} & -af_{1,2}^{(0)} & 0 & 0 & 0 \\
-af_{2,1}^{(0)} & -af_{2,2}^{(0)} & 0 & 0 & 0 \\
0 & 0 & -af_{3,3}^{(0)} & 0 & 0 \\
0 & 0 & 0 & -af_{4,4}^{(0)} & 0 \\
0 & 0 & 0 & 0 & -af_{5,5}^{(0)}
\end{pmatrix}.
$$

The superscript (0) of the functions indicates evaluation at $q_i^{(0)}$, but from equations (7.26)-(7.27), we find that the matrix $\mathbf{M}_1$ can be expressed in terms of $q_1^{(0)}$ and the material parameters a and b only. Therefore, as previously done in section 5.4.2 for the two dimensional case, we consider the characteristic equation of the system

$$
\det\left(\mathbf{M}_0 + \epsilon \mathbf{M}_1 - \lambda \mathbf{I} + \mathrm{O}(\epsilon^2)\right) = 0, \tag{7.33}
$$

where the eigenvalue λ is expanded in powers of ϵ, $\lambda = \lambda_0 + \epsilon \lambda_1 + \mathrm{O}(\epsilon^2)$ as $\epsilon \to 0$. Then, performing an expansion of the characteristic equation in terms of ϵ we obtain

$$
-(\lambda_0^5 + \frac{5}{4}\lambda_0^3 + \frac{1}{4}\lambda_0) - g(\lambda_0, \lambda_1, q_1^{(0)})\epsilon + \mathrm{O}(\epsilon^2) = 0,
$$

where

$$
g(\lambda_0, \lambda_1, q_1^{(0)}) = \Big\{972ab^2(1 + 3\lambda_0^2 - 10\lambda_0^4) + 1458ab^3(3 + 16\lambda_0^2 + 16\lambda_0^4)
$$

$$
\begin{aligned}
&+(9b+q_1^{(0)})(1+15\lambda_0^2+20\lambda_0^4)\lambda_1+162ab^2(9+46\lambda_0^2+40\lambda_0^4)q_1^{(0)}\\
&+9a(18b+q_1^{(0)})(1-\lambda_0^2-20\lambda_0^4)q_1^{(0)}\\
&+6a(27b+q_1^{(0)})(1+5\lambda_0^2+4\lambda_0^4)(q_1^{(0)})^2\Big\}\Big\{4q_1^{(0)}+36b\Big\}^{-1}.
\end{aligned}
$$

At leading order, equation (7.33) gives that λ_0 is 0, $\pm i$ or $\pm i/2$. Therefore the five eigenvalues are: a real eigenvalue $\lambda^{(1)}$, and two complex conjugate pairs $\lambda^{(2)}$, $\overline{\lambda}^{(2)}$ and $\lambda^{(3)}$, $\overline{\lambda}^{(3)}$, where the overbar indicates complex conjugate. These eigenvalues can be expanded in terms of ϵ as follows

$$
\begin{aligned}
\lambda^{(1)} &= \lambda_1^{(1)}\epsilon+\mathrm{O}(\epsilon^2)\,,\\
\lambda^{(2)} &= i+\lambda_1^{(2)}\epsilon+\mathrm{O}(\epsilon^2)\,,\\
\lambda^{(3)} &= \frac{i}{2}+\lambda_1^{(3)}\epsilon+\mathrm{O}(\epsilon^2)\,.
\end{aligned}
$$

Then, at first order in ϵ, the characteristic equation (7.33) gives

- $\lambda_0^{(1)}=0$. The condition obtained form the characteristic equation (7.33) is $g(0,\,\lambda_1^{(1)},q_1^{(0)})=0$, which yields

  $$\lambda_1^{(1)}=-\frac{3a\,(2q_0^3+3(1+18b)q_0^2+54b(1+9b)q_0+162b^2(2+9b))}{q_0+9b}\,, \qquad (7.34)$$

  where $q_0=q_1^{(0)}$.

  The eigenvalue $\lambda^{(1)}$ is zero at the limit point, therefore solving (7.34) for $q_1^{(0)}$, with $\lambda_1^{(1)}=0$ gives us the locus of the limit point as $\delta\to\infty$, and employing the relationships (7.26)-(7.31), with values of the material constants $a=4/450$, $b=-3/4$ we obtain that

  $$
  \begin{aligned}
  &\tau^{\mathrm{LP}}=-14.972954+\mathrm{O}(\delta^{-1})\,,\\
  &(q_1^{\mathrm{LP}},\,q_2^{\mathrm{LP}},\,q_3^{\mathrm{LP}},\,q_4^{\mathrm{LP}},\,q_5^{\mathrm{LP}})=(3.317004,\,-10.182996,\,0,\,0,\,0)+\mathrm{O}(\delta^{-1})\,.
  \end{aligned}
  $$

  The eigenvalue $\lambda^{(1)}$ is positive for values of $q_1\in(q_1^{\mathrm{LP}},\,-9b)$ and negative otherwise.

- We have $\lambda_0^{(2)}=i$, and the condition from the characteristic equation is $g(i,\,\lambda_1^{(2)},q_0)=0$, where $q_0=q_1^{(0)}$. This provides the following expression for $\lambda_1^{(2)}$ in terms of q_0

  $$\lambda_1^{(2)}=\frac{27a\,(q_0^2+3b(6-b)q_0+9b^2(8-3b))}{q_0+9b}\,. \qquad (7.35)$$

  The eigenvalues $\lambda^{(2)}$ and its conjugate are a purely imaginary pair when $\lambda_1^{(2)}=0$, and therefore from substituting this condition into the equation (7.35) we obtain the locus of the two Hopf bifurcations of the system as $\delta \to \infty$. These, for $a = 4/450$ and $b = -3/4$, are given by

$$\tau^{\mathrm{H1}} = -21.08088508 + \mathrm{O}(\delta^{-1})$$
$$(q_1^{\mathrm{H1}},\, q_2^{\mathrm{H1}},\, q_3^{\mathrm{H1}},\, q_4^{\mathrm{H1}},\, q_5^{\mathrm{H1}}) = (5.19074895,\, -8.30925105\,0,\, 0,\, 0) + \mathrm{O}(\delta^{-1})\,,$$

and

$$\tau^{\mathrm{H2}} = -10.71794304 + \mathrm{O}(\delta^{-1})$$
$$(q_1^{\mathrm{H2}},\, q_2^{\mathrm{H2}},\, q_3^{\mathrm{H2}},\, q_4^{\mathrm{H2}},\, q_5^{\mathrm{H2}}) = (9.99675105,\, -3.50324895,\, 0,\, 0,\, 0) + \mathrm{O}(\delta^{-1})\,,$$

The eigenvalue $\lambda^{(2)}$ and its complex conjugate $\overline{\lambda}^{(2)}$ have positive real part when $q_1 \in (q_1^{\mathrm{H1}},\, -9b) \bigcup (q_1^{\mathrm{H2}},\, \infty)$ and negative otherwise;

- We have $\lambda_0^{(3)} = i/2$ and, proceeding as above, the condition from the term at first order in the characteristic equation is $g(i/2,\, \lambda_1^{(3)},\, q_1^{(0)}) = 0$. Hence we obtain

$$\lambda_1^{(3)} = -\frac{243ab^2}{q_1^{(0)} + 9b}\,,$$

  and therefore the complex pair of eigenvalues $\lambda^{(3)}$ and $\overline{\lambda}^{(3)}$ has positive real part when $q_1 \in (-\infty,\, -9b)$.

Therefore, in the interval $q_1 \in (-9b,\, q_1^{\mathrm{H1}})$ the real eigenvalue is negative and the two complex pairs of eigenvalues both have negative real part, thus the solution is stable only in this interval, which corresponds to the in-plane nematic state. Hence we also obtain that the log-rolling state is unstable for the three dimensional case as $\delta \to \infty$. The loci of the limit point and Hopf bifurcations as calculated in this section have excellent agreement with the numerical results shown in figure 7.7, as also does the linear stability of the system.

7.2.4 The state diagram for the three dimensional case

In section 7.3 we study the time dependent behaviour of the system (7.3)-(7.7) but firstly, in this section, we summarise the steady states of a three dimensional system of a liquid crystal in a shear flow.

We have seen that the equilibrium state in the three dimensional case are the in-plane nematic phase, which exists for values of the material parameters within the shaded region of the state diagram showed in figure 7.8, and the log-rolling state, which is

stable only for very negative temperatures and very small strain rates.
We label as (τ^{BP}, δ^{BP}) the value of the parameters at the branch point occurring at a higher temperature. The pair (τ^{HB}, δ^{HB}) denotes the Hopf bifurcation of the IPN branch and, as done before, we mark the Takens-Bogdanov point as (τ^{TB}, δ^{TB}). The critical points at which (τ^{BP}, δ^{BP}) $=$ (τ^{HB}, δ^{HB}) are labelled (τ^{c1}, δ^{c}) and (τ^{c2}, δ^{c2}), with $\delta^{c1} < \delta^{c2}$. The strain rate δ^{M} is the maximum value of δ at which a branch point occurs. Therefore, the behaviour of the liquid crystal can be described as follows

- if $0 < \delta < \delta^{\mathrm{TB}}$ the system exhibits an in-plane nematic state for values of the dimensionless temperature $\tau > \tau^{\mathrm{BP}}$. At this temperature the in-plane nematic phase loses its stability leaving the system without any equilibrium solution. An example of this behaviour can be seen in figure 7.1. When the strain rate is very small, $\delta \lessapprox 10^{-3}$, the log-rolling state is also an stable solution of the system, as figure 7.5 shows;
- at $\delta = \delta^{\mathrm{TB}}$ the branch of Hopf bifurcation exists.
- if $\delta^{\mathrm{TB}} < \delta < \delta^{c1}$, the Hopf bifurcation occurs at a higher temperature than the branch point, however the nematic state is stable for temperatures higher than τ^{BP};
- when $\delta^{c1} < \delta < \delta^{c2}$ the Hopf bifurcation occurs to the left of the branch point, i.e. $\tau^{\mathrm{HB}} < \tau^{\mathrm{BP}}$, and the nematic state is stable for temperatures higher than that at the branch point. Figure 7.2 exemplifies this behaviour;
- $\delta^{c2} < \delta < \delta^{\mathrm{M}}$. For strain rates within this range $\tau^{\mathrm{BP}} < \tau^{\mathrm{HB}}$ and the in-plane nematic state which is stable for temperatures higher than τ^{HB}, loses its stability at the Hopf bifurcation point;
- when $\delta > \delta^{\mathrm{M}}$ the branch points do not exist and the only stable state, the in-plane nematic phase, loses its stability at the Hopf bifurcation point. An example of this behaviour is seen in figure 7.4.

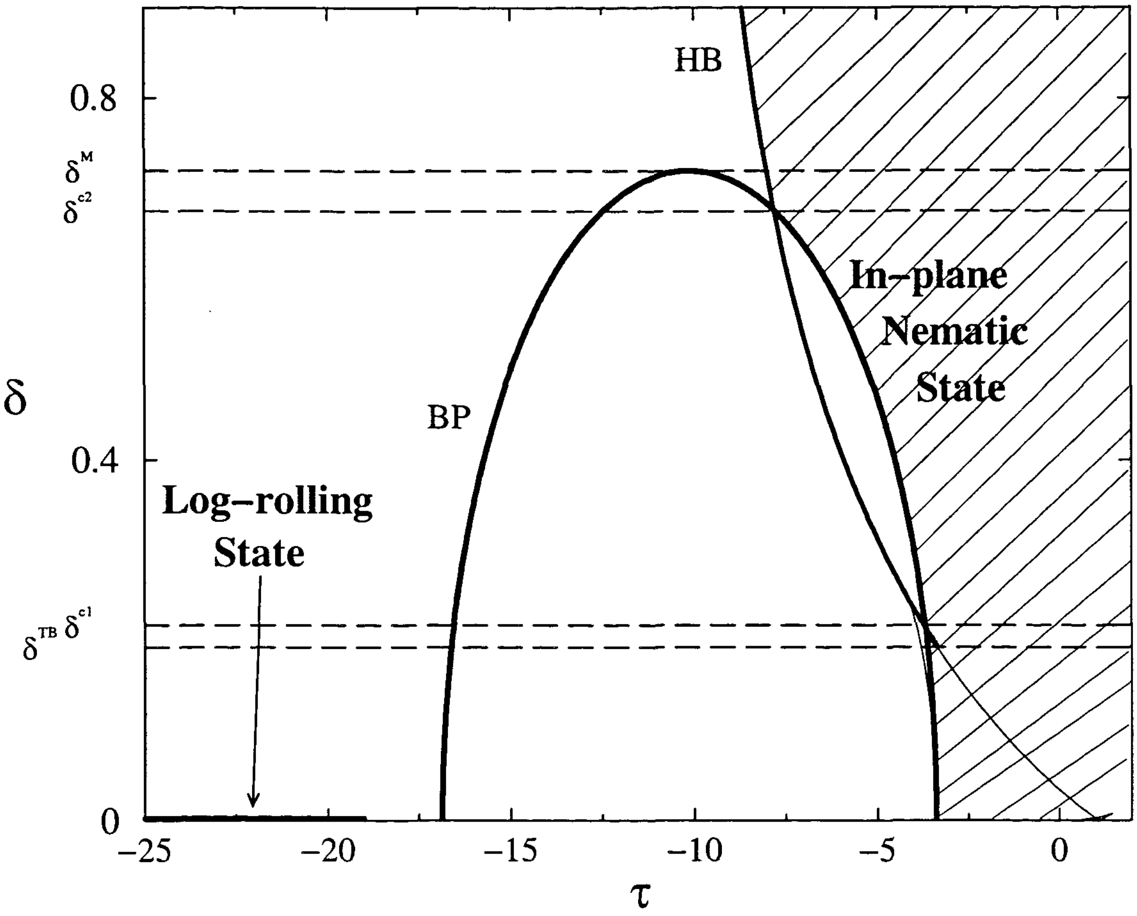

Figure 7.8: State diagram for the steady state and values of the material parameters $\widetilde{B} = -1.2$, $\beta_1 = 0.9$. The shaded region is the area where the in-plane nematic state occurs. For very small strain rates and very negative temperatures the log-rolling state is also an stable solution of the system.

7.3 The time dependent solutions: tumbling, wagging and kayaking

In the previous section we have studied the steady state behaviour of a liquid crystal in simple shear flow, and our aim in this section is to describe the time dependent behaviour of a liquid crystal in the three dimensional case. We use the continuation software AUTO97 and values of the material parameters $\widetilde{B} = -1.2$ and $\beta_1 = 0.9$ to perform numerical calculations of the time dependent solution branches of system (7.3)-(7.7) for several fixed values of the strain rate: $\delta = 0.1$, $\delta = 0.6$ and $\delta = 0.8$.

In the figures within this section the time dependent states are plotted using different symbols depending on the alignment and stability of the different phases: in-plane solutions are plotted using circles while out-of-plane solutions are represented with diamonds; the stable states are solid symbols and unstable solutions are plotted using white symbols. In the figures of this section the maximum of q_1 in the periodic orbit is plotted against the correspondent dimensionless temperature.

Figure 7.9 shows the behaviour of the liquid crystal for a fixed strain rate $\delta = 0.1$. The computation of the time dependent branch was done by continuation on δ of a time dependent solution branch at a fixed temperature, and subsequently continuation on τ of the solution with $\delta = 0.1$. Here we observe that for $\delta = 0.1$ and very negative temperatures the only time dependent stable solution is the in-plane tumbling state, labelled IPT in the figure. As the temperature increases the system reaches a period doubling bifurcation at $\tau = \tau^{\mathrm{PD}} = -13.32855$. From here two branches emanate: one unstable periodic solution branch and a stable branch (OPK) of doubled period with out-of-plane components, q_4 and q_5, non zero. This out-of-plane behaviour can be seen in the inset diagram of figure 7.9, where the solution branch is plotted in the (q_4, q_1)-space. This time dependent solution is the so-called kayaking state, labelled OPK in the figure, that has also been found by Larson and Öttinger [30] and Faraoni et al. [32] for the Doi model [26] and by Tsuji and Rei [46] using their own complete theory [47].

The computation of the two time dependent branches to the right of the period doubling bifurcation terminates at $\tau = \tau^{\mathrm{BP}}$, the temperature of the branch point bifurcation at the steady state solution, and there is no time dependent behaviour of the system at larger values of the dimensionless temperature.

By using the continuation software AUTO97 we can compute the locus of the period doubling bifurcation in terms of the parameters of our system τ and δ. This continuation is shown in figure 7.10, where the locus of the period doubling bifurcation is

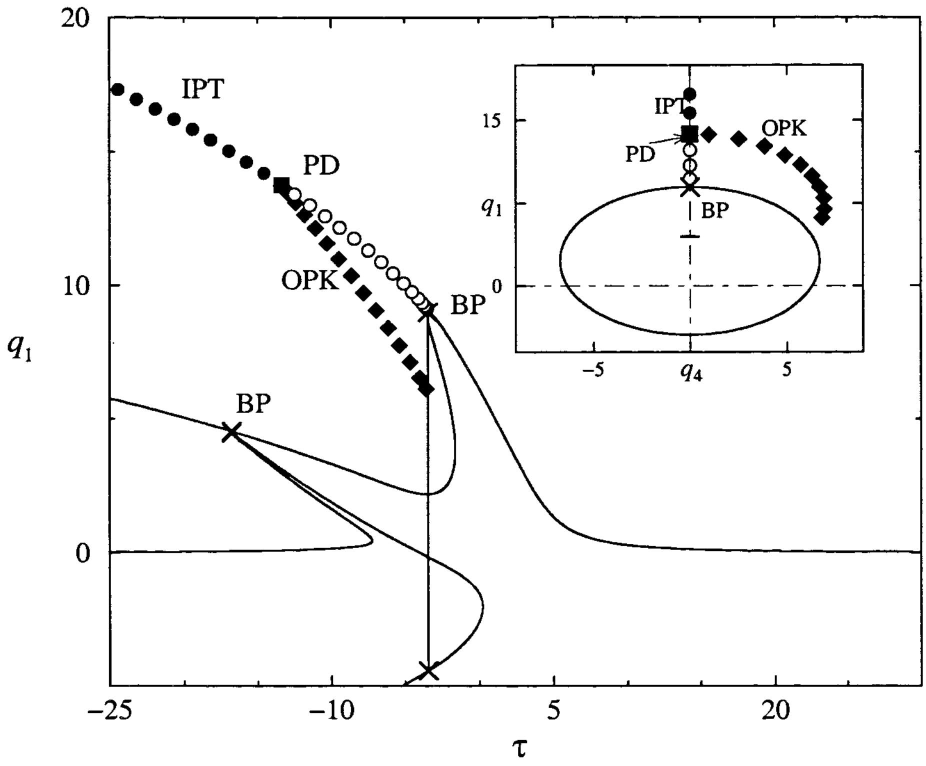

Figure 7.9: Solution branch plotted in the (τ, q_1)-space and computed with a fixed value of the dimensionless strain rate $\delta = 10^{-1}$ and values of the material parameters $\widetilde{B} = -1.2$ and $\beta_1 = 0.9$. The steady states are plotted with lines while the maximum of q_1 in the periodic orbits is plotted with symbols: in-plane time dependent solutions are plotted with circles and out of plane time dependent solutions with diamonds. Solid symbols denote stable states while white symbols denote unstable states. The time dependent solution links a stable in-plane tumbling state (IPT) at very low temperatures to an out-of-plane time dependent state (OPK), the so-called kayaking solution. The inset diagram shows the same solutions in the (q_4, q_1)-space.

shown in the $(\tau,\ q_1)$-space. Here the thick solid line is the locus of the bifurcation, and the arrows indicate the direction of increasing δ. The critical points at which the period doubling branch appears and dissapears are labelled $(\tau^{\mathrm{p}0},\ \delta^{\mathrm{p}0})$, $(\tau^{\mathrm{p}1},\ \delta^{\mathrm{p}1})$ and $(\tau^{\mathrm{p}2},\ \delta^{\mathrm{p}2})$. Hence we can explain the behaviour of the time dependent solutions as δ increases:

- $0 \leq \delta < \delta^{\mathrm{p}0}$, with $\delta^{\mathrm{p}0} = 7.321577 \times 10^{-3}$. For strain rates within this range the liquid crystal does not show any period doubling bifurcation. The understanding of the behaviour for very small strain rates will require further analytical study, since numerical methods using AUTO97 are not conclusive due to the inaccuracy of calculating the Floquet multipliers and the linearized Poincaré map at very small values of the strain rate;
- $\delta^{\mathrm{p}0} \leq \delta < \delta^{\mathrm{p}1}$, with $\delta^{\mathrm{p}1} = 2.321207 \times 10^{-1}$. At $\tau = \tau^{\mathrm{p}0} = -13.31682$ a period doubling bifurcation appears, and for strain rates within this range the in-plane tumbling state occurring at low temperatures bifurcates at the period doubling bifurcation point to an out-of-plane kayaking solution as shown in figure 7.9;
- $\delta^{\mathrm{p}1} \leq \delta < \delta^{\mathrm{p}2}$. At $(\tau,\ \delta) = (\tau^{\mathrm{p}1},\ \delta^{\mathrm{p}1}) = (-4.041843,\ 2.321207\delta \times 10^{-1})$ a new period doubling bifurcation appears, and therefore in this interval the system exhibits two period doubling bifurcations. The computation of the time dependent solution branches for strain rates within this range (as figures 7.11 and 7.12 for $\delta = 0.6$ and figure 7.13 for $\delta = 0.55$), will help us to understand the behaviour of the liquid crystal at intermediate values of the strain rate and is explained below;
- $\delta = \delta^{\mathrm{p}2}$, with $\delta^{\mathrm{p}2} = 7.220094\delta \times 10^{-1}$. At this critical strain rate the two period doubling bifurcations collide for a value of the dimensionless temperature $\tau^{\mathrm{p}2} = -12.04119$;
- $\delta > \delta^{\mathrm{p}2}$. The time dependent solutions do not present any period doubling bifurcation and the behaviour of the periodic solution is simple: an in-plane periodic solution generates from the Hopf bifurcation occurring on the IPN branch. This behaviour is shown in figure 7.14, where the time dependent states are plotted in the $(\tau,\ q_1)$-space for a strain rate $\delta = 0.8$.

We have already understood the time dependent behaviour of the liquid crystal for low shear rates, as shown in figure 7.9, and for very high shear rates, as seen in figure 7.14, therefore in order to complete the state diagram of the time dependent behaviour of

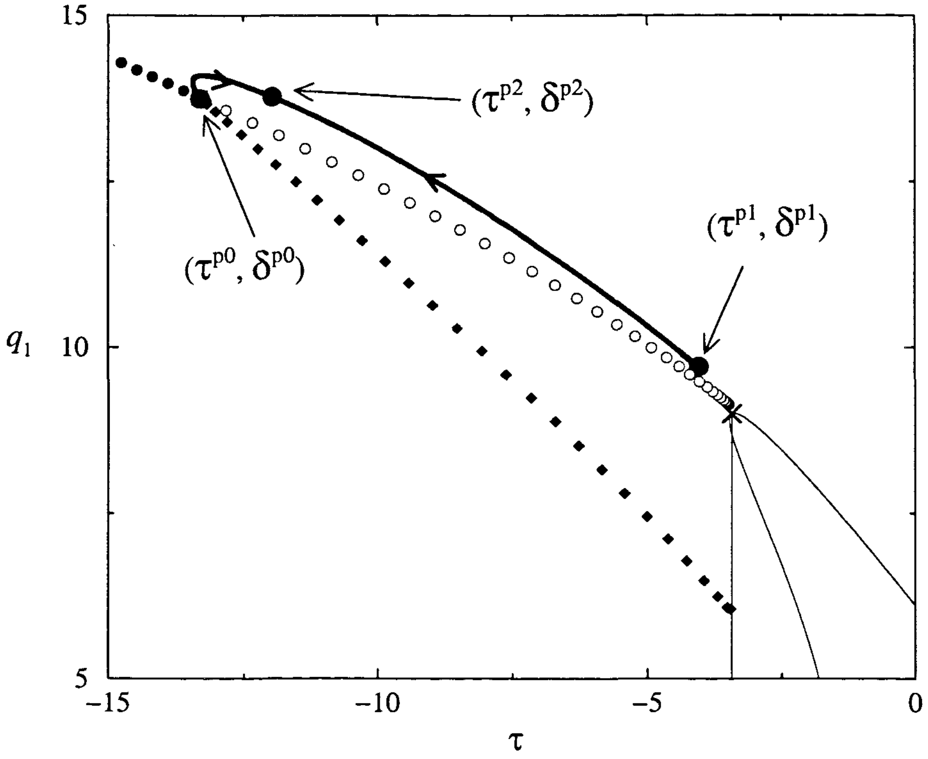

Figure 7.10: The thick solid line represents the locus of the period doubling bifurcation in the (τ, q_1)-space. The arrows in the figure indicate the direction of increasing δ and the critical points are $(\tau^{p0}, \delta^{p0}) = (-13.32855, 7.321577\delta \times 10^{-3})$, $(\tau^{p1}, \delta^{p1}) = (-4.041843, 2.321207\delta \times 10^{-1})$ and $(\tau^{p2}, \delta^{p2}) = (-12.04119, 7.220094\delta \times 10^{-1})$. The solution branch plotted with symbols has been computed for $\delta = 0.1$.

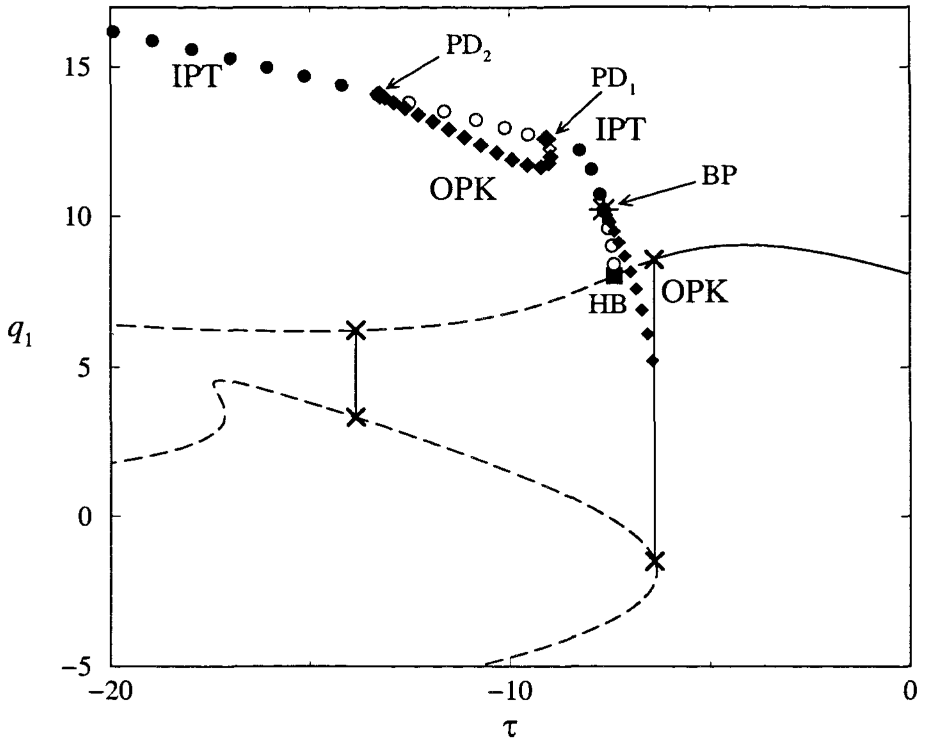

Figure 7.11: Solution branches plotted in the (τ, q_1)-space and computed with a fixed value of the dimensionless strain rate $\delta = 0.6$ and values of the material parameters $\widetilde{B} = -1.2$ and $\beta_1 = 0.9$. The lines are the steady states already explained in section 7.1, while the symbols indicate time dependent solutions. The solid circles are stable in-plane tumbling regimes (IPT) while the solid diamonds denote the out-of-plane kayaking state (OPK). The white symbols mark the unstable solutions. In the figure we can see the Hopf bifurcation (HB) from where an unstable solution emerges, this branch bifurcates at a branch point (BP), marked with a star symbol. The diamonds label the two period doubling bifurcations PD$_1$ and PD$_2$.

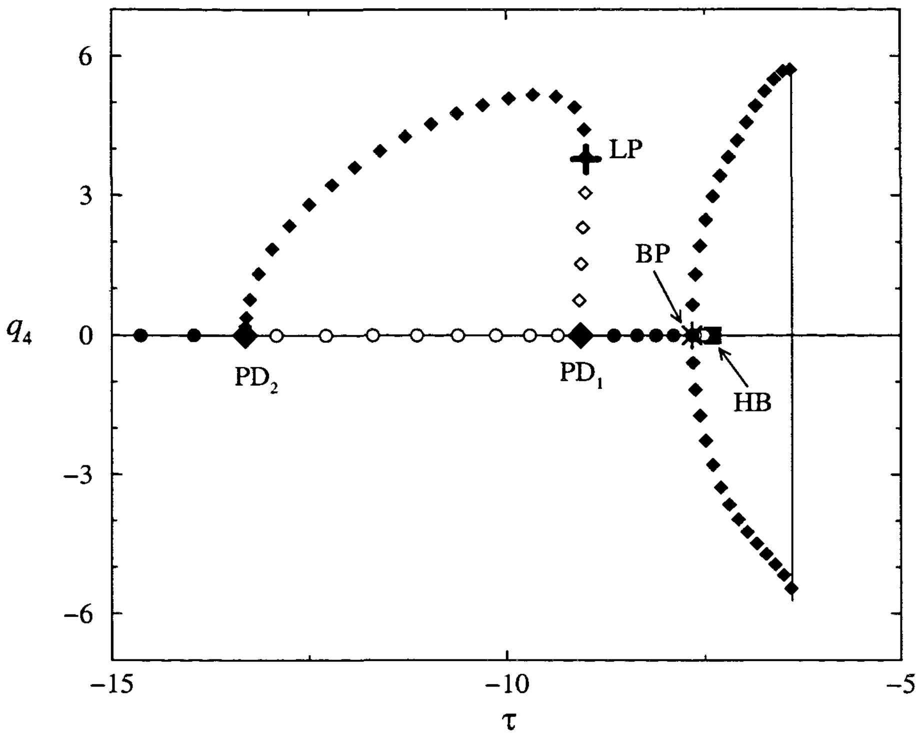

Figure 7.12: Solution of the system (7.3)-(7.7) for values of the material parameters $\beta_1 = 0.9$ and $\widetilde{B} = -1.2$ and fixed strain rate $\delta = 0.6$, plotted in the $(\tau,\ q_4)$-space. The circle symbols are the in-plane solutions, while the diamonds represent out-of-plane solutions. Solid symbols indicate stable states and white symbols denote the instability of the system. A solid square is the Hopf bifurcation (HB), the star symbol denotes a branch point (BP), large diamonds are period doubling bifurcations(PD$_1$ and PD$_2$) and a cross symbol is a limit point in the periodic solution (LP).

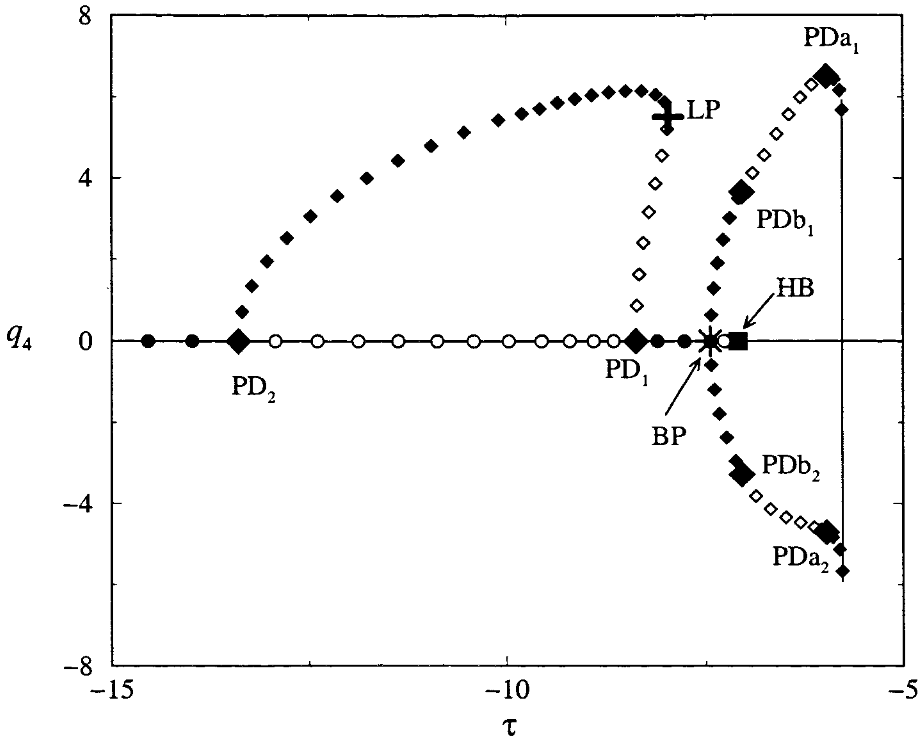

Figure 7.13: Solution of the system (7.3)-(7.7) for values of the material parameters $\beta_1 = 0.9$ and $\widetilde{B} = -1.2$ and fixed strain rate $\delta = 0.55$, plotted in the $(\tau,\ q_4)$-space. The circle symbols are the in-plane solutions, while the diamonds represent out-of-plane solutions. Solid symbols indicate stable states and white symbols denote the instability of the system. A solid square is the Hopf bifurcation (HB), the star symbol denotes a branch point (BP), large diamonds are period doubling bifurcations (PD_1 and PD_2, PDa and PDb) and a cross symbol is a limit point in the periodic solution (LP).

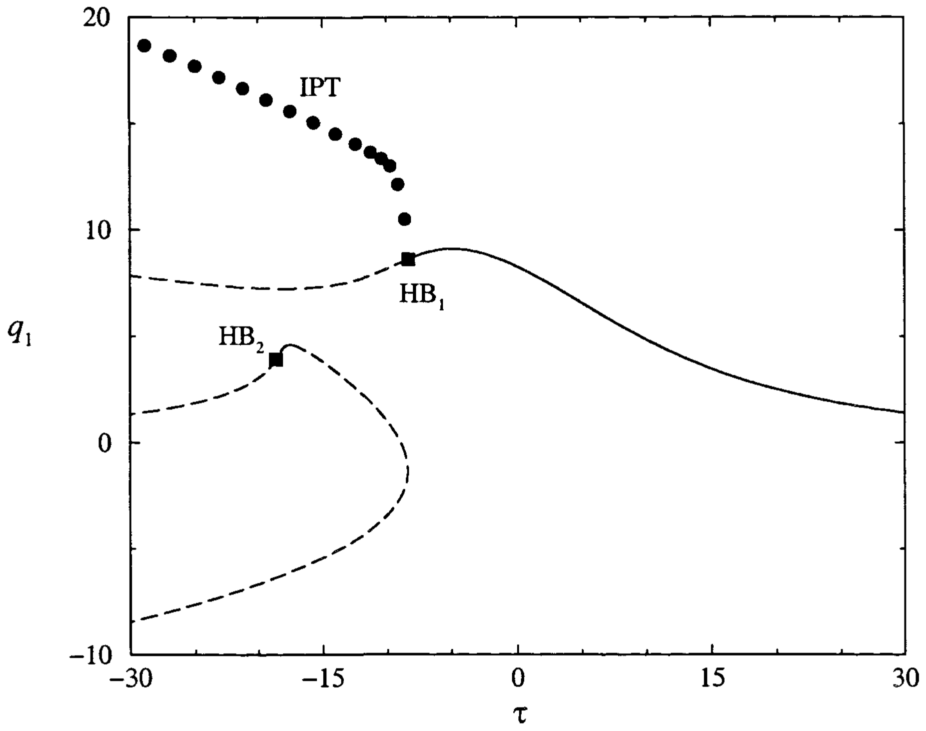

Figure 7.14: Solution branches computed with a fixed value of the dimensionless strain rate $\delta = 0.8$ and values of the material parameters $\widetilde{B} = -1.2$ and $\beta_1 = 0.9$. The thin solid line are the steady states discussed in previous sections. The square symbols are the Hopf bifurcations (HB). From HB_1 emerges the in-plane tumbling solution (IPT), being this the only stable time dependent solution.

the liquid crystal for the three dimensional case we compute the solution branches for fixed strain rates in the range ($\delta^{\mathrm{p}1}$, $\delta^{\mathrm{p}2}$). The solution for $\delta = 0.6$ is shown in figures 7.11 and 7.12, where the thin lines are the steady state solutions which have been described in section 7.1.

Figure 7.11 shows the solution in the (τ, q_1)-space, while in figure 7.12 the out-of-plane component q_4 is plotted against the dimensionless temperature, τ. We observe in the figures that an unstable in-plane branch emerges from the Hopf bifurcation. This solution becomes stable at a branch point (BP), which occurs at a lower temperature. Following the solution along the in-plane branch, as temperature decreases, we observe that the in plane tumbling state (IPT) loses its stability at a period doubling bifurcation (PD_1) and recovers stability at a lower temperature, by passing through a second period doubling bifurcation, (PD_2). For temperatures lower than that of PD_2 the in-plane tumbling state remains stable.

Switching branches at the branch point (BP) we find, as the temperature decreases, an stable out-of-plane kayaking state, that ends singularly at the temperature at which the steady degenerate solution occurs. This behaviour is shown in figure 7.12.

We can also switch branches at the period doubling bifurcations, to find another out-of-plane solution linking both bifurcations PD_1 and PD_2. This branch, which is clearly seen in figure 7.12, emerges from PD_1 and is unstable while temperature decreases until it reaches a limit point (LP) which changes the stability of the solution, so that from LP to PD_2 the kayaking state will be a stable time dependent solution.

Along the periodic orbits emerging from the branch point q_4 does not change sign and therefore the maximum of q_4 plotted against τ, can be either positive or negative, as seen in figure 7.12, while along the period doubled orbits the q_4 component changes sign and therefore the maximum of q_4 on the out-of-plane kayaking state emerging from the period double bifurcations is positive. This can be seen in 7.15, where several periodic orbits computed for $\delta = 0.6$ are plotted in the (q_1, q_2)-space. Those orbits emerging from the branch point can have either positive q_4 ($\tau = -6.962515$) or negative ($\tau = -7.157980$), while period doubled orbits ($\tau = -13.01108$) are symmetric with respect to $q_4 = 0$.

The appearance or not of the branch point in the in-plane solution determines the existence of one region of kayaking state, as seen for $\delta = 0.1$, or, as seen in the latter example for $\delta = 0.6$, two different regions of kayaking. Therefore, the computation of the locus of the branch point will allow us to understand the behaviour of the out-of-plane time dependent solutions of our system.

We used the software AUTO97 to continue in two parameters the locus of the branch points on time dependent solutions and we show the result in figure 7.16, where

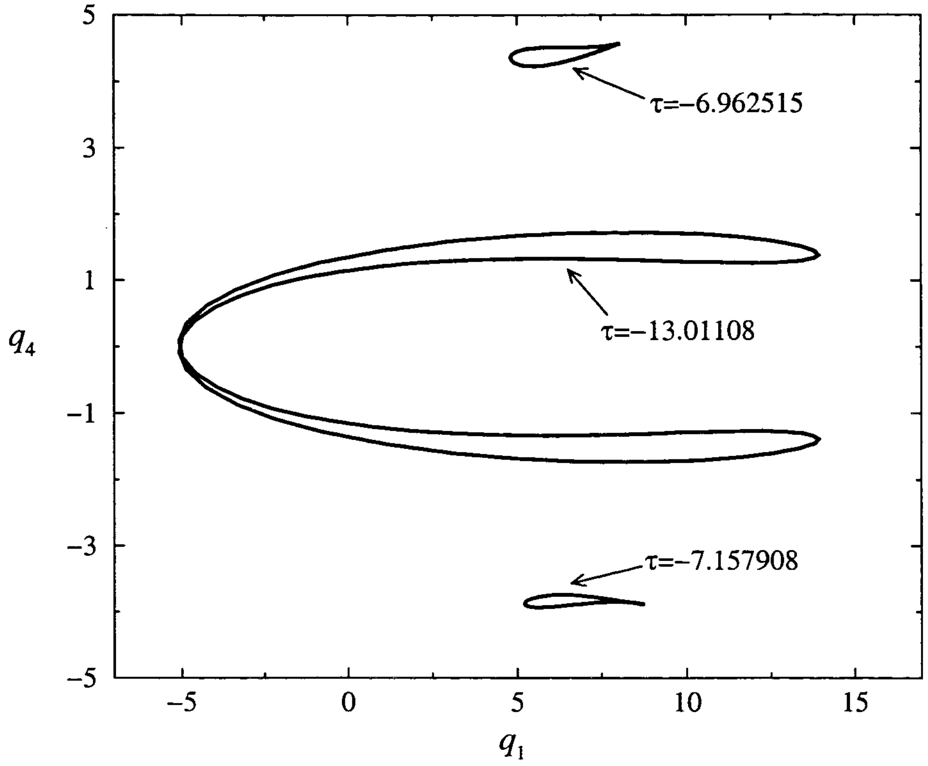

Figure 7.15: Periodic orbits computed for $\delta = 0.6$ and material parameters $\beta_1 = 0.9$ and $\widetilde{B} = -1.2$. The orbits have been computed for values of the dimensionless temperature $\tau = -6.962515$, $\tau = -7.157598$ and $\tau = -13.01108$. These last orbit emerges from a period doubling bifurcation and therefore has its period doubled.

this locus is plotted in the (τ, q_1)-space. Here the thick solid line labelled BP is the locus of the branch points, and the arrows indicate the direction of increasing δ. The critical values at which the branch point appears and disappears are (τ^{b1}, δ^{b1}) = (-4.042090, 0.2321365) and (τ^{b2}, δ^{b2}) = (-7.808064, 0.676255), respectively. The other branches in figure 7.16 are the solution branch for a fixed strain rate $\delta = 0.6$ which is plotted with thin lines and the locus of the period doubling bifurcation, plotted with a thick solid line and labelled PD. From our numerical calculations (τ^{b1}, δ^{b1}) and (τ^{p1}, δ^{p1}) differ by on 0.0001 % in each component and we conject that they represent the same point.

However, these are not the only bifurcations of the system. Figure 7.13 shows the time dependent solution calculated for a strain rate $\delta = 0.55$, where we observe that, the bifurcations of the time dependent solution branches are not only those described above, but also four new period doubling bifurcations, $\mathrm{PDa_1}$, $\mathrm{PDa_2}$, $\mathrm{PDb_1}$ and $\mathrm{PDb_2}$, occurring on one of the out-of-plane branches. These four bifurcations occur for two different values of τ: $\mathrm{PDa_1}$ and $\mathrm{PDa_2}$ both occur for $\tau = -5.973818$, while $\mathrm{PDb_1}$ and $\mathrm{PDb_2}$ occur at $\tau = -7.047385$.

Switching branches at these bifurcations will only produce unstable solutions, that, for the sake of clarity, we do not plot in figure 7.13, since they do not provide new information on the dynamics of the liquid crystal.

The locus of these period doubling bifurcations will be shown in the state diagram described in the next section. However, in order to achieve a better understanding of the dynamics of the liquid crystal for the small range of parameters where the secondary bifurcations exist a more detailed numerical and analytical study of the time dependent branches will be needed. Nevertheless, the results described in this section allow us to explain the three dimensional time dependent behaviour of a nematic liquid crystal under a shear flow, for the majority of the parameter space.

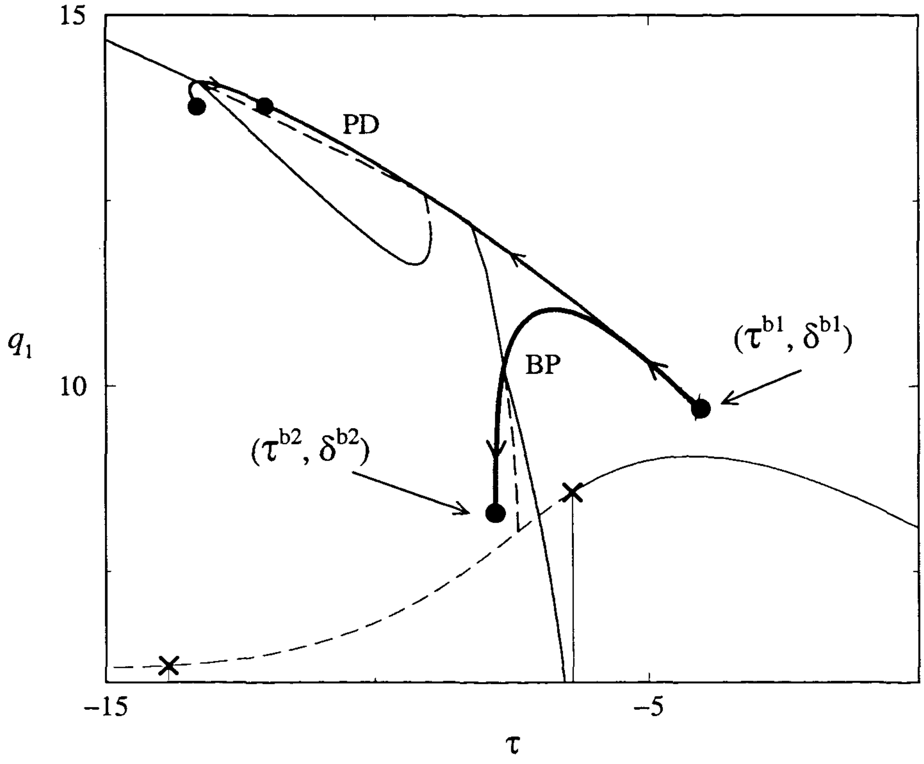

Figure 7.16: The thick solid line labelled BP is the locus of the branch point of the time dependent solution. This solution is plotted together with the locus of the period doubling bifurcation, labelled PD in the figure, and the solution for $\delta = 0.6$ plotted with thin solid lines. The critical points occur at $(\tau^{b1}, \delta^{b1}) = (-4.042090, 2.321365 \times 10^{-1})$ and $(\tau^{b2}, \delta^{b2}) = (-7.808064, 6.76255 \times 10^{-1})$.

7.4 The state diagram for the three dimensional case

We have seen in the previous section, 7.3, that the time dependent behaviour of a three dimensional nematic liquid crystal falls into one of the following types:

- in-plane tumbling, where the director rotates in the shear plane continuously on time,
- in-plane wagging state, where the director angle is periodic and therefore the director vector wags backwards and forwards in the shear plane,
- out-of-plane kayaking state, where the orbit of the director vector comes out of the shear plane.

We have used AUTO97 to produce the state diagram shown in figure 7.17. Here we plot the locus of some of the bifurcations of the steady state solution: the Hopf bifurcation of the IPN branch (labelled HB in the figure) and the locus of the branch point (BP). In the figure are also shown the bifurcations of the time dependent solutions which are the period doubling bifurcation (PD) and branch point (PBP), and the locus of the bifurcations on the kayaking branches, a limit point (labelled PLP) and period doubling bifurcations (SPD).
In figure 7.17 we distinguished two different regions:

$\boxed{1}$ This region, shaded with vertical lines, is the set of values of the parameter space where the tumbling state is a stable solution of the system. The boundary between tumbling and wagging, that would divided this area into two subregions has not been calculated here. However, by comparison with the two dimensional case we can establish that for very small strain rates and temperatures to the left of the period doubling bifurcation (PD) the stable solution is of the tumbling type, while for strain rates and temperatures within region 1 that are near the locus of the Hopf bifurcation (HB) the liquid crystal adopts a wagging state.

$\boxed{2}$ Inside this region, shaded with oblique lines, the kayaking state is a time dependent stable solution.
For strain rates smaller than δ^{p1}, the smallest value at which two period doubling bifurcations appear, the kayaking state exists for temperatures bounded between

the locus of the branch point of the steady state solution (BP) and the period doubling bifurcation (PD).

For strain rates larger than δ^{p1} the kayaking state splits into two out-of-plane solutions (see figures 7.9 and 7.11), but the dynamics of the splitting of the time dependent solution have not been fully understood. However, we know that in a very small triangular region bounded by PLP on the top and by PBP and SPD on the sides, two different kayaking states coexist.

Also in the region bounded by PLP, PBP and PD the kayaking state coexists with an in-plane time dependent solution, as it can be seen in figure 7.13.

For strain rates larger than δ^{p2}, the value at which the two period doubling bifuration points merge, the system does not exhibit any out-of-plane periodic solution.

This summary is an accurate description of the time dependent dynamics of the liquid crystal on the three dimensional case, however several questions are left unanswered: the behaviour of the liquid crystal for very small strain rate, $\delta = O(10^{-3})$ or smaller; the mechanism of formation of several kayaking solutions and the time dependent behaviour inside the small unshaded region in figure 7.17, situated to the left of the locus of the branch point (BP).

Combining this state diagram with that of the steady state solutions, shown in figure 7.8, we obtain the full state diagram for the three dimensional case from where we conclude that the in-plane nematic solution does not coexist with any time dependent state, while the log-rolling solution, stable only for very small strain rates coexists with the tumbling regime.

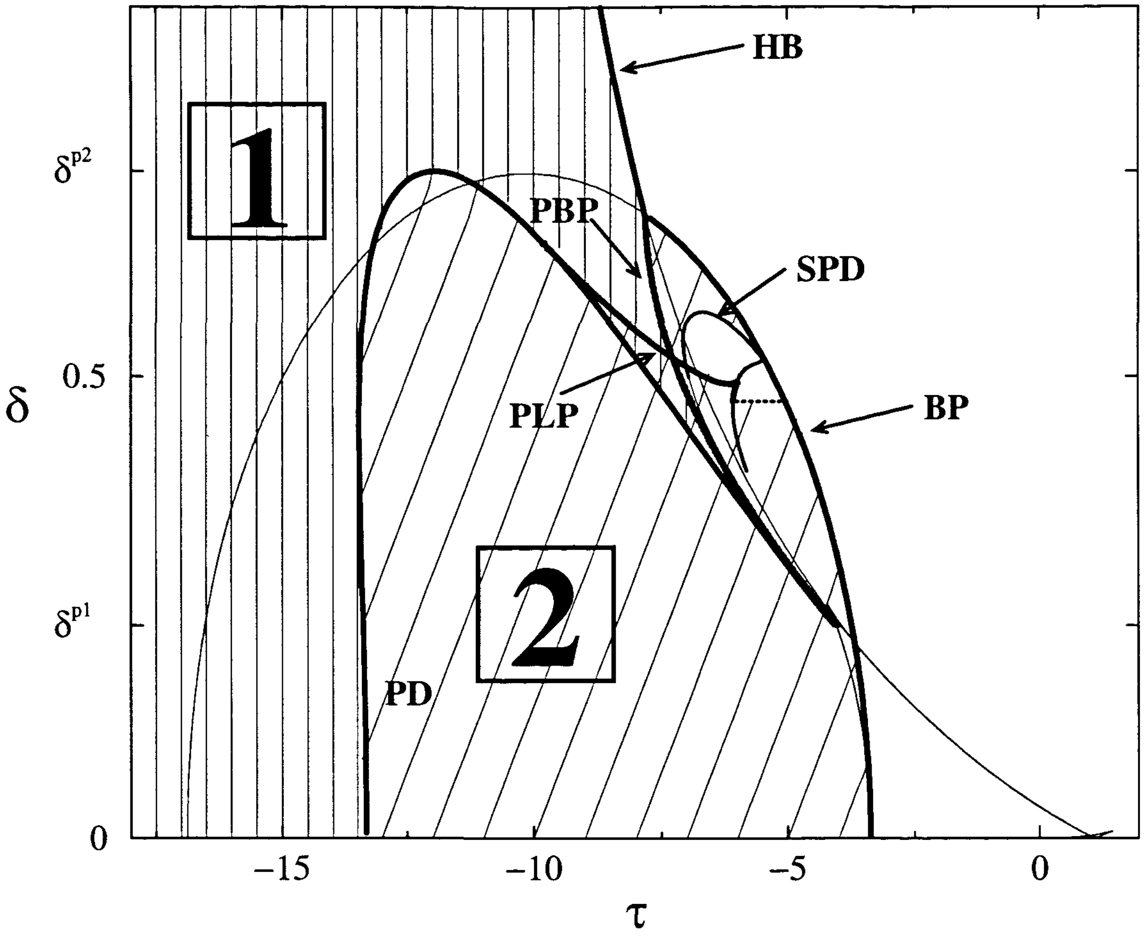

Figure 7.17: State diagram for the time dependent solutions. Region 1, shaded with vertical lines, is where the in-plane periodic solutions are stable, while region 2, shaded with oblique lines, is where the out-of-plane time dependent solution is stable. The HB curve is the locus of the Hopf bifurcation, BP is the locus of the branch point of the steady state solution, PD and SPD are the locus of period doubling bifurcations in the in-plane and out-of-plane solutions, respectively, PBP is the locus of the branch point on a periodic solution and PLP is the locus of a limit point on an out-of-plane state. The strain rate δ^{p1} is the smallest value at which the system exhibits two period doubling bifurcations, while δ^{p2} is the critical strain at which these two bifurcations merge.

Chapter 8

Future Directions and Conclusions

In this thesis we have described the nonlinear dynamics of a thermotropic nematic liquid crystal in a shear flow for the two and three dimensional cases and we have analysed the behaviour of a two dimensional liquid crystal under a general flow, explaining the influence of strain and vorticity in the dynamics of the system.

8.1 Future Directions

A natural next step in our research would be to consider a nematic liquid crystal confined between two parallel plates and study the effects of strong and weak anchoring conditions on the sheared material, as well as the effects of homeotropic and planar anchoring. Other geometries as concentrical cylinders could also be of interest in order to compare the analytical results to experimental data. Experiments have also been carried out with elongational flows [36] and therefore solving the system for this type of flows we could analyse the agreement between experimental and numerical results. Considering the effects of non-homogeneity in the different types of systems could offer an explanation of the banded textures [20] and defects found experimentally in liquid crystalline materials.

Finally, the study of phase transitions in a nematic liquid crystal [43, 40] was the original problem we intended to solve but the development of our research took us along different paths, leaving the phase transition as a subject for further research.

8.2 Conclusions

This thesis is a structured description of the nonlinear dynamical behaviour of a nematic liquid crystal under a shear flow.
In chapter 2 we have described the bulk states, introducing the concepts of distribution function and tensor order parameter as measures of the degree of macroscopic alignment of the molecules that constitute a liquid crystal. In this chapter we have explained the concept of Landau free energy density and find that the equilibrium bulk states, those that minimize the free energy, fall into one of the following categories

- an isotropic state which exists for non negative values of the dimensionless temperature;
- a uniaxial nematic state with preferred direction of alignment in the xy-plane. This state exists for values of the dimensionless temperature smaller than 9/8;
- a uniaxial nematic state with preferred direction of alignment perpendicular to the xy-plane, which exists for dimensionless temperatures smaller than 9/8.

In chapter 3 we discuss at length the Landau-de Gennes model for the dynamics of a liquid crystal in a flow. We derive the governing equations of the Olmsted and Goldbart model [41] and compare the obtained equations to those of the classical Leslie-Ericksen theory in order to find correspondences between the parameters of both theories. These relationships will allow us to establish a comparison between our results obtained using the Landau-de Gennes model and many results obtained in terms of the widely used Leslie-Ericksen theory.
In chapter 5 we explain the dynamics of a homogeneous nematic liquid crystal under a shear flow when it is confined to the shear plane. A complex array of behaviours is described in this chapter in terms of the parameters of the system; the temperature and the strain rate. The continuation of the solution branches and the state diagram of the system were computed using the continuation and bifurcation software AUTO97. We have found, for any fixed strain rate, four steady solution branches that correspond to two physically distinctive states: the IPN branch, described in section 5.3, where an in plane nematic state is the only stable solution, and the LRN branch, where the stable state corresponds to a uniaxial nematic aligned perpendicularly to the shear plane, the so-called log-rolling state, described in section 5.4.
The IPN branch, for small shear rates and positive temperatures adopts a paranematic

state, aligning close to a $\pi/4$ angle with respect to the positive x-axis. As temperature decreases the system evolves into a stable in-plane nematic state which loses its stability when the system is aligned almost parallely to the x-axis. We have also proved that, for very small shear rates and very negative temperatures, the system tumbles, finding excellent agreement between numerical and analytical results. In section 5.3.1.2 we have established a correspondence between our prediction of tumbling and that of the Leslie-Ericksen theory, which has been successfully employed to model experimental results of director tumbling.

The existence of a Takens-Bogdanov point in the underlying bifurcation scheme of the IPN branch organises the steady and time dependent states. We have predicted analytically the Takens-Bogdanov bifurcations as well as the locus of a Hopf bifurcation local to the this point, and also the locus of a homoclinic bifurcation, where the orbits have infinite period and eventually break up. The analytical approximations of these loci are in excellent agreement with the numerical results computed using AUTO97, as seen in section 5.3.2.1.

The locus of the Hopf bifurcation determines the existence of wagging solutions for intermediate values of the strain rate, and in section 5.3.3 we explain, by introducing a new set of variables, the difference between the wagging and tumbling states and the mechanism of continuation from one time dependent state to the other.

The out-of-plane log-rolling state which exists for all values of the strain rate, is described in section 5.4 while in section 5.4.2 we perform an analysis of the system for very large values of the strain rate, finding that the locus of the limit point of the LRN branch and the locus of the HB on the IPN branch present vertical asymptotes in the state diagram.

A complete summary of the behaviour of a two dimensional nematic liquid crystal in a shear flow is given by the state diagram described in section 5.5.

In order to complete the analysis of the two dimensional case, and to achieve a better understanding of the behaviour of an homogeneous liquid crystal in a planar flow, we study, in chapter 6, the importance of strain and vorticity in the system, concluding that the prevalence of strain over vorticity favours the alignment of the liquid crystal with flow, while flows with stronger vorticity than strain will favour the appearance of tumbling regimes at higher temperatures. The stability of the log-rolling state is independent of the type of flow, this being a stable solution for any planar flow.

The three dimensional case, described in chapter 7, presents a more complex array of behaviours and hence a more complicated underlying bifurcation diagram. The steady state solutions are described in section 7.2. Here we show that the only out-of-plane solutions that the system has are two degenerate continuum of equilibria which have been calculated analytically and numerically with excellent agreement between both results. In agreement with other theories we observe that the steady states solutions are the nematic states for large temperatures and that the log-rolling state is only stable for very small strain rates and negative dimensionless temperatures. Further analysis of the log-rolling solution for very small strain rates could bring light on the range of values for which this solution is stable, since in this thesis we have not produce an explanation of the dynamic mechanism that destabilizes the LRN branch for larger values of the strain rate.

In section 7.3 we classified the time dependent solutions into tumbling or wagging states when the director remains in the shear plane, or kayaking solutions when the director comes out of the shear plane. The existence of period doubling bifurcations in the underlying bifurcation diagram organises the in-plane and out-of-plane periodic solutions. However, bifurcations of the periodic solutions complicate the state diagram, making it very difficult to understand the behaviour of the system in every region of the parameter plane. Nevertheless, we were able to determine the steady and time dependent behaviour of the system on a wide range of values of the parameter space, as shown in the state diagrams in sections 7.2.4 and 7.4.

Appendix A

Asymptotic analysis about the supercooling limit

The supercooling limit $\tau = S_1 = S_2 = 0$, where the isotropic phase in the absence of flow becomes unstable is a singularity of the system. In order to understand how the system behaves near this point we conduct a local analysis about this point with δ small. In order to obtain a consistent expansion about $(S_1,\, S_2,\, \theta) = (0,\, 0,\, \pm\pi/4)$ of the steady form of the system (5.4)-(5.6) we define $\epsilon = \delta^{1/2}$ and make the expansion

$$\begin{aligned}
\tau &= \tau^{(1)}\epsilon + \mathrm{O}(\epsilon^2)\,, \\
S_1 &= S_1^{(1)}\epsilon + \mathrm{O}(\epsilon^2)\,, \\
S_2 &= S_2^{(1)}\epsilon + \mathrm{O}(\epsilon^2)\,, \\
\theta &= \pm\frac{\pi}{4} + \theta^{(1)}\epsilon + \mathrm{O}(\epsilon^2)\,.
\end{aligned}$$

Inserting these forms into the system (5.4)-(5.6), at second order in ϵ we have two systems of three equations (one system from expanding about $\theta = \pi/4$ and the other from expanding about $\theta = -\pi/4$) for the three unknowns, $S_1^{(1)}$, $S_2^{(1)}$, $\theta^{(1)}$ and the one parameter $\tau^{(1)}$.

The expansion about $\theta = \pi/4$ gives

$$\tau^{(1)} S_1^{(1)} - 3 S_1^{(1)^2} + 9 S_2^{(1)^2} = \frac{-3^5\beta_1}{4\widetilde{B}^3}\,, \tag{A.1}$$

$$\tau^{(1)} S_2^{(1)} + 6 S_1^{(1)} S_2^{(1)} = \frac{3^4\beta_1}{4\widetilde{B}^3}\,, \tag{A.2}$$

$$\theta^{(1)} = \frac{\widetilde{B}}{6\beta_1}\left(S_1^{(1)} - S_2^{(1)}\right), \tag{A.3}$$

and from expanding about $-\pi/4$ we obtain the following system

$$\tau^{(1)}S_1^{(1)} - 3S_1^{(1)^2} + 9S_2^{(1)^2} = \frac{3^5\beta_1}{4\widetilde{B}^3}, \tag{A.4}$$

$$\tau^{(1)}S_2^{(1)} + 6S_1^{(1)}S_2^{(1)} = \frac{-3^4\beta_1}{4\widetilde{B}^3}, \tag{A.5}$$

$$\theta^{(1)} = \frac{\widetilde{B}}{6\beta_1}\left(S_2^{(1)} - S_1^{(1)}\right). \tag{A.6}$$

Equations (A.1)-(A.6) define the relations between $\tau^{(}1)$, $\S_1^{(1)}$, $\S_2^{(1)}$ and $\theta^{(1)}$, and the result of this analysis is plotteded in the ($\tau^{(1)}$, $S_1^{(1)}$)-plane and in the ($S_1^{(1)}$, $S_2^{(1)}$)-plane is shown in figures A.1a and A.1b respectively , the solid lines represent the analytical solution and the solid dots are the numerical results computed using AUTO97 on the full system. We observe a good agreement between the analytical and numerical results.

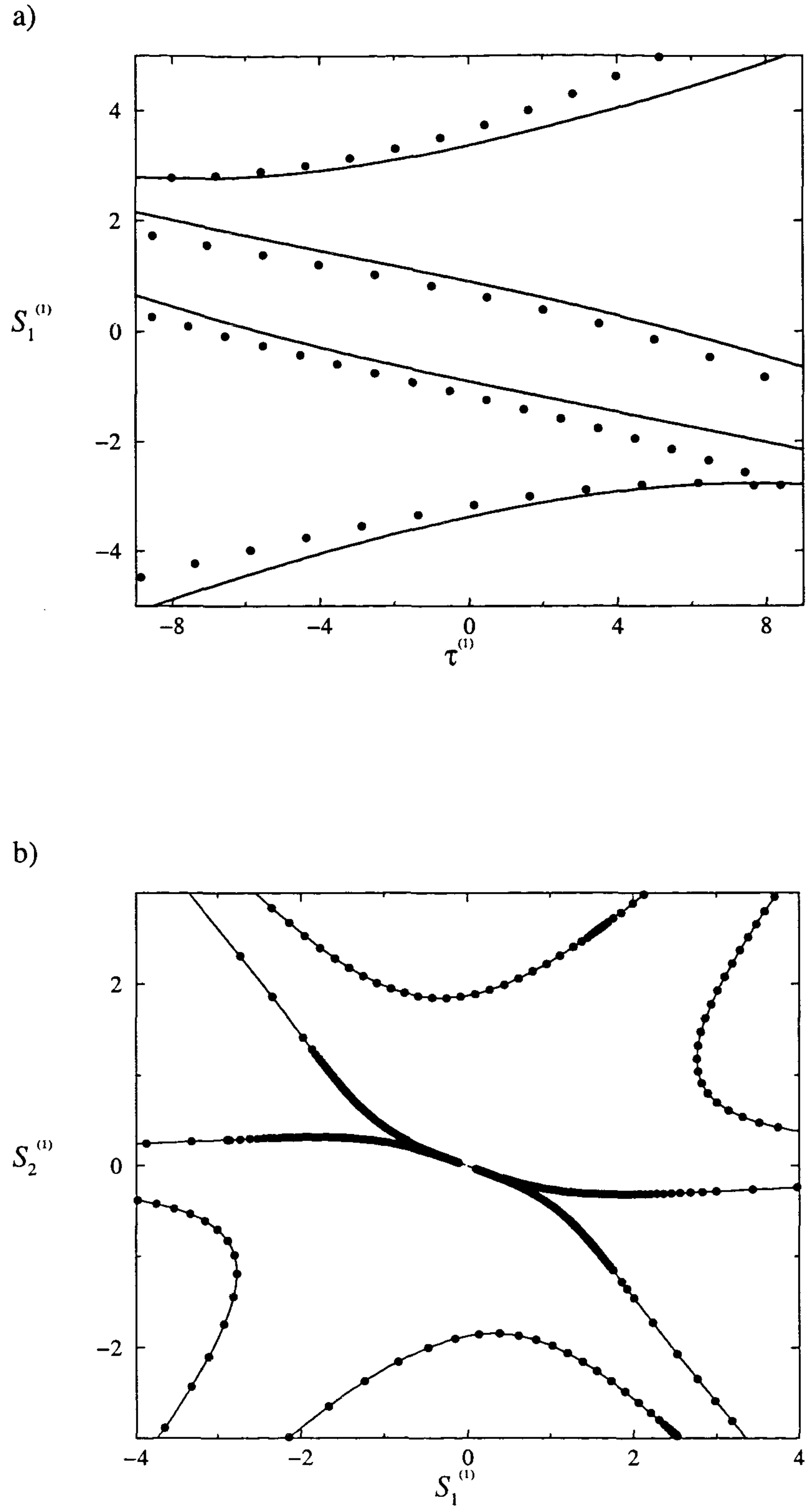

Figure A.1: The solid lines represent the asymptotic solutions for small strain rate obtained from systems (A.1)-(A.3) and (A.4)-(A.6) and the solid dots are the numerical calulations obtained using AUTO97. Figure a) shows a comparison of our results in $\tau^{(1)}$ and $S_1^{(1)}$ while Figure b) shows the comparison in the ($S_1^{(1)}$, $S_2^{(1)}$)-plane.

Appendix B

Bifurcation diagram of the normal form at the Takens-Bogdanov point

Local to the Takens Bogdanov point the original system (5.4)-(5.6) can be reduced to its normal form (5.36)-(5.37) by applying centre of manifold theory [55] and normal form reduction [56] (see section 5.3.2.1). The reduced system is

$$\dot{\eta}_1 = \eta_2 \,, \tag{B.1}$$

$$\dot{\eta}_2 = \xi_1 + \xi_2\eta_1 + \eta_1^2 - \eta_1\eta_2 \,, \tag{B.2}$$

where $(\xi_1,\, \xi_2)$ is the parameter space and the Takens-Bogdanov bifurcation occurs at $\xi_1 = \xi_2 = 0$. We now proceed to study the bifurcation diagram of this system about the origin as was done by Kuznetsov [56]. This diagram is shown in figure B.1, where the Takens-Bogdanov point is the origin of the $(\eta_1,\, \eta_2)$-space.The solid bold line are the loci of the limit points and Hopf bifurcation, labelled **LP** and **H** respectevely. The dashed line is the locus of the saddel homoclinic bifurcation, **SHB**.
The equilibria of the system are

$$E_1 : (E_1^0,\, 0) = (-\frac{1}{2}\xi_2 - \frac{1}{2}\nu,\, 0)$$

and

$$E_2 : (E_2^0,\, 0) = (-\frac{1}{2}\xi_2 + \frac{1}{2}\nu,\, 0),$$

where $\nu = \sqrt{\xi_2^2 - 4\xi_1}$ is the distance between E_1 and E_2.
The locus of limit points, where the two equilibria are coincident, is given by

$$\mathbf{LP} = \{\xi_2^2 - 4\xi_1 = 0\}. \tag{B.3}$$

In the region of the parameter space to the right of **LP** there are no equilibrium points, but when we cross **LP** from right to left two equilibria are created. For negative values of ξ_2 the equilibria are a stable node, E_1, and a saddle, E_2, while for $\xi_2 > 0$, the equilibria are an unstable node, E_1, and a saddle point E_2.
From the Takens-Bogdanov point a branch of Hopf bifurcations emerges, i.e., a locus of points were the linearised system has a pair of pure imaginary eigenvalues. Analysing the system (B.1)-(B.2) we observe that this occurs on

$$\mathbf{H} = \{\xi_1 = 0,\ \xi_2 < 0\}. \tag{B.4}$$

On **H** the phase portrait presents a saddle and a centre, that evolves into an unstable node and a stable limit cycle to the left of **H**.
Therefore the bifurcation diagram local to the Takens-Bogdanov point, shown in figure B.1, is as follows

- To the right of the locus of the limit points **LP** the system has noequilibria. This region is labelled 1 in figure B.1.

- For negative values of ξ_2 to the left of **LP** and to the right of the locus of the Hopf Bifurcation given by **H**, region 2 in the figure, the system has two equilibrium points: a saddle and a stable node.

- On the Hopf bifurcation branch, **H**, the equilibrium points are a saddle and a centre.

- To the left of the Hopf bifurcation the centre evolves into an unstable node and a stable limit cycle, therefore periodic orbits are generated. This occurs on region 3 of figure B.1.

- However, to the left of **LP** with positive values of ξ_2, region 4, the equilibrium points are a saddle and an unstable node, and there is no limit cycle.

- Consequently there exists a global bifurcation branch where the limit cycles break down and which separates regions 3 and 4. This phenomena occurs at a saddle homoclinic bifurcation labelled as **SHB** in figure B.1.

Our next task is to approximate the locus of the global bifurcation, **SHB**, on the parameter space. We transform the system (B.1)-(B.2) into an orbitally equivalent system, and by analyzing the locus of the homoclinic orbits of the latter we find the locus of the homoclinic orbits of the original system. Here, by orbitally equivalent systems we understand that we can transform one into the other by a smooth invertible change of coordinates and multiplication of the variables by a positive function.

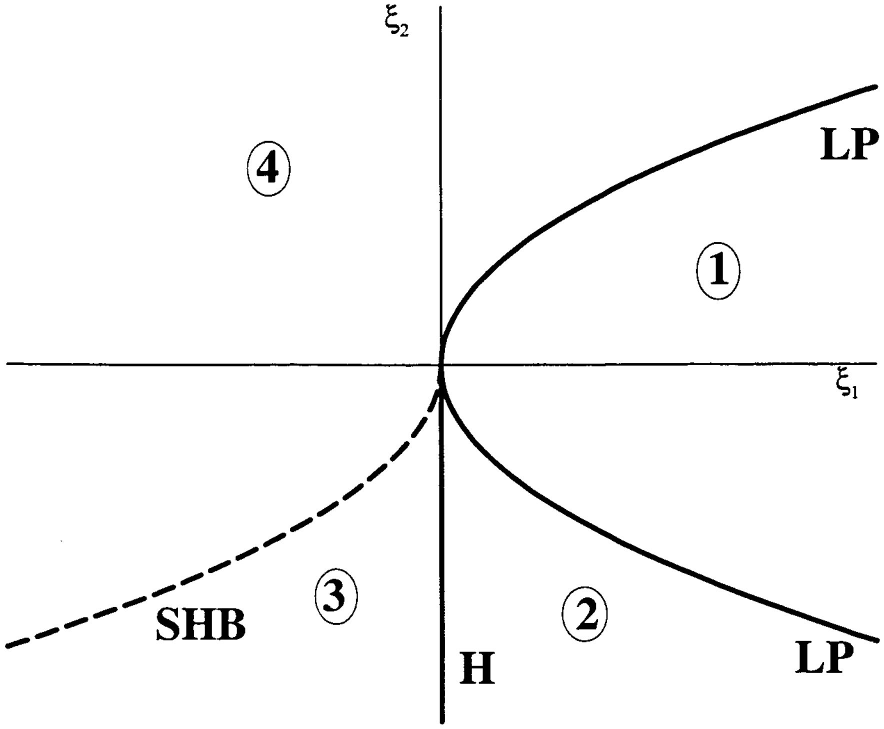

Figure B.1: Bifurcation diagram of the normal form local to the Takens-Bogdanov point. The Takens-Bogdanov bifurcation is located at the origin of the parameter space (ξ_1, ξ_2). The parabola **LP** is the locus of the limit points given by (B.3). The curve **H** represents the locus of the Hopf bifurcation given by (B.4) and the curve **SHB** is an approximation of the saddle-homoclinic bifurcation. In region 1 there is not equilibrium points. In region 2 there is a saddle and a stable node that evolves into a centre on **H**. In region 3 the centre has changed into an unstable node and a limit cycle, while the saddle is still present. The limit cycle breaks down in **SHB** to leave in region 4 a saddle and an unstable node.

We perform a translation of the variables (η_1, η_2) such that E_1 is set to be the new origin of coordinates

$$\bar{\eta}_1 = \eta_1 - E_1^0 ,$$
$$\bar{\eta}_2 = \eta_2 ,$$

so that the system (B.1)-(B.2) becomes

$$\dot{\bar{\eta}}_1 = \bar{\eta}_2 ,$$
$$\dot{\bar{\eta}}_2 = \bar{\eta}_1(\bar{\eta}_1 - \nu) - \bar{\eta}_2(E_1^0 + \bar{\eta}_1) .$$

We now re-scale the variables in such a way that the distance between the two equilibria is set to one. The appropriate new variables and time scale are given by

$$\zeta_1 = \nu^{-1}\bar{\eta}_1 ,$$

$$\zeta_2 = \nu^{-3/2}\bar{\eta}_2\,,$$
$$\bar{t} = \nu^{1/2}t$$

and the re-scaled system is

$$\dot{\zeta}_1 = \zeta_2\,, \tag{B.5}$$
$$\dot{\zeta}_2 = \zeta_1(\zeta_1 - 1) - \zeta_2(\gamma_1 + \gamma_2\zeta_1)\,, \tag{B.6}$$

where the new parameters are

$$\gamma_1 = E_1^0\nu^{-1/2} \tag{B.7}$$

and

$$\gamma_2 = \nu^{1/2}\,, \tag{B.8}$$

with $\gamma_2 \geq 0$.

This system is orbitally equivalent to (B.1)-(B.2), therefore the locus of the homoclinic orbits of (B.5)-(B.6) will provide us the locus of the homoclinic orbits of the original system.

We study the behaviour of the system locally to the origin of the (ξ_1, ξ_2)-space which corresponds to the origin of the (γ_1, γ_2)-plane and in order to find an approximation of the locus of the saddle homoclinic bifurcation we consider $||(\gamma_1, \gamma_2)|| \ll 1$, and to the zero-th order ($\gamma_1 = \gamma_2 = 0$), the system (B.5)-(B.6) becomes the Hamiltonian system

$$\dot{\zeta}_1 = \frac{\partial H}{\partial \zeta_2}\,, \tag{B.9}$$
$$\dot{\zeta}_2 = -\frac{\partial H}{\partial \zeta_1}\,, \tag{B.10}$$

with the Hamilton function

$$H = \frac{1}{2}\zeta_1^2 + \frac{1}{2}\zeta_2^2 - \frac{1}{3}\zeta_1^3\,.$$

The equilibria of (B.9)-(B.10) are a centre at $E_1\!:(0,0)$ and a saddle at $E_2\!:(1,0)$. The values of the Hamiltonian at these points are $H(E_1) = 0$, $H(E_2) = 1/6$, while the orbits of (B.9)-(B.10) are the curves $H(\zeta_1, \zeta_2) = h$ where h is a real number. The closed orbits of the system correspond to $h \in (0, 1/6)$ and the curve $H = 1/6$ corresponds to the saddle separatrices, which form an homoclinic orbit to the left of the saddle. The phase portrait of the Hamiltonian system is sketched in figure B.2.

We introduce the parameters γ_1 and γ_2 back in the system, with $||(\gamma_1, \gamma_2)|| \ll 1$, the closed orbits of the Hamiltonian system will split, see figure B.3, and if we re-parameterize the interval $\zeta_1 \in (0,\,1)$ of the ζ_1 axis by $h \in (0,\,1/6)$ such that $h = H(\zeta_1,\,0)$, then for any given number h in the interval $(0, 1/6)$ one orbit crossing

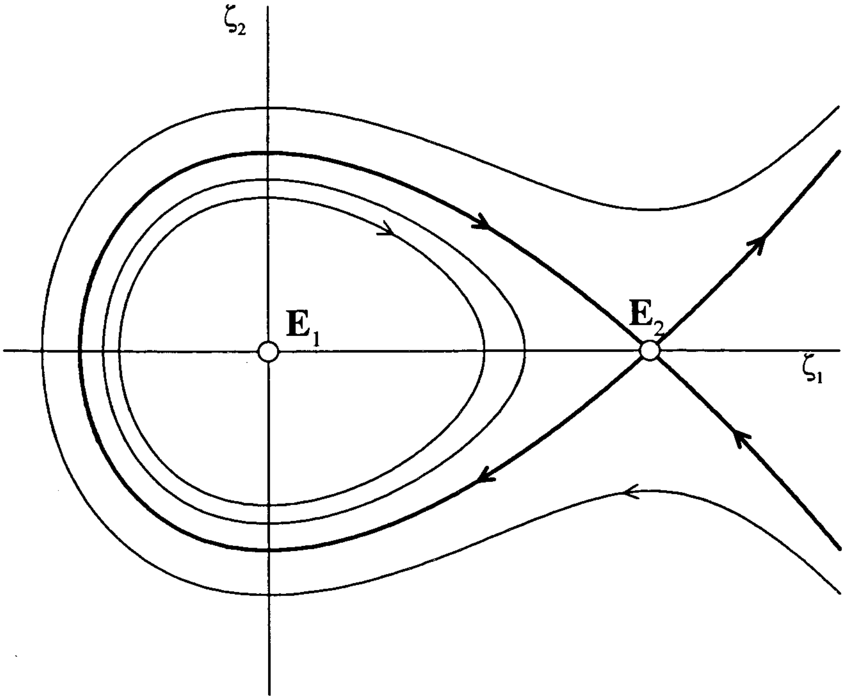

Figure B.2: The labelled points are the equilibria of the system (B.9)-(B.10): $\mathbf{E}_1$ is a centre and $\mathbf{E}_2$ is a saddle, while solid lines are its orbits, corresponding to the Hamiltonian function being a constant. The bold lines are the saddle separatrices that form a homoclinic orbit to the left of the saddle.

the ζ_1- axis at $\zeta_1 = h$ will intersect the ζ_1-axis in backwards time at $\zeta_1 = \zeta_-$ with $t = t_-$ and in forwards time, $t = t_+$, at $\zeta_1 = \zeta_+$, therefore we can define the split function, $\Delta(h,\, \gamma_1, \gamma_2)$, as the difference between the Hamilton function evaluated at the intersection at backwards time and evaluated at the intersection at forwards time. Then

$$\Delta(h,\, \gamma_1, \gamma_2) = H(\zeta_-, 0) - H(\zeta_+, 0) = \int_{t_+}^{t_-} \dot{H}\, dt\,, \tag{B.11}$$

with $h \in (0, 1/6)$. This definition can be extended to the closed interval by defining $\Delta(0,\, \gamma_1,\, \gamma_2) = 0$ and $\Delta(1/6,\, \gamma_1,\, \gamma_2)$ equal to the difference of the value of the Hamilton function at the points $(\zeta_-,\, 0)$ and $(\zeta_+,\, 0)$ of the saddle separatrices.
Given this definition of Δ the equation

$$\Delta(h,\, \gamma_1,\, \gamma_2) = 0 \tag{B.12}$$

with $h \in (0\, 1/6)$ provide us an expression for the locus of the closed orbits of the system (B.5)-(B.6) that intersect the horizontal axis at $\zeta_1 = h$, while the equation

$$\Delta(1/6,\, \gamma_1,\, \gamma_2) = 0 \tag{B.13}$$

gives a curve on the half upper plane of the $(\gamma_1,\, \gamma_2)$-space which corresponds to the locus of the saddle homoclinic bifurcation of (B.5)-(B.6). Therefore, if we have an approximation of the split function, we can find the locus of the saddle homoclinic bifurcation in the parameter space (γ_1, γ_2).

We evaluate the derivative of the Hamilton function on orbits of (B.5)-(B.6) to obtain

$$\dot{H} = \frac{\partial H}{\partial \zeta_1}\dot{\zeta}_1 + \frac{\partial H}{\partial \zeta_2}\dot{\zeta}_2 = -\zeta_2^2(\gamma_1 + \gamma_2\zeta_1)\,,$$

and combining this result with the definition of the split function given in equation (B.11) we have

$$\Delta(h, \gamma_1, \gamma_2) = \int_{t_+}^{t_-} \dot{H}\,dt = -\int_{t_-}^{t_+} \dot{H}\,dt = \int_{t_-}^{t_+} \zeta_2^2(\gamma_1 + \gamma_2\zeta_1)\,dt\,. \tag{B.14}$$

Since $d\zeta_1 = \zeta_2\,dt$, from equation (B.9), we can re-write equation (B.14) as

$$\Delta(h, \gamma_1, \gamma_2) = \gamma_1 \int_{\Gamma(h)} \zeta_2\,d\zeta_1 + \gamma_2 \int_{\Gamma(h)} \zeta_1\zeta_2\,d\zeta_1\,, \tag{B.15}$$

where $\Gamma(h)$ is the orbit corresponding to h oriented in the direction of increasing time. We want an approximation of the split function valid for $||(\gamma_1, \gamma_2||) \ll 1$, so we can consider the orbits of the system (B.5)-(B.6) to be a perturbation of the orbits of the Hamiltonian system (B.9)-(B.10), and therefore we can approximate the integrals along the orbit $\Gamma(h)$ by the integrals along $H = h$. Then equation (B.15) yields

$$\Delta(h, \gamma_1, \gamma_2) = \gamma_1 I_1(h) + \gamma_2 I_2(h)\,, \tag{B.16}$$

where $I_1(h)$ and $I_2(h)$ are the integrals

$$I_1(h) = \int_{H=h} \zeta_2\,d\zeta_1 \tag{B.17}$$

and

$$I_2(h) = \int_{H=h} \zeta_1\zeta_2\,d\zeta_1. \tag{B.18}$$

Therefore if we apply the Implicit Function Theorem to equation (B.12), considering the definition of the split function given by (B.16), we obtain that the locus of the closed orbits of system (B.5)-(B.6), for $||(\gamma_1, \gamma_2)|| \ll 1$ is given by

$$\gamma_1 = -\frac{I_2(h)}{I_1(h)}\gamma_2 + \mathrm{O}(||(\gamma_1, \gamma_2)||^2), \tag{B.19}$$

with $\gamma_2 > 0$. The locus of the saddle homoclinic bifurcation, **SHB**, is given by equation (B.13), thus we can derive an expression for it by evaluating (B.19) at $h = 1/6$, where the integrals $I_1(1/6)$ and $I_2(1/6)$ are given by

$$I_1\left(\frac{1}{6}\right) = \int_{H=\frac{1}{6}} \zeta_2\,d\zeta_1 = 2\int_{-\frac{1}{2}}^{1} \sqrt{\frac{2}{3}\zeta_1^3 - \zeta_1^2 + \frac{1}{3}}\,d\zeta_1 = \frac{6}{5} \tag{B.20}$$

and

$$I_2\left(\frac{1}{6}\right) = \int_{H=\frac{1}{6}} \zeta_1 \zeta_2 \, d\zeta_1 = 2\int_{-\frac{1}{2}}^{1} \zeta_1 \sqrt{\frac{2}{3}\zeta_1^3 - \zeta_1^2 + \frac{1}{3}} \, d\zeta_1 = \frac{6}{35} . \tag{B.21}$$

Therefore the curve **SHB** in the (γ_1, γ_2)-plane is given by

$$\mathbf{SHB} = \left\{ (\gamma_1, \gamma_2) : \ \gamma_1 = -\frac{1}{7}\gamma_2 + O(\|(\gamma_1, \gamma_2)\|^2), \ \gamma_2 \geq 0 \right\} . \tag{B.22}$$

It can be proved than the quotient $I_1(h)/I_2(h)$ is positive for every $h \in [0, 1/6]$, Kuznetsov [56], and therefore the cycles are unique for every h, in particular the locus of the saddle homoclinic bifurcation given by **SHB** in (B.22) is also unique.

Finally we express the curve **SHB** in the (ξ_1, ξ_2)-plane, by considering the homeomorphism between the regions of the real plane $A = \{(\xi_1, \xi_2) : \ \xi_2^2 - 4\xi_1 > 0\}$ and $B = \{(\gamma_1, \gamma_2) : \ \gamma_2 > 0\}$ given by the relationships (B.7) and (B.8), which can be re-written as

$$\begin{aligned} \xi_1 &= \gamma_1 \gamma_2^2 (\gamma_1 + \gamma_2) , \\ \xi_2 &= -\gamma_2 (\gamma_2 + 2\gamma_1) . \end{aligned}$$

Here we can use the Inverse Function theorem to obtain γ_1 and γ_2 as functions of (ξ_1, ξ_2) and therefore we find an expression for the locus of the saddle homoclinic bifurcation in the (ξ_1, ξ_2)-parameter space given by

$$\mathbf{SHB} = \left\{ (\xi_1, \xi_2) : \ \xi_1 = -\frac{6}{25}\xi_2^2 + O(\|(\xi_1, \xi_2)\|^3), \ \xi_2 < 0 \right\} ,$$

which is equation (5.39) of section 5.3.2.1.

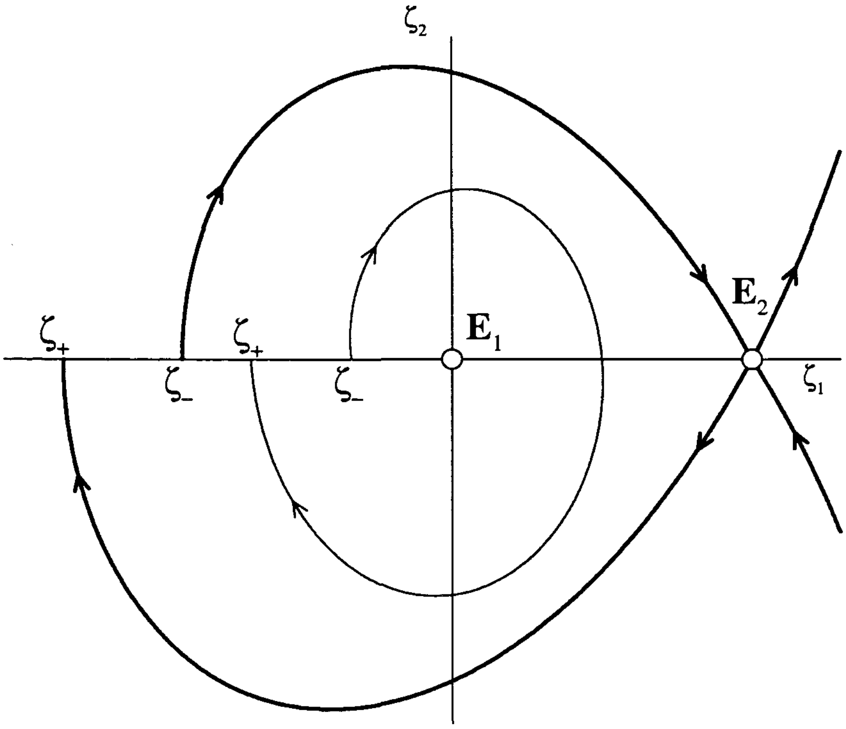

Figure B.3: The labelled points $\mathbf{E}_1$ and $\mathbf{E}_2$ are the equilibria of the system (B.5)-(B.6) for any given γ_1 and γ_2 and the solid lines are the sketch of some of its orbits. The split function Δ given by (B.11) evaluates the difference between the values of the Hamiltonian at ζ_- and ζ_+. The bold lines are the saddle separatrices and the value of the Δ at $h = 1/6$ is given by the difference of the Hamilton function at the correspondent ζ_- and ζ_+.

Bibliography

[1] P.G. de Gennes and J. Prost. *The Physics of Liquid Crystals*, volume 83 of *International Series of Monographs on Physics.* Clarendon Press, Oxford, 2nd. edition, 1993.

[2] G. Vertogen and W. H. de Jeu. *Thermotropic liquid crystals, fundamentals.* Springer Series in Chemical Physics. Springer-Verlag, Berlin, 1988.

[3] T.J. Sluckin. Lecture notes of graduate course on liquid crystals, 1998.

[4] A.D. Rey and T. Tsuji. Recent advances in theoretical liquid crystal rheology. *Macromol. Theory Simul.*, 7:623, 1998.

[5] J.L. Ericksen. Anisotropic Fluids. *Arch. Rational Mech. Anal.*, 4:231, 1960.

[6] J.L. Ericksen. Conservation laws for liquid crystals. *Trans. Soc. Rheol.*, 5:23, 1961.

[7] F.M. Leslie. Some constitutive equations for anisotropic fluids. *Quart. J. Mech. Appl. Math.*, 19(3):357, 1966.

[8] F.M. Leslie. Some constitutive equations for liquid crystals. *Arch. Ration. Mech. Anal.*, 28:265, 1968.

[9] F.M. Leslie. Theory of flow phenomena in liquid crystals. *Adv. Liq. Cryst.*, 4:1, 1979.

[10] F.M. Leslie. An analysis of a flow instability in nematic liquid crystals. *J. Phys. D: App. Phys.*, 9:925, 1976.

[11] I. Zúñiga and F.M. Leslie. Shear flow instabilities in nonaligning nematic liquid crystals. *Europhys. Lett.*, 9(7):689, 1989.

[12] I. Zúñiga and F.M. Leslie. Shear flow instabilities in non-flow-aligning nematic liquid crystals. *Liq. Cryst.*, 5(2):725, 1989.

[13] P. Pieranski and E. Guyon. Two shear flow regimes in nematic *p-n*-hexyloxybenzilidene-*p′*-aminobenzonitrile. *Phys. Rev. Lett.*, 32(17):924, 1974.

[14] P.E. Cladis and S. Torza. Stability of nematic liquid crystals in Couette flow. *Phys. Rev. Lett.*, 35(19):1283, 1975.

[15] I. Zúñiga. Orientational instabilities in Couette flow of non-flow-aligning nematic liquid crystals. *Phys. Rev. A*, 41(4):2050, 1990.

[16] P.K. Currie and G.P. MacSithigh. The stability and dissipation of solutions for shearing flow of nematic liquid crystals. *Q. J. Mech. Appl. Math.*, XXXII(4):499, 1979.

[17] J.G. McIntosh, F.M. Leslie, and D.M. Sloan. Stability for shearing flow of nematic liquid crystals. *Continuum Mech. Thermodyn.*, 9:293, 1997.

[18] W.H. Han and A.D. Rey. Orientation symmetry breakings in shearing liquid crystals. *Phys. Rev. E*, 50(2):1688, 1994.

[19] W.H. Han and A.D. Rey. Dynamical simulations of shear-flow-induced chirality and twisted-texture transitions of a liquid-crystalline polymer. *Phys. Rev. E*, 49(1):597, 1994.

[20] W.H. Han and A.D. Rey. Theory and simulation of optical banded textures of nematic polymers during shear flow. *Macromolecules*, 28(24):8401, 1995.

[21] G. Marrucci and F. Greco. Flow behavior of liquid crystalline polymers. *Adv. Chem. Phys.*, LXXXVI:331, 1993.

[22] G. Marrucci. Tumbling regime of liquid crystalline polymers. *Macromolecules*, 24(14):4176, 1991.

[23] W.R. Burghardt and G.G. Fuller. Role of director tumbling in the rheology of polymer liquid crystal solutions. *Macromolecules*, 24(9):2546, 1991.

[24] W.R. Burghardt and G.G. Fuller. Transient shear flow of nematic liquid crystals: Manifestations of director tumbling. *J. Rheol.*, 34(6), 1990.

[25] M. Srinivasarao and G.C. Berry. Rheo-optical studies on aligned nematic solutions of a rodlike polymer. *J. Rheol*, 35(3):379, 1991.

[26] M. Doi. Molecular dynamics and rheological properties of concentrated solutions of rodlike polymers in isotropic and liquid crystalline phases. *J. Polym. Sci. Polym Phys. Ed.*, 19:229, 1981.

[27] M. Doi and S.F. Edwards. *The Theory of Polymer Dynamics*, volume 73 of *International Series of Monographs on Physics.* Clarendon Press, Oxford, 1986.

[28] G. Marrucci and P.L. Maffettone. Description of the liquid-crystalline phase of rodlike polymers at high shear rates. *Macromolecules*, 22(10):4076, 1989.

[29] R.G. Larson. Arrested tumbling in shearing flows of liquid crystal polymers. *Macromolecules*, 23(17):3983, 1990.

[30] R.G. Larson and H.C. Öttinger. The effects of molecular elasticity on out-of-plane orientations in shearing flows of liquid crystalline polymers. *Macromolecules*, 24:6270, 1991.

[31] P.L. Maffettone and S. Crescitelli. Bifurcation analysis of a molecular model for nematic polymers in shear flows. *J. Non-Newtonian Fluid Mech.*, 59:73, 1995.

[32] V. Faraoni, M. Grosso, and S.Crescitelli. The rigid-rod model for nematic polymers: An analysis of the shear flow problem. *J. Rheol.*, 43(3):829, 1999.

[33] C.V. Chaubal et al. A comparison of closure approximation for the doi theory of LCPs. *J. Rheol.*, 39(1):73, 1995.

[34] P.L. Maffettone and S. Crescitelli. The rigid-rod model for nematic polymers: Testing closure approximations with bifurcation analysis. *J. Rheol.*, 38(5):1559, 1994.

[35] J.J. Magda, Seong-Gi Baek, and K.L. DeVries. Shear flows of liquid crystal polymers: measurements of the second normal stress difference and the Doi molecular theory. *Macromolecules*, 24:4460, 1991.

[36] T. Maruyama, G.G. Fuller, M. Grosso, and P.L. Maffettone. The dynamics of two dimensional polymer nematics. *J. Non-Newtonian Fluid Mech.*, 76:233, 1998.

[37] M.C. Friedenberg, G.G. Fuller, C.W. Frank, and C.R. Robertson. In situ optical studies of flow-induced orientation in a two dimensional polymer solution. *Macromolecules*, 29:705, 1996.

[38] P.L. Maffettone, M. Grosso, M.C. Friedenberg, and G.G. Fuller. Extensional flow of a two-dimensional polymer liquid crystal. *Macromolecules*, 29(26):8473, 1996.

[39] S. Hess. Fokker-Planck-equation approach to flow alignment in liquid crystals. *Z. Naturforsch.*, 31A:1034, 1976.

[40] P. D. Olmsted. *The effect of shear flow on the isotropic-nematic transition in liquid crystals.* PhD thesis, University of Illinois at Urbana-Champaign, 1991.

[41] P.D. Olmsted and P.M. Goldbart. Isotropic-nematic transition in shear flow: State selection, coexistence, phase transitions, and critical behavior. *Phys. Rev. A*, 46(8):4966, 1992.

[42] P.D. Olmsted and P. Goldbart. Theory of the nonequilibrium phase transition for nematic liquid crystals under shear flow. *Phys. Rev. A*, 41(8):4578, 1990.

[43] P.D. Olmsted and P. Goldbart. Non-equilibrium phase transitions in nematic liquid crystals under shear flow. *Mol. Crys. Liq. Cryst.*, 198:265, 1991.

[44] V. Popa-Nita, T.J. Sluckin, and A.A.Wheeler. Statics and kinetics at the nematic-isotropic interface: effects of biaxiality. *J.Phys.II France*, 9:1997, 1997.

[45] Y. Farhoudi and A.D. Rey. Shear flows of nematic polymers. I. Orienting modes, bifurcations, and steady state rheological predictions. *J. Rheol.*, 37(2):289, 1993.

[46] T. Tsuji and A.D. Rey. Orientation mode selection mechanisms for sheared nematic liquid crystalline materials. *Phys. Rev. E*, 57(5):5609, 1998.

[47] T. Tsuji and A.D. Rey. Effect of long range order on sheared liquid crystalline materials. part 1: compatibility between tumbling behavior and fixed anchoring. *J. Non-Newtonian Fluid Mech.*, 73:127, 1997.

[48] T.C. Lubensky. Molecular description of nematic liquid crystals. *Phys. Rev. A*, 2(6):2497, 1970.

[49] D.R.J. Chillingworth, E. Vicente Alonso, and A.A. Wheeler. Geometry and dynamics of a nematic liquid crystal in a uniform shear flow. *J. of Physics A*, 2000. submitted.

[50] P. G. de Gennes. Short range order effects in the isotropic phase of nematics and cholesterics. *Mol. Cryst. and Liq. Cryst.*, 12:193, 171.

[51] S.R. de Groot and P. Mazur. *Non-equilibrium Thermodynamics.* North-Holland Publishing Co., Amsterdam, 1962.

[52] T. Qian and P. Sheng. Generalized hydrodynamic equations for nematic liquid crystals. *Phys. Rev. E*, 58(6):7475, 1998.

[53] R. S. Schechter. *The Variational Method in Engineering.* Chemical Engineering Series. McGraw-Hill, 1967.

[54] P.G. Drazin. *Nonlinear Systems.* Cambridge Texts in Applied Mathematics. Cambridge University Press, 1992.

[55] S. Wiggins. *Introduction to Applied Nonlinear Dynamical Systems and Chaos*, volume 2 of *Texts in Applied mathematics.* Springer-Verlag, New York, 1990.

[56] Y.A. Kuznetsov. *Elements of Applied Bifurcation Theory*, volume 112 of *Applied Mathematical Sciences.* Springer-Verlag, New York, 1995.

[57] J. Guckenheimer and P. Holmes. *Nonlinear Oscillations, Dynamical Systems, and Bifurcations of Vector Fields*, volume 42 of *Applied Mathematical Sciences.* Springer-Verlag, New York, 1983.

[58] E.J. Doedel et al. *AUTO97: continuation and bifurcation software for ordinary differential equations (with HomCont)*, 1997.